Proceedings of the

8th INTERNATIONAL CONFERENCE ON SANDWICH STRUCTURES (ICSS8)

6-8 MAY 2008, PORTO, PORTUGAL

Edited by

António J. M. Ferreira

Faculty of Engineering, University of Porto, Portugal

Organized by

Faculty of Engineering, University of Porto

Sponsored by

The Office of Naval Research, USA,
(Dr. Yapa D. S. Rajapakse, Program Manager, Solid Mechanics)

ALCAN Composites, Switzerland

University of Porto, Portugal

INEGI, Portugal

Evonik – Rohm, Germany

FCT – Portuguese Foundation for Science and Technology

Endorsed by

American Society for Composites
International Committee for Composite Materials
Society of Plastics Engineers Europe
Portuguese Association for Theoretical, Applied and Computational Mechanics

May 2008, Porto, Portugal

Cover design: Publindústria, Produção de Comunicação, Lda.

Impresso por: Publindústria, Produção de Comunicação, Lda.
Legal Deposite: ??????/??
ISBN: 978-972-????-??-?

PRINTED IN PORTUGAL

PREFACE

Sandwich materials and structures have an increasing relevance in engineering, in various industrial applications.
This volume of proceedings contains 4 keynote lectures, and 80 contributed papers presented at the 8th International Conference on Sandwich Structures held on 6-8 May 2008 in Porto, Portugal.

The conference provided an international forum for discussion and dissemination of recent advances in sandwich structures science and technology and its industrial applications. The papers presented at the conference cover a wide spectrum of topics and were contributed from 20 countries around the world. They report the current state-of-the-art and point to future directions of research of this promising and exciting area.

The organization of such a conference would not have been possible without the support and contributions of many individuals and organizations. The conference was supported by The Office of Naval Research, USA, with Dr. Yapa D. S. Rajapakse as the program manager, by the Rector of the University of Porto, Portugal, by INEGI, Portugal, by the industrial companies ALCAN Composites, Switzerland and Evonik – Rohm, Germany, and finally by the FCT – Portuguese Foundation for Science and Technology. The conference received the kind endorsement of the American Society for Composites, the International Committee for Composite Materials, the Society of Plastics Engineers Europe and the Portuguese Association for Theoretical, Applied and Computational Mechanics. I am indebted to Professor Ole Thybo Thomsen of Aalborg University, Denmark for continuous discussion and assistance during the organization of this conference. I am also indebted to Professor António Torres Marques for the organization of the Advanced School on Sandwich Structures, held just before the ICSS8 conference. The support of all members of the Scientific Committee in the review of abstracts is highly appreciated. In particular the support of Professor Jack Vinson will provide authors the opportunity to submit extended versions of their papers for review and potential publication at the Journal of Sandwich Structures and Materials. This conference would not have its success without the kind support of Dr. Yapa D. S. Rajapakse, organizer of ONR special sessions on marine applications.

Thanks to all contributions for their careful preparation of the manuscripts and all the Plenary Speakers for their special support.

I would like to thank my colleagues Paulo Neves, Ana Neves, and Carla Roque for their patience in helping the organization.

INTERNATIONAL SCIENTIFIC COMMITTEE

CONTENTS	

PLENARY LECTURES

8th International Conference on Sandwich Structures
ICSS 8
A. J. M. Ferreira (Editor)

RESEARCH IN SANDWICH STRUCTURES AT ONR

Yapa D. S. Rajapakse

Office of Naval Research
Arlington, VA 22203-1995, USA
e-mail: Yapa.Rajapakse@navy.mil

Summary. The design and effective utilization of advanced marine structures, with enhanced performance characteristics and reduced life-cycle costs, provides many significant challenges to the engineering community. These structures operate in severe environments, and are designed to withstand complex multi-axial loading conditions, including highly transient loads. The unique and hostile marine environment requires us to account for the presence of sea water and moisture, temperature extremes, time-dependent three-dimensional loading due to wave/hull slamming and high sea states, hydrostatic pressure, and other factors. Additional requirements on Naval structures include the ability to withstand extreme dynamic loading, due to weapons impact, or to air or underwater explosions and implosions.

The Solid Mechanics Research Program of the Office of Naval Research (ONR) provides the scientific basis for the effective design of affordable and reliable Naval structures, and for the assessment of structural integrity. The current focus is on mechanics of marine composite materials and composite sandwich structures. The program deals with understanding and modelling the physical processes involved in the response of glass-fiber and carbon-fiber reinforced composite materials and composite sandwich structures to static, cyclic, and dynamic, multi-axial loading conditions, in severe environments. The establishment of these models, with predictive capabilities, require multi-scale, multi-physics analysis. Avenues for enhancing the performance of marine composite structures through the introduction of nanoparticles (and nanotubes), and through the incorporation of novel design concepts, are also being explored. Research on multifunctional composites seeks to enhance performance through the incorporation of additional beneficial attributes, without compromising on the mechanical properties.

Recent achievements of the leading researchers in mechanics of composite materials and sandwich structures, supported by the ONR Solid Mechanics Program, will be summarized. Topics covered include: sea water effects on marine composites, long term durability, size/scale effects, impact damage, fatigue and failure theories, strain rate effects, interfacial failure, interactions of multiple delaminations, failure and fatigue of foam core, fluid-structure interaction effects, and concepts for the mitigation of damage. Future directions of research include greater emphasis on shock/blast effects, implosions, and hull slamming.

8th International Conference on Sandwich Structures
ICSS 8
A. J. M. Ferreira (Editor)

THE DYNAMIC PERFORMANCE OF SANDWICH BEAMS WITH LATTICE CORES

Norman A. Fleck *

*Cambridge University Engineering Dept.,
Trumpington St., Cambridge, CB2 1PZ, UK

Summary. A combined experimental and numerical study has been performed to assess the potential of sandwich structures in resisting shock loading. The sensitivity of static and dynamic core strength to core topology is explored, and the effects of fluid-structure interaction is included in the finite element analysis. Experiments are performed on clamped beams and panels, using metal foam projectiles as a means of imposing the shock loading: the pressure-time transient is similar to that imposed by an underwater blast. The core topologies investigated include the corrugated core, Y-core, square honeycomb, diamond core and prismatic core. We take as specific examples here the dynamic response of the corrugated and Y-core.

The dynamic response of fully clamped, monolithic and sandwich plates of equal areal mass has been measured by loading rectangular plates over a central patch with metal foam projectiles. All plates are made from AISI 304 stainless steel, and the sandwich topologies comprise two identical face-sheets and either Y-frame or corrugated cores. The resistance to shock loading is quantified by the permanent transverse deflection at mid-span of the plates as a function of projectile momentum. At low levels of projectile momentum both types of sandwich plate deflect less than monolithic plates of equal areal mass. However, at higher levels of projectile momentum, the sandwich plates tear while the monolithic plates remain intact. Three-dimensional finite element (FE) calculations adequately predict the measured responses, prior to the onset of tearing. These calculations reveal that the accumulated plastic strains in the front face of the sandwich plates exceed those in the monolithic plates. These high plastic strains lead to failure of the front face sheets of the sandwich plates at lower values of projectile momentum than for the equivalent monolithic plates.

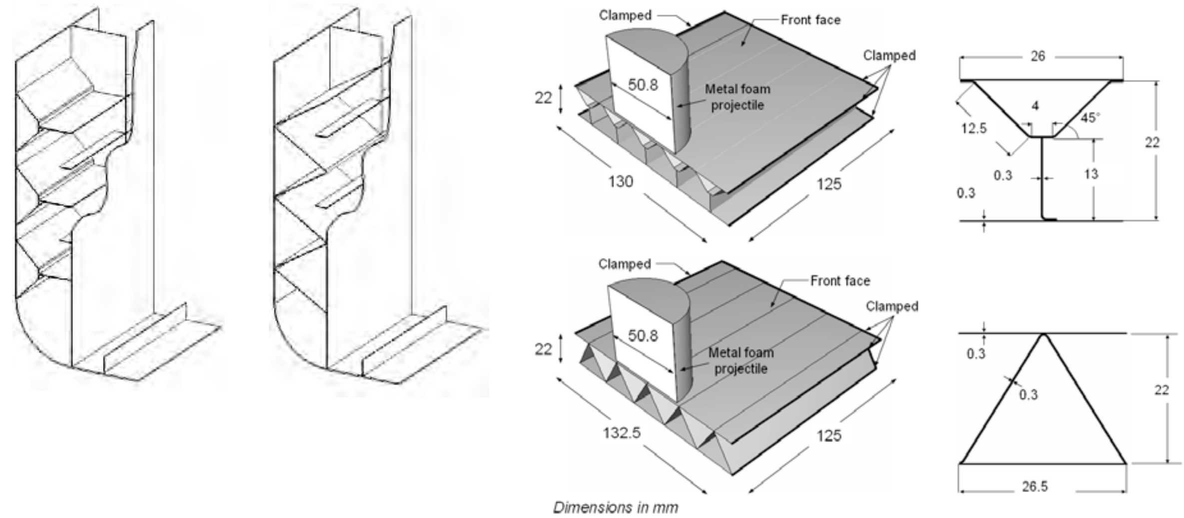

(a) (b) (c)

Sketch of the (a) Y-frame and (b) corrugated sandwich cores as used in ship hull construction. The core is sandwiched between the inner and outer hulls of the ship. (c) Sketch of the clamped sandwich plate geometry and the loading arrangement. The cross-section is also shown for each topology. All dimensions are in mm.

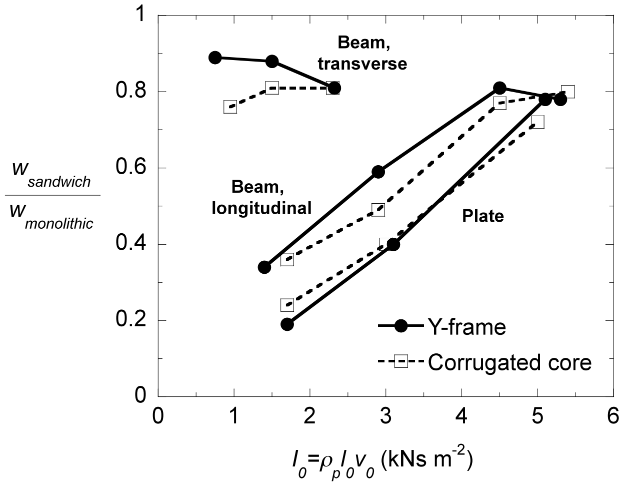

Comparison of the measured normalized permanent rear-face deflections at mid-span of the dynamically loaded Y-frame and corrugated core sandwich structures, as a function of the foam projectile momentum I_0. The rear-face deflection of the sandwich structure is normalized with the rear-face deflection of the corresponding monolithic structure of the same mass.

8th International Conference on Sandwich Structures
ICSS 8
A. J. M. Ferreira (Editor)

SANDWICH STRUCTURES IN ROTOR BLADES FOR WIND TURBINES

Torben K. Jacobsen
R&D Department
LM Glasfiber A/S
Rolles Møllevej 1
DK-6640 Lunderskov
tkj@lmglasfiber.com

Introduction

Rotor blades for wind turbines have grown in length with approximately 3-5 m per year during the last decade. Today, the typical length of a blade is 35-45 m and three blades are used to create a 1.5 to 3 MW turbine. One of the largest blades in the world is produced by LM Glasfiber, see Figure 1. It is 61.5 m long and mounted on a 5 MW turbine. The development trend has been towards light-weight blades and the use of sandwich structures in blades have thus been increasing. Today, sandwich structures constitute a large part of the materials used in a blade.

Figure 1: LM Glasfiber's 61.5 m long blade next to the F-16 military fighter.

At LM Glasfiber the main processing technique for producing blades is the vacuum assisted resin transfer moulding process (VARTM). Therefore, we will focus on the sandwich structures that go hand in hand with this processing technique and the necessary advances in technology that would lead to even more competitive blade designs.

Sandwich structures in rotor blades

The sandwich structures are created in-situ during the infusion process and the core materials are thus also used as processing media. Typical this is done by making grid-scoring patterns in the bulk core material to create highly flexible cores that can follow double curved surfaces. The saw cuts enable resin flow during the vacuum infusion process. The two most commonly used core materials are PVC foam and balsa wood.

In the shells the primary function of the sandwich structures is to distribute the shear forces from the surface air pressure (lift) between the edge- and the flap-wise primary structure. The stability of the two shells is managed by one or more shear webs connecting the two shells. The shear webs are flat sandwich structures, where there is no need for drapability. Besides this there is a minor use of sandwich structures as e.g. bulk heads to make local reinforcements (e.g. lifting points) or as platforms and covers inside the blade.

Requirements to core materials for rotor blades

In this section we will outline the issues that have to be considered when choosing and designing a core material for sandwich structures in rotor blades for wind turbines.

<u>Mechanical properties</u>

A high specific out-of-plane shear modulus and strength is the main mechanical property of the core material itself to enable the sandwich structure to carry large shear loads and restrict buckling. Besides this it is desirable that the following properties are as high as possible:

- Yield shear stress within a temperature range of (-50 C to +60 C).
- Interfacial shear strength between glass fibre skin and core material
- Fatigue resistance that prevents shear failure in core and interfacial delaminations developing from small processing defects.

<u>Processing properties</u>

The core material has to be an integrated part of the vacuum infusion of the composite structure and thus assist in distributing the resin to impregnate the glass fibre skins. The resin uptake in the core material should be kept at a minimum. Low density foams usually have larger cells and the amount of resin uptake therefore increase. Coatings are usually applied to balsa wood to reduce the resin uptake within the wood structure. To enable the cores to follow the double curvature geometry of a rotor blade it is state of art to cut or saw the cores into small blocks and glue these blocks on e.g. a thin glass fibre mesh. The space between the blocks acts as fast resin transportation lanes. The resin mesh created in between the core blocks also adds additional shear stiffness to the core. However, the additional resin increases the weight of the sandwich structure and today it is not common to include the additional stiffness of the resin mesh in the calculations of the structure. The reason is that the stiffness contribution will depend heavily on the geometry of the blade i.e. how much the rectangular blocks separate from each other.

The core materials must also be suitable for machining and be tough enough such that e.g. thin sections at the end of a tapering core do not break off during handling and layup of the cores in the mould. Dimensional stability is also a pre-requisite for a successful fit in the mould.

During the curing of thermoset resins a high temperature of 60-120 C is usually needed to speed up the production throughput. The temperature can be created by either heating the mould, take advantage of exo-thermic curing or combinations thereof. The high temperature exposure takes usually around 1 to 6 hours. The core must not release gasses entrapped during foaming or release moisture as this can create air-voids and interfacial delaminations.

Environmental impact

Core materials must be recyclable to protect the environment and lower the cost of disposal.

Challenges

New core developments arising are mostly focused on matching the properties of either PVC or balsa wood and thus act as sources of alternative supply (substitution materials). Furthermore, the market for PVC foam and balsa wood is largely controlled by a few large players. The large growth within the composites industry has led to shortage in supply of core materials with significant cost increases as a result.

The future challenge is therefore to develop a “game-changer” type of core material for industrial applications. In particular, this material must fulfill the following requirements:

- Large reduction in cost of specific shear modulus.
- Materials can be locally sourced, produced world-wide and thus exhibit short lead times.
- Low variation in properties.

8th International Conference on Sandwich Structures
ICSS 8
A. J. M. Ferreira (Editor)

FUTURE NEEDS FOR SANDWICH STRUCTURES RESEARCH AND DEVELOPMENT

Dan Zenkert*

*Department of Aeronautical and Vehicle Engineering
Kungliga Tekniska Högskolan
SE-10044 Stockholm, Sweden
e-mail: danz@kth.se, web page: http://www.ave.kth.se

The advantages of sandwich structures are commonly claimed to be that not only can one design a structure with very high stiffness and strength to weight ratio, but also that one inherently obtains a number of added functions. Those functions are for example thermal insulation, good sound reduction, high specific energy absorption, and particularly that one has a wide choice of materials to select from. That one can obtain high stiffness and strength is not arguable, but one can debate whether all the integrated functions are really possible. This depends on the material selection, the design and the application.

In some areas of applications sandwich structures have been used for quite some time, mainly due to the above advantages, or combinations thereof. In Naval structures for example, the development has lead to designs that further enables integration of functions, resulting in even more efficient structures. This development has by no means slowed down and future hull structures are being developed for which the requirements are even more demanding. To enable this, new materials, material combinations and structural concepts are being investigated.

In other areas of applications sandwich structures are not used much. There are many reasons for that, for example structural integrity issues, damage tolerance, sound and vibration, joining, or manufacturing. A not uncommon problem for the further and wider use of sandwich structure is the lack of experience among engineers. Another is the cost of materials and completely new manufacturing methods (compared to traditional metals structure manufacturing). In some sense, the sandwich “community” is faced with a pedagogical problem trying to convince the industry of the potential advantages of using sandwich structures. Low weight alone is usually not enough as an argument.

The theory of sandwich structures has over the years evolved and today the engineer has a wide range of available tools to design sandwich structures. There is still need however for more research work into issues like damage tolerance, sound absorption, etc. One of the next major hurdles is to further develop efficient manufacturing methods, both in terms of making sandwich panels but also in the joining of complete structures and fastening of equipment.

A more generic problem is that of multi-disciplinary design. Although we have (most of) the tools required to design a sandwich structure for high structural efficiency or, for example, for good acoustic properties, these designs are commonly not compatible meaning that the best structure for carrying load is not necessarily the best one for acoustics, and vice versa. The “sub-optimization” for individual requirements often leads to higher cost and higher weight. This creates a need for integrated design. Since most of the costs and weight are assigned during the preliminary design phase of a structure, such integrated design processes are particularly suited for that phase. Optimization procedures are nowadays more frequently used for this purpose, for example for minimizing structural weight given certain design constraints. Integrated design using optimization, or multi-disciplinary design optimization (MDO), which couples many different constraints is something that holds great potential in the future, particularly for sandwich structures. MDO would include structural constraints, as well as acoustical, manufacturing, dynamics, etc. aiming at finding better overall structural solutions. Potentially also materials selection could be included.

Since low weight is the main driver for sandwich structures one needs to find arguments for the exploitation of that. One option is to assign a cost on weight. If so, one can compare different concepts on an equal basis. For example, is a higher manufacturing cost or the use of more expensive materials balanced against lower weight? This requires a more long-term strategy from the end-users of structures. One way of estimating the cost of weight for a vehicle is simply to calculate the life-time fuel burn cost per unit structural weight. This cost would differ between different applications. A commercial airliner or passenger ferry will have a fairly high cost since the total energy consumption over the life-time will be high, while for example a car will have a much lower cost. Another important issue in this discussion is that different people will have different views being a vehicle manufacturer or an end-user.

An interesting possible future scenario is to use life cycle cost (LCC) as an objective for multi-disciplinary design optimization. What does the structure look like that gives the lowest life cycle cost? Another potentially very influential driver towards more high-performing structural concepts that could dramatically increase the use of light-weight sandwich structures is the threatening climate chance. It will very likely in the near future increase the price of fuels and possibly also force a wide introduction of CO_2-emission taxes. This will undoubtedly increase the cost of weight allowing for the introduction of light weight materials and structures in a much wider range of applications.

Although the environmental concerns are a great challenge, it also provides opportunities both for academia and industry. Future vehicles will have to be more fuel efficient and thus lighter enforcing the use of high performing materials and structures. One obvious route towards that is an extended use of sandwich structures and materials.

CONTRIBUTED PAPERS

ONR SESSIONS

8th International Conference on Sandwich Structures
ICSS 8
A. J. M. Ferreira (Editor)

EFFECT OF SEA WATER ON MECHANICAL PROPERTIES OF POLYMERIC FOAM AND SANDWICH COMPOISTES

Akawat Siriruk*, Dayakar Penumadu+ and Y. Jack Weitsmanº

*Graduate Student
+Professor and Joint Institute for Advanced materials (JIAM) Chair of Excellence
ºProfessor Emeritus and Distinguished Scientist
Department of Civil and Environmental Engineering, 223 Perkins Hall
University of Tennessee, Knoxville, TN 37996-2010, USA
E-mail: dpenumadu@utk.edu

Key words: Sandwich structures, Sea water effects, Modeling, Environmental degradation

Summary. *This article provides an up-to-date review of research findings concerning the effects of sea water on closed cell polymeric foams and sandwich structures. Those foams, as well as the carbon/vinyl ester composite facings, were studied individually and in their sandwiched combination. The investigations considered the processes of water ingress, water induced damage, wet and dry material properties and expansional deformations. Experimental results were supported by appropriate analytical models.*

1 INTRODUCTION

The utilization of polymeric composite based sandwich structures in naval craft is of current interest to US and several European navies. Their lightweight lowers the center of gravity of the naval vessels, when incorporated in the super structure, and similarly increase the buoyancy of submersibles.

Exposure to sea ambience induces environmental effects into both polymeric facings and polymeric foams. It was established in earlier works that the ingress of sea water is essentially confined to the outer, exposed, facing of the sandwich structure and to just a few adjacent cells of the foam core. Similarly, it was found that the effect of exposure to external temperature remain delimited to the outer facings for a significant time due to the high thermal insulation provided by the PVC foam and polymeric resin in the facing. Consequently, both foregoing environmental effects induce an essentially one-sided expansion into the sandwich structure that tends to distort its shape.

Sea water tends to swell and reduce the mechanical properties of both foam and facing components of the sandwich lay-up. The above reduction, which is most pronounced within the cellular foam, was investigated experimentally by means of custom made shear apparatus and test specimens and supported by analysis.

The aforementioned findings, which were obtained in several previous works [1,2,3,4,5,6], are discussed in this article.

2 SEA WATER EFFECTS ON CLOSED CELL POLYMERIC FOAMS

2.1 Water ingress and water induced damage

Weight gain data were obtained by immersing flat foam samples of several thicknesses and recording results against immersion time up to saturation. Results for the saturated weight gains of H-100 foams are shown in Figure 1 vs. sample thickness [1].

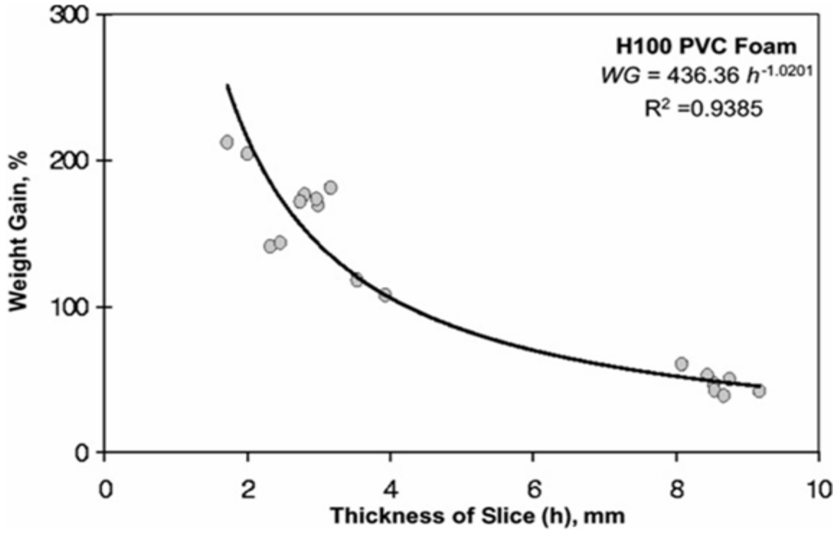

Figure 1: Typical relative weight gain of H100 PVC foam

The results, which could be approximated by $M = 1/h$ (M denoting % weight-gain at saturation and h sample thickness) suggested that sea water is confined to within thin layers of fixed dimensions near the exposed boundaries.

The above proposition was confirmed by detailed observations, such as shown in Figure 2, demonstrating that sea water was indeed confined to within the outer, exposed, cells [2].

Additional verification of the above observation was obtained by the immersion of a 25 mm thick slab of foam up to saturation, then slicing it into 2 mm thin layers parallel to its exposed surface and recording weight losses. Results are shown in Figure 3, where most of the weight-loss was recorded for the outer layer.

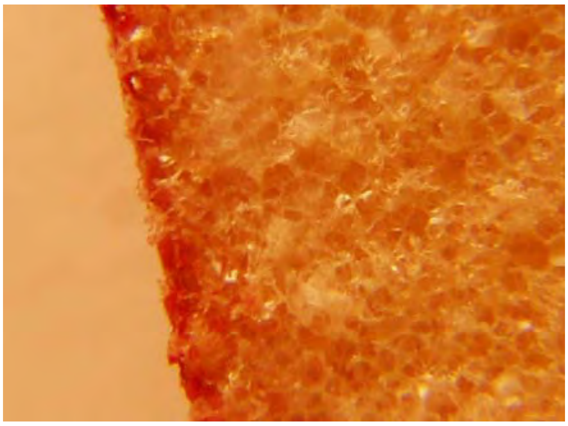

Figure 2: Photo of water confinement to outer cells

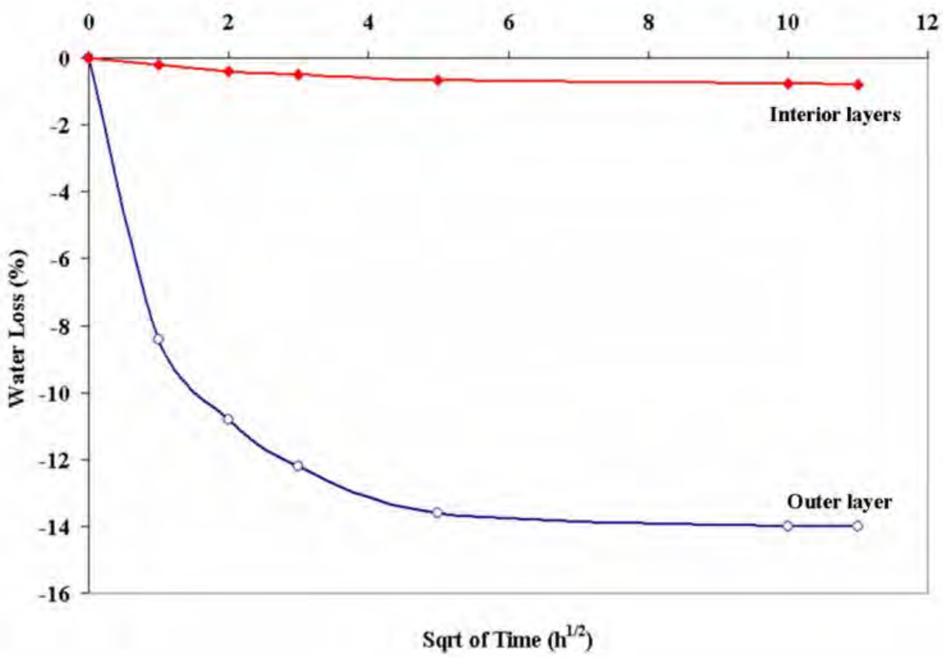

Figure 3: Weight loss data for 2 mm thin slices cut from the outer and interior layers of a $(25\ mm)^3$ H100 foam

Note that the 0.6% weight loss from the inner layers is consistent with experimental data, not included herein, that some water enters the foam due to its permeability.

It was established, by means of confocal microscopy, that sea water damages the cell's walls by deforming them into what appears to be buckled shapes and puncturing them as well. Microscopic observations are shown in figures 4a and 4b [1].

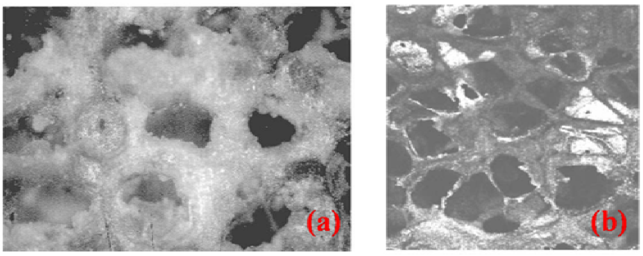

Figure 4a: Sea water causes swelling of foam cell walls, 4b Confocal microscope photograph shows damage (pits and breakage of cell walls) inside the core, 1.78 mm below the surface

A mechanics based model was generated for the purpose of explaining the three paramount issues associated with the aforementioned data, namely, what is the mechanism of water ingress, why is it time dependent, and why does it stop. The basic premises of the above model are that water ingress is caused by the sequential buckling of cellular walls – where sea water induced swelling within the outer layers is inhabited by the dry, inner core of the foam. The buckling process is time dependents because of the viscoelastic relaxation of the walls' moduli as they absorb water, and the process comes to a halt when the water-filled cells are bounded by short walls that resist further buckling. Typical model predictions are shown in Figures 5 and 6. While Figure 5a demonstrates the time-dependent configurations of wet/dry boundaries for a specific cellular configuration, Figure 5b exhibits the scatter in weight-gain predictions in several randomly selected such configurations.

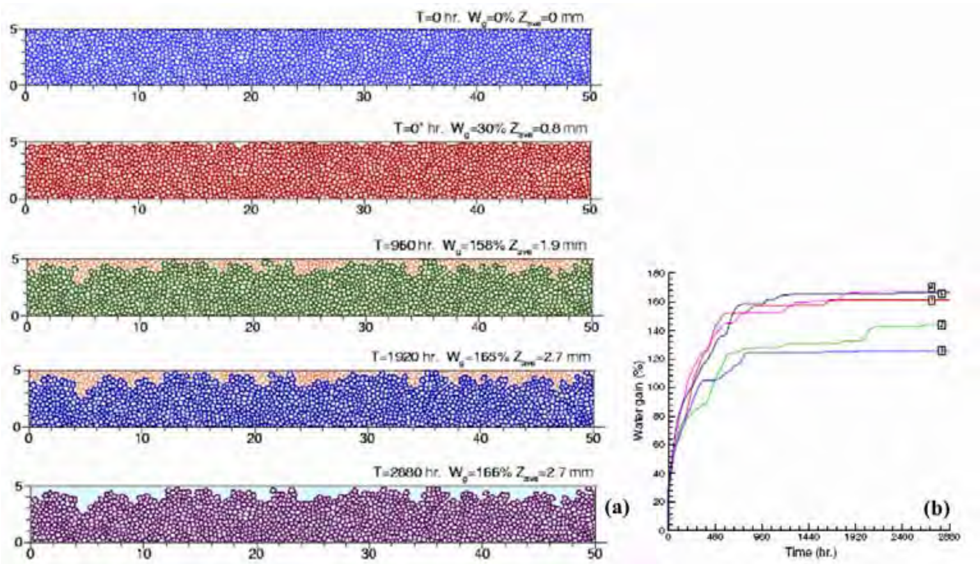

Figure 5(a, b): Sequential water ingress into a Voronoi cell representation of foam. Progressive ''equilibrium'' configurations at increasing time are shown in Fig 5a for a specific random choice of cellular configuration Figure 5b shows predicted weight gain vs. time for five random configurations

2.2 Material properties

Dry values of tensile and shear moduli were obtained by means of specially designed test specimens and test fixtures shown below in Figures 6 and 7, resulting in E = 60 MPa and $G \sim$ 25 Mpa.

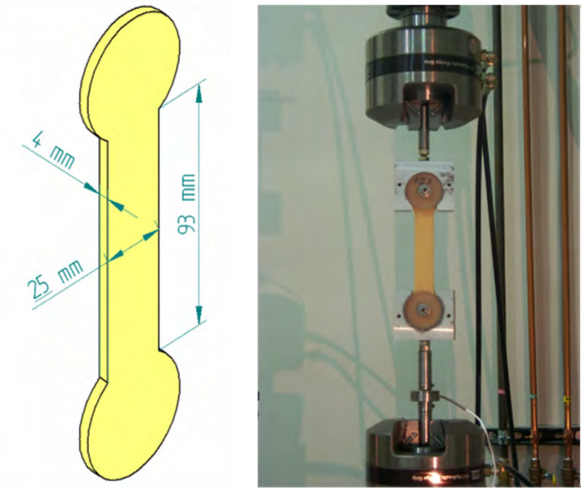

Figure 6a: Specimen shape and dimensions, 6b: Loading system in tension

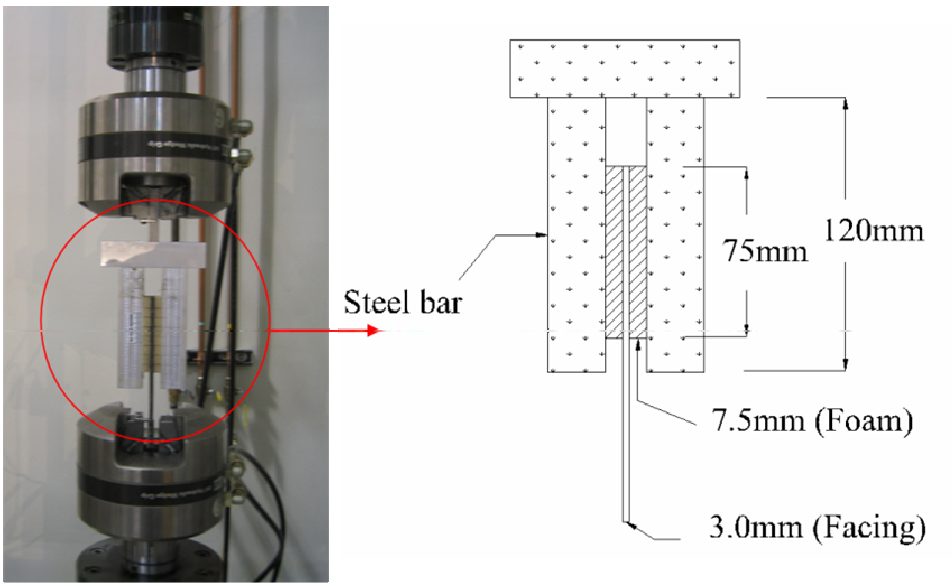

Figure 7: Shear modulus experimental set up

In view of the aforementioned information that the presence of sea water was confined to the outer layer of the test specimen, it was decided to measure its effect on the degradation of the shear modulus by means of torsional shear tests. Results are shown in Figure 8, indicating a 20 % reduction in the overall shear stiffness of the saturated sample within the linear range [3].

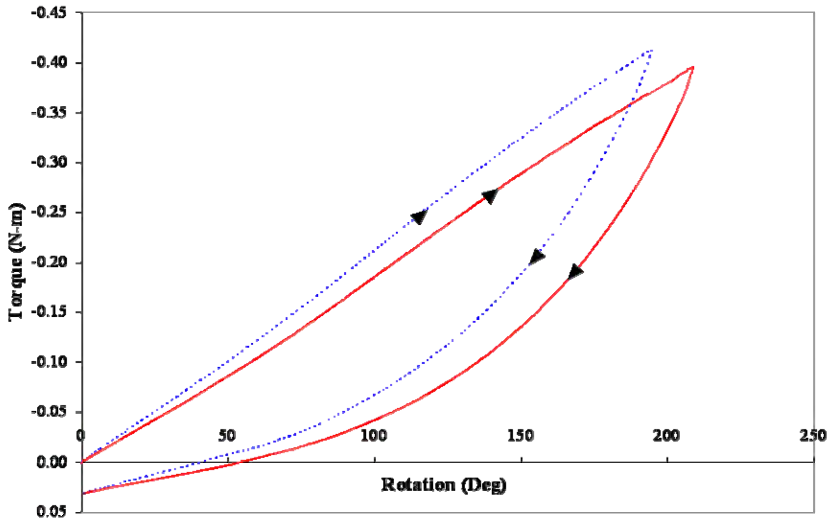

Figure 8: Torque vs. rotation angle for dry (---) and saturated (—) samples

Since the depth δ of the saturated layer could be inferred from previous data (δ = 0.145 mm) this information, together with the knowledge of the specimen's cross-sectional dimensions and the value of G within the dry inner core, yielded a value of $G_w \sim 0.28G = 7.3\,\text{MPa}$, which matched the above overall experimental reduction of 20 %. Considering the incompressibility of the water filled saturated layer, it followed that $E_w \sim 22\,\text{MPa}$ [3].

2.3 Expansional strains and fracture toughness

The expansional strains caused by sea water were recorded during the drying of saturated foam samples by means of extensometer, resulting in ε_H = 2200 με. Thermal conductivity was recorded means of a one sided heating imposed on a 25 mm thick foam slab and a careful recording of temperatures across its thickness vs. time. Thermal expansion was recorded by means of an extensometer. The resulting was ε_T = 70 με/1°C.

Mode I fracture toughness was recorded in five dry cases by splitting a pre-cracked sandwich sample across its mid-plane under displacement control. The crack was channeled to stay within the mid-plane by means of side notches that were cut along the sample's length. The value of G_I was obtained from the standard load/unload data for intermittent values of crack length. For dry foam, this resulted in Average G_I = 770 J/m^2 (STD ~ 100 J/m^2).

3 FACINGS

The facing material consisted of a symmetrical lay-up of woven cross-ply pairs of graphite/vinyl ester polymeric composite with total thickness of 2.7 mm. The modulus of this material along the 0° direction was recorded to be 80 GPa, with minimal reduction when saturated in sea water. Saturation upon immersion at 40°C was achieved within approximately three months, with a weight gain of about 0.4 %. Thermal and sea water induced expansions were recorded in the same manner reported above, resulting in α = 10 $\mu\varepsilon/1^{\circ}$C and ε_H = 450 $\mu\varepsilon$ per 1 % weight gain at saturation. The latter test is being repeated at present.

4 SANDWICH SAMPLES

4.1 Wet and dry interfacial debonding

Wet and dry debonding toughnesses were recorded by means of a custom-made testing set-up, employing 250 mm long specimens measuring 29 mm in height and 25 mm in width, and containing an interfacial pre-crack 25 mm long away from the location of load application, as shown in Figures 9 and 10 below [4,5].

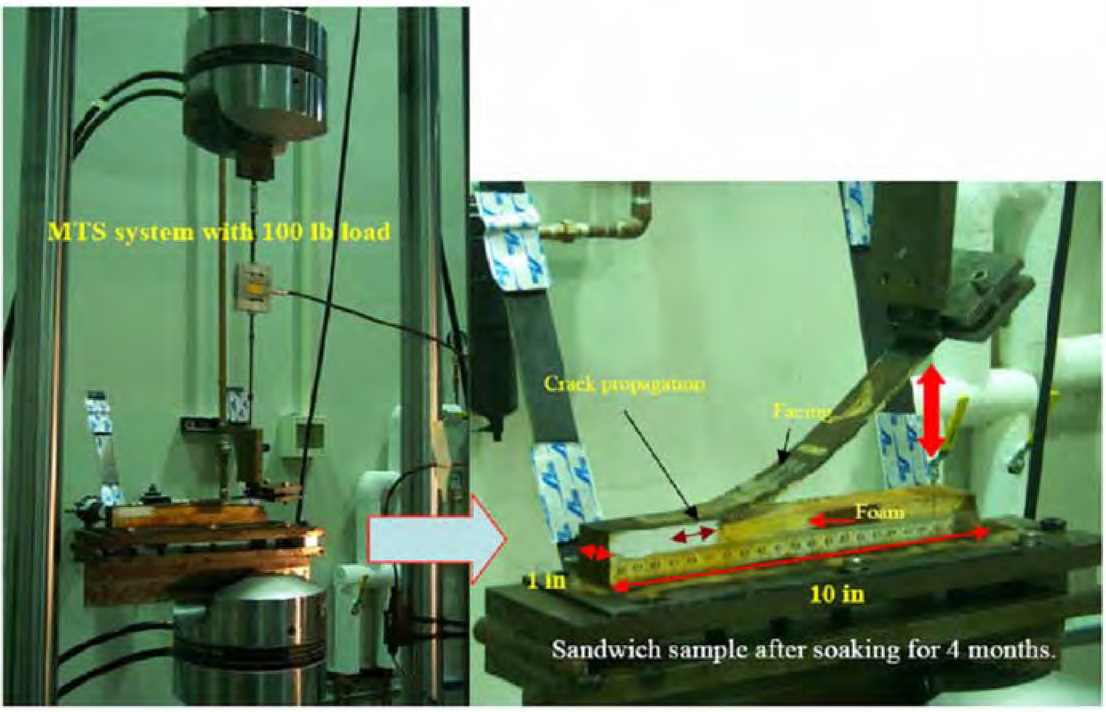

Figure 9: Delamination testing setup using 0.44 kN load cell

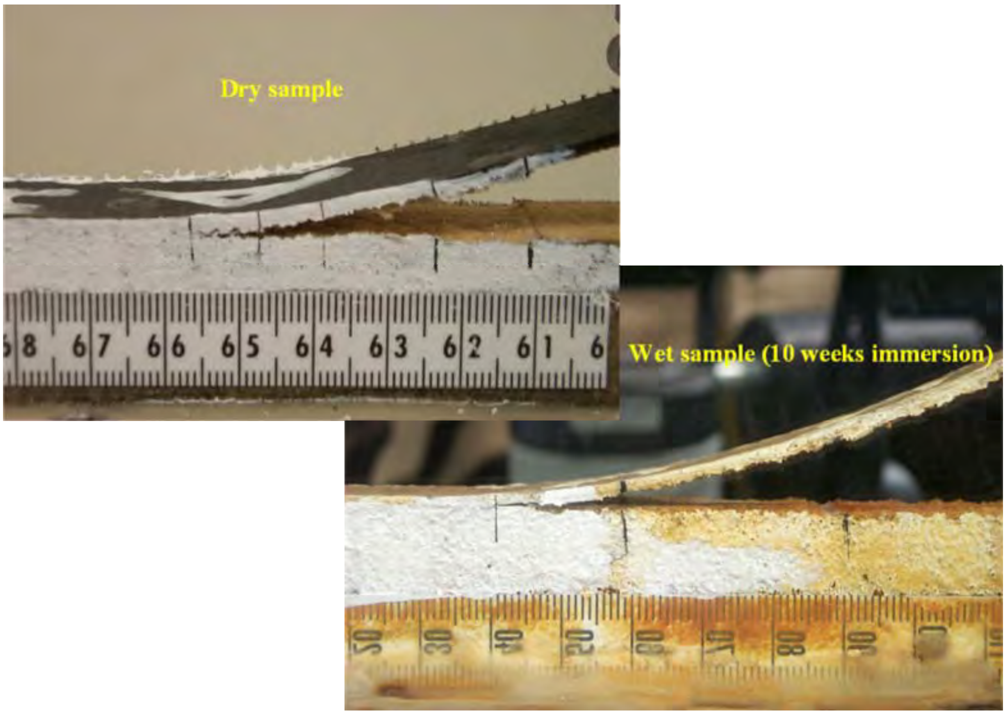

Figure 10: Typical delamination cracks (Dry and Wet sample)

Testing was done under displacement control, resulting in intermittent crack growth and yielding load/unload data for various crack lengths. It should be noted that in the "wet" case it was necessary to re-soak the specimen in sea water for approximately two weeks after each unloading step to ascertain the presence of a wet crack-tip prior to re-loading. These tests yielded a substantial data scatter, whereby G_c in the dry case varied between 541 and 963, while the saturated case resulted in values ranging between 432 and 632 all in J/m^2. Obviously, the exposure to sea water resulted in about 30% reduction in the interfacial G_c.

With both wet and dry material properties available at hand, it was possible to calculate the corresponding values of G_c for the tested debonding geometry. These computations yielded values of G_c = 780-890 for the dry case, and G_c = 522-588 for the wet case (all in J/m^2), thus agreeing reasonably well with experimental data.

4.2 Sea water induced deflection. Load-expansion analogy

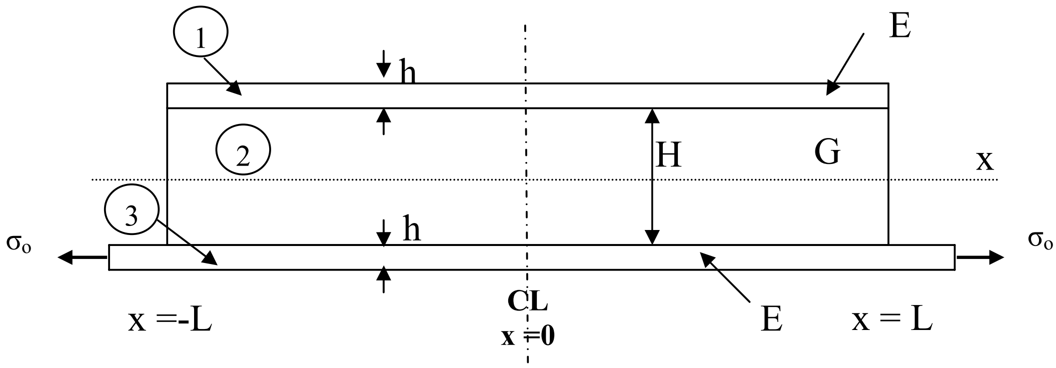

Figure 11: Configuration for tensile loading on bottom facing "3"

Consider the sandwich configuration shown in Figure 11. When this lay-up is subjected to tensile stresses σ_o acting on the bottom facing, a straightforward application of the shear-lag model yields the following expressions for the stresses the top and bottom facings.

$$\sigma_1, \sigma_3 = \frac{\sigma_o}{2}\left(1 \mp \frac{\cosh \alpha x}{\cosh \alpha L}\right) \tag{1}$$

where $\alpha^2 = \dfrac{2G}{hHE}$

In addition, the above loading causes bending, with maximal deflection Δ at x = 0, given by equation (2):

$$\Delta = -\frac{k^2}{\alpha^2}\left(\cosh \alpha L - 1\right) \tag{2}$$

where $k^2 = \dfrac{\sigma_o}{EH \cosh \alpha L}$

Note that while the accompanying strain $(\varepsilon_1, \varepsilon_3) = \dfrac{(\sigma_1, \sigma_3)}{E}$ can be readily validated experimentally for the test set-up shown in Figure 11, it is rather complicated to perform an analogous experiment under a one sided exposure to sea water and temperature.

It is therefore worthwhile to note the existence of a complete analogy, whereby for a uniformly distributed expansional strain e_o along the bottom facing, expressions (1) and (2) remain valid with σ_o replaced by Ee_o.

5 CONCLUDING REMARK

A range of experimental methods, some utilizing custom made testing devices and specifically designed test specimens, were employed to characterize the properties and response of sandwich components. When combined with analytical considerations, the resulting data yield the following values.

Property	Facing	Foam	Dimension
Coefficient of thermal expansion (α)	10	70	$\mu\varepsilon/^{\circ}C$
Moisture expansinal strain at saturation (ε_H)	450	2200	$\mu\varepsilon$ at saturation
Longitudinal modulus (Dry)	80	0.060	GPa
Longitudinal modulus (Wet)	80	0.022	GPa
Shear modulus (Dry)	-	25	MPa
Shear modulus (Wet)	-	7.3	MPa
Delamination toughness (Dry)	780-890		J/m^2
Delamination toughness (Wet)	522-588		J/m^2

Table 1: Summary of experimental results

ACKNOWLEGDEMENTS

This research was supported by ONR Contract N00014710504, under a program managed by Dr.Yapa Rajapakse. The material supplies were provided by Dr. Kunigal Shivakumar of North Carolina A&T State University.

REFERENCES

[1] Xiaoming, Li., Weitsman, Y.J.: "Sea-water effects on foam cored composite sandwich lay-ups." *Composites, Part B:Engineering* Vol.35, pp.451–459 (2004).

[2] Ionita, A., and Weitsman, Y.J.: "A Model for Fluid Ingress in Polymeric Closed Cell Foams." *Mechanics of Materials.*, Vol.39, pp.434-444 (2007).

[3] Akawut Siriruk, Y. Jack Weitsman, and Dayakar Penumadu: "Polymeric foams and their sandwich lay-ups: material properties, Testing, environmental effects and shear-lag modeling," Submitted to *Composites Science and Technology*.

[4] Penumadu, D., Weitsman, Y.J., and Siriruk, A.: "Effect of Sea Water on Interfacial Delamination Behavior of Sandwich Layups." *16th International Conference on Composite Materials*, July 8 – 13, Kyoto, Japan (2007).

[5] Akawut Siriruk, Dayakar Penumadu, and Y. Jack Weitsman: "Effect of sea environment on interfacial delamination behavior of polymeric sandwich structures," To appear in *Composites Science and Technology*.

[6] Weitsman, Y.J. , Siriruk, A., and Penumadu, D.: "Sea Water Effects on Polymeric Composites." *16th International Conference on Composite Materials*, July 8 – 13, Kyoto, Japan (2007).

8th International Conference on Sandwich Structures
ICSS 8
A. J. M. Ferreira (Editor)

BLAST PERFORMANCE OF SANDWICH COMPOSITES

Arun Shukla[*] and Srinivasan Arjun Tekalur[†]

[*] Simon Ostrach Professor & Chair
University of Rhode Island
Kingston, RI , USA
e-mail: shuklaa@egr.uri.edu

[†] Post Doctoral Research Scholar
California Institute of Technology
Pasadera, CA, USA
e-mail: tsarjun@caltech.edu

Key words: Sandwich composites, Blast loading, Experimental mechanics, Component response, Combined response.

Summary *The strength of a sandwich construction is affected by the strength of its individual components, namely, the skin, core and their interface properties. The present study focuses on understanding the role of these individual components in the overall strength and failure behavior of a sandwich composite construction. A carbon fiber vinyl ester skin material, and balsa core material, were studied under controlled blast loading conditions. Experimental results from these components and their sandwich construction (carbon fiber – balsa sandwich) are presented. Rectangular plate elements of these skin, core and sandwich materials were subjected to highly transient loading conditions in a shock tube. Damage modes and failure behavior of the individual elements and the sandwich construction were analyzed using real time and visual post impact observations. A high speed camera was utilized for recording the deformation response of the plate specimens. It was observed that balsa wood could not sustain even low levels of blast loading (0.36 MPa) and can not be utilized as a structural material in itself for blast resistance. As expected, the carbon fiber composite plates sustained higher levels of blast loadings (1 MPa) than balsa wood. When these components were combined to form a sandwich construction, they could sustain blast levels up to 3.5 MPa without any considerable damage to them. It was observed that the failure initiation in the components occurs at lower pressure levels than it occurs in sandwich construction.*

1 INTRODUCTION

The response of composite plates to blast loading conditions is an area of interest owing to applications of these composites in several structures including naval and aerospace architecture. With the need to reduce weight in these structures without any reduction in strength, the design and utilization of sandwich construction is considered an efficient option. Several researchers have studied sandwich composites under quasi-static and low velocity impact loading conditions. Steeves et al [1] studied the collapse mechanisms in sandwich composite when loaded in quasi-static three point bending. Using beam theory, they identified and developed critical loads for some of the major failure modes such as indentation, core shear, micro-buckling and face wrinkling of skin components. In general, the response and failure of metallic foam core based sandwich composites, under quasi-static loadings and low velocity impact type are studied in literature [2-5]. The utilization of balsa wood and PVC foam as core materials is gaining significance in the recent times. The individual properties of these core materials are also studied in several research works, both in quasi-static and dynamic regimes [6-10]. Carbon fiber composite and E-glass fiber composites are the most widely utilized composite materials in naval applications, due to their superior advantages suited for ship building. The effect of in-plane loading on these materials is well studied and known. The effect of transverse loading on the response of these composites needs to be understood, for their efficient utilization in structural applications. Naik et al. [11] studied the response of carbon fiber based composite plates under quasi-static transverse loadings. They found that laminated composite damage in the transverse direction can be attributed to delamination initiation and propagation and in-plane failure of different layers which leads to the subsequent loss of strength and stiffness. But in a wide variety of applications, particularly in marine and aerospace, composite structures are subjected to intense and distributed transient loadings, particularly in the transverse direction. The effect of shock loading, particularly experimental studies on effect of air and water blast on composite structures are lacking. The current study utilizes a circular shock tube to impart air blast loading on sandwich composite plate structures. Also, the ratio of loading area to the area of the sandwich composite exposed to the blast is large in this study, which is typical of far field blast loading experienced by naval structures. The construction, design and calibration of the shock tube can be found in Le Blanc et al [12]. Tekalur et al [13-14] have investigated the effect of highly transient blast loading on failure of fully clamped composite plates and simply supported layered composite plates. The damage mechanisms in such materials under transient loadings are shown to be dependent on the material composition and boundary conditions. The response of sandwich composite plates to highly transient loadings is presented in the current study. The primary objectives of the experimental study are

(1) To understand the failure mechanisms in the components of a sandwich composite by subjecting them to high intensity air blast loadings.

(2) To understand the failure mechanisms in these components while being subjected to air blast loadings as a sandwich composite

(3) To quantify the dynamic deformation of the skin component while being utilized as a stand alone structure or sandwich structure.

2 MATERIALS

Rectangular sections of sandwich composites were used in the present analysis. The skin material, namely the Carbon fiber vinyl ester plates were each 0.254 m x 0.102 m (10"x4"). The carbon composite plate was 3.94 mm (0.155") thick and consisted of 10 layers, symmetrically arranged with a layup of $[0/0/45/90/-45]_s$ (0 and 90's are woven, 45's are stitched). The fibers were T700Sc/12k/FOE with Derakane 510A -40 resin. The smeared elastic properties for the carbon laminate are: E_x=E_y=39.64 GPa, G_{xy} = 3.36 GPa ?$_{xy}$=0.24.

The specimens of the core material, namely Balsa wood, were rectangular plates measuring 0.254 m x 0.102 m (10"x4") and were 50.8 mm (2") thick. From the manufacturer's data, the density of the balsa core was 155 kg/m^3. The compressive strength and modulus of the core were given as 12.7 MPa and 4.1 GPa respectively. The shear strength and modulus were 3 MPa and 0.166 GPa respectively.

The Carbon fiber – Balsa wood sandwich construction comprised of two plates of carbon fiber skin material with a balsa wood core in between. The dimension of the sandwich construction was 0.254 m x 0.102 m (10"x4") with a 58.67 mm (2.31") thickness.

3 EXPERIMENTAL CONDITIONS

3.1 Loading – Shock Tube Apparatus

The controlled blast loading was produced using a circular shock tube. The shock tube used consisted of a driver and driven section separated by a Mylar diaphragm. The driver section was filled with an inert gas until the diaphragm ruptures producing a shock wave that propagated into the driven side, while an expansion wave traveled in the driver side. Controlling the pressure at which the diaphragm bursts controlled the strength and speed of shock wave. Detailed description of the shock tube and its operation can be found in [12]. The length of the driver section of the shock tube was 1.83 m and had a diameter of 0.15 m. The intermediate and convergent section spanned 4.27 m and finally the driven section was 1.83 m long with a diameter of 76.2 mm, with an opening at the end through which the shock wave exits. Two dynamic pressure sensors (PCB Piezotronics A123) were mounted at a distance of 17.78 mm (0.7") and 170.18 mm (6.7") from the shock wave exit, which measured the shock wave reflected pressure history and the shock wave velocity. The shock tube has been calibrated for operations up till 17 MPa (2500 Psi) corresponding to a reflected pressure of 22 MPa (3200 Psi). The maximum shock velocity that can be obtained in the shock tube is 1020 m/s (Mach 3). Calibration of the shock tube has shown that pressures between tests are reproducible to a high degree of accuracy.

3.2 Boundary Conditions

The experimented specimens were held under simply supported conditions. This was done to keep minimum constraints on the composites and minimize the damage due to gripping and clamping boundary conditions. The span of the simply supported plate was 152 mm (6") and the overhangs measured 50.8 mm (2") from along each end. The center of the specimen was kept in line with the center of the shock tube. The ratio of the loading diameter to the span was 0.5. The specimen was loaded from the exit of the shock tube and was simply supported as illustrated in Fig 1.

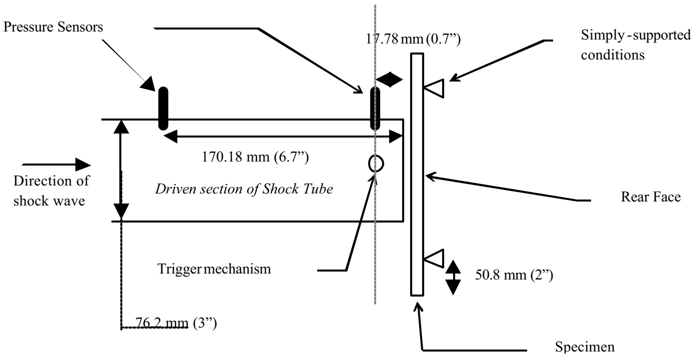

Fig 1. Schematic showing the experimental conditions and different components

An ultra high speed digital camera (IMACON 200) was used to capture real time images of the specimen due to the dynamic blast loading. The camera was triggered using a trigger mechanism which activated when the shock wave arrived at the exit of the shock tube. Subsequently, real time images were captured in intervals ranging from 70-200 microseconds, set as per the experimental conditions.

4 RESULTS AND DISCUSSIONS

4.1 Skin Material – Carbon Fiber Vinyl Ester Composite Plate

A series of eight experiments were performed on the carbon fiber skin material. These experiments were performed under three different reflected pressures and hence three different levels of imparted impulse on the plate specimens. The different levels were repeated at least twice to ensure repeatability of the data points collected. It was observed that the pressure and deflections observed in the plates were repeatable to a high degree of confidence. The velocity of the impinged shock wave on the plates were measured in all the

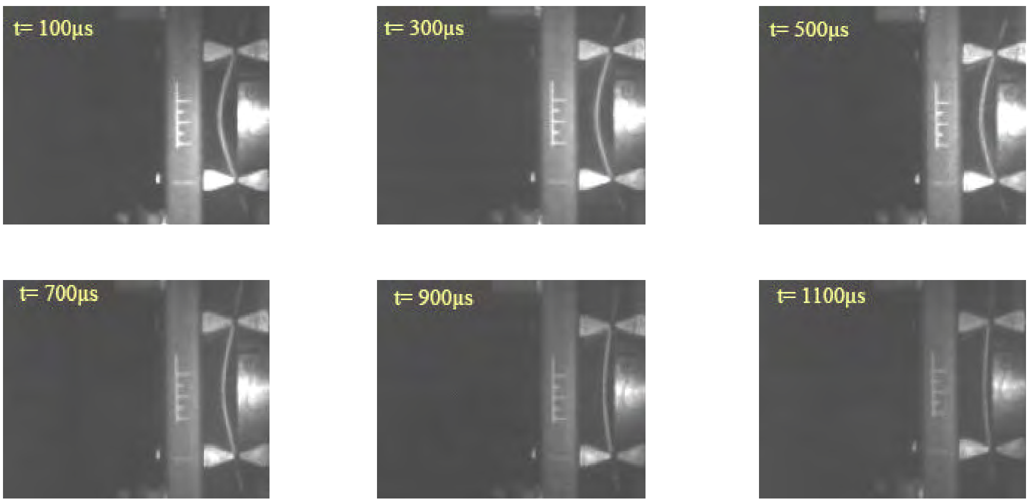

Fig 2. Real time High speed images of Carbon Fiber composite under mild blast loading of 0.9 MPa

experiments and ranged from Mach 2 to Mach 3.

Fig. 2 depicts a typical real time event in the dynamic deflection of carbon composite plate when subjected to controlled blast loading. Under dynamic loading conditions, the energy dissipation in the skin material can be attributed to three major stages, based on the input energy, namely,

(1) Elasto-dynamic bending of the plate
(2) Failure initiation and accumulation in the plate beyond the elastic limits and subsequent increase in the plate deflections – depending on the properties of the composite, these deflections may lead to permanent deformations or interlaminar failure
(3) Rigid body motion of the plate beyond the above mechanisms, under very high input energy levels (This can be observed as “tearing” in clamped boundary conditions)

In carbon fiber composites subjected to a mild shock of 0.9 MPa, the elastic bending of the plate is observed in the real time observations as seen in Fig. 2. When the pressure is subsequently increased, the failure in the plate occurs predominantly in the form of interlaminar delaminations (observed from post mortem), owing to strong in-plane properties compared to the interlaminar shear strength of these composites. The occurrence of this failure leads to overall weakening of the structure and initiates rigid body motion of the plate itself.

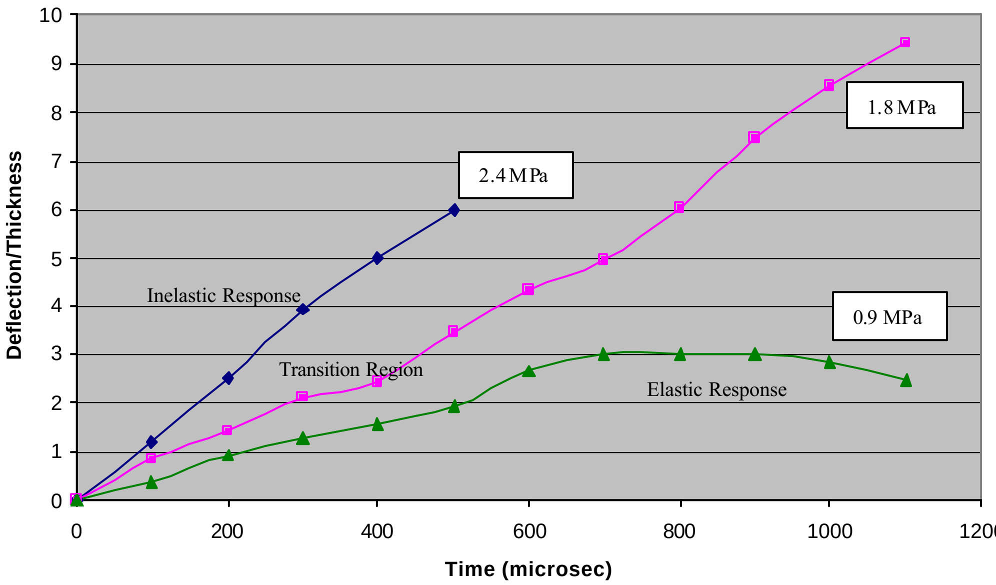

Fig 3. Real time plots of deflection per unit thickness of composite plates under applied blast loadings

Fig. 3 plots the real time deflection per unit thickness of the carbon composite plates under the three different levels of blast loadings. The deflection plots depict three different response regimes, namely elastic regime, transition regime and inelastic regime. In these three regimes, the macroscopic deflection of the plate and the damage observed are proportional. When the deflection is less than three times the plate thickness, the plate behaves in a predominantly elastic manner with damage beginning to occur only on the strike face of the plate. On application of blast loadings higher than this level, the damage propagates from the strike face to the rear face. The internal damages are expected to initiate at time frames that are difficult to capture given the macroscopic level of imaging techniques and microscopic initiations of damage. A quantitative estimate of these initiation points can be obtained by examining the semi-log plots of the deflections, as seen in Fig. 4. The semi-log plots show a distinct point at which the slope of these curves change. For plates that behaved in near elastic response and had minimal damage, the curve changes to a line which

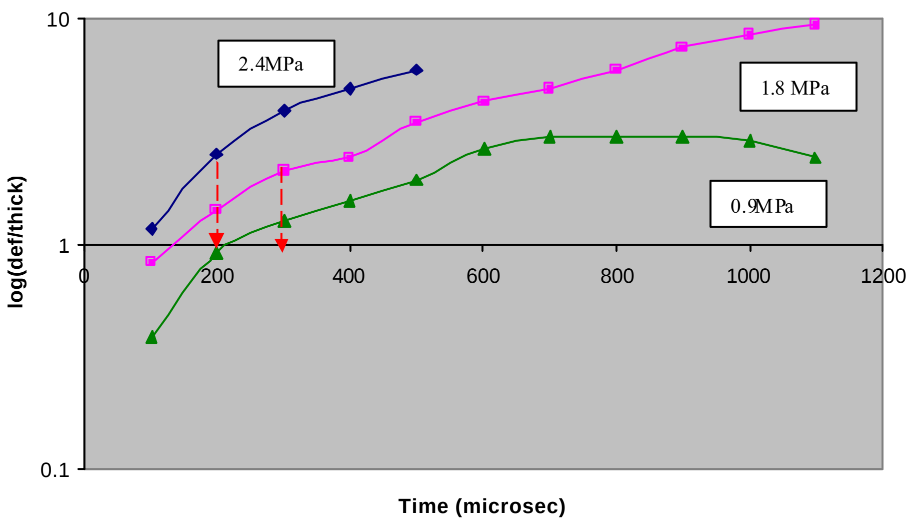

Fig 4. Semi-log plots of real time deflections

indicates no further change in the slope. For plates that were subjected to higher loadings, where extensive damage was observed, a distinct point or region of slope change can be observed. At the intermediate pressure of 1.8 MPa, the slope change occurs at 300 microsecond and at the high blast pressure loading, the change occurs at 200 microsecond (these points are marked with a dotted line arrow in the Fig 4). These can also be deduced from deflection-time plots (Fig. 3) where the plate deflection are 3 times their thickness at earlier time points as the blast loading is increased.

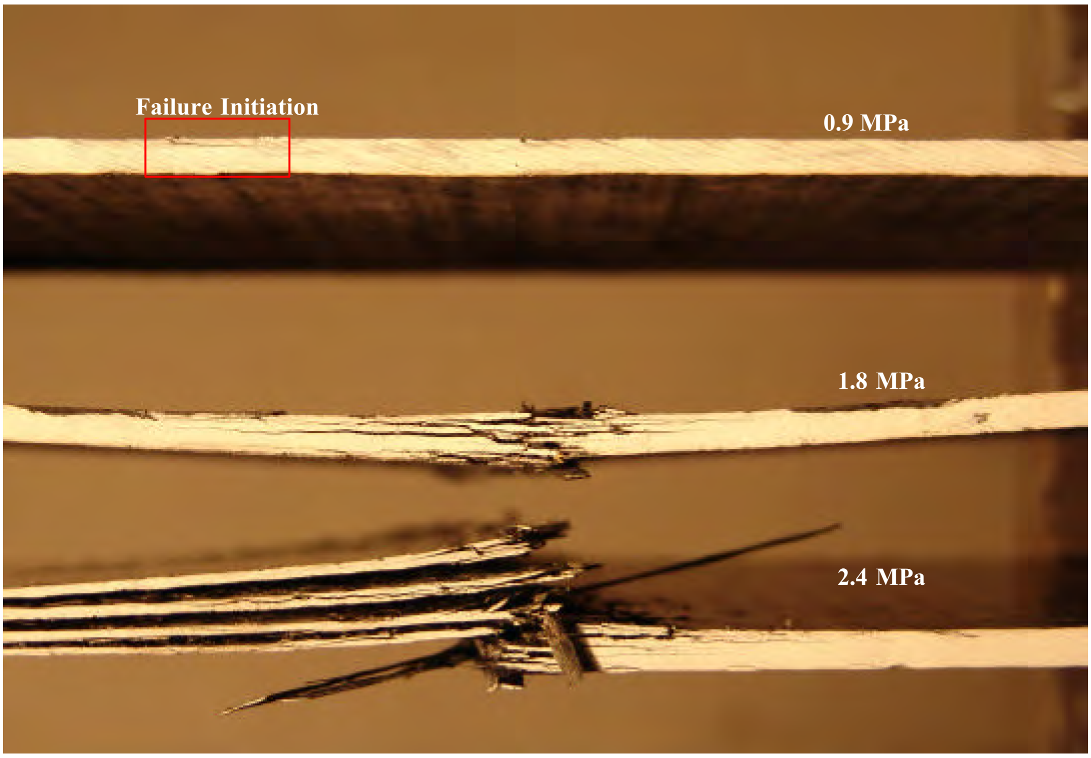

Fig 5. Progressive failure in the carbon composite under increasing blast loading. (Zoom of the area in box is shown in Fig 6)

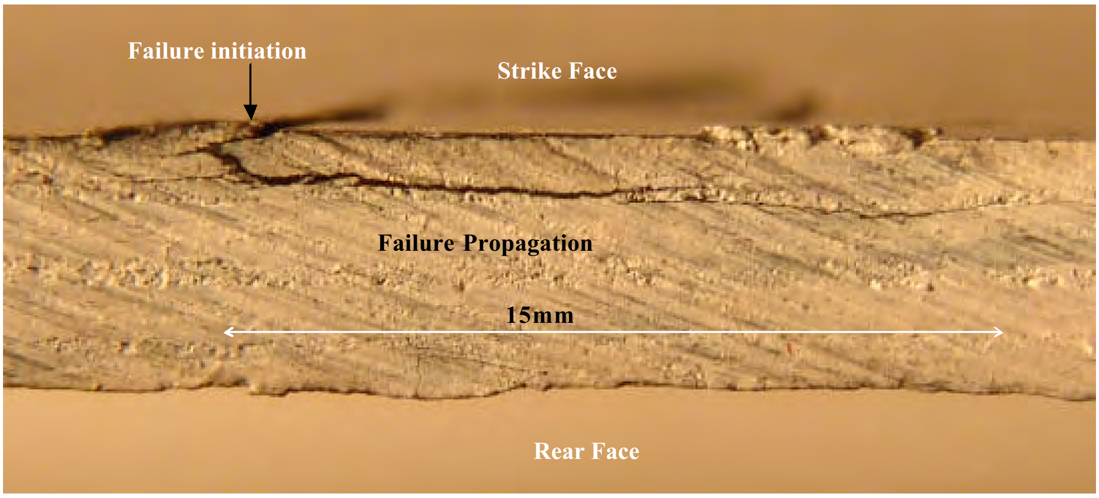

Fig 6. Initiation of Interlaminar shear in carbon composite from the strike face – Through thickness view

In the post mortem evaluation of these composites, the failure mechanisms are further understood. Fig. 5 depicts the damage progression in carbon fiber composite plates after being subjected to blast loadings of increasing intensities. The damage mechanism in these composites was dominated by interlaminar failure. Under the lowest applied blast pressure, the initiation of fiber shear (in-plane) on the strike face and delamination close to the strike face was visible, as highlighted in Fig 6. This failure accounts for the initial loss of strength in the strike face leading to subsequent failure in one of the layers of lamina as shown in the figure. Upon increasing the applied blast, the extent and the number of lamina failing also increases. The failure initiates at the strike face, which is under compressive loading due to plate bending. It can be deduced that the combination of in-plane and interlaminar shear in the first lamina facing the shock leads to progressive failure of the composite plate structure. The effect of in-plane stresses on the failure mechanisms like fiber breakage, fiber buckling and matrix cracking was evident only after the initiation of these shear failure points. Again, the strong dependence of failure initiation in carbon composites on shear properties can be attributed to their inherently strong tensile and compressive failure strengths and weaker shear failure strength.

4.2 Core Material – Balsa Wood

As with the skin material, the core material was subjected in a series of experiments to three different shock loading intensities. The bending axis of the specimen was perpendicular to the grain direction in the balsa wood. It was observed from the real time images that the major failure mechanism evident in this component is fracture failure. Based on the

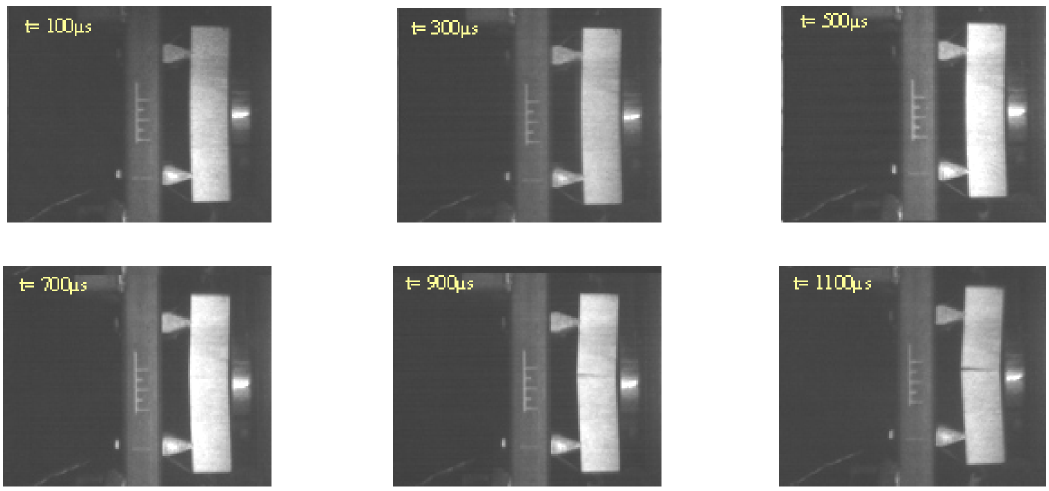

Fig 7. Real time High speed images of Balsa wood under low intensity blast loading of 0.36 MPa

magnitude of the input energy, single or multiple cracks emanate in the specimen, always along the rear side (the side in tension, as expected). Fig 7 and Fig 8 show a selected series of real-time images of balsa wood under blast loading. When subjected to the low intensity blast of 0.36 MPa, there is no evident macroscopic bending or failure in the plate till $t = 800\,\mu s$. The initiation of the crack along the center (and along the grain) of the specimen is observed at $t = 900\,\mu s$. The propagation of this crack leads to overall reduction in the strength of the core specimen and hence complete breakage occurs at the end of the blast loading event ($t = 1100\,\mu s$). The velocity of this crack propagation can be calculated from the above and is approximately 254 m/s.

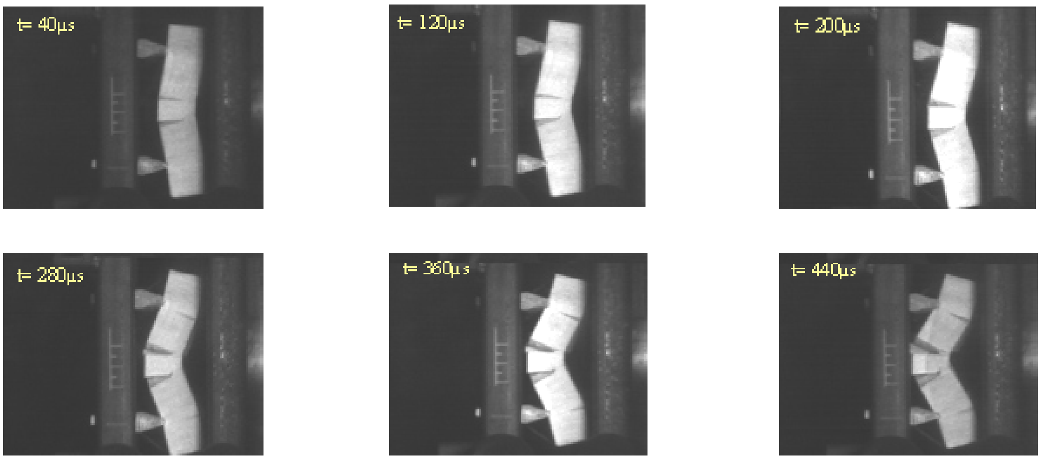

Fig 8. Real time High speed images of Balsawood under high intensity blast loading of 1.17 MPa

It can be observed that catastrophic damage occurs in balsa wood at much lower reflected pressures than that of the skin materials. The crack propagation in the balsa wood can be characterized by a single central crack under low pressure (low applied input energy). As the loading is progressively increased, the excess energy available for the plate is dissipated through multiple cracks, running close the central crack, as evident in Fig 8. Under the blast of 1.17 MPa, multiple cracks have initiated at $t = 40\mu s$, and the indentation of the supports in to the specimen can be observed at $t = 280\,\mu s$. At the same time instant, cracks in the strike face also emanate and lead to catastrophic failure.

Post mortem evaluation of the core element reveals clean failure along the center line and visible indentation of the support lines. The real time images combined with the post-mortem shows that under the dynamic loading, the fracture of the core resembled a brittle fracture process.

4.3 Sandwich Construction – Carbon fiber - Balsa wood

The deformation and damage behavior of sandwich composites was different from the mechanism observed in its individual components. The balsa core in itself showed fracture behavior like a brittle material with initiation at single crack tip, preferably at the center of the specimen initiating from the rear side. When sandwiched between stiff skins, the number and initiation of these cracks were different and were dependent on the applied blast loading. The

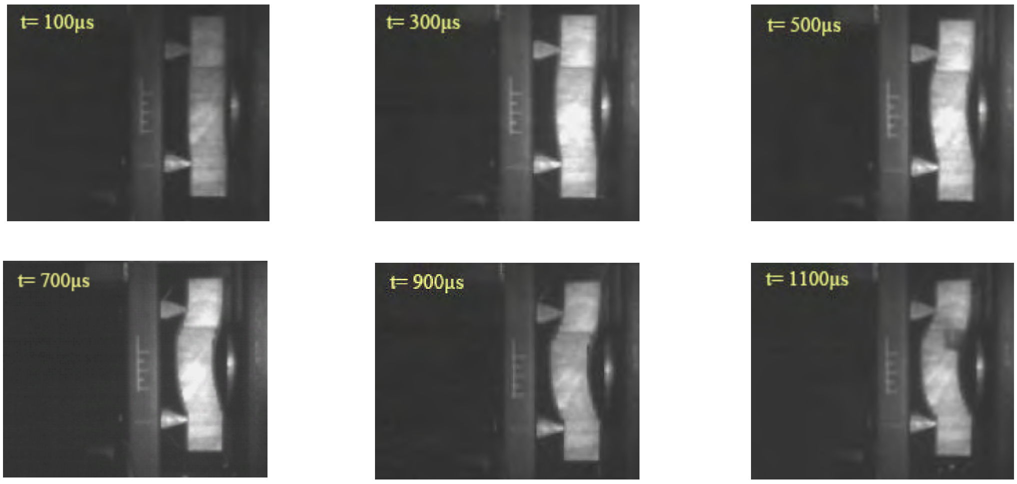

Fig 9. Real time High speed images of Carbon Fiber - Balsa wood under intermediate blast loading of 5.85 MPa

blast loading to initiate failure in the sandwich is considerably higher than the individual components and when the failure does occur, core shear is the major mode, as seen in the real time observations and explained below.

Under low blast pressures (<2.8 MPa), any macroscopic crack initiation phenomenon were not observed. The observed maximum deflections in the front and rear skin of the sandwich were negligible and were almost less than or equal to their thicknesses (4 mm). The overall damage to the sandwich is minimal and hence is intact for structural purposes. As the blast pressure is increased to 5.8 MPa, the observed deflections were quantitatively higher and in the order of 4-5 times the thickness of the skin components. A real time deformation event of the sandwich composite when subjected to such a blast loading is shown in Fig 9. The deformation and failure mechanism in this blast regime was dominated by the interface failure between the strike face skin and the balsa core. Until $t = 200\,\mu s$, there is no macroscopic damage observed and deflections are less than skin thickness (4 mm). At $t = 300\,\mu s$, the initiation of core-front skin debond can be observed. This debond further propagates with time and progressive failure of the sandwich through core shear and interface debond can be observed. At $t = 400\,\mu s$, debond between the core and the back skin and hinging of the sandwich about the support points can be observed. The two important aspects of failure observed in real time are:

1. Shear cracks in the core

   These cracks initiate very close to the boundary region, travel progressively towards center, failing layers of balsa wood as the loading progresses. All these cracks are along the grain direction of balsa.

2. Skin – Core debond

   The shear failure of the core leads to subsequent debonding between the core and the skin components. As explained above, the first sign of debond is observed between the core and the front skin and this progresses towards the rear skin with the applied blast loading. At $t = 900\,\mu s$, several debond regions can be observed in the real time image. The overall strengthening mechanism of a sandwich composite is lost at this time and the response is dominated by the flexural strength of the skin components alone.

The post mortem analysis of this sandwich composite reveals that the front skin had suffered interlayer delaminations and minimal shear cracks on the surface. The core suffered shear crack along the grain direction and are inclined along the loading direction. The debond failure between the core and the front skin is predominantly seen in the post mortem, particularly in regions closer to the loading area and confined to the span of the specimen. At the same time, interlaminar delaminations (in the skin) are much more severe near the boundaries (stronger interface between the core and composite) as compared to the central region, with possible initiation of these delaminations at the boundary regions of the plate and traveling towards the center of the specimen. The rear skin showed relatively lower damage in the form of interlayer delaminations.

Under higher blast loadings (7.6 MPa), the overall mechanism of failure seen in real time is similar to the mechanism observed before. But the quantitative measure of deflections is higher and is achieved at earlier time instants than before. The initiation of the skin-core debond can be observed at $t = 200\,\mu s$ and at the same instant the core shear failures can also be observed. After the initial damage mechanism of interface failure sets in, the center of the front skin was observed to be hinged at several points on the balsa core ($t = 500\,\mu s$). These regions are subjected to the transient wave loadings. At the same time, the fragments of balsa displaced by the shear failure transfer load to the rear skin of the sandwich in a progressive fashion, starting from the loading region to the boundaries. At $t = 1100\,\mu s$, several shear cracks in the core and macroscopic large bending of the skins are observed Post mortem evaluation of these sandwich composites reveals that the front skin had suffered extensive failure in the form of complete interlayer separations and fiber fracture. The core does disintegrate under this high blast loading and the adhesion between the back skin and the remnant core is still maintained. It can be concluded that at this level of blast loading, the structural integrity of this sandwich is completely lost.

5 CONCLUSIONS

Carbon fiber vinyl ester skin material, balsa wood core material and sandwich composite fabricated from these were studied under highly transient blast loading conditions. Balsa wood could not sustain even low levels of blast loading (0.36 MPa) and can not be utilized as a structural material in itself for blast resistance. As expected, the carbon fiber composite plates sustained higher levels of blast loadings (1 MPa) than balsa wood. When these components were combined to form a sandwich construction, they could sustain blast levels up to 3.5 MPa without any considerable damage in them. For each of these materials, major failure modes and mechanisms were identified.

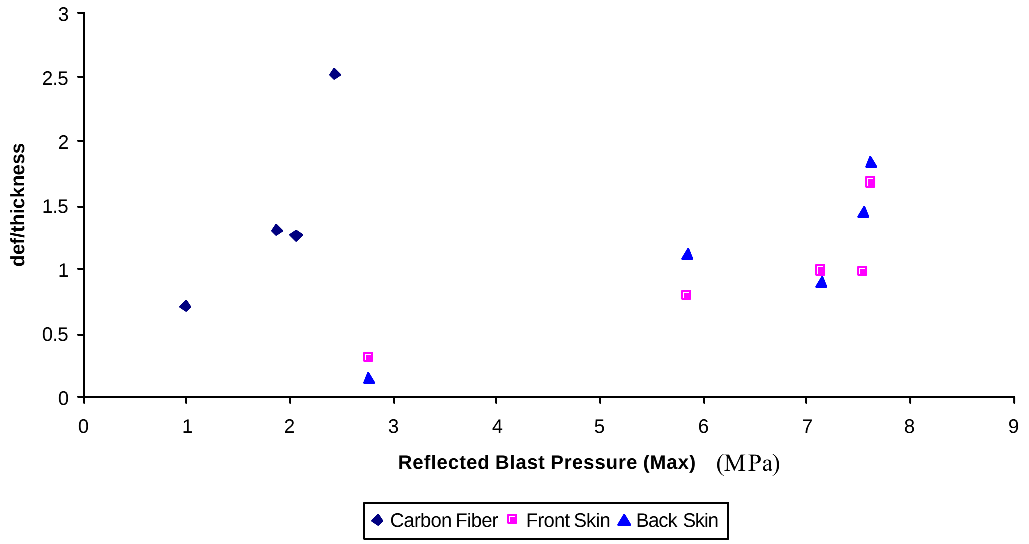

Fig 10. Ratio of deflection to thickness of the component (4 mm) at a specific time frame t=200 microsecond for the skin component alone and while present in the sandwich

Deflection of the skin component was utilized as a parameter for comparison of blast resistance. Fig. 10 plots such a response of the carbon fiber component (normalized with its thickness) at a specified time frame, $t = 200\,\mu s$, while subjected to blast loading as a stand alone component and while present in the sandwich composite. It was observed that the failure initiation in the component occurs at lower pressure levels than while the skin is present in sandwich construction. The presence of balsa wood as a core reduced the overall deflection of each of the skin components and conversely the skin components eliminated the failure of balsa itself through brittle fracture. The overall strength of the sandwich though was dependent on the shear failure of the balsa core. Though the sandwich construction weighed approximately twice more than the laminated composite skin alone, it needed more than 300% of reflected pressure to cause the same damage as of that in a skin composite. The overall benefits of sandwich construction have been understood by analysis of each component failure.

ACKNOWLEDGEMENTS

The authors acknowledge the financial support of the Office of Naval Research (Program Manager Dr. Y.D.S. Rajapakse) under grant No. N000140410268 and the support of Material Sciences Corporation under grant No. 01742.

REFERENCES

[1] Steeves, C.A., Fleck, N.A., "Collapse mechanisms of sandwich beams with composite faces and a foam core, loaded in three-point bending", Part I and II, *International*

Journal of Mechanical Sciences, v 46, n 4, April, 2004, p 561-608.
[2] Styles, M., Compston, P., Kalyanasundaram, S., The effect of core thickness on the flexural behaviour of aluminium foam sandwich structures, Composite Structures, v 80, n 4, October, 2007, p 532-538.
[3] Zhao, H., Elnasri, I.,Girard, Y., Perforation of aluminium foam core sandwich panels under impact loading-An experimental study, International Journal of Impact Engineering, v 34, n 7, July, 2007, p 1246-1257.
[4] Lee, S., Barthelat, F., Hutchinson, J.W., Espinosa, H.D., Dynamic failure of metallic pyramidal truss core materials - Experiments and modeling, International Journal of Plasticity, v 22, n 11, November, 2006, p 2118-2145.
[5] Xue, Zhenyu, Hutchinson, J.W., Constitutive model for quasi-static deformation of metallic sandwich cores, International Journal for Numerical Methods in Engineering, v 61, n 13, Dec 7, 2004, p 2205-2238.
[6] Vural, M., Ravichandran, G., Dynamic response and energy dissipation characteristics of balsa wood: Experiment and analysis, International Journal of Solids and Structures, v 40, n 9, May, 2003, p 2147-2170.
[7] Tagarielli, V.L., Deshpande, V.S., Fleck, N.A., Chen, C., A constitutive model for transversely isotropic foams, and its application to the indentation of balsa wood, International Journal of Mechanical Sciences, v 47, n 4-5 SPEC. ISS., April/May, 2005, p 666-686.
[8] Easterling, K. E., Harrysson, R., Gibson, L. J., Ashby, M. F., On The Mechanics Of Balsa And Other Woods, Proceedings of The Royal Society of London, Series A: Mathematical and Physical Sciences, v 383, n 1784, Sep 8, 1982, p 31-41.
[9] Gdoutos, E.E., Daniel, I.M., Wang, Kuang-An, Multiaxial characterization and modeling of a PVC cellular foam, Journal of Thermoplastic Composite Materials, v 14, n 5, September, 2001, p 365-373.
[10] Thomas, T., Mahfuz, H., Carlsson, L. A., Kanny, K., Jeelani, S., High strain rate response of PVC foams, American Society of Mechanical Engineers, Applied Mechanics Division, AMD, v 247, Dynamic Failure in Composite Materials and Structures - 2001, 2001, p 93-101.
[11] Naik, N.K., Reddy K. Satyanarayana, and Raju N. Bulli, Damage Evolution in woven fabric composites: Transverse Static Loading, Journal of Composite Materials, Vol. 37, No. 1, 2003.
[12] LeBlanc, J., Shukla, A., Rousseau, C. and Bogdanovich, A. "Shock loading of three-dimensional woven composite materials". Composite Structures, Vol. 79, No. 3, pp 344-355, 2007.
[13] Tekalur, S.A., Shivkumar, K., and Shukla, A., Mechanical behavior and damage evolution in E-glass vinyl ester and carbon composites subjected to static and blast loads, Composites Part B: Engineering, In Press, Corrected Proof, March 2007.
[14] Arjun Tekalur, S., Blast resistance of woven and layered composite materials, Proceedings of the 2006 SEM Annual Conference and Exposition on Experimental and Applied Mechanics 2006, v 2, Proceedings of the 2006 SEM Annual Conference and Exposition on Experimental and Applied Mechanics 2006, 2006, p 586-587.

For ONR sessions organized by Yapa Rajapakse
8th International Conference on Sandwich Structures
ICSS 8
A. J. M. Ferreira (Editor)

BLAST RESPONSE OF COMPOSITE SANDWICH PANELS

Michelle S. Hoo Fatt and Leelaprasad Palla

Department of Mechanical Engineering
The University of Akron
Akron, OH 44325-3903
e-mail: hoofatt@uakron.edu, web page: http: //www.uakron.edu

Key words: Composite sandwich, Blast, Analytical model.

Summary. *Analytical solutions were derived for the transient response of a foam-core composite sandwich panel subjected to blast loading. The panel response consisted of two consecutive phases: (1) a through-thickness wave propagation phase leading to permanent core crushing deformations and (2) a transverse shear wave propagation phase resulting in global panel deflections. The predicted transient deformation of the sandwich panel was within 7% of FEA results using ABAQUS Explicit.*

1 INTRODUCTION

There is growing interest in using lightweight composite sandwich panels for construction of naval ships, which can be exposed to blast and impact during combat. Tagarielli et al. [1] have recently demonstrated that glass fiber vinyl sandwich beams with PVC foam cores and balsa wood have higher ballistic resistance than monolithic beams of equal weight. While there has been much research concerning localized projectile impact damage of composite sandwich panels, very little work has been done to address damage of composite sandwich panels under distributed pressure pulse loading, such as that caused by an underwater or air blast. Several recent articles have dealt with the blast resistance of metal sandwich panels with metallic foam, honeycomb, truss and wide variety of metal sandwich core topologies [2-5] but none of these can be directly applied to a composite sandwich panel made of anisotropic elastic facesheets and polymeric foam or balsa wood cores. The purpose of this paper is to present an analytical model that can be used to determine the blast performance of a composite sandwich panel. The paper specifically provides an analytical model for predicting the transient response and failure of a composite sandwich panel subjected to pressure pulse or impulsive loading, i.e., load durations are on the order of the through-thickness wave travel time and are short compared to the time associated with overall bending/shear panel deformation.

2 PROBLEM FORMULATION

Consider a fully clamped, composite sandwich panel of radius a, as shown in Fig. 1. The facesheets consist of orthotropic composite plates of thickness h, and the core is crushable polymeric foam of thickness H. Assume for simplicity that the panel is subjected to a uniformly distributed pressure pulse

$$p(t) = \begin{cases} p_o\left(1 - \dfrac{t}{\tau}\right), & 0 \le t \le \tau \\ 0, & t \ge \tau \end{cases} \tag{1}$$

where p_o is the peak pressure and τ is the load duration. Other pressure transients can be used to more accurately simulate underwater and air explosions [6,7]; they will produce similar impulsive sandwich response as the triangular pressure pulse in Eq. (1).

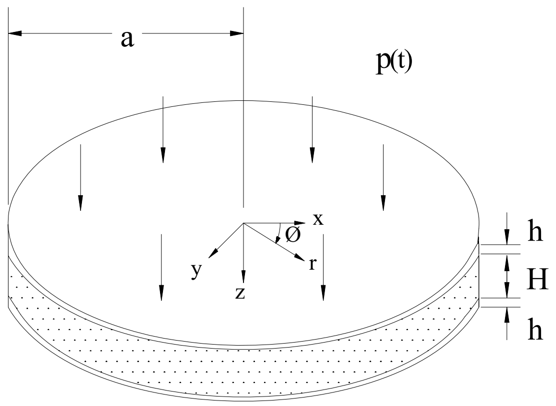

Figure 1: Composite sandwich panel subjected to uniformly distributed, pressure pulse.

Provided no failure has occurred to the panel during the blast, the response of the composite sandwich panel may be described by the three phases of motion shown in Fig. 2. In Phase I, a through-thickness stress wave propagates from the incident facesheet to the rear facesheet. In this phase the sandwich panel experiences local core crushing and local facesheet deformation, while an impulsive transverse shear reaction force is induced at the clamped boundaries. At the end of Phase I, kinetic energy is transferred globally to the panel and the impulsive transverse shear reaction force propagates from the clamped boundaries towards the panel center. Phase II consists of the propagation of an elastic unloading transverse shear wave. The pressure pulse has already ended and momentum is transferred to the sandwich panel, with reduced core thickness from Phase I. The transverse shear stress wave due to the reaction forces at the clamped boundary propagates from the clamped boundary towards the center of the panel. This transverse stress wave is an unloading wave, causing bending and shear deformations to develop behind the wave front. The elastic unloading transverse shear wave brings the panel to maximum deflection. At the end of Phase II, the panel rebounds and vibrates. Elastic vibrations take place in Phase III.

During Phase I, high intensity transverse shear stresses are developed at the clamped boundary and these may cause transverse shear fracture at the clamped boundaries of the panel. Transverse shear fracture is usually avoided by using reinforcements at boundaries. The second mode of failure that can occur during blasts is tensile fracture in the center of the panel when bending strains are at a maximum at the end of Phase II. These two failure modes in addition to permanent deformation were first observed on impulsively loaded aluminum beams by Menkes and Opat [8] and later on aluminum plates by Teeling-Smith and Nurick [9]. They have also been experimentally observed on composite plates by Franz et al. [10].

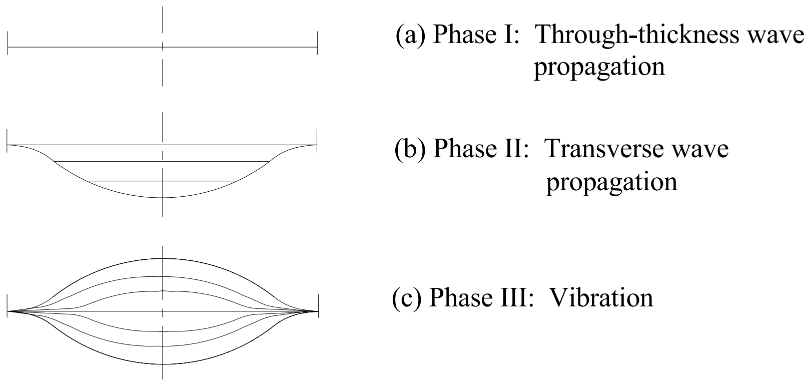

Figure 2: Three phases of blast response: (a) Phase I: Through-thickness wave propagation, (b) Phase II: Transverse wave propagation and (c) Phase III: Vibration.

This paper focuses on the first two phases of blast response described in Fig. 2 because they are relevant to the failure of the composite sandwich panel subjected to blast effects. The analytical solutions presented for the panel response is to be distinguished from previous models in which the Phase II was treated as the forced modal response of sandwich panels [11]. In this paper, Phase II is taken as an initial-value problem since the load duration is short compared to the transverse wave propagation time and the natural period of vibration in Phase III.

3 PHASE I – THROUGH-THICKNESS WAVE PROPAGATION

In most blast situations the load duration is short compared to the natural period of the global sandwich response and the pressure pulse can be realized as an impulsive loading to the sandwich. However, the wave speed in polymeric foam is low and a thick composite sandwich panel with a polymeric foam core is likely to undergo transient local facesheet indentation and core crushing while the pressure pulse is still acting. Take for example, H100 PVC foam core with a density of 100 kg/m^3 and a compressive elastic modulus of 35 MPa. Elastic waves propagate through a 25 mm thick core made of H100 PVC foam in 0.04 ms. Blast pressure pulse durations of this magnitude are not uncommon for naval composite sandwich ships subjected to underwater and air blast explosions [6,7]. Thus one can assume that permanent plastic deformations of the core will take place from a transient event, i.e., during the load application.

3.1 Transmission and reflection at interfaces

The transmission and reflection of plane strain stress waves through the multi-layered composite sandwich panel is shown in Fig. 3. Stress waves are transmitted from the incident facesheet to the foam at Interface 1 and from the foam to the distal facesheet at Interface 2. When the incident stress σ_I first reaches Interface 1, the transmitted stress σ_{T_1} and the reflected stress σ_{R_1} are given as follows:

$$\sigma_{T_1} = -k_{T_1} p(t-t_1)u\langle t-t_1 \rangle, \quad k_{T_1} = \frac{2\rho_c C_c}{\left(\rho_f C_f + \rho_c C_c\right)} \tag{2}$$

and

$$\sigma_{R_1} = -k_{R_1} p(t-t_1)u\langle t-t_1 \rangle, \quad k_{R_1} = \frac{\left(\rho_c C_c - \rho_f C_f\right)}{\left(\rho_f C_f + \rho_c C_c\right)} \tag{3}$$

where $t_1 = h/C_f$ is the wave transit time through the facesheet, C_f and C_c are the wave speeds in the facesheet and core, respectively; ρ_f and ρ_c are the density of the facesheet and core, respectively; and $u\langle\ \rangle$ is the unit step function. The wave speed in an orthotropic plate in plane strain is given by

$$C_f = \sqrt{\frac{E_{33}\left(1-\nu_{12}\right)}{\left[1-\nu_{12}-\nu_{32}\left(\nu_{13}+\nu_{23}\right)\right]\rho_f}} \tag{4}$$

where E_{ij} and ν_{ij} are elastic modulus and Poisson's ratio of the orthotropic facesheet. The wave speed in the foam will be discussed in the following section.

The reflected wave in the incident facesheet is tensile because $\rho_f C_f >> \rho_c C_c$. This reflected wave is again reflected, but as a compressive stress wave, when it reaches the outer surface of the incident facesheet. The process of reflection and transmission of waves at Interface 1 repeats itself over and over again at intervals $2t_1$. Thus the transmitted stress in the foam at Interface 1 is given as

$$\begin{aligned}\sigma_{T_1} = -k_{T_1} p(t-t_1)u\langle t-t_1 \rangle + k_{T_1}k_{R_1} p(t-3t_1)u\langle t-3t_1 \rangle - k_{T_1}k_{R_1}^2 p(t-5t_1)u\langle t-5t_1 \rangle \\ \ldots + \left(-1\right)^{n+1} k_{T_1}k_{R_1}^n p(t-\left(2n+1\right)t_1)u\langle t-\left(2n+1\right)t_1 \rangle\end{aligned} \tag{5}$$

where n is the number of reflections up to that time.

The transmitted stress wave in the foam σ_{T_1} will reflect back as a compressive wave into the foam and be transmitted as a compressive stress wave in the distal facesheet when it first reaches Interface 2. The transmitted stress in the distal facesheet σ_{T_2} is further reflected as a tensile stress wave from the outer surface of the distal facesheet. This reflected stress waves will then be transmitted as tensile stress wave in the foam and reflected back as compressive stress wave into the facesheet. The part that is transmitted to the foam will add to the reflected stress waves in the foam σ_{R_2}. This process repeats itself indefinitely so that the reflected stress wave at any time is given by

$$\begin{aligned}\sigma_{R_2} &= -k_{R_2} p(t-t_1-t_2)u\langle t-t_1-t_2\rangle + k_{T_2}k_{T_1} p(t-3t_1-t_2)u\langle t-3t_1-t_2\rangle + \\ &- k_{T_2}k_{T_1}k_{R_1} p(t-5t_1-t_2)u\langle t-5t_1-t_2\rangle + k_{T_2}k_{T_1}k_{R_1}^2 p(t-7t_1-t_2)u\langle t-7t_1-t_2\rangle \\ &\ldots + (-1)^{n+1} k_{T_2}k_{T_1}k_{R_1}^n p(t-(2n+1)t_1-t_2)u\langle t-(2n+1)t_1-t_2\rangle\end{aligned} \quad (6)$$

where $t_2 = H/C_c$, $k_{T_2} = \dfrac{2\rho_f C_f}{(\rho_f C_f + \rho_c C_c)}$ and $k_{R_2} = \dfrac{(\rho_f C_f - \rho_c C_c)}{(\rho_f C_f + \rho_c C_c)}$. The reflected stress is a tensile unloading elastic stress wave. Permanent plastic strains or local indentation of the foam results after elastic unloading.

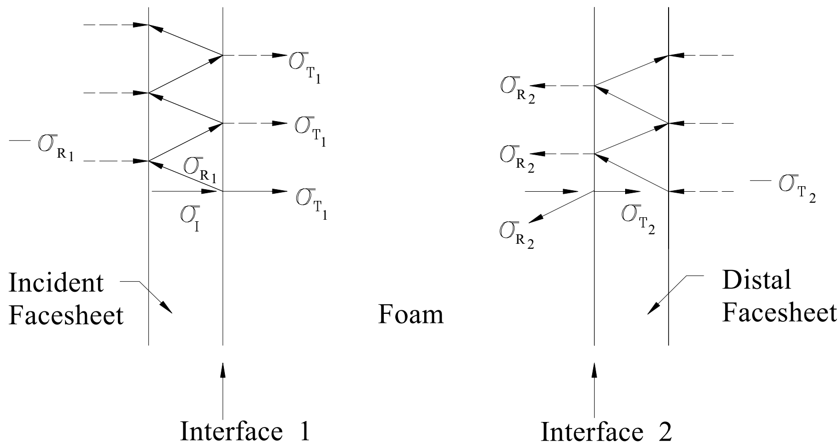

Figure 3: Transmission of stress waves through facesheets and foam of sandwich panel.

3.2 Elastic and plastic stress waves in polymeric foam

The facesheets are very stiff and remain elastic during wave transmissions but the polymeric foam core is elastic-plastic with a compressive stress-strain characteristic as shown in Fig. 4 [12]. The foam is linear elastic with a compressive modulus of E_c until yielding at a flow stress q. Rapid compaction of cells causes the density to change during the plateau region until full densification has occurred at ε_D. The stress rises to a maximum plastic stress σ_p at the densification strain.

Elastic and plastic waves could therefore be generated in the foam during Phase I. The elastic wave speed in the foam is given by $C_e = \sqrt{E_c/\rho_c}$ and the plastic wave speed is given by $C_p = \sqrt{\dfrac{\sigma_p - q}{\rho_c \varepsilon_D}}$ [13], where σ_p is the stress in the densification region (see Fig. 4). Elastic waves propagated first in the core and are later followed by plastic waves, as shown in Fig. 5.

The densification strain is related to particle velocities in the elastic and plastic regions, V_e and V_p, respectively, by

$$\varepsilon_D = \frac{V_p - V_e}{C_p} \tag{7}$$

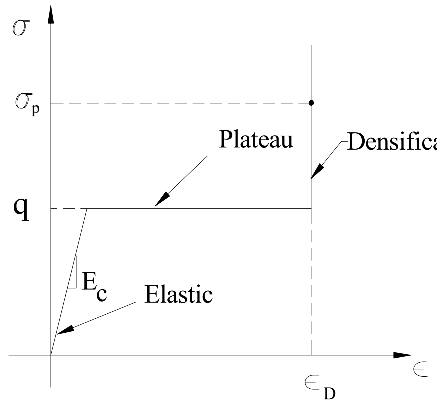

Figure 4: Compressive stress-strain curve of polymeric foam.

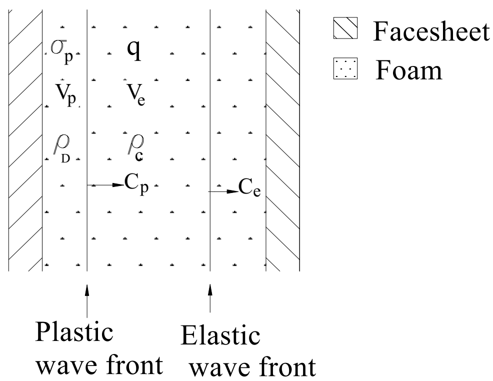

Figure 5: Elastic and plastic wave fronts in foam.

The particle velocity in the plastic region is in turn related to the plastic stress σ_p and density of foam after densification ρ_D:

$$V_p = \frac{\sigma_p}{\rho_D C_p} \tag{8}$$

where $\rho_D = \dfrac{\rho_c}{(1-\varepsilon_D)}$. Similarly, $V_e = \dfrac{q}{\rho_c C_e}$. Expressing C_p in terms of σ_p and combining Eqs. (7) and (8) give the following quadratic equation that can be solved for σ_p :

$$\left(\frac{\rho_c-\rho_D}{\rho_c}\right)^2\sigma_p^2+\left[\frac{2\rho_D q}{\rho_c}\left(\frac{\rho_c-\rho_D}{\rho_c}\right)-\frac{V_e^2\rho_D^2 q}{\rho_c\varepsilon_D}\right]\sigma_p+\frac{\rho_D^2 q^2}{\rho_c^2}+\frac{V_e^2\rho_D^2 q}{\rho_c\varepsilon_D}=0 \tag{9}$$

3.3 Local indentation

Permanent plastic strains arise when the elastic unloading wave reaches the plastic wave front. The local indentation is given by

$$\delta=\varepsilon_D C_p \Delta T \tag{10}$$

where ΔT is the time from the start of transmission of σ_p to the time when the elastic unloading wave reaches the plastic wave front. A simple expression for ΔT is

$$\Delta T=\frac{\left(2H/C_e+3t_1-t_p\right)}{\left(1+C_p/C_e\right)} \tag{11}$$

where t_p is the start time of transmission of σ_p at Interface 1.

4 PHASE II– GLOBAL SHEAR/BENDING

Subsequent to Phase I, the load has ended and the core has crushed permanently to a height $H'=H-\delta$. Momentum is transferred to the sandwich panel, which has become impulsively loaded with a uniformly distributed velocity field (see Figs. 6 (a) and (b)). Conservation of momentum gives the initial velocity of the panel as

$$v_i=\frac{p_o\tau}{2\left(\rho_c H+2\rho_f h\right)} \tag{12}$$

Denote the distance from the center of the panel to the wave front of the transverse shear wave as ξ. A transverse shear elastic unloading wave propagates from the clamped boundaries with velocity $\dot{\xi}$. This unloading wave instantaneously brings the plate to rest behind the wave front. As the plate is brought to rest, it undergoes shear and bending deformations as exemplified in Fig. 6(a).

4.1 System Lagrangian

Dynamic equilibrium of the complete sandwich can be expressed in terms of the maximum deflection at the center, Δ, and an equivalent shear angle, α_o. These two degrees of freedom have associated velocities, v_i and Ω, respectively. The kinetic energy for the sandwich is thus $T=\frac{1}{2}m_{eff}v_i^2+\frac{1}{2}I_{eff}\Omega^2$, where $m_{eff}=\pi\xi^2\left[2\rho_f h+\rho_c H\right]$ is the effective sandwich mass and I_{eq} is the effective sandwich rotary inertia. The elastic potential energy of the system is equivalent to the bending/shear strain energy of the sandwich, $\Pi=U$. The Lagrangian for the whole model is $L = T - \Pi$. For dynamic equilibrium,

$$\frac{\partial}{\partial t}\left(\frac{\partial L}{\partial v_i}\right) - \frac{\partial L}{\partial \Delta} = 2\pi\xi\dot{\xi}\left[2\rho_f h + \rho_c H\right]v_i + \frac{\partial U}{\partial \Delta} = 0 \tag{13}$$

and

$$\frac{\partial}{\partial t}\left(\frac{\partial L}{\partial \Omega}\right) - \frac{\partial L}{\partial \alpha_o} = \Omega\frac{\partial I_{eff}}{\partial t} + I_{eff}\frac{\partial \Omega}{\partial t} + \frac{\partial U}{\partial \alpha_o} = 0 \tag{14}$$

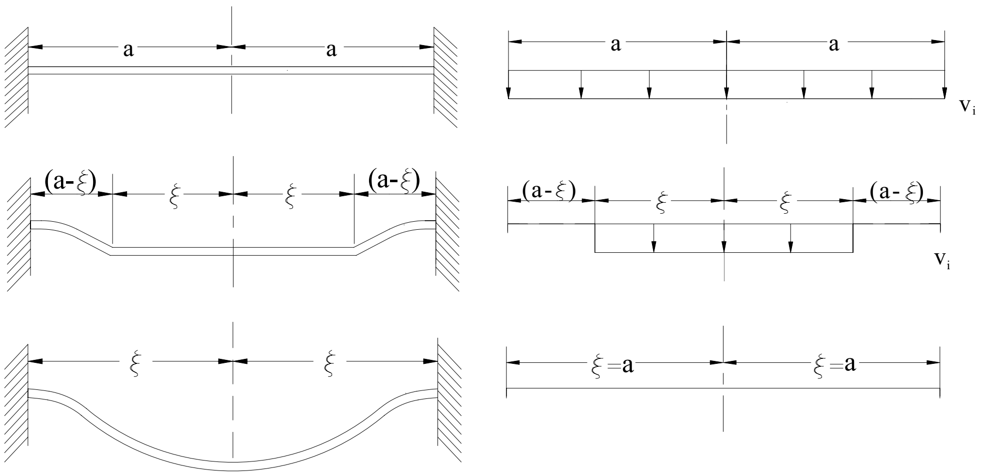

(a) Deformation profiles. (b) Velocity fields.

Figure 6: Global panel bending/shear response: (a) Deformation profiles and (b) Velocity fields.

4.2 Bending/shear strain energy

Assume in-plane deformations are negligible compared to the transverse deformation. The elastic strain energy of the symmetric sandwich panel with orthotropic facesheet is then given as

$$\begin{aligned} U = 4\int_0^{\pi/2}\int_\xi^a \Bigg\{ & \frac{D_{11}^s}{2}\left(\frac{\partial \overline{\alpha}}{\partial x}\right)^2 + D_{12}^s\left(\frac{\partial \overline{\beta}}{\partial y}\right)\left(\frac{\partial \overline{\alpha}}{\partial x}\right) + \frac{D_{22}^s}{2}\left(\frac{\partial \overline{\beta}}{\partial y}\right)^2 + A_{55}^s\left[\frac{\overline{\alpha}^2}{2} + \overline{\alpha}\frac{\partial w}{\partial x} + \frac{1}{2}\left(\frac{\partial w}{\partial x}\right)^2\right] \\ & + A_{44}^s\left[\frac{\overline{\beta}^2}{2} + \overline{\beta}\frac{\partial w}{\partial y} + \frac{1}{2}\left(\frac{\partial w}{\partial y}\right)^2\right] + D_{66}^s\left[\frac{1}{2}\left(\frac{\partial \overline{\alpha}}{\partial y}\right)^2 + \frac{\partial \overline{\alpha}}{\partial y}\frac{\partial \overline{\beta}}{\partial x} + \frac{1}{2}\left(\frac{\partial \overline{\beta}}{\partial x}\right)^2\right]\Bigg\} r\,dr\,d\theta \end{aligned} \tag{15}$$

where w is the transverse deflections, $\overline{\alpha}$ and $\overline{\beta}$ are shear angles associated with the x- and y-directions, respectively, D_{ij}^s is the sandwich bending stiffness matrix, and A_{44}^s and A_{55}^s are the transverse shear stiffnesses. The superscript "s" is used to denote the sandwich. Derivatives with respect to x and y can be transformed to polar coordinates before evaluating the above-mentioned integral expression.

Finite element analysis using ABAQUS Explicit indicates that the transverse deformation, w, and the shear rotations with respect to the radial direction $\overline{\alpha}$ are of the following forms:

$$w(r)=\begin{cases}0, & 0<r<\xi\\ \Delta\left(1-\left(\dfrac{r-\xi}{a-\xi}\right)^2\right)^2, & \xi<r<a\end{cases} \tag{16}$$

and

$$\overline{\alpha}(r)=\begin{cases}0, & 0<r<\xi\\ 4\alpha_o\dfrac{(r-\xi)(a-r)}{(a-\xi)^2}, & \xi<r<a\end{cases} \tag{17}$$

where Δ is the global deflection and α_o is the rotation at $r=(a+\xi)/2$. Substituting derivatives of the expressions in Eqs. (16) and (17) into Eq. (15) gives the following expression for the strain energy:

$$U=\frac{8}{3}\frac{(a+\xi)}{(a-\xi)}\left[\pi D_{11}+2D_{12}+(2+\pi)D_{66}\right]\alpha_o^2+$$
$$\frac{2}{105}\frac{A_{55}}{(a-\xi)}\left[28\pi\left(a^3-a\xi^2-a^2\xi+\xi^3\right)\alpha_o^2+\left(-176a^2+16\xi a+160\xi^2\right)\alpha_o\Delta+(29\pi\xi+35\pi a)\Delta^2\right] \tag{18}$$

4.3 Equations of motion

Assume the rate of angular rotation is similar to the shear rotation field in Eq. (17):

$$\dot{\alpha}(r)=\begin{cases}0, & 0<r<\xi\\ 4\Omega\dfrac{(r-\xi)(a-r)}{(a-\xi)^2}, & \xi<r<a\end{cases} \tag{19}$$

Then, the effective rotary inertia for the sándwich is $I_{eff}=\frac{8\pi}{15}\tilde{I}\left(a^2-\xi^2\right)$, where $\tilde{I}=\sum_{k=1}^{3}\rho_k\left(z_k^3-z_{k-1}^3\right)=\frac{\rho_f}{12}\left(3hH^2+3h^2H+h^3\right)+\frac{\rho_c}{12}H^3$. Denoting $\dot{\xi}=\frac{-(a-\xi)}{t}$ and $\Delta=v_i t$, one gets the following coupled equations of motion from Eqs. (13) and (14):

$$-2\pi\left[2\rho_f h+\rho_c H\right]\xi\frac{(a-\xi)}{t}v_i+\frac{2}{105}\frac{A_{55}}{(a-\xi)}\left[\left(-176a^2+16\xi a+160\xi^2\right)\alpha_o+2(29\pi\xi+35\pi a)v_i t\right]=0 \tag{20}$$

and

$$\frac{8\pi}{15}\tilde{I}\left(a^2-\xi^2\right)\frac{d^2\alpha_o}{dt^2}+\frac{16\pi}{15}\tilde{I}\xi\frac{(a-\xi)}{t}\frac{d\alpha_o}{dt}+\frac{16}{3}\frac{(a+\xi)}{(a-\xi)}\left[\pi D_{11}+2D_{12}+(2+\pi)D_{66}\right]\alpha_o+$$
$$\frac{2}{105}\frac{A_{55}}{(a-\xi)}\left[56\pi\left(a^3-a\xi^2-a^2\xi+\xi^3\right)\alpha_o+\left(-176a^2+16\xi a+160\xi^2\right)v_i t\right]=0 \tag{21}$$

where $\alpha_o(0) = 0$ and $\dot{\alpha}_o(0) = 0$.

5 AN EXAMPLE

As an example consider a fully clamped, sandwich panel made of E-glass vinyl ester facesheets and H100 foam core, with a radius 250 mm, facesheet thickness 2 mm, and core thickness 25 mm. Material properties for the E-glass vinyl ester and H100 are given in Table 1. Let the sandwich panel be subject to a uniformly distributed pressure pulse of the form given in Eq. (1), where $p_o = 10$ MPa and $\tau = 0.05$ ms.

Table 1 : Facesheet and foam material properties.

	E-Glass/Vinyl Ester	Divinycell H100
Density (kg/m^3)	1391.3	100
Thickness (mm)	2	25
E_{11} (+) (GPa)	17	0.126
E_{22} (+) (GPa)	17	0.126
E_{33} (+) (GPa)	8.5	0.126
E_{11} (-) (GPa)	17	0.035
E_{22} (-) (GPa)	17	0.035
E_{33} (-) (GPa)	8.5	0.035
ν_{12}	0.13	0
ν_{13}	0.28	0
ν_{23}	0.28	0
G_{12}=G_{21} (GPa)	4.0	0.0175
G_{23}=G_{32} (GPa)	4.2	0.0175
G_{13}=G_{31} (GPa)	4.2	0.0175
q (MPa)	--	1.66
ε_D	--	0.8

This problem was modeled in 2D assuming plane strain conditions for Phase I response and in full 3D for both Phase I and II responses using ABAQUS Explicit. The H100 foam was modeled as an elastomeric foam with volumetric hardening. Additional foam properties, such as the plastic hardening curve were taken from Ref. [14].

5.1 Local core crushing: Phase I response

The transmitted stress transient at Interface 1, Eq. (5), and the same stress transient from FEA are shown in Fig. 7. The highest transmitted stress was calculated from Eq. (9) as $\sigma_p = 2.42$ MPa, which occurs at $t_p = 0.037$ ms from Fig. 7. This was about 10% higher than the maximum compressive stress of 2.2 MPa found from FEA. From the calculated values of σ_p and t_p, local core crushing was estimated as 3.2 mm from Eqs. (10) and (11).

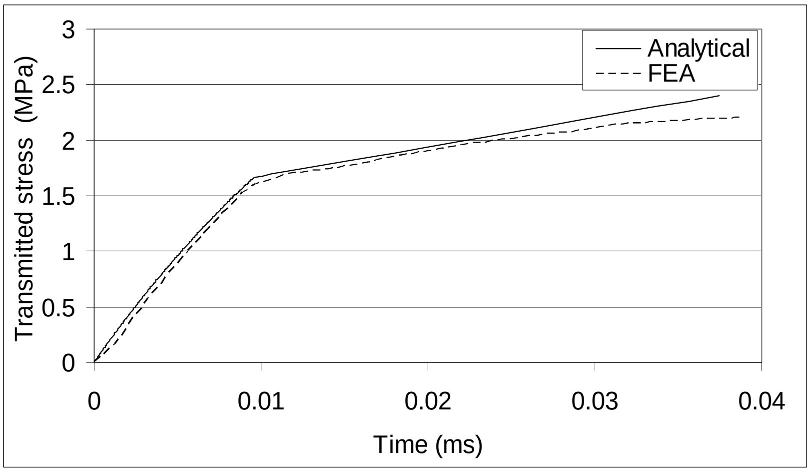

Figure 7: Transmitted stress at Interface 1 up to peak stress.

5.2 Global bending /shear: Phase II response

The initial global panel velocity was determined from Eq. (12) as $v_i = 31$ m/s. The sandwich bending and shear stiffness were evaluated with a reduced core thickness $H' = 21.8$ mm. A MATLAB program was written to solve Eqs. (20) and (21) for ξ and α_o. As shown in Fig. 8, the predicted transient deformation profiles compared very well to FEA results; the predicted value for ξ was within 7% of FEA.

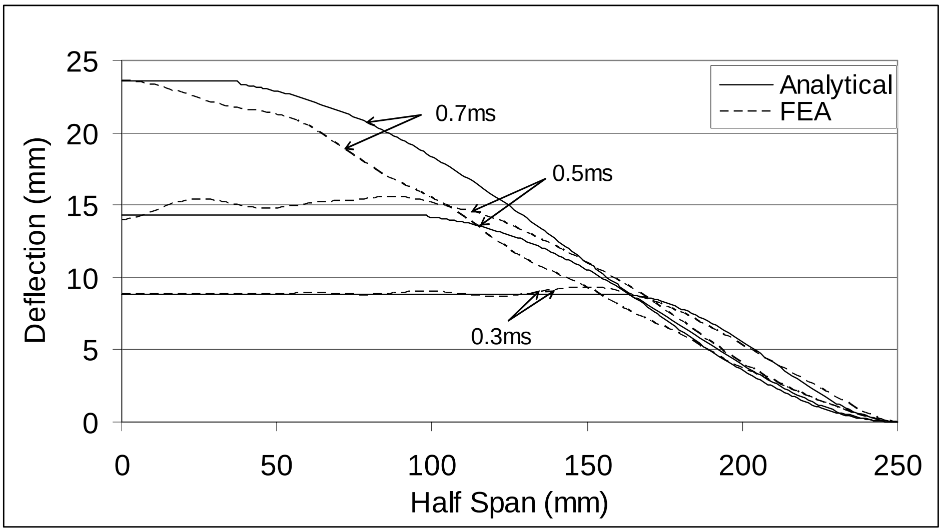

Figure 8: Transient deflection profiles of composite sandwich.

6 CONCLUDING REMARKS

Analytical solutions for the blast response of a foam-core composite sandwich panel were derived considering two phases: (a) core crushing during through-thickness wave propagation and (b) global panel bending/shear during transverse shear wave propagation. Global equilibrium equations of motion were used to obtain transverse deflection and shear rotations. The predicted transient deformation of the sandwich panel was within 7% of FEA results using ABAQUS Explicit.

ACKNOWLEDGEMENT

This work was support by Dr. Y. Rajapakse under ONR grant N00014-07-1-0423.

REFERENCES

[1] V.L. Tagarielli, V.S. Deshpande and N.A. Fleck, "The dynamic response of composite sandwich beams to transverse impact", *Int. J. Solids Struct.*, 44, 2442-2457 (2007).
[2] A. Vaziri and J.W. Hutchinson, "Metal sandwich plates subject to intense air shocks", *Int. J. Solids Struct.*, 44, 2021-2035 (2007).
[3] V.S. Deshpande and N. Fleck, "One-dimensional response of sandwich plates to underwater shock loading", *J. Mech. Phys. Solids*, 53, 2347-2383 (2005).
[4] J.W. Hutchinson and Z. Xue, "Metal sandwich plates optimized for pressure impulses", *Int. J. Mech. Sci.*, 47, 545-569 (2005).
[5] Z. Xue and J.W. Hutchinson, "A comparative study of impulse-resistant metal sandwich plates", *Int. J. Impact Engng.*, 30, 1238-1305 (2004).
[6] R.H. Cole, *Underwater Explosions*, Princeton University Press, New Jersey (1948).
[7] P.D. Smith and J.G. Hetherington, *Blast and Ballistic Loading of Structures,* Butterworth Heinemann, Oxford (1994).
[8] S.B. Menkes and H.J. Opat, "Broken Beams", *Exp. Mech.*, 13, 480-486 (1974).
[9] R.G. Teeling-Smith and G.N. Nurick, "The deformation and tearing of thin circular plates subjected to impulsive loads", *Int. J. Impact Engng.*, 11, 77-91 (1991).
[10] T. Franz, G.N. Nurick and M.J. Perry, "Experimental investigation into the response of chopped-strand mat glass fibre laminates to blast loading", *Int. J. Impact Engng.*, 27, 639-667 (2002).
[11] L. Librescu, S.-Y. Oh and J. Hohe, "Dynamic response of anisotropic sandwich flat panels to underwater and in-air explosions", *Int. J. Solids Struct.*, 43, 3794-3816 (2006).
[12] L.J. Gibson and M.F. Ashby, *Cellular Solids Structures and Properties*, Cambridge University Press, Cambridge (1999).
[13] M.F. Ashby, A.G. Evans, N.A. Fleck, L.J. Gibson, J.W. Hutchinson, H.N.G. Wadley, *Metal Foams: A Design Guide,* Butterworth Heinemann, London (2000).
[14] R.A.W. Mines and A. Alias, "Numerical simulation of the progressive collapse of polymer composite sandwich beams under static loading", *Composites Part A*, 33, 11- 26 (2002).

8th International Conference on Sandwich Structures
ICSS 8
A. J. M. Ferreira (Editor)

BLAST NON-LINEAR RESPONSE OF COMPOSITE SANDWICH PLATES WITH COMPRESSIBLE CORES

Renfu Li*, George A. Kardomateas†, and George J. Simitses†

*G.W. Woodruff School of Mechanical Engineering,

†Daniel Guggenheim School of Aerospace Engineering
Georgia Institute of Technology
Atlanta, Georgia 30332, USA
e-mail: renfu.li@me.gatech.edu
e-mail: george.kardomateas@aerospace.gatech.edu
e-mail: george.simitses@aerospace.gatech.edu

Key words: Blast, Impact, Sandwich, Composite, Plate, Compressible Core, Energy Absorption

Summary. *This paper addresses the transient dynamic behavior of sandwich plates subjected to transverse impulsive loading. A high order shear core theory, which was first proposed for shells by the authors [1] has been further developed for sandwich plates in [2]. This high order core theory is employed currently to investigate the transient response of sandwich plates under a typical sinusoidally distributed blast loading exerted on the top face sheet of the plates. Numerical results for the influences of the material properties and the geometrical parameters such as the ratio of face sheet thickness and core thickness of the sandwich plate on the transverse deformation and stress distribution in the core are presented. This work and method can be further extended to study the energy absorption capability and the dynamic buckling of a sandwich plate under sudden loading.*

1 Introduction

A typical sandwich plate consists of two stiff metallic or composites thin face sheets separated by a soft honeycomb or foam thick core of low density. This configuration gives the sandwich material system the integrity of high stiffness and strength with little resultant weight penalty and high-energy absorption capability with regard to the application of sandwich structures in the construction of aerospace vehicles, submarines and civil infrastructure. Most of the studies in sandwich composites neglect the transverse deformation of the core [2]. The core of a sandwich structure is treated as infinitely rigid in the thickness direction and only its shear stresses are taken into account. This assumption may work well in the analysis of sandwich structures subject to a static or dynamic loading of long-duration. Although, the two transversely compressive core models [3,4] are available, transverse strain of the core is assumed linear and constant respectively. However, several studies [5, 6, 1] have shown that the core transverse deformation/strain in a sandwich structure subject to impulsive loading is highly non-linear with regard to the variable in the thickness direction. Therefore, in this paper we will extend this non-linear core model developed in the authors' previous work for shells [1] to study effects from the material properties and structural parameters on the transverse displacement and stress distributions in the cores of composite sandwich plates under a typical blast loading.

Because of the core compressibility, the displacements of the top and bottom face sheets are not equal. We shall employ the following assumptions: (1) The face sheets satisfy the Kirchhoff-Love assumption and the thicknesses are small compared with the overall thickness of the sandwich section. Moreover, in the current study, the two face sheets are assumed to have an identical thickness. (2) The core is compressible in the transverse direction, that is, its thickness may change. (3) The bonding between the face sheets and the core is assumed perfect. (4) The top face sheet is subjected to a sinusoidally distributed shock wave pressure.

2 Formulation

2.1 Kinematic relations

Let a coordinate system (x, y, z) be located at the middle plane of the face sheets with z as outward normal direction and $(u,\ v,\ w)$ as the corresponding displacements. For thin face sheets, the displacements in first approximation can be expressed as:

$$\begin{aligned} u^{t,b}(x,y,z,t) &= u_{\text{o}}^{t,b}(x,y,t) - z w_{,x}^{t,b}(x,y,t) \\ v^{t,b}(x,y,z,t) &= v_{\text{o}}^{t,b}(x,y,t) - z w_{,y}^{t,b}(x,y,t) \\ w^{t,b}(x,y,z,t) &= w^{t,b}(x,y,t), \qquad -\frac{h_f}{2} \le z \le \frac{h_f}{2} \end{aligned} \tag{1}$$

where h_f is the face sheet thickness; the u_{o} and v_{o} are the middle plane displacements in x and y directions; superscript ^{t} and ^{b} denote the corresponding values in top face sheet and bottom face sheet, respectively; subscript $_,$ denotes differentiation with respect to corresponding variables.

Omitting the superscripts ^{t} and ^{b}, the non-linear strain-displacement relations for top and bottom face sheets can take the following forms:

$$[\epsilon] = \begin{pmatrix} \epsilon_x \\ \epsilon_y \\ \gamma_{xy} \end{pmatrix} = [\epsilon^{\text{o}}] \pm z[k] = \begin{pmatrix} \epsilon_x^{\text{o}} \pm z k_x \\ \epsilon_y^{\text{o}} \pm z k_y \\ \gamma_{xy}^{\text{o}} \pm z k_{xy} \end{pmatrix} \tag{2}$$

in which the $'\pm'$ sign in variable z are for the top and bottom face sheets, respectively. For sandwich plate, the middle surface strain $[\epsilon_o]$ can be given by

$$[\epsilon^{\text{o}}] = \begin{pmatrix} \epsilon_x^{\text{o}} \\ \epsilon_y^{\text{o}} \\ \gamma_{xy}^{\text{o}} \end{pmatrix} = \begin{pmatrix} u_{\text{o},x} + \frac{1}{2} w_{,x}^2 \\ v_{\text{o},y} + \frac{1}{2} w_{,y}^2 \\ u_{\text{o},y} + v_{\text{o},x} + w_{,x} w_{,y} \end{pmatrix} \tag{3}$$

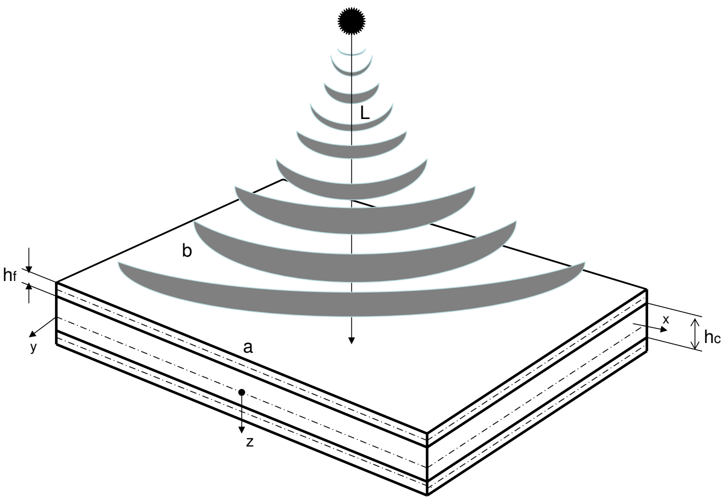

Figure 1: A composites sandwich plate subject to blast impact loading

and $[k]$ is the curvature,

$$[k] = \begin{pmatrix} k_x \\ k_y \\ k_{xy} \end{pmatrix} = \begin{pmatrix} -w_{,xx} \\ -w_{,yy} \\ -2w_{,xy} \end{pmatrix} \tag{4}$$

2.2 The high order shear core theory

During the impulsive loading process, the core may undergo large deformation in transverse direction. Therefore, the compressibility of the core in a sandwich plate should be considered when dealing with the transient response of the plate subject to blast loading. The complete derivation of a high order shear core theory is presented in [2] and a summary is as follows:

$$\begin{aligned} w^c(x,y,z,t) &= [1 - \frac{2z^2}{h_c^2} - \frac{8z^4}{h_c^4}]w^c_{\mathrm{o}}(x,y,t) \\ &+ [\frac{2z^2}{h_c^2} + \frac{8z^4}{h_c^4}]\check{w}(x,y,t) - [\frac{z}{h_c} + \frac{4z^3}{h_c^3}]\bar{w}(x,y,t), \quad -\frac{h_c}{2} \le z \le \frac{h_c}{2}, \end{aligned} \tag{5}$$

is the transverse displacement of the core; and

$$\begin{aligned} u^c(x,y,z,t) &= \check{u}(x,y,t) - \frac{z}{h_c/2}\bar{u}(x,y,t) + z\frac{h_f}{h_c}w^c_{,x}(x,y,z,t) \\ v^c(x,y,z,t) &= \check{v}(x,y,t) - \frac{z}{h_c/2}\bar{v}(x,y,t) + z\frac{h_f}{h_c}w^c_{,y}(x,y,z,y) \end{aligned} \tag{6}$$

is the in-plane displacements of the core. In the above equations, h_c is the core thickness, $w_{\text{o}}^c(x,y,t)$ is the transverse displacements of the initial middle surface of the core, $\breve{w}(x,y,t)$, $\bar{w}(x,y,t)$, $\breve{u}(x,y,t)$, $\bar{u}(x,y,t)$ and $\breve{v}(x,y,t)$, $\bar{v}(x,y,t)$ are defined as:

$$\begin{aligned}
\breve{w}(x,y,t) &= \frac{1}{2}[w^t(x,y,t)+w^b(x,y,t)], \qquad \bar{w}(x,y,t) = \frac{1}{2}[w^t(x,y,t)-w^b(x,y,t)] \\
\breve{u}(x,y,t) &= \frac{1}{2}[u_{\text{o}}^t(x,y,t)+u_{\text{o}}^b(x,y,t)], \qquad \bar{u}(x,y,t) = \frac{1}{2}[u_{\text{o}}^t(x,y,t)-u_{\text{o}}^b(x,y,t)] \\
\breve{v}(x,y,t) &= \frac{1}{2}[v_{\text{o}}^t(x,y,t)+v_{\text{o}}^b(x,y,t)], \qquad \bar{v}(x,y,t) = \frac{1}{2}[v_{\text{o}}^t(x,y,t)-v_{\text{o}}^b(x,y,t)]
\end{aligned} \tag{7}$$

The strain-displacement relation in the core can be obtained from equations (5) and (6). It reads as:

$$\begin{aligned}
\epsilon_z^c &= (-\frac{1}{2h_c}+\frac{2z}{h_c^2}-\frac{6z^2}{h_c^3}+\frac{16z^3}{h_c^4})w^t(x,y,t)-(\frac{4z}{h_c^2}+\frac{32z^3}{h_c^4})w_o^c(x,y,t) \\
&\quad +(\frac{1}{2h_c}+\frac{2z}{h_c^2}+\frac{6z^2}{h_c^3}+\frac{16z^3}{h_c^4})w^b(x,y,t) \\
\gamma_{xz}^c &= -\frac{2}{h_c}\bar{u}(x,y,t)+\Gamma_1(z)w_{,x}^t(x,y,t)+\Gamma_2(z)w_{o,x}^c(x,y,t)+\Gamma_3(z)w_{,x}^b(x,y,t) \\
\gamma_{yz}^c &= -\frac{2}{h_c}\bar{v}(x,y,t)+\Gamma_1(z)w_{,y}^t(x,y,t)+\Gamma_2(z)w_{o,y}^c(x,y,t)+\Gamma_3(z)w_{,y}^b(x,y,t)
\end{aligned} \tag{8}$$

in which,

$$\begin{aligned}
\Gamma_1(z) &= -\frac{1}{2}(1+2\frac{h_f}{h_c})\frac{z}{h_c}+(1+3\frac{h_f}{h_c})\frac{z^2}{h_c^2}-2(1+4\frac{h_f}{h_c})\frac{z^3}{h_c^3}+4(1+5\frac{h_f}{h_c})\frac{z^4}{h_c^4} \\
\Gamma_2(z) &= (1+\frac{h_f}{h_c})-2(1+\frac{3h_f}{h_c})\frac{z^2}{h_c^2}-8(1+\frac{5h_f}{h_c})\frac{z^4}{h_c^4} \\
\Gamma_3(z) &= \frac{1}{2}(1+2\frac{h_f}{h_c})\frac{z}{h_c}+(1+3\frac{h_f}{h_c})\frac{z^2}{h_c^2}+2(1+4\frac{h_f}{h_c})\frac{z^3}{h_c^3}+4(1+5\frac{h_f}{h_c})\frac{z^4}{h_c^4}
\end{aligned} \tag{9}$$

The core is considered undergoing large rotation with a small displacement, and the in-plane strains could be neglected.

2.3 Constitutive relations

We will assume the face sheets are made of orthotropic laminated composites and the core is also orthotropic. The constitutive equations based on classic laminated composite theory for the face sheets can be written as:

$$\begin{pmatrix} N_x \\ N_y \\ N_{xy} \end{pmatrix} = \begin{pmatrix} A_{11} & A_{12} & A_{16} \\ A_{12} & A_{22} & A_{26} \\ A_{16} & A_{26} & A_{66} \end{pmatrix} \begin{pmatrix} \epsilon_x^{\text{o}} \\ \epsilon_y^{\text{o}} \\ \gamma_{xy}^{\text{o}} \end{pmatrix} + \begin{pmatrix} B_{11} & B_{12} & B_{16} \\ B_{12} & B_{22} & B_{26} \\ B_{16} & B_{26} & B_{66} \end{pmatrix} \begin{pmatrix} k_x \\ k_y \\ k_{xy} \end{pmatrix} \tag{10}$$

for resultant force, and

$$\begin{pmatrix} M_x \\ M_y \\ M_{xy} \end{pmatrix} = \begin{pmatrix} B_{11} & B_{12} & B_{16} \\ B_{12} & B_{22} & B_{26} \\ B_{16} & B_{26} & B_{66} \end{pmatrix} \begin{pmatrix} \epsilon_x^o \\ \epsilon_y^o \\ \gamma_{xy}^o \end{pmatrix} + \begin{pmatrix} D_{11} & D_{12} & D_{16} \\ D_{12} & D_{22} & D_{26} \\ D_{16} & D_{26} & D_{66} \end{pmatrix} \begin{pmatrix} k_x \\ k_y \\ k_{xy} \end{pmatrix} \tag{11}$$

for resultant moment. The extensional A, B coupling and D bending stiffness matrices are respectively defined as,

$$[A_{ij}, B_{ij}, D_{ij}] = \begin{cases} \int_{h_c/2}^{h_c/2+h_f} Q_{ij} \times [1,\ z,\ z^2]dz, & \text{for top face} \\ \int_{-h_c/2-h_f}^{-h_c/2} Q_{ij} \times [1,\ z,\ z^2]dz, & \text{for bottom face} \end{cases} \qquad i,j = 1,2,6 \tag{12}$$

The stress-strain relations for the orthotropic core are as follows:

$$\sigma_z^c = E^c \epsilon_z^c, \quad \sigma_{xz} = G_{xz}^c \gamma_{xz}^c, \quad \sigma_{yz}^c = G_{yz}^c \gamma_{yz}^c \tag{13}$$

2.4 Equations of motion

The governing equations and appropriate boundary conditions can be derived using Hamilton's principle. The sandwich plate is assumed subject to impulsive transverse loading $q(x, y, t)$ on the top face sheet. Let T be the kinetic energy, U be the strain energy, W be external potential, then the variational principle states,

$$\delta[T - (U - W)] = 0 \tag{14}$$

in which,

$$\delta T = \int_0^t \int_{-b/2}^{b/2} \int_{-a/2}^{a/2} [\int_{-h_c/2-h_f}^{-h_c/2} \rho^f (\dot{u}^t \delta \dot{u}^t + \dot{v}^t \delta \dot{v}^t + \dot{w}^t \delta \dot{w}^t) dz \tag{15}$$
$$+ \int_{-h_c/2}^{h_c/2} \rho^c (\dot{u}^c \delta \dot{u}^c + \dot{v}^c \delta \dot{v}^c + \dot{w}^c \delta \dot{w}^c) dz + \int_{h_c/2}^{h_c/2+h_f} \rho^f (\dot{u}^b \delta \dot{u}^b + \dot{v}^b \delta \dot{v}^b + \dot{w}^b \delta \dot{w}^b) dz] dxdydt$$

$$\delta U = \int_0^t \int_{-b/2}^{b/2} \int_{-a/2}^{a/2} [\int_{-h_c/2-h_f}^{-h_c/2} (\sigma_x^t \delta \epsilon_x^t + \sigma_y^t \delta \epsilon_y^t + \sigma_{xy}^t \delta \gamma_{xy}^t) dz \tag{16}$$
$$+ \int_{-h_c/2}^{h_c/2} (\sigma_z^c \delta \epsilon_z^c + \sigma_{xz}^c \delta \gamma_{xz}^c + \sigma_{yz}^c \delta \gamma_{yz}^c) dz + \int_{h_c/2}^{h_c/2+h_f} (\sigma_x^b \delta \epsilon_x^b \sigma_y^b \delta \epsilon_y^b + \sigma_{xy}^b \delta \gamma_{xy}^b) dz] dxdydt$$

$$\delta W = \int_0^t \int_{-b/2}^{b/2} \int_{-a/2}^{a/2} q(x, y, t) \delta w^t dxdydt \tag{17}$$

The equations of motion and the boundary conditions can be obtained by substituting the constitutive relations into (15) and (16), then into (14) and employing integration by parts. The equations for the top face sheet can be written as:

$$\begin{aligned}\delta u_{\circ}^{t}:\ & (\rho^f h_f + \frac{1}{3}\rho^c h_c)\ddot{u}_{\circ}^{t} - \frac{\rho^c h_c h_f}{420}(23\ddot{w}_{,x}^{t} + 17\ddot{w}_{\circ,x}^{c} - 5\ddot{w}_{,x}^{b}) + \frac{\rho^c h_c}{6}\ddot{u}_{\circ}^{b} - N_{x,x}^{t} - N_{xy,y}^{t} \\ & - G_{xz}^{c}[-\frac{1}{h_c}(u_{\circ}^{t} - u_{\circ}^{b}) + \frac{11}{15}w_{\circ,x}^{c} + \alpha_0(w_{,x}^{t} + w_{,x}^{b})] = 0\end{aligned} \tag{18}$$

$$\begin{aligned}\delta v_{\circ}^{t}:\ & (\rho^f h_f + \frac{1}{3}\rho^c h_c)\ddot{v}_{\circ}^{t} - \frac{\rho^c h_c h_f}{420}(23\ddot{w}_{,y}^{t} + 17\ddot{w}_{\circ,y}^{c} - 5\ddot{w}_{,y}^{b}) + \frac{\rho^c h_c}{6}\ddot{v}_{\circ}^{b} - N_{xy,x}^{t} - N_{y,y}^{t} \\ & - G_{yz}^{c}[-\frac{1}{h_c}(v_{\circ}^{t} - v_{\circ}^{b}) + \frac{11}{15}w_{\circ,y}^{c} + \alpha_0(w_{,y}^{t} + w_{,y}^{b})] = 0\end{aligned} \tag{19}$$

$$\begin{aligned}\delta w_{\circ}^{t}:\ & \frac{23}{420}\rho^c h_c h_f(\ddot{u}_{\circ,x}^{t} + \ddot{v}_{\circ,y}^{t}) + (\rho^t h_f + \frac{29}{315}\rho^c h_c - \frac{19}{1155}\rho^c h_c h_f^2\bigtriangledown^2)\ddot{w}^t + (\frac{37}{630}\rho^c h_c \\ & - \frac{119}{27720}\rho^c h_c h_f^2\bigtriangledown^2)\ddot{w}_{\circ}^{c} + \frac{1}{84}\rho^c h_c h_f(\ddot{u}_{\circ,x}^{b} + \ddot{v}_{\circ,y}^{b}) + (-\frac{11}{630}\rho^c h_c + \frac{61}{27720}\rho^c h_c h_f^2\bigtriangledown^2)\ddot{w}^b \\ & - [M_{x,xx}^{t} + 2M_{xy,xy}^{t} + M_{y,yy}^{t} + (N_x^t w_{,x}^{t})_{,x} + (N_{xy}^t w_{,x}^{t})_{,y} + (N_{yx}^t w_{,y}^{t})_{,x} + (N_y^t w_{,y}^{t})_{,y}] \\ & - \alpha_1 h_c(G_{xz}^c w_{,xx}^{t} + G_{yz}^c w_{,yy}^{t}) - \alpha_2 h_c(G_{xz}^c w_{\circ,xx}^{c} + G_{yz}^c w_{\circ,yy}^{c}) \\ & + \alpha_3 h_c(G_{xz}^c w_{,xx}^{b} + G_{yz}^c w_{,yy}^{b}) + \alpha_0[G_{xz}^c(u_{\circ,x}^{t} - u_{\circ,x}^{b}) + G_{yz}^c(v_{\circ,y}^{t} - v_{\circ,y}^{b})] \\ & + \frac{E^c}{h_c}(\frac{61}{21}w^t - \frac{358}{105}w_{\circ}^{c} + \frac{53}{105}w^b) - q(x,y,t) = 0,\end{aligned} \tag{20}$$

Similar equations can be obtained for the bottom face sheet. The equations for the compressive core read as

$$\begin{aligned}\delta w_{\circ}^{c}:\ & \frac{17}{420}\rho^c h_c h_f(\ddot{u}_{\circ,x}^{t} + \ddot{v}_{\circ,y}^{t}) + (\frac{37}{630}\rho^c h_c - \frac{199}{27720}\rho^c h_c h_f^2\bigtriangledown^2)(\ddot{w}^t + \ddot{w}^b) \\ & + (\frac{194}{315}\rho^c h_c - \frac{181}{6930}\rho^c h_c h_f^2\bigtriangledown^2)\ddot{w}_{\circ}^{c} - \frac{17}{420}\rho^c h_c h_f(\ddot{u}_{\circ,x}^{b} + \ddot{v}_{\circ,y}^{b}) \\ & \frac{358}{105}\frac{E^c}{h_c}(2w_{\circ}^{c} - w^t - w^b) + \frac{11}{15}G_{xz}^c(u_{\circ,x}^{t} - u_{\circ,x}^{b}) + \frac{11}{15}G_{yz}^c(v_{\circ,y}^{t} - v_{\circ,y}^{b}) \\ & - \alpha_2 h_c[G_{xz}^c(w_{,xx}^{t} + w_{,xx}^{b}) + G_{yz}^c(w_{,yy}^{t} + w_{,yy}^{b})] - \alpha_4 h_c(G_{xz}^c w_{\circ,xx}^{c} + G_{yz}^c w_{\circ,yy}^{c}) = 0,\end{aligned} \tag{21}$$

The constants $\alpha_i (i = 0...4)$ in the above equations relate to the ratio of face thickness and core thickness which are defined as:

$$\begin{aligned}&\alpha_0 = \frac{2}{15} + \frac{h_f}{2h_c}, \quad \alpha_1 = \frac{29}{315} + \frac{373}{630}\frac{h_f}{h_c} + \frac{247}{252}(\frac{h_f}{h_c})^2, \quad \alpha_2 = \frac{37}{630} + \frac{37}{630}\frac{h_f}{h_c} - \frac{383}{630}(\frac{h_f}{h_c})^2, \\ &\alpha_3 = \frac{11}{630} + \frac{11}{630}\frac{h_f}{h_c} - \frac{23}{180}(\frac{h_f}{h_c})^2, \quad \alpha_4 = \frac{194}{315} + \frac{194}{315}\frac{h_f}{h_c} + \frac{383}{315}(\frac{h_f}{h_c})^2\end{aligned} \tag{22}$$

The corresponding boundary conditions x = 0,a read as follows:

$$\begin{aligned}
&u_\circ^t = \widetilde{u}^t \ \text{ or } \ N_x^t = \widetilde{N}_x^t \\
&v_\circ^t = \widetilde{v}^t \ \text{ or } \ N_{xy}^t = \widetilde{N}_{xy}^t \\
&w^t = \widetilde{w}^t \ \text{ or } \ N_x^t w_{,x}^t + M_{x,x}^t + N_{xy}^t w_{,y}^t + 2M_{xy,x}^t \\
&\qquad\qquad + G_{xz}^c[\alpha_0(u_\circ^b - u_\circ^t) + \alpha_1 h_c w_{,x}^t + \alpha_2 h_c w_{\circ,x}^c - \alpha_3 h_c w_{,x}^b] = \widetilde{Q}_x^t \\
&w_{,x}^t = \widetilde{w}_{,x}^t \ \text{ or } \ M_x^t = \widetilde{M}_x^t
\end{aligned} \tag{23}$$

$$w_\circ^c = \widetilde{w}_\circ^c \ \text{ or } \ \frac{11}{15}(u_\circ^b - u_\circ^t) + \alpha_2 h_c w_{,x}^t + \alpha_4 h_c w_{\circ,x}^c + \alpha_2 h_c w_{,x}^b = \widetilde{Q}_c \tag{24}$$

$$\begin{aligned}
&u_\circ^b = \widetilde{u}^b \ \text{ or } \ N_x^b = \widetilde{N}_x^b \\
&v_\circ^b = \widetilde{v}^b \ \text{ or } \ N_{xy}^b = \widetilde{N}_{xy}^b \\
&w^b = \widetilde{w}^b \ \text{ or } \ N_x^b w_{,x}^b + M_{x,x}^b + N_{xy}^b w_{,y}^b + 2M_{xy,x}^b \\
&\qquad\qquad + G_{xz}^c[\alpha_0(u_\circ^b - u_\circ^t) - \alpha_3 h_c w_{,x}^t + \alpha_2 h_c w_{\circ,x}^c + \alpha_1 h_c w_{,x}^b] = \widetilde{Q}_x^t \\
&w_{,x}^b = \widetilde{w}_{,x}^b \ \text{ or } \ M_x^b = \widetilde{M}_x^b
\end{aligned} \tag{25}$$

where, superscript $\widetilde{}$ denotes the known external boundary values. Similar equations can be written for y = 0,b.

For the sandwich plates made of orthotropic materials, one can rewrite the equations for the top face sheet as:

$$\begin{aligned}
&(\rho^f h_f + \frac{1}{3}\rho^c h_c)\ddot{u}_\circ^t - \frac{\rho^c h_c h_f}{420}(23\ddot{w}_{,x}^t + 17\ddot{w}_{\circ,x}^c - 5\ddot{w}_{,x}^b) + \frac{\rho^c h_c}{6}\ddot{u}_\circ^b \\
&- [A_{11}^t\frac{\partial^2}{\partial x^2} + A_{66}^t\frac{\partial^2}{\partial y^2} - \frac{G_{xz}^c}{h_c}]u_\circ^t - (A_{12}^t + A_{66}^t)\frac{\partial^2 v_\circ^t}{\partial x \partial y} - G_{xz}^c\alpha_0 w_{,x}^t - G_{xz}^c\frac{11}{15}w_{\circ,x}^c \\
&- \frac{G_{xz}^c}{h_c}u_\circ^b - G_{xz}^c\alpha_0 w_{,x}^b = \hat{F}_1^t
\end{aligned} \tag{26}$$

$$\begin{aligned}
&(\rho^f h_f + \frac{1}{3}\rho^c h_c)\ddot{v}_\circ^t - \frac{\rho^c h_c h_f}{420}(23\ddot{w}_{,y}^t + 17\ddot{w}_{\circ,y}^c - 5\ddot{w}_{,y}^b) + \frac{\rho^c h_c}{6}\ddot{v}_\circ^b - (A_{21}^t + A_{66}^t)\frac{\partial^2}{\partial xy}u_\circ^t \\
&- [A_{66}^t\frac{\partial^2}{\partial x^2} + A_{22}^t\frac{\partial^2}{\partial y^2} - \frac{G_{yz}^c}{h_c}]v_\circ^t - G_{yz}^c\alpha_0 w_{,y}^t - G_{yz}^c\frac{11}{15}w_{\circ,y}^c \\
&- \frac{G_{yz}^c}{h_c}v_\circ^b - G_{yz}^c\alpha_0 w_{,y}^b = \hat{F}_2^t
\end{aligned} \tag{27}$$

$$\frac{23}{420}\rho^c h_c h_f(\ddot{u}^t_{\text{o},x}+\ddot{v}^t_{\text{o},y})+(\rho^t h_f+\frac{29}{315}\rho^c h_c-\frac{19}{1155}\rho^c h_c h_f^2\nabla^2)\ddot{w}^t+(\frac{37}{630}\rho^c h_c \tag{28}$$
$$-\frac{119}{27720}\rho^c h_c h_f^2\nabla^2)\ddot{w}^c_\text{o}+\frac{1}{84}\rho^c h_c h_f(\ddot{u}^b_{\text{o},x}+\ddot{v}^b_{\text{o},y})-(\frac{11}{630}\rho^c h_c+\frac{61}{27720}\rho^c h_c h_f^2\nabla^2)\ddot{w}^b$$
$$[D^t_{11}\frac{\partial^4}{\partial x^4}+2(D^t_{12}+2D^t_{66})\frac{\partial^4}{\partial x^2 y^2}+D^t_{22}\frac{\partial^4}{\partial y^4}+\frac{61}{21}\frac{E^c}{h_c}-\alpha_1 h_c(G^c_{xz}\frac{\partial^2}{\partial x^2}+G^c_{yz}\frac{\partial^2}{\partial y^2})]w^t$$
$$-[\frac{358}{105}\frac{E^c}{h_c}+\alpha_2 h_c(G^c_{xz}\frac{\partial^2}{\partial x^2}+G^c_{yz}\frac{\partial^2}{\partial y^2})]w^c_\text{o}+[\frac{53}{105}\frac{E^c}{h_c}+\alpha_3 h_c(G^c_{xz}\frac{\partial^2}{\partial x^2}+G^c_{yz}\frac{\partial^2}{\partial y^2})]w^b$$
$$+\alpha_0 G^c_{xz}\frac{\partial}{\partial x}(u^t_\text{o}-u^b_\text{o})+\alpha_0 G^c_{yz}\frac{\partial}{\partial y}(v^t_\text{o}-v^b_\text{o})=q(x,y,t)+\hat{F}^t_3$$

in which,

$$\hat{F}^t_1=A_{11}w^t_{,x}w^t_{,xx}+(A_{12}+A_{66})w^t_{,y}w^t_{,xy}+A_{66}w^t_{,x}w^t_{,yy} \tag{29}$$
$$\hat{F}^t{}_2=(A_{21}+A_{66})w^t_{,x}w^t_{,xy}+A_{66}w^t_{,xx}w^t_{,y}-A_{22}w^t_{,y}w^t_{,yy}$$
$$\hat{F}^t{}_3=(N^t_x w^t_{,x})_{,x}+(N^t_{xy}w^t_{,x})_{,y}+(N^t_{yx}w^t_{,y})_{,x}+(N^t_y w^t_{,y})_{,y}$$

Similar equations can be obtained for the bottom face sheet. One can also recast the equations for the core as follows:

$$\frac{17}{420}\rho^c h_c h_f(\ddot{u}^t_{\text{o},x}+\ddot{v}^t_{\text{o},y})+(\frac{37}{630}\rho^c h_c-\frac{199}{27720}\rho^c h_c h_f^2\nabla^2)(\ddot{w}^t+\ddot{w}^b) \tag{30}$$
$$+(\frac{194}{315}\rho^c h_c-\frac{181}{6930}\rho^c h_c h_f^2\nabla^2)\ddot{w}^c_\text{o}-\frac{17}{420}\rho^c h_c h_f(\ddot{u}^b_{\text{o},x}+\ddot{v}^b_{\text{o},y})$$
$$+\frac{11}{15}G^c_{xz}\frac{\partial}{\partial x}(u^t-u^b)+\frac{11}{15}G^c_{yz}\frac{\partial}{\partial y}(v^t-v^b)-[\frac{358}{105}\frac{E^c}{h_c}+\alpha_2 h_c(G^c_{xz}\frac{\partial^2}{\partial x^2}+G^c_{yz}\frac{\partial^2}{\partial y^2})]w^t$$
$$+[\frac{716}{105}\frac{E^c}{h_c}-\alpha_4 h_c(G^c_{xz}\frac{\partial^2}{\partial x^2}+G^c_{yz}\frac{\partial^2}{\partial y^2})]w^c_o-[\frac{358}{105}\frac{E^c}{h_c}+\alpha_2 h_c(G^c_{xz}\frac{\partial^2}{\partial x^2}+G^c_{yz}\frac{\partial^2}{\partial y^2})]w^b=0$$

3 Solution procedure

The solution procedure for the response of sandwich plates will be demonstrated through the study of simply supported case under transversely applied loading. The boundary conditions along the $x=0,\ a$ and $y=0,\ b$ (Figure 1) read as:

$$u^t_\text{o}=0,\ u^b_\text{o}=0;\quad v^t_\text{o}=0,\ v^b_\text{o}=0;\quad w^t=0,\ w^c=0,\ w^b=0 \tag{31}$$

and

$$M^t_{xx}=0,\ M^b_{xx}=0 \qquad \text{for x = 0, a} \tag{32}$$
$$M^t_{yy}=0,\ M^b_{yy}=0 \qquad \text{for y = 0, b}$$

The displacements can be expressed in a series form:

$$u_{\circ}^{t} = \sum_{m,n} U_{mn}^{t}(t)\text{cos}(m\pi x/a)\text{sin}(n\pi y/b), \qquad v_{\circ}^{t} = \sum_{m,n} V_{mn}^{t}(t)\text{sin}(m\pi x/a)\text{cos}(n\pi y/b) \quad (33)$$

$$u_{\circ}^{b} = \sum_{m,n} U_{mn}^{b}(t)\text{cos}(m\pi x/a)\text{sin}(n\pi y/b), \qquad v_{\circ}^{b} = \sum_{m,n} V_{mn}^{b}(t)\text{sin}(m\pi x/a)\text{cos}(n\pi y/b)$$

$$w^{t} = \sum_{m,n} W_{mn}^{t}(t)\text{sin}(m\pi x/a)\text{sin}(n\pi y/b), \qquad w^{b} = \sum_{m,n} W_{mn}^{b}(t)\text{sin}(m\pi x/a)\text{sin}(n\pi y/b)$$

$$w^{c} = \sum_{m,n} W_{mn}^{c}(t)\text{sin}(m\pi x/a)\text{sin}(n\pi y/b)$$

where $U_{mn}^{t},\ V_{mn}^{t},\ U_{mn}^{b},\ V_{mn}^{b},\ W_{mn}^{t},\ W_{mn}^{b}$, and W_{mn}^{c} are unknown constants. Substituting Eq. (33) into equations of motion with applied loading $q(x,y)$ being expressed as:

$$q(x,y) = \sum_{mn} \hat{Q}_{mn}\text{sin}(m\pi x/a)\text{sin}(n\pi y/b) \qquad (34)$$

one can obtain sets of nonlinear equations in matrix form:

$$M_{mn}\ddot{U}_{mn} + C_{mn}\dot{U}_{mn} + \kappa_{mn}U_{mn} = F_{mn} \qquad (35)$$

where the displacement vector U_{mn} is defined as $U_{mn} = [U_{mn}^{t},\ V_{mn}^{t},\ W_{mn}^{t},\ W_{mn}^{c},\ U_{mn}^{b},\ V_{mn}^{b},\ W_{mn}^{b}]^{T}$ and the loading vector F_{mn} is a non-linear function vector of U_{mn}. To solve the set of non-linear equations, one first finds the solution with the initial loading vector $F_{mn}^{0} = [0,\ 0,\ \hat{Q}_{mn},\ 0,\ 0,\ 0,\ 0]$. The next approximate values of displacements can be obtained by solving equation (35) with the updated loading vector. This procedure is continued until a series of approximate solutions for in-plane and transverse displacements are determined by the nth iteration with convergent tolerance ϵ, such as $\epsilon \leq 10^{-5}$ between two consecutive solutions.

4 Numerical Results and Discussions

In this section, we shall present numerical results for typical sandwich plates with orthotropic phases. The face sheets are made of orthotropic Graphite/Epoxy composite materials and the core is made of orthotropic honeycomb. Since the sandwich structures consist of orthotropic phases, the relationship for Poisson's ratios as: $\nu_{ij} = \nu_{ji}E_i/E_j$ will be applied. In the following study, two face sheets of each sandwich plate are assumed identical with thickness h_f. Its core thickness is ten times of that of the face sheet, i.e. $h_c = 10h_f$. The total thickness of a plate is defined as $H_{tot} = 2h_f + h_c$. Let us consider Graphite/Epoxy faces with elastic constants (in GPa): $E_1^f = 40.0$, $E_2^f = 10.0$, $E_3^f = 10.0$, $G_{12}^f = 4.5$, $G_{23}^f = 3.5$, $G_{31}^f = 4.5$; Poisson's ratios: $\nu_{12}^f = 0.065$, $\nu_{31}^f = 0.260$, $\nu_{23}^f = 0.400$. The core is made of orthotropic honeycomb material with elastic constants (in GPa): $E_1^c = E_2^c = 0.032$, $E_3^c = E_z^c = 0.30$, $G_{12}^c = 0.013$, $G_{31}^c = 0.048$, $G_{23}^c = 0.048$; Poisson's ratios: $\nu_{12}^c = \nu_{31}^c = \nu_{32}^c = 0.25$. The top face of the sandwich plate is assumed to be blasted by the following sinusoidally distributed impulsive loading:

$$p(x,y) = p_0(t)\,\sin(\pi x/a)\,\sin(\pi y/b), \qquad 0 \le x \le a, \;\; 0 \le y \le b \tag{36}$$

Using expression (34) one can write the loading (36) in transformed space as:

$$\hat{Q}_{mn} = \delta_{m1}\delta_{n1}\; p_0(t) \tag{37}$$

where δ_{mn} is the Kronecker delta function. Plotted in Figure 2 is the distribution of the normal-

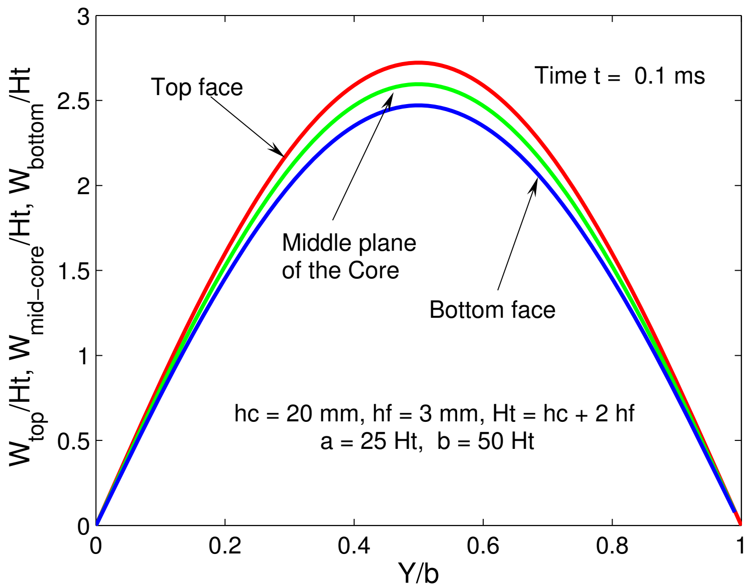

Figure 2: Transverse displacements the sandwich plate as function of y at time 0.1 ms & x = 0.5 a

ized transverse displacements as functions of y for the face sheets and middle plane of the core at x = a/2 when time t = 0.1 ms. It clearly shows that the displacements of top face and bottom face are not identical. Because the maximum intensity of blast loading is in the center point of the plate, the maximum values of the displacements can be observed at (x=a/2, y=b/2), the center of the face sheets and middle plane of the core. The differences among these displacements justify this advanced sandwich model which can capture the compressibility of the core, and this in turn implies that the transverse stress in the core may not be constant as assumed by the classical sandwich model. Figure 3 are the stress profiles in the core following the blast during different time period: 2.5ms $\le t \le$ 2.7ms; 5ms $\le t \le$ 5.2ms; 10ms $\le t \le$ 10.2ms. The following three observations can be made from the results plotted here: (1) the maximum compressive stress occurs at the interface between the core and top face on which the blast loading is applied and the stress on this interface is always negative, i.e. compressive. (2) the stress at the

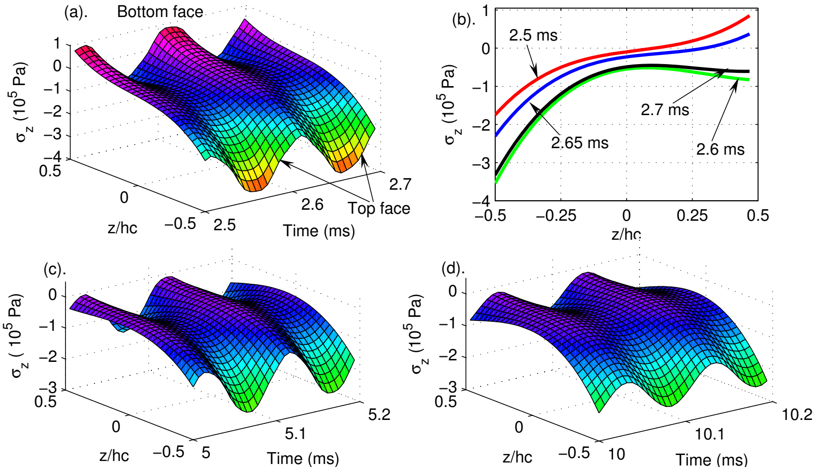

Figure 3: Stress profiles in the core following the blast

interface between the core and the bottom face sheet can be negative (compressive) or positive as shown in Fig. 3-b. The positive stress is induced by the shock wave pressure inside the core, a phenomenon which has been explained in [1]. (3) the stresses are attenuated as time goes by as demonstrated from Fig. 3-a, Fig. 3-c to Fig. 3-d. These observations agree with physical intuition. The results presented in Figure 4 and Figure 5 show the effects from the variation of geometrical parameters on the response of the sandwich plates subject to blast loading.

Table 1: Maximum values of the displacements in Fig. 4

hf/hc	1.5/20	2/20	2.5/20	3/20
$W_{top}^{Max.}$	26.8 mm	23.7 mm	21.9 mm	20.5 mm

It can be seen from Fig. 4 and Table 1 that when the ratio of the thickness of the face sheet and the core increases, the maximum value of the transverse displacement of the top face decreases at the very early stage of blast loading . One can see that after t = 20 ms, the displacements of the plate with h_f/h_c = 2/20, 2.5/20 and 3/20 are very close to each other. It can also be seen that the increase on the maximum value is relatively small when h_f/h_c changes from 3/20 to 2.5/20. This may imply that the optimum ratio of the h_f/h_c is around 2.5/20 for this sandwich combination with regard to a design criterion in term of displacement. The effects from variation of the ratio of h_f/h_c on the stress distribution in the core are demonstrated in Fig. 5. One may see that the stress distribution profiles are different for different values of h_f/h_c. However, the maximum compressive (negative) stress occurs at the interface between the core and the top face and the maximum extension (positive) stress occurs at the surface between the core and the bottom face sheet for different values of h_f/h_c. The observations from the results in Fig. 5 suggest that damage or crushing of the core could be initiated from the interface between the core and the top face on which the blast loading is exerted.

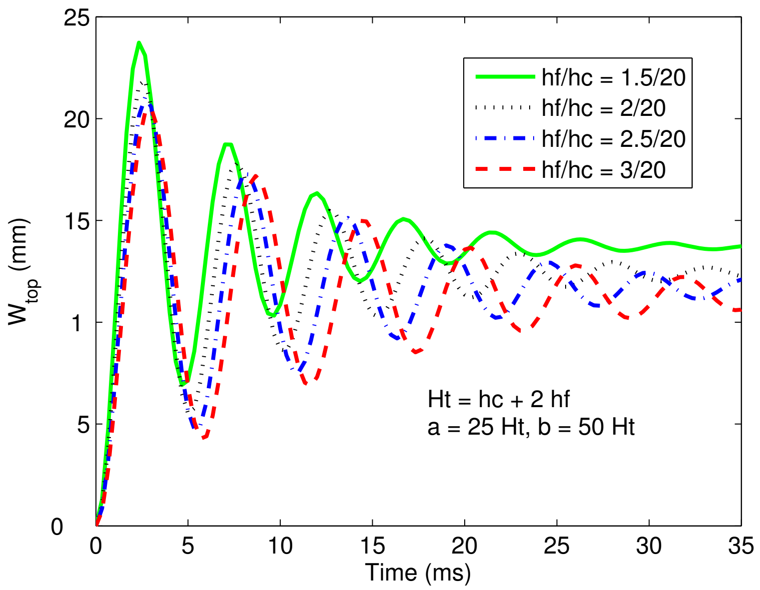

Figure 4: Influence of the ratio of face sheet thickness over core thickness on the displacements of top faces

5 Conclusions and future work

In the current work the response of a composite sandwich plate under blast loading is investigated using a high order compressible core theory. The results show that the displacements of the two face sheets are not identical under blast loading. The maximum compressive stress in the core occurs at the interface between the core and the face where the blast loading is applied. The thickness ratio between the face sheet and the core influences the maximum value of the transverse displacement of the sandwich plate. There exists an optimum value for this ratio with reference to displacement constraints. The geometrical parameters also have an influence on the stress distribution in the core. The current work can be extended to study failure modes such the core crushing, face sheet/core debonding, local and global buckling of sandwich plates, and analyze the overall resistance of plates to blast/impact loading.

Acknowledgments

The financial support of the Office of Naval Research, Grant N00014-07-10373, and the interest and encouragement of the Grant Monitor, Dr. Y.D.S. Rajapakse, are both gratefully acknowledged.

REFERENCES

[1] R. Li, G.A. Kardomateas and G.J. Simitses. ”Non-Linear Response of a Shallow Sandwich Shell with Compressible Core to Blast Loading”, ASME, J. Appl. Mech, *in press,* 2007.

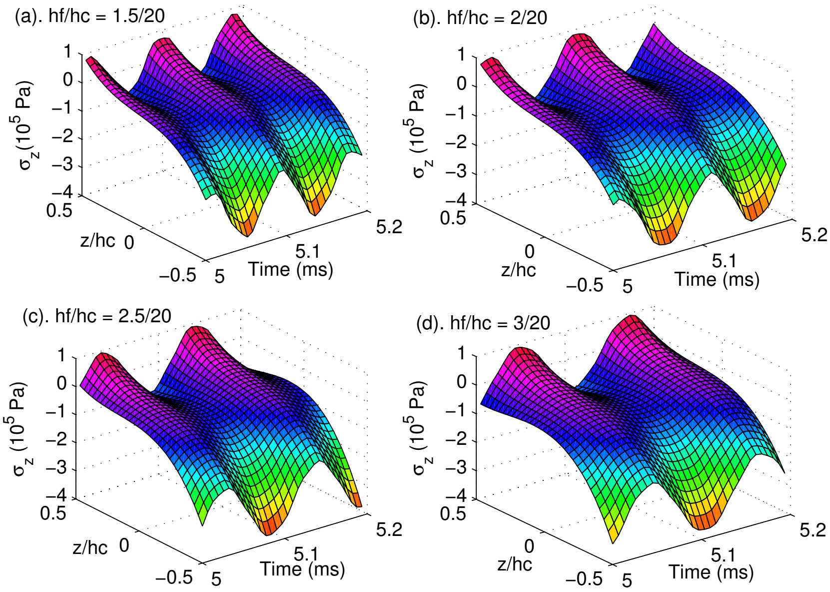

Figure 5: Influence from ratio of the thickness between face sheet and core on stress profiles in the cores following blast loading

[2] R. Li, G.A. Kardomateas and G.J. Simitses. "A New High Order Theory for Sandwich Plates with Orthotropic Phases", ASME, J. Appl. Mech, *submitted,* 2008.

[3] R. Li, G.A. Kardomateas and G.J. Simitses. "Transient Response of Transversely Compressible Sandwich Plates under Sudden Impulse Loading", *submitted,* 2008.

[4] J.R. Vinson. *The behavior of sandwich structures of isotropic and composite materials*, Lancester, PA: Technomic Publishing Company, 1999.

[5] Y. Frostig. "Behavior of Delaminated Sandwich Beams with Transversely Flexible Core-Hight Order Theory," Composite Structures, 20, pp.1-16,1992.

[6] J. Hohe, L. Librescu and S.Y. Oh. "Dynamic buckling of flat and curved sandwich panels with transvely compressible core", Composite Structures, 74, pp.10-24, 2006

[7] Y. Liang, A.V. Spuskanyuk, S.E. Flores,D.R. Hayhurst, J.W. Hutchinson, R.M. McMeeking, and A.G. Evans, "The Response of Metallic Sandwich Panels to Water Blast", ASME, J. Appl. Mech., 74(1), pp.81-99, 2007.

[8] S. Nemat-Nasser, W.J. Kang, J.D. McGee, W.-G., Guo, J.B. Issacs. "Experimental Investigation of Energy-Absorption Characteristics of Components of Sandwich Structures", Int. J. of Impact Engng, 34, pp.1119-1146, 2007.

8th International Conference on Sandwich Structures
ICSS 8
A. J. M. Ferreira (Editor)

THE INFLUENCE OF CORE PROPERTIES ON FAILURE OF COMPOSITE SANDWICH BEAMS

Isaac M. Daniel

Robert R. McCormick School of Engineering and Applied Science
Northwestern University, Evanston, IL 60208, USA

Keywords: Sandwich structures, Experimental methods, Characterization, Failure modes.

Summary. *The various failure modes occurring in composite sandwich beams are described and their relationship to the relevant core properties is explained and discussed. Experimental mechanics methods are used to illustrate the failure modes and verify analytical predictions.*

1 INTRODUCTION

The overall performance of sandwich structures depends in general on the properties of the facesheets, the core, the adhesive bonding the core to the skins, as well as geometrical dimensions. Sandwich beams under general bending, shear and in-plane loading display various failure modes. Their initiation, propagation and interaction depend on the constituent material properties, geometry, and type of loading. Failure modes and their initiation can be predicted by conducting a thorough stress analysis and applying appropriate failure criteria in the critical regions of the beam. This analysis is difficult because of the nonlinear and inelastic behavior of the constituent materials and the complex interactions of failure modes. Possible failure modes include tensile or compressive failure of the facesheets, debonding at the core/facesheet interface, indentation failure under localized loading, core failure, wrinkling of the compression facesheet, and global buckling. Following initiation of a particular failure mode, this mode may trigger and interact with other modes and final failure may follow a different failure path. A general review of failure modes in composite sandwich beams was given by Daniel et al. [1]. Individual failure modes in sandwich columns and beams have been discussed by Gdoutos et al. [2, 4] and Abot et al. [3]. Of all the factors influencing failure initiation and mode, the properties of the core material are the most predominant.

Commonly used materials for facesheets are composite laminates and metals, while cores are made of metallic and non-metallic honeycombs, cellular foams, balsa wood, or trusses. The facesheets carry almost all of the bending and in-plane loads while the core helps to stabilize the facesheets and defines the flexural stiffness and out-of-plane shear and compressive behavior. A number of core materials, including aluminum honeycomb, various types of closed-cell PVC foams, a polyurethane foam, foam-filled honeycomb and balsa wood, were characterized under uniaxial and biaxial states of stress.

In the present work, failure modes were investigated experimentally in axially loaded composite sandwich columns and sandwich beams under bending. Failure modes observed and studied include indentation failure, core failures, and facesheet wrinkling. The transition from one failure mode to another for varying loading or state of stress and beam dimensions was discussed. Experimental results were compared with analytical predictions.

2 CHARACTERIZATION OF CORE MATERIALS

The core materials characterized were four types of a closed-cell PVC foam (Divinycell H80, H100, H160 and H250, with densities of 80, 100, 160 and 250 kg/m^3, respectively), an aluminum honeycomb (PAMG 8.1-3/16 001-P-5052, Plascore Co.), a polyurethane foam, a foam-filled honeycomb, and balsa wood. All core materials were characterized in uniaxial tension, compression and shear along the in-plane and through-the-thickness directions. Typical stress-strain curves are shown in Figs. 1 and 2. Some of their characteristic properties are tabulated in Table 1. The core materials (honeycomb or foam) were provided in the form of 25.4 mm (1 in.) thick plates. The honeycomb core was bonded to the top and bottom faceshees with FM73 M film adhesive and the assembly was cured under pressure in an oven following the recommended curing cycle for the adhesive. The foam cores were bonded to the facesheets using a commercially available epoxy adhesive (Hysol EA 9430) (Daniel and Abot [5]). Beam specimens 25.4 mm (1 in.) wide and of various lengths were cut from the sandwich plates.

Property	Divinycell H80	Divinycell H100	Divinycell H160	Divinycell H250	Balsa Wood CK57	Aluminum Honeycomb PAMG 5052	Foam Filled Honeycomb Style 20	Poly-urethane FR-3708
Density, ρ, kg/m^3	80	100	160	250	150	130	128	128
In-plane modulus, E_1, MPa	77	95	140	255	110	8.3	25	38
In-plane modulus, E_2, MPa	77	95	140	245	110	6.0	7.6	38
Out of plane modulus, E_3, MPa	110	117	250	360	4600	2200	240	110
Transverse shear modulus, G_{13}, MPa	18	25	26	73	60	580	8.7	10
In-plane compressive strength, F_{1c}, MPa	1.0	1.4	2.5	4.5	0.8	0.2	0.4	1.2
In-plane tensile strength, F_{1t}, MPa	2.3	2.7	3.7	7.2	1.2	1.2	0.5	1.1
In-plane compressive strength, F_{2c}, MPa	1.0	1.4	2.5	4.5	0.8	0.2	0.3	1.1
Out of plane compressive strength, F_{3c}, MPa	1.4	1.6	3.6	5.6	9.7	11.8	1.4	1.8
Transverse shear strength, F_5, MPa	1.1	1.4	2.8	4.9	3.7	3.5	0.75	1.4

Table 1. Properties of sandwich core materials

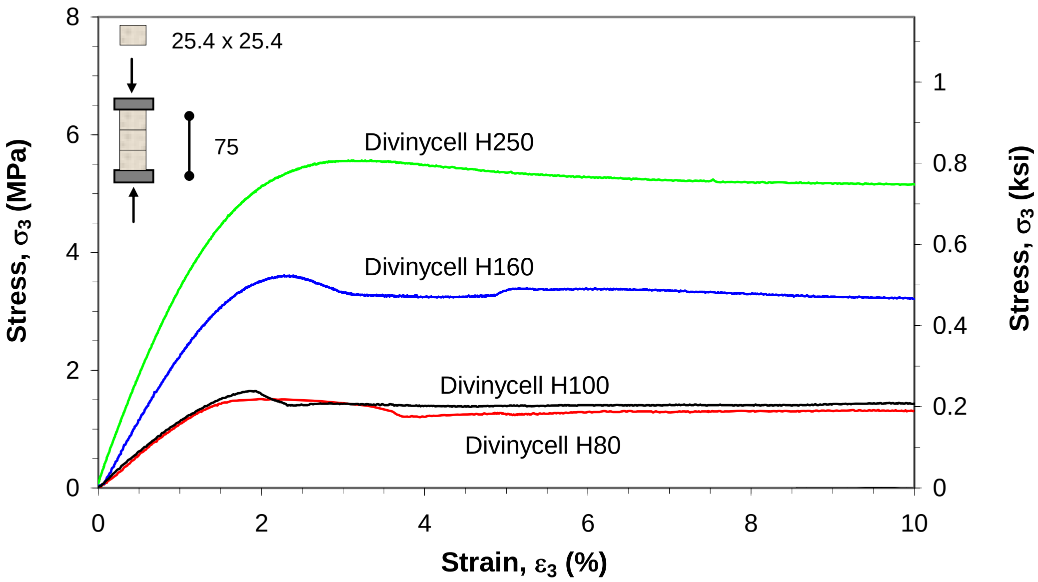

Figure 1: Stress-strain curves of PVC foam cores under compression in the through-thickness direction

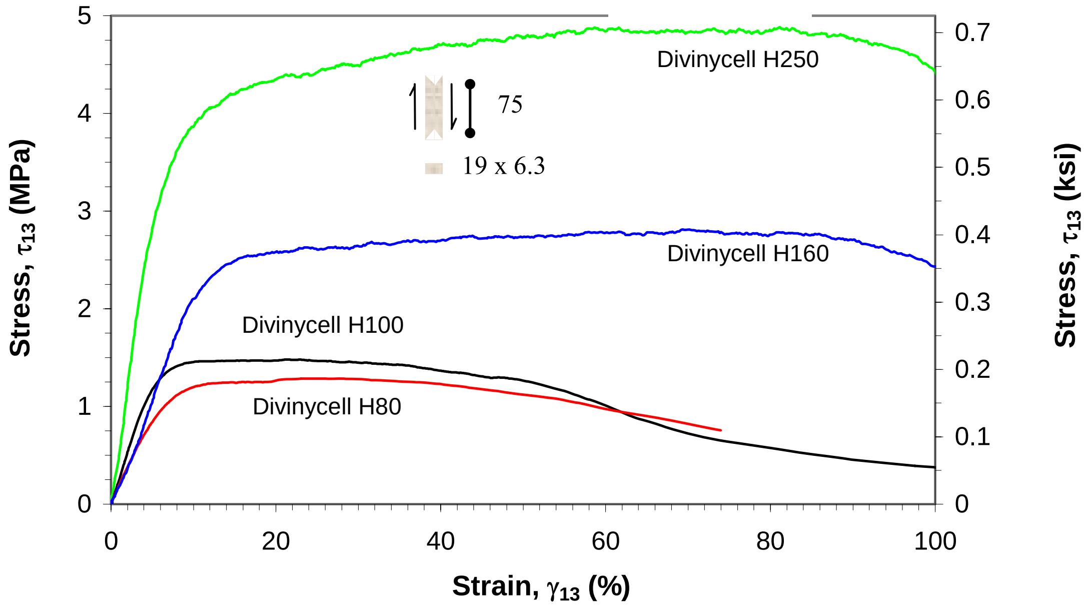

Figure 2: Shear stress-strain curves of PVC foam cores under through-thickness shear

Two core materials, Divinycell H100 and H250 were fully characterized under multiaxial stress conditions [6]. A series of biaxial tests were conducted including constrained strip specimens in tension and compression with the strip axis along the through-thickness and in-plane directions; constrained thin-wall ring specimens in compression and torsion; thin-wall tube specimens in tension and torsion; and thin-wall tube specimens under axial tension, torsion and internal pressure. From these tests and uniaxial results in tension, compression and shear, failure envelopes were constructed. It was shown that the failure envelopes were described well by the Tsai-Wu criterion as shown in Fig.3 [7].

The Tsai-Wu criterion for a general two-dimensional state of stress on the 1-3 plane is expressed as follows

$$f_1\,\sigma_1 + f_3\,\sigma_3 + f_{11}\,\sigma_1^2 + f_{33}\,\sigma_3^2 + 2 f_{13}\,\sigma_1\,\sigma_3 + f_{55}\,\tau_5^2 = 1 \tag{1}$$

where

$$f_1 = \frac{1}{F_{1t}} - \frac{1}{F_{1c}},\ f_3 = \frac{1}{F_{3t}} - \frac{1}{F_{3c}}$$

$$f_{11} = \frac{1}{F_{1t}\,F_{1c}},\ f_{33} = \frac{1}{F_{3t}\,F_{3c}},\ f_{13} = -\frac{1}{2}\left(f_{11}\,f_{33}\right)^{1/2},\ f_{55} = \frac{1}{F_5^2}$$

$F_{1t}, F_{1c}, F_{3t}, F_{3c} =$ tensile and compressive strengths in the in-plane (1,2) and out-of-plane (3) directions

$F_5 =$ shear strength on the 1-3 plane

Setting $\tau_5 = k\,F_5$, Eq. (1) is rewritten as

$$f_1\,\sigma_1 + f_3\,\sigma_3 + f_{11}\,\sigma_1^2 + f_{33}\,\sigma_3^2 + 2 f_{13}\,\sigma_1\,\sigma_3 = 1 - k^2 \tag{2}$$

It was assumed that the failure behavior of all core materials can be described by the Tsai-Wu criterion. Failure envelopes of all core materials constructed from the values of F_{1t}, F_{1c} and F_5 are shown in Fig. 4. Note that the failure envelopes of all Divinycell foams are elongated along the σ_1-axis, which indicates that these materials are stronger under normal longitudinal stress than in-plane shear stress. Aluminum honeycomb and balsa wood show the opposite behavior. For all materials, the most critical combinations of shear and normal stress fall in the second and third quadrants (the failure envelopes are symmetrical with respect to the σ_1-axis).

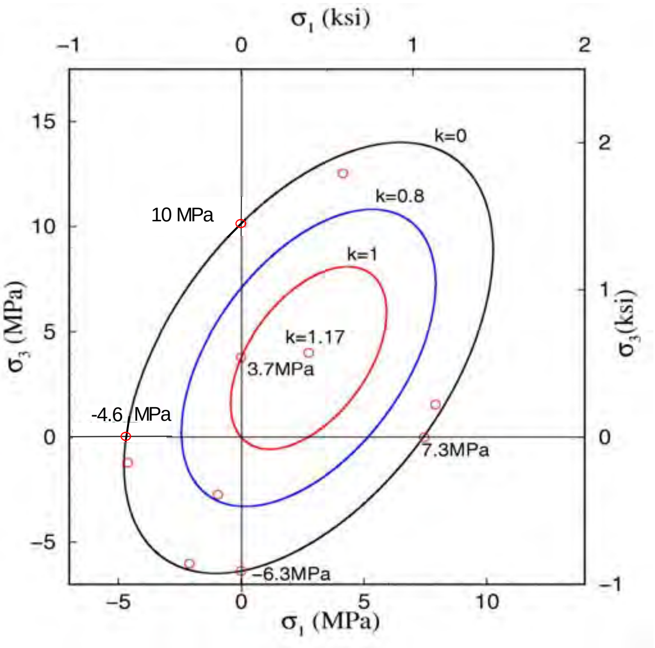

Figure 3: Failure envelopes predicted by the Tsai-Wu failure criterion for PVC foam (Divinycell H250) for k=0, 0.8 and 1, and experimental results ($k = \tau_{13}/F_{13} = \tau_5/F_5$)

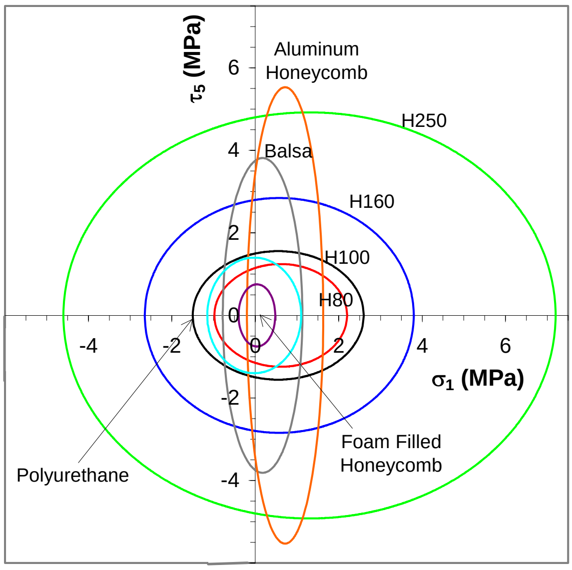

Figure 4: Failure envelopes for various core materials based on the Tsai-Wu failure criterion for interaction of normal and shear stress

3 CORE FAILURES

The deformation and failure mechanisms in the core of sandwich beams have been studied by means of moiré gratings and photoelastic coatings. Figure 5 shows photoelastic coating fringe patterns for a beam under three-point bending for various values of applied load P. The fringe pattern for a low applied load (2.3 kN) is nearly uniform, indicating that the shear strain (stress) in the core is constant. This pattern remains uniform up to an applied load of 3.3 kN which corresponds to an average shear stress in the core of 2.55 MPa. This is close to the proportional limit of the shear stress-strain curve of the core material (Fig. 2). For higher loads, the core begins to yield and the shear strain becomes highly nonuniform peaking at the center and causing plastic flow. The onset of core failue in beams is directly related to the core yield stress in the thickness direction. A critical condition for the core occurs at points where shear stress is combined with compressive stress.

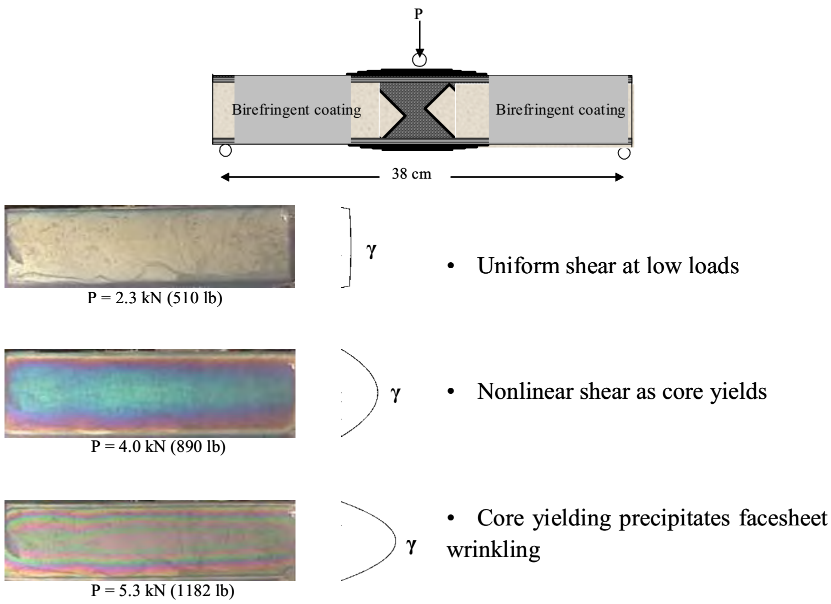

Figure 5: Isochromatic fringe patterns in birefringent coating of sandwich beam under three-point bending (Divinycell H250 core)

The deformation and failure of the core is obviously dependent on its properties and especially its anisotropy. Honeycomb and balsa wood cores are highly anisotropic with much higher stiffness and strength in the thickness direction, a desirable property. Figure 6 shows isochromatic fringe patterns in the photoelastic coating and the corresponding load deflection curve for a composite sandwich beam under three-point bending. The beam consists of glass/vinylester facesheets and balsa wood core. The fringe patterns indicate that the shear deformation in the core is initially nearly uniform, but it becomes nonuniform and concentrated in a region between the support and the load at a distance of approximately one beam depth from the support. The pattern at the highest load shown is indicative of a vertical crack along the cells of the balsa wood core. The loads corresponding to the fringe patterns are marked on the load deflection curve. It is seen that the onset of nonlinear behavior corresponds to the beginning of fringe concentration and failure initiation in the critical region.

Figure 7 shows the damaged region of the beam. Although the fringe patterns did not show that, it appears that a crack was initiated near the upper facesheet/core interface and propagated parallel to it. The crack traveled for some distance and then turned downwards along the cell walls of the core until it approached the lower interface. It then traveled parallel to the interface towards the support point.

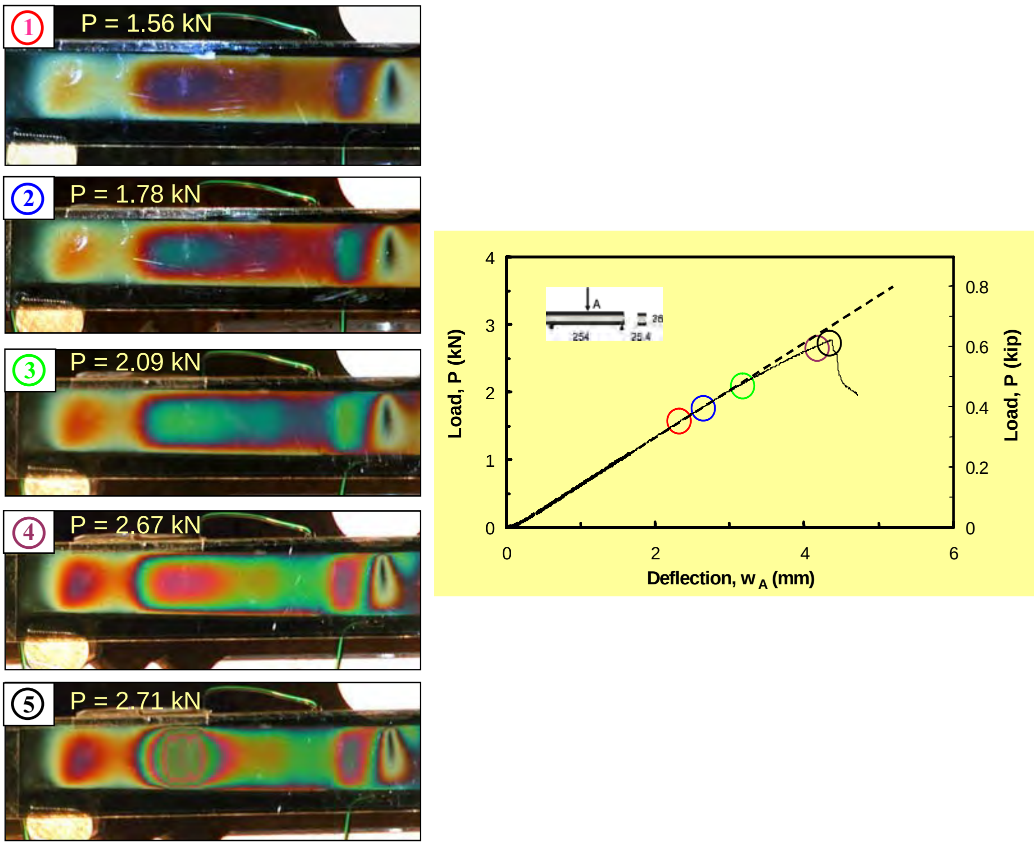

Figure 6: Isochromatic fringe patterns in photoelastic coating and load deflection curve of a composite sandwich beam under three-point bending (glass/vinylester facesheets; balsa wood core)

Figure 7. Cracking in balsa wood core of sandwich beam under three-point bending near support

4. INDENTATION FAILURE

Indentation failure in composite sandwich beams occurs under concentrated loads, especially in the case of soft cores. Under such conditions, significant local deformation takes place of the loaded facesheet into the core, causing high local stress concentrations. The indentation response of sandwich panels was first modeled by Meyer-Piening [8] who assumed linear elastic bending of the loaded facesheet resting on a Winkler foundation (core). Soden modeled the core as a rigid-perfectly plastic foundation, leading to a simple expression for the indentation failure load [9]. Thomsen and Frostig studied the local bending effects in sandwich beams experimentally and analytically [10, 11].

For linear elastic behavior, the core is modeled as a layer of linear tension/compression springs. The stress at the core/facesheet interface is proportional to the local deflection w

$$\sigma = kw \tag{4}$$

where the foundation modulus k is given by [12]

$$k = 0.64 \frac{E_c}{h_f} \sqrt[3]{E_c / E_f} \tag{5}$$

and where E_f and E_c are the facesheet and core moduli, respectively, and h_f is the facesheet thickness. Initiation of indentation failure occurs when the core under the load starts yielding. The load at core yielding was calculated as

$$P_{cy} = 1.70 \sigma_{cy}\ b h_f \sqrt[3]{E_f / E_c} \tag{6}$$

where $\sigma_{cy} =$ yield stress of the core, and b = beam widthCore yielding causes local bending of the facesheet which, combined with global bending of the beam, results in compression failure of the facesheet. The compressive failure stress in the facesheet is related to the critical beam loading P_{cr} as follows

$$\sigma_f = F_{fc} = \frac{9P_{cr}^2}{16b^2 h_f^2 F_{cc}} + \frac{p_{cr} L}{4bh_f(h_f + h_c)} \tag{7}$$

where h_c is the core thickness, L the span length, b the beam width, and F_{cc} , F_{fc} the compressive strengths of the core (in the thickness direction) and facesheet materials, respectively. In the above equation, the first term on the right hand side is due to local bending following core yielding and indentation and the second term is due to global bending. The onset and progression of indentation failure is illustrated by the moiré pattern for a sandwich beam under three-point bending (Fig. 8).

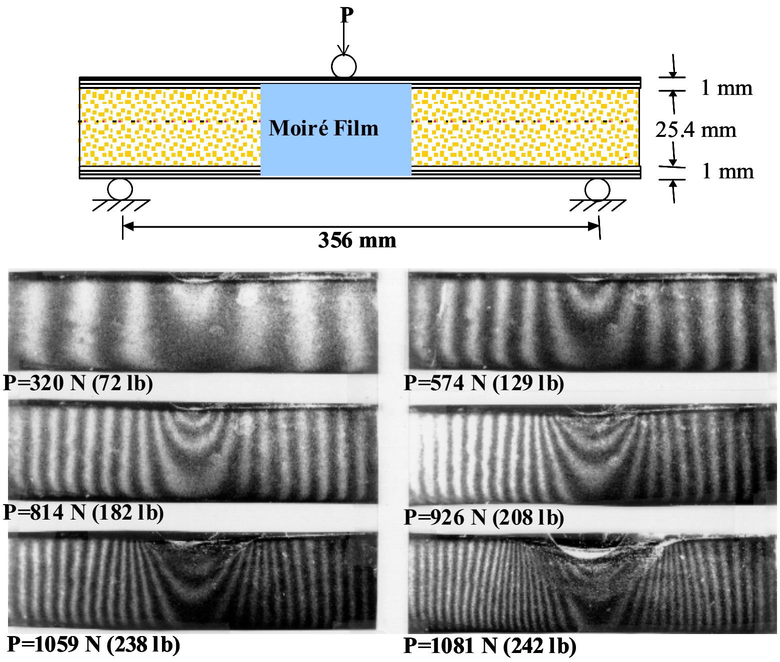

Figure 8: Moiré fringe patterns in sandwich beam with foam core corresponding to vertical displacements at various applied loads (11.8 lines/mm grating; carbon/epoxy facesheet; Divinycell H100 core)

Figure 9 shows load displacement curves for beams of the same dimensions but different cores.. The displacement in these curves represents the sum of the global beam deflection and the more dominant local indentation. Therefore, the proportional limit of the load-displacement curves is a good indication of initiation of indentation.

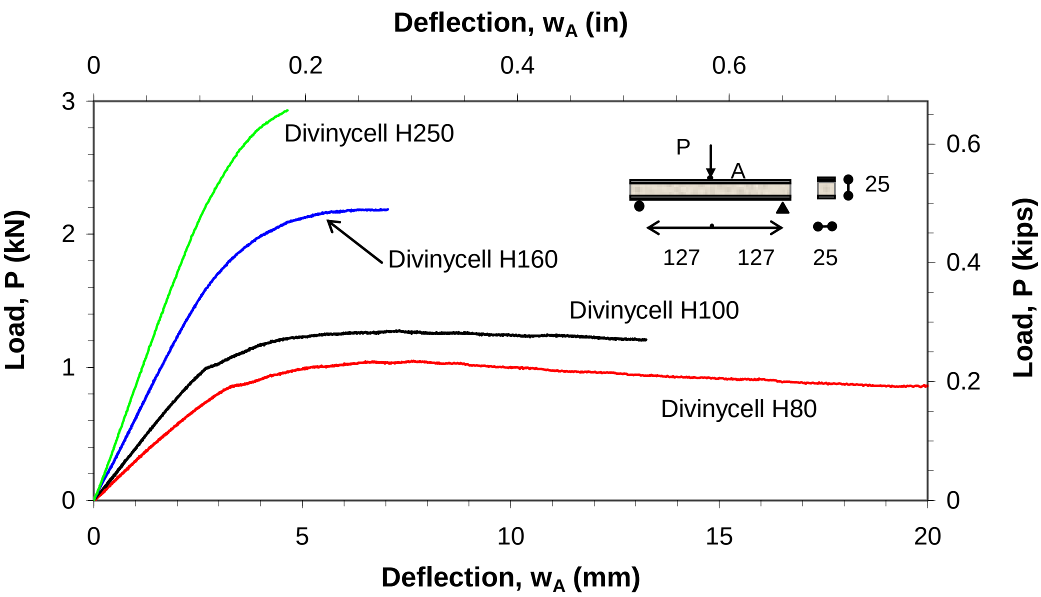

Figure 9: Load versus deflection under load of sandwich beam under three-point bending (carbon/epoxy facesheets, Divinycell H250 core)

The measured critical indentation loads in Fig. 9 were compared with predicted values using Eq. (7) which can be approximated as [9]

$$P_{cr} \cong \frac{4}{3} b h_f \sqrt{F_{fc} \sigma_{cy}} \tag{8}$$

Thus, the critical indentation load is proportional to the square root of the core material yield stress. The results obtained are compared as follows:

Indentation Load (N)	H80	H100	H160	H250
Measured	1,050	1,250	2,150	2,900
Calculated	1,370	1,500	2,000	2,380

The approximate theory with the assumption of rigid-perfectly plastic behavior overestimates the indentation failure load for soft cores, but it underestimates it for stiff cores.

5. FACESHEET WRINKLING FAILURE

The compressive facesheet of the sandwich beam can undergo local buckling (wrinkling) [4]. Wrinkling may be viewed as buckling of the compression facesheet supported on an elastic foundation. An early estimate of the critical wrinkling stress was given by Hoff and Mautner [13].

$$\sigma_{cr} \cong 0.5 \sqrt[3]{E_{f1} E_{c3} G_{c13}} \tag{9}$$

where

E_{f1}, E_{c3} = Young's moduli of facesheet and core, in the axial and through thickness directions,respectively

G_{c13} = Shear modulus of core on the 13 plane

In the relation above, the core moduli are the initial ones while the material is in the linear range. After the core yields and its stiffnesses degrade (E_c', G_c'), it does not provide adequate support for the facesheet, thereby precipitating facesheet wrinkling. The reduced critical stress after core degradation is

$$\sigma_{cr} \cong 0.5 \sqrt[3]{E_f E_c' G_c'} \tag{11}$$

Sandwich beams with foam cores were tested in three-point bending and as cantilever beams The moment-strain curves shown in Fig. 10 illustrate the onset of facesheet wrinkling. Critical stresses obtained from the figure for the maximum moment for specimens 1 and 2 are $\sigma_{cr} = 910$ *and* $715\, MPa$, respectively. The predicted value , by Eq. (9) is σ_{cr} = 945 MPa. In the case of the short beam (specimen 3), core failure preceded wrinhkling. The formula (11) is more applicable at this time.

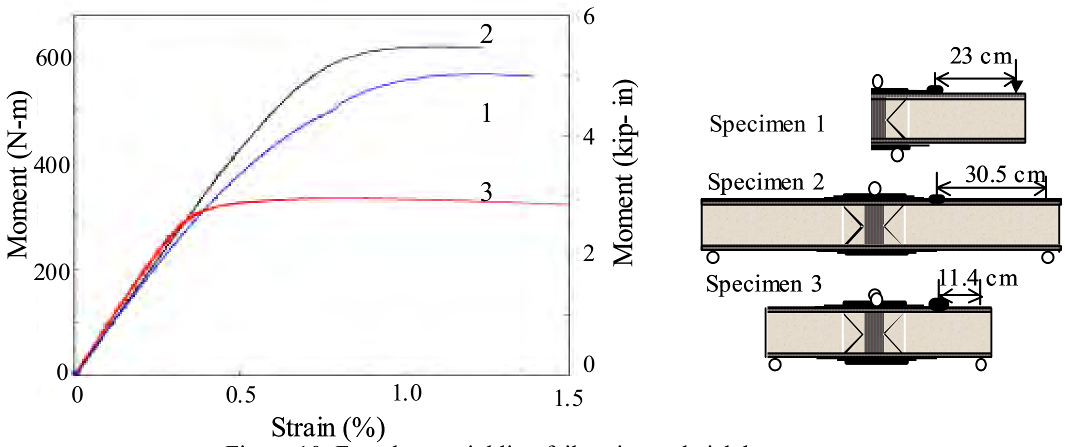

Figure 10: Facesheet wrinkling failure in sandwich beams

6. CONCLUSIONS

The initiation of failure in composite sandwich beams is heavily dependent on properties of the core material. Plastic yielding or cracking of the core occurs when the critical yield stress or strength (usually shear) of the core are reached. Indentation under localized loading depends principally on the square root of the core yield stress. Available theory predicts indentation failure approximately, overestimating it for soft cores and underestimating it for stiffer ones. The critical stress for facesheet wrinkling is proportional to the cubic root of the product of the core Young's and shear moduli in the thickness direction. The ideal core should be highly anisotropic with high stiffness and strength in the thickness direction.

ACKNOWLEDGEMENT

The work discussed in this paper was sponsored by the Office of Naval Research (ONR). The author is grateful to Dr. Y. D. S. Rajapakse of ONR for his encouragement and cooperation.

REFERENCES

[1] I. M. Daniel, E. E. Gdoutos, K.-A. Wang and J. L. Abot, "Failure modes of composite sandwich beams," *Int. J. Damage Mechanics*, 11, 309-334 (2002).
[2] E. E. Gdoutos, I. M. Daniel and K.-A. Wang, "Indentation failure in composite sandwich structures," *Exper. Mech.*, 42, 426-431 (2002).
[3] J. L. Abot, I. M. Daniel and E. E. Gdoutos, "Contact law for composite sandwich beams," *J. of Sandwich Structures and Materials*, 4, 157-173 (2002).
[4] E. E. Gdoutos, I. M. Daniel, K.-A. Wang and J. L. Abot, "Compression facing wrinkling of composite sandwich structures," *Mech. of Materials*, 35, 511-522 (2003).
[5] Daniel, I. M. and Abot, J. L., 2000, "Fabrication, Testing and Analysis of Composite Sandwich Beams," *Comp. Science and Technology*, Vol. 60, pp. 2455-2463.
[6] Gdoutos, E. E., Daniel, I. M. and Wang, K.-A., "Failure of Cellular Foams under Multiaxial Loading," *Composites, Part A*, Vol. 33, No. 2, Feb. 2002, pp. 163-176.
[7] Tsai, S. W. and Wu, E. M., 1971, "A General Theory of Strength for Anisotropic Materials," *Journal of Composite Materials*, Vol. 5, pp. 58-80.
[8] H. R. Meyer-Piening, "Remarks on higher order sandwich stress and deflection analysis," *Proc. First Int. Conference on Sandwich Construction*, 107-127 (1989).
[9] P. D. Soden, "Indentation of composite sandwich beams," *J. Strain Analysis*, 31, 353-360 (1996).
[10] O. T. Thomsen and Y. Frostig, "Localized bending effects in sandwich panels: Photoelastic investigation versus high-order sandwich theory results," *Composite Structures,* 37, 97-108 (1997).
[11] O. T. Thomsen, "Analysis of local bending effects in sandwich panels subjected to concentrated loads," *Proc. Second Int. Conference on Sandwich Construction*, 417-440 (1992).
[12] M. Hetenyi, *Beams on Elastic Foundation*, The University of Michigan Press, (1946).
[13] N. J. Hoff and S. E. Mautner,"The buckling of sandwich type panels," *J. Aero. Sciences,* 12, 285-297, (1945).

8th International Conference on Sandwich Structures
ICSS 8
A. J. M. Ferreira (Editor)

INFLUENCE OF SKIN DAMAGE ON THE INDENTATION BEHAVIOR OF SANDWICH BEAMS

Francesca Campi and Roberta Massabò

Department of Civil, Environmental and Architectural Engineering (DICAT)
University of Genova
Via Montallegro 1, 16145, Genova, Italy
e-mail: Francesca.Campi@unige.it
roberta.massabo@unige.it

Key words: Composite sandwich beams, Indentation, Delamination.

Summary. *An analytical investigation of the problem of the indentation of composite sandwich beams with partially delaminated face sheets is presented in this paper. A model has been formulated that represents the damaged face as an elastic beam resting on an elastic-perfectly plastic foundation. The results show the influence of the damaged area on the behavior of the system: the indentation load is lower than that of an intact beam and the reduction is more important on increasing the number of delaminations or their lengths; the critical load for progressive yielding of the core is also affected by the presence of a damaged area whose influence decreases on increasing the size of the plastic zone.*

1 INTRODUCTION

Different damage and failure mechanisms control the post-elastic behavior and final collapse of composite and sandwich structures subject to quasi-static and dynamic loading conditions; among them are the multiple delamination of laminated skins, fiber and matrix cracking, core crushing, fracture at the face/core interface and face wrinkling. The interaction of these mechanisms has important effects on the mechanical response of the systems and on key properties, such as energy absorption, damage and impact tolerance, loading capacity and stiffness. This has been shown in [1-3] where the interaction of multiple delaminations in composite laminates subject to static and dynamic loading conditions has been studied and important conclusions, which are relevant to the optimal design of materials/structures, have been drawn. In homogeneous systems, for instance, energy absorption through multiple delamination fracture is optimized if the material is designed so that multiple delaminations will form at equal through-thickness spacing.

Our current research deals with composite sandwich systems subject to static and dynamic loading conditions and aims at formulating physically based models that account for the interaction between different damage and collapse mechanisms. The study presented here focuses on the problem of indentation, which is a likely mode of failure of sandwich beams with thin faces and low strength cores when they are subjected to concentrated loads, derived for instance from collisions or dropping of objects.

Failure by indentation has been extensively studied and analytical models have been proposed by several authors: Soden [4] adopted the schematization of an elastic beam upon a rigid-perfectly plastic foundation and derived a simple expression for the load at which the upper face fails. Shuaeib and Soden [5], following the analysis proposed by Zingone [6], modeled the core as an elastic-ideally plastic foundation and obtained theoretical predictions of the loads at which yielding of the core first occurs, the indentation load, and the upper face fails. Steeves and Fleck [7] investigated the indentation failure of sandwich beams in three-point bending, accounting for the overall bending of the beam and solving a stability problem. They proposed two models: the first considers a rigid-ideally plastic foundation and leads to an analytical expression of the failure load for local indentation; the second assumes the core as an elastic-ideally plastic foundation and allows to study the influence of the compliance of the core on the indentation response. Zenkert, Shipsha and Persson [8] adopted an elastic-perfectly plastic model in order to study indentation and predict the load-displacement response of sandwich beams; their study focuses on the unloading response. Gdoutos, Daniel and Wang [9] used the model of a beam on an elastic-perfectly plastic foundation in order to explain experimental results.

This work deals with the indentation of a sandwich beam with a homogeneous, isotropic and elastic-perfectly plastic core, e.g. a polymeric foam, and homogeneous, isotropic/orthotropic and elastic-brittle faces, e.g. a unidirectional composite laminate. The upper face is assumed to be partially damaged with multiple delaminations. The face is modeled as an elastic beam resting on an elastic-perfectly plastic foundation and analytical expressions are obtained for the indentation load and for the load for progressive yielding of the core; the influence of the number and the extension of the delaminations on the response of the system is studied.

2 THEORETICAL MODEL FOR THE INDENTATION OF A SANDWICH BEAM WITH A PARTIALLY DELAMINATED UPPER FACE

The indentation response of a sandwich beam with a partially delaminated upper face subject to a transverse force P is considered (Fig. 1). A system of Cartesian coordinates x-y-z is introduced with origin in the mid-point of the upper face, where the load is applied, with z the longitudinal axis of the beam. The problem has been solved analytically under the following assumptions:

- the sandwich beam is continuously supported by a rigid plane, so that overall bending can be neglected;
- the upper face of the sandwich, of thickness t and width b, is modeled as an infinitely long, linear elastic Euler Bernoulli beam, with Young's modulus E_f, resting on an elastic (in tension) and elastic-perfectly plastic (in compression) Winkler foundation, with elastic modulus K and yield strength $q_{cr} = \sigma_{cr}\, b$, with σ_{cr} the crushing strength of the core (Fig. 1c);
- the n delaminations in the upper face are equally spaced; they have equal lengths, $2a$, and are symmetrically located about the applied force; they are accounted for in the

formulation by reducing the moment of inertia of the intact face sheet, $I_f = 1/12\ b\ t^3$, to that of a sheet composed of n+1 sub-beams that may slide on each other, $I_{fdel} = I_f/(n+1)^2$ [1];

- during both the elastic phase and the progressive yielding of the core the delaminations in the upper face do not reach critical conditions for propagation and remain stationary.

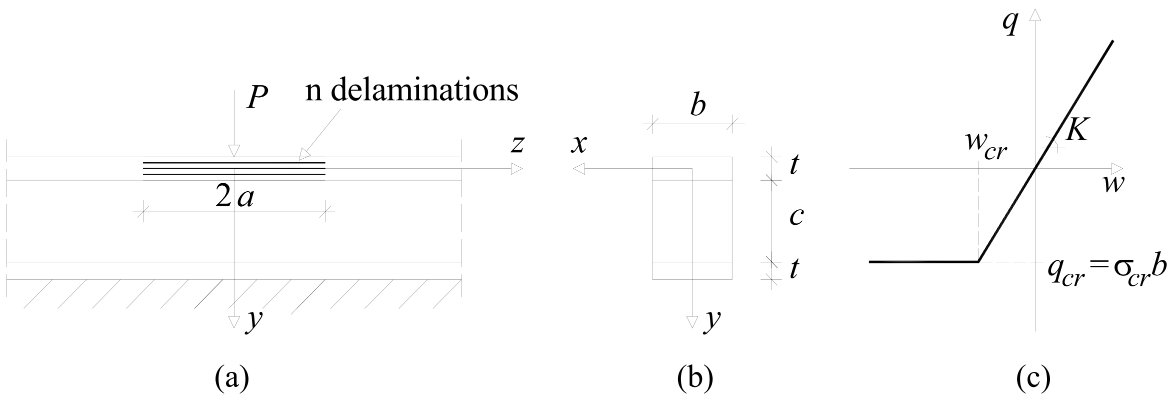

Figure 1: (a) Sandwich system with a partially delaminated upper face subject to a transverse force. (b) Cross section of the sandwich beam. (c) Constitutive law of the nonlinear Winkler foundation used to simulate the core.

2.1 Indentation load

Due to the symmetry of the problem only half of the system in Fig. 1 is studied. For small values of the applied load, the Winkler foundation is fully elastic (Fig. 2a) and the governing equations of the beam, in terms of the transverse displacement w, are:

$$\tilde{w}^{IV} + 4\tilde{\lambda}^4 (n+1)^2\ \tilde{w} = 0 \tag{1}$$

for $\tilde{z} \le \tilde{a}$, and

$$\tilde{w}^{IV} + 4\tilde{\lambda}^4 \tilde{w} = 0 \tag{2}$$

for $\tilde{z} \ge \tilde{a}$. The equations (1) and (2) are in dimensionless form with $\tilde{z} = z/t$, $\tilde{a} = a/t$, $\tilde{w} = w/t$ and $\tilde{\lambda} = t\sqrt[4]{K/4E_f I_f}$.

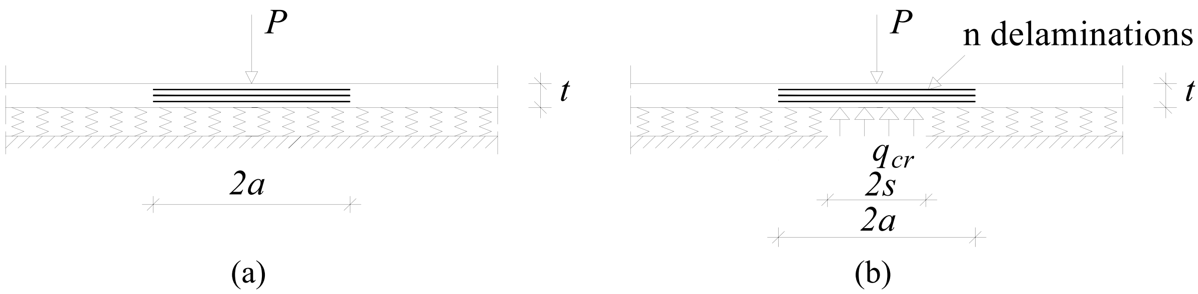

Figure 2: (a) Elastic beam on an elastic foundation. (b) Elastic beam on an elastic-perfectly plastic foundation.

The general solutions of the equations (1) and (2) are, respectively:

$$\tilde{w}(\tilde{z}) = e^{\tilde{\lambda}\sqrt{n+1}\tilde{z}}\left[c_1\cos\left(\tilde{\lambda}\sqrt{n+1}\tilde{z}\right)+c_2\sin\left(\tilde{\lambda}\sqrt{n+1}\tilde{z}\right)\right]+ e^{-\tilde{\lambda}\sqrt{n+1}\tilde{z}}\left[c_3\cos\left(\tilde{\lambda}\sqrt{n+1}\tilde{z}\right)+c_4\sin\left(\tilde{\lambda}\sqrt{n+1}\tilde{z}\right)\right] \quad \text{for } \tilde{z}\le\tilde{a} \tag{3}$$

and

$$\tilde{w}(\tilde{z}) = e^{\tilde{\lambda}\tilde{z}}\left[c_5\cos\left(\tilde{\lambda}\tilde{z}\right)+c_6\sin\left(\tilde{\lambda}\tilde{z}\right)\right]+e^{-\tilde{\lambda}\tilde{z}}\left[c_7\cos\left(\tilde{\lambda}\tilde{z}\right)+c_8\sin\left(\tilde{\lambda}\tilde{z}\right)\right] \quad \text{for } \tilde{z}\ge\tilde{a}. \tag{4}$$

The eight constants are determined by imposing that the solution remains bounded at infinity, the bending rotation at the origin is zero and the shear force $P/2$ and imposing continuity in displacements and stress resultants at $z = a$.

The indentation load of the partially delaminated beam, P_{crDel}, is defined as the load at which the foundation first undergoes plastic deformation (crushing) at the coordinate $z = 0$ when:

$$\tilde{w}(\tilde{z}=0) = \tilde{w}_{cr} = \frac{1}{\tilde{K}} \tag{5}$$

where $\tilde{K} = Kt/q_{cr}$.

In Fig. 3 the indentation load of the partially delaminated beam, P_{crDel}, is normalized with respect to the indentation load of an intact beam, $P_{cr}=2\sigma_{cr}b/\lambda$, where $\lambda = \sqrt[4]{K/4E_fI_f}$. The dimensionless load is depicted as a function of the dimensionless half length of the delaminations, $a\lambda$, for different numbers of delaminations, n. The indentation load is strongly affected by the presence of a damaged area. All curves in the figure show a similar trend: there is a first sudden and important drop of the indentation load for small values of $a\lambda$; on increasing $a\lambda$, the indentation load P_{crDel} shows a transition from the indentation load of an intact sheet P_{cr} (for $a\lambda \to 0$) to that of a fully delaminated sheet P_{crLim}; the curves tend to the horizontal asymptotes:

$$\frac{P_{crLim}}{P_{cr}} = \frac{1}{\sqrt{n+1}} \tag{6}$$

Both the number and the length of the delaminations strongly influence the indentation load. In a sandwich beam with a Divinycell H100 foam core and glass fiber-epoxy face sheets, with Young's modulus of the core $E_c = 120$ MPa, $\sigma_{cr} = 1.45$ MPa, $E_f = 30$ GPa, $c = 20$ mm and $t = 4$ mm, the presence of a single delamination of length $2a = 20$ mm, corresponding to $a\lambda = 0.5$, produces a 20% reduction of the indentation load of the intact beam; if the number of delaminations is $n = 10$ the reduction is 65%; if a single delamination is longer than 60 mm, corresponding to $a\lambda = 1.5$, the reduction is approximately 30% (in the calculations, the modulus K of the foundation has been assumed $K = E_c b/c$).

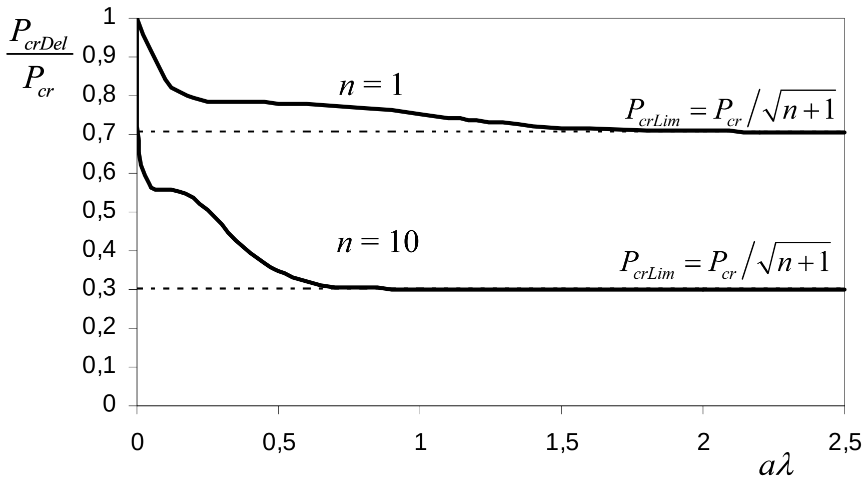

Figure 3: Dimensionless diagram of the indentation load of a partially delaminated beam normalized to the indentation load of an undamaged beam as a function of the dimensionless length of the delaminations $a\lambda$ for different values of n.

2.2 Load for progressive yielding of the core

When the transverse displacement at the coordinate $z = 0$ reaches the critical value w_{cr}, a plastic zone forms in the foundation (Fig. 2b). In the plastic zone, of length $2s$, the reactions of the foundation are constant, $q = q_{cr}$, and the governing equation becomes:

$$\tilde{w}^{IV} + \frac{12\left(n+1\right)^2}{\tilde{E}_f} = 0 \tag{7}$$

for $\tilde{z} \le \tilde{s}$, with general solution:

$$\tilde{w}\left(\tilde{z}\right) = -\frac{\tilde{z}^4\left(n+1\right)^2}{2\tilde{E}_f} + c_9\frac{\tilde{z}^3}{6} + c_{10}\frac{\tilde{z}^2}{2} + c_{11}\tilde{z} + c_{12} \tag{8}$$

where $\tilde{E}_f = E_f / \sigma_{cr}$.

The governing equation for $\tilde{s} \le \tilde{z} \le \tilde{a}$ is Eq. (1) and for $\tilde{z} \ge \tilde{a}$ is Eq. (2), with general solutions (3) and (4). Besides the boundary conditions required for the solution of the elastic portion of the beam, new conditions must be imposed on the continuity of generalized displacements and stress resultants at the boundary $z = s$ between the plastic and the elastic foundation.

The critical load for progressive yielding of the core $P_{yLim,}$ of a fully delaminated sheet ($a \to \infty$), normalized with respect to the indentation load P_{crLim}, is given as a function of the dimensionless half length of the plastic zone, $s\lambda\sqrt{n+1}$, by the following equation:

$$\frac{P_{yLim}}{P_{crLim}} = \frac{2s^3\lambda^3(n+1)^{3/2} + 6s\lambda\sqrt{n+1} + 6s^2\lambda^2(n+1) + 3}{3(1+s\lambda\sqrt{n+1})^2}. \tag{9}$$

The equation is presented in the diagram of Fig. 4. The response is strain hardening, namely the load for progressive yielding of the core is an increasing function of the size of the plastic zone. The limiting solution of Eq. (9) and Fig. 4 describes the response of the system in all cases where $a >> s$.

In addition, for $n = 0$ and $P_{crLim} = P_{cr}$, Eq. (9) and the curve in Fig. 4 describe the load for progressive yielding of an undamaged beam, P_y, that is given by:

$$\frac{P_y}{P_{cr}} = \frac{2s^3\lambda^3 + 6s\lambda + 6s^2\lambda^2 + 3}{3\left(1+s\lambda\right)^2}. \tag{10}$$

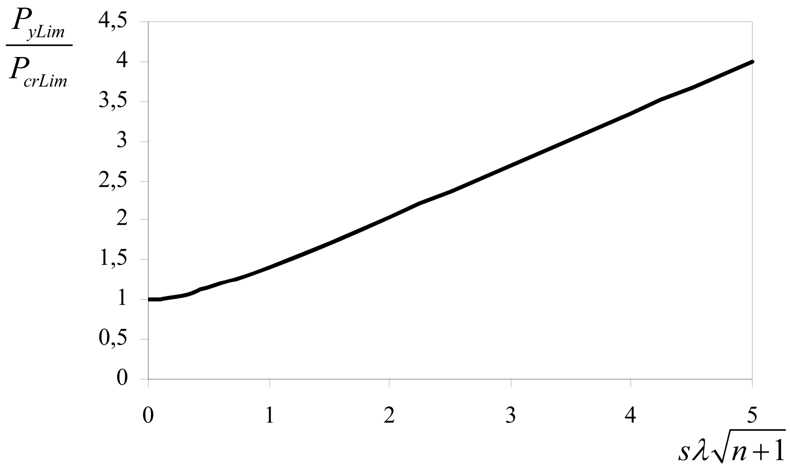

Figure 4: Dimensionless diagram of the indentation load for progressive yielding of the core normalized to the indentation load as a function of the dimensionless half length of the plastic zone, $s\lambda\sqrt{n+1}$, in the limit configuration of a fully delaminated beam (or $a >> s$).

The influence of the number of delaminations on the load for progressive yielding of the core of a fully delaminated beam is better highlighted in Fig. 5 where P_{yLim} is normalized to the indentation load for progressive yielding of an intact face sheet, P_y, and depicted as a function of the dimensionless product $s\lambda$ for different values of n. As already noted in Fig. 3, the indentation load (for $s\lambda = 0$) is strongly affected by the presence of multiple delaminations in the face sheet. The effect of the delaminations on the indentation response decreases on increasing the length of the plastic zone and for $s\lambda \rightarrow \infty$ the curves approach the solution of an intact beam ($n = 0$).

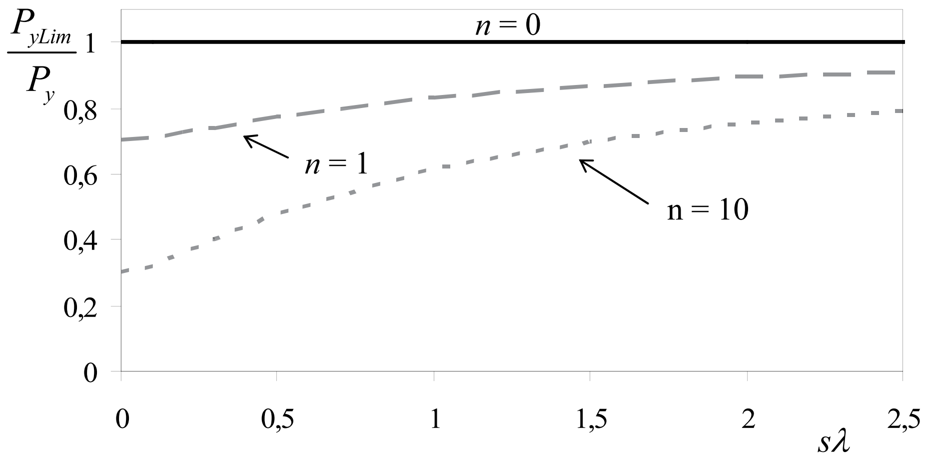

Figure 5: Dimensionless diagram of the load for progressive yielding of the core normalized to the indentation load for progressive yielding of an intact beam, as a function of the nondimensional half length of the plastic zone, $s\lambda$, for different values of n, in the limit configuration of a fully delaminated beam.

The influence on the load for progressive yielding of the core, $P_{yDel,}$ of a delaminated region of finite size, with $a\lambda = 0.8$, is studied in Fig. 6; P_{yDel} is normalized with respect to the indentation load of an undamaged beam, P_{cr}, and presented as a function of the dimensionless half length of the plastic zone, $s\lambda$, for n = 1 (Fig. 6a) and n = 10 (Fig. 6b). In the exemplary beam described above, $a\lambda = 0.8$ would correspond to a length of the damage portion 2a = 30 mm. The responses of an undamaged beam, Eq. 10, thin solid line, and a fully delaminated beam, Eq. 9, dashed line, are also presented in the diagrams. As expected, the curve of the undamaged beam defines the upper threshold of the solution. The curve of the fully delaminated beam defines the lower threshold for $s < a$: the load for progressive yielding of beams with finite size damage always falls within the two limits independently of the length of the damage and the number of delaminations. On the other hand, for $s > a$, the presence of a damaged area of finite size can lead to loads for progressive yielding of the core that are below those of a fully delaminated beam. This effect is more important if the number of delaminations is high (Fig. 6b) and tends to disappear only for large values of $s\lambda$ (not shown), when the solution for the damaged beam approaches that of an intact beam.

4 CONCLUSIONS

An analytical model has been formulated to study the problem of the indentation of a sandwich beam with a partially delaminated upper face. The model represents the delaminated face sheet as an Euler Bernoulli beam resting on a Winkler elastic-perfectly plastic foundation and assumes the delaminations to be stationary. The work is preliminary to the more complex problem of the interaction between different damage and collapse mechanisms in sandwich systems subject to static and dynamic loading conditions.

The results of the model show that the number and lengths of the delaminations strongly control all phases of the indentation response. In the exemplary sandwich beam considered in the main text (Divinycell H100 foam core, glass fiber-epoxy face sheets, with E_c = 120 MPa, σ_{cr} = 1.45 MPa, E_f = 30 GPa, c = 20 mm and t = 4 mm), for instance, the presence of a single delamination of length 20 mm induces a 20% reduction of the indentation load and if the length of the delamination is longer than 60 mm the reduction grows up to 30%. If there is more than one delaminations the effect becomes even more important.

The indentation response of the beam is strain hardening; this suggests the possibility that modes of failures other than the yielding of the foundation can occur, e.g. the propagation of the delaminations in the face sheets or interfacial fracture at the face/core interface. The interaction of these damage mechanisms will be considered in future work.

The indentation response of an undamaged beam (Eq. 10) defines an upper threshold to the solutions of damaged beams with defects of different sizes. The indentation response of a fully delaminated beam (Fig. 9) defines a lower threshold only when the size of the plastic zone is shorter than the damage size, for $s < a$. For $s > a$ the load for progressive yielding of the core of a beam with a finite size damage can be lower than that of a fully delaminated beam. This effect is controlled by the number of delaminations and lasts also for $s >> a$.

A consideration on one of the assumptions of the model needs to be done. The sandwich beams have been considered to be continuously supported by a rigid plane, so that global bending could be ignored. Models exist in literature that account for the effects of compressive forces in the upper face sheet. Steeves and Fleck [7] considered a sandwich beam in three-point bending, accounted for the effects of global bending and determined the indentation response solving a stability problem. Their analysis shows that, in the presence of compressive axial forces in the face sheet, the strain hardening curve that describes the indentation load as a function of the length of the plastic zone is followed by a strain softening branch. Consequently a maximum value of the applied load is defined for the indentation collapse. The extension of the model formulated here to account for geometric instabilities is in progress.

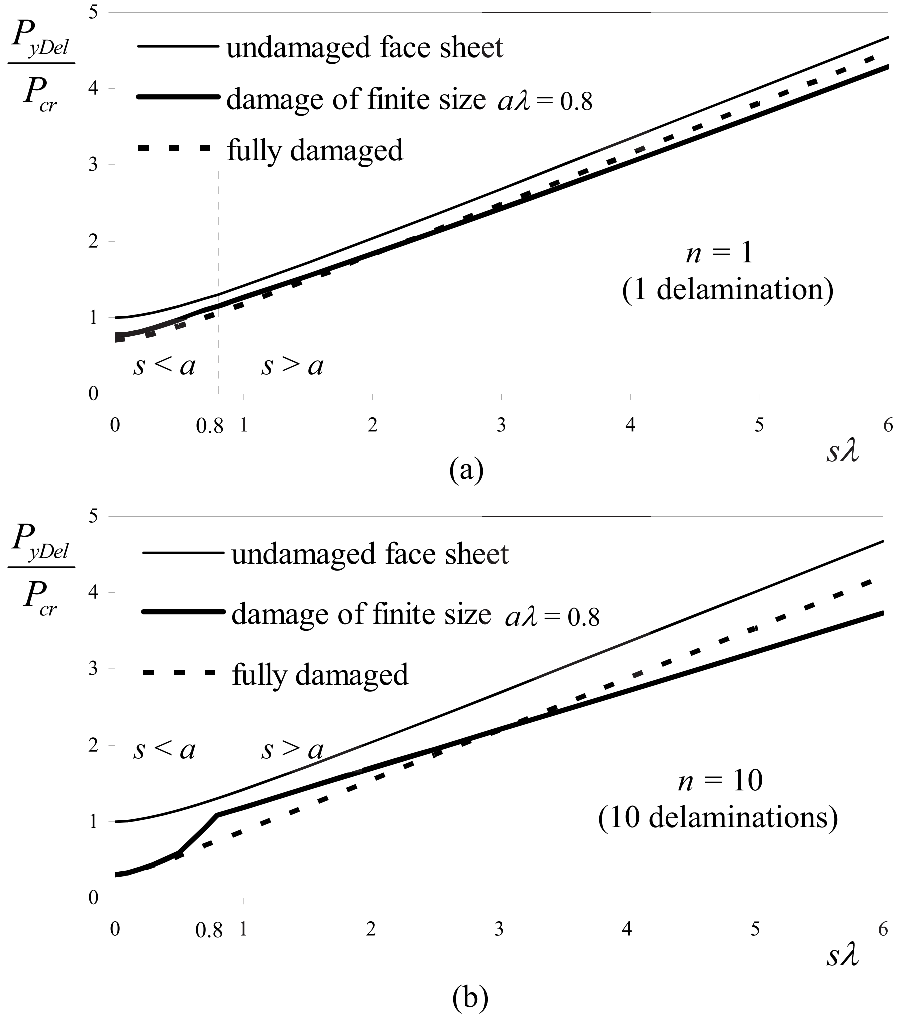

Figure 6: Dimensionless diagrams of the indentation load for progressive yielding of the core for a partially delaminated beam as a function of the dimensionless half length of the plastic zone $s\lambda$, for $s\lambda = 0.8$; (a) $n = 1$; (b) $n = 10$.

ACKNOWLEDGEMENTS

The work has been supported by the U.S. Office of Naval Research through contract no. N00014-05-1-0098, administered by Dr. Yapa D.S. Rajapakse.

REFERENCES

[1] M.G. Andrews, R. Massabò and B.N. Cox, Elastic interaction of multiple delaminations in plates subject to cylindrical bending, *Int. J. Solids Struct.*, 43(5), 855-886 (2006).
[2] M.G. Andrews, R. Massabò, B.N. Cox and A. Cavicchi, The dynamic interaction of multiple delaminations in plates subject to cylindrical bending, submitted.
[3] R. Massabò and A. Cavicchi, Influence of crack wake mechanisms on the dynamic fracture of multiply delaminated plates, Proceedings of the 16th Int. Conference on Composite Materials, ICCM16, Kyoto, July 2007, CDrom pp.1-7, Japan Society of Composite Materials.
[4] P. Soden, Indentation of composite sandwich beams, *J. Strain Analysis*, 31(5), 353-360 (1996).
[5] F. Shuaeib and P. Soden, Indentation failure of composite sandwich beams, *Compos. Sci. Technol.*, 57, 1249-1259 (1997).
[6] G. Zingone, Limit analysis of a beam in bending immersed in an elasto-plastic medium, *Meccanica*, 3, 48-56 (1968).
[7] C.A. Steeves and N.A. Fleck, Collapse mechanisms of sandwich beams with composite faces and a foam core, loaded in three-point bending. Part. I: analytical models and minimum weight design, *Int. J. Mech. Sci.*, 46, 561-583 (2004).
[8] D. Zenkert, A. Shipsha and K. Persson, Static indentation and unloading response of sandwich beams, *Composites: Part. B*, 35, 511-522 (2004).
[9] E.E. Gdoutos, I.M. Daniel and K.A. Wang, Indentation failure in composite sandwich structures, *Exper. Mech.*, 42(4), 426-431 (2002).

8th International Conference on Sandwich Structures
ICSS 8
A. J. M. Ferreira (Editor)

For ONR sessions organized by Yapa Rajapakse

FRACTURE MECHANICS MODELLING AND EXPERIMENTAL MEASUREMENTS OF CRACK KINKING AT SANDWICH CORE-CORE INTERFACES

Johnny Jakobsen, Jens H. Andreasen, Ole T. Thomsen, and Elena Bozhevolnaya

Department of Mechanical Engineering, Aalborg University
Pontoppidanstraede 101, 9220 Aalborg East, Denmark
Email: jja@ime.aau.dk. web page: http://www.me.aau.dk

Key words: Sandwich structures, Numerical Analysis, Fracture Modelling, Experimental investigation.

Summary. *The paper deals with deflected delaminations at core-core interfaces in sandwich structures. The background for this is a new concept for the control of delaminations in sandwich structures. This delamination control mechanism has previously been referred to as a peel stopper. Special attention is drawn to the correlation between the obtainable propagation length along a core-core interface prior to crack kinking and the core junction angle. In order to obtain a robust functional peel stopper the risk of initiating new interface cracks at the peel stopper-face interface after the parent delamination has been the deflected should be minimized. This has been considered in this paper through numerical analyses, and it is further demonstrated that experimentally measured crack propagation lengths and results from previous studies agree very well.*

1 INTRODUCTION

A numerical and experimental investigation of the kink tendency of core-core interface cracks in sandwich structures is the focus of this paper. This particular problem is especially interesting in relation to sandwich structures and a newly invented concept, which is called a “Peel stopper”.

Even though the sandwich concept offers superior advantages with respect to stiffness and strength per unit weight of structure, some drawbacks do exist. Thus, sandwich structures are vulnerable to face sheet peeling, which is a damage mode where the face sheets delaminate from the core, which may occur very rapidly and without prior warning. This type of damage mode can be detrimental for the structural integrity of e.g. an air plane or a ship structure. Due to this, the issue of prevention and delay of crack/delamination initiation and propagation has been topics of significant interest for the past decades. Overall this is covered by the concept of damage tolerance. A few concepts for enhancement of the resistance against face peeling have been proposed. One such concept was suggested by J. Grenestedt [1, 2]. In this concept certain areas/zones of the face sheets are allowed to peel off, thus preventing the debonding/delamination to propagate beyond these allowable face sheet areas/zones. Face stitching is another concept which has been investigated by several researchers [3,4]. The principal idea is to stitch the two outer face sheets together. This method increases the interlaminar/interface strength (and interlaminar fracture toughness) of sandwich structures by several orders of magnitude. However, both concepts involve rather complex and costly manufacturing methods.

Another method of enhancing the debonding/delamination resistance of sandwich structures, which may overcome the problems of the two other conceptual methods mentioned above, is proposed by a new peel stopper concept [5,6,7]. The idea is to embed a specially shaped component made of an appropriately chosen material into the core of a sandwich panel. A sandwich core with inserts, edge stiffeners or other embedded appliances is usually assembled/prepared before the face sheets are attached, and the proposed peel stopper concept can easily be included when the sandwich core is prepared. The governing principle behind this invention is to control the debonding/delamination progression and face peeling by forcing the delamination crack to propagate away from the face-core interface into a confined area within the sandwich core, which restricts further crack propagation. It has been demonstrated experimentally that the peel stopper concept effectively reroutes and stops propagating face/core delaminations/debonds in sandwich structures [6, 7]. However, a more thorough physical understanding of functionality of the peel stopper is still needed. This will be addressed in this paper.

A numerical model of a sandwich beam with a crack located at an inclined peel stopper/core interface was analyzed with respect to the crack kinking tendency [8]. The optimal peel stopper will not allow crack kinking out of the peel-stopper/core interface, and therefore it is important assess/estimate under which conditions interface propagation is favoured compared to crack kinking. Similar studies of interface cracking, kinking, and deflection has previously been studied by He, Suo, and Hutchinson [9-12].

The objective of the paper is to characterize the conditions under which new cracks between the peel stopper and face sheet interface may be initiated and further propagate. Furthermore it is the objective to examine, through experimental investigations, the correlation between core junction angle and the crack propagation length. The experimental results are then compared with the numerical results reported in [8].

2 POSSIBILITY OF INITIATING NEW INTERFACE CRACKS

It is of vital importance for the peel stopper concept that new cracks do not initiate from the peel stopper-face interface after the parent delamination has been deflected by the peel stopper wedge. Special attention is drawn to the transverse normal- and shear stresses at the interface in the vicinity of the tri-material corner (cf. Figure 1). The model is analyzed for a core junction angel of θ=20º.

The beam model is simple supported near the edges and loaded statically with a fixed downward displacement of 20mm in the centre. The core constituents consist of two different density foams. The stiffer core is located near the edges and in the centre, and the compliant core is located between the stiffer core parts. The face sheets are modelled as homogeneous isotropic layers. This represents a simplification of the actual material from the tests described in the next section, but it is assessed that this simplification will not qualitatively alter the conclusion drawn from the results presented in this section. The elastic properties used for the modelling are given in Table 1.

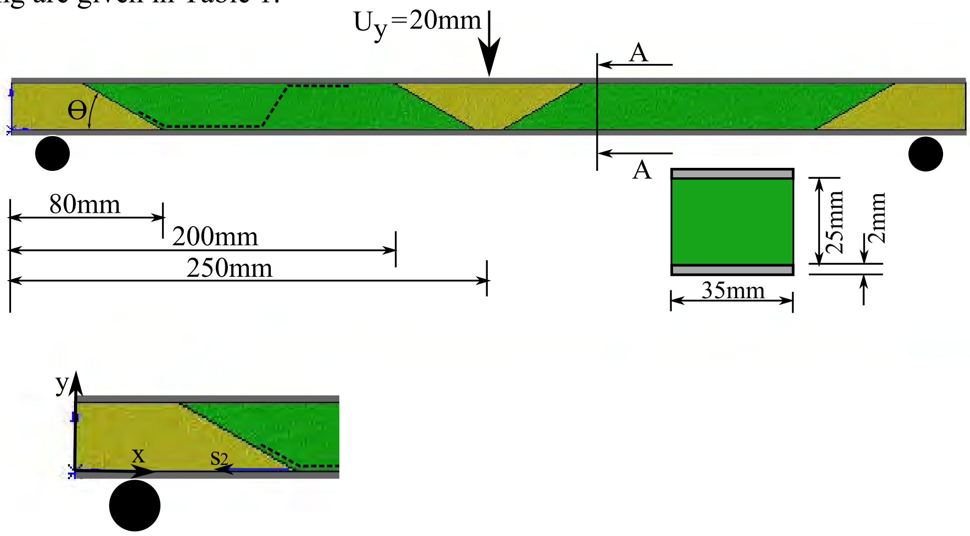

Figure 1: Sketch of the analysed model. The finite element software package ABAQUS® was used to perform the analyses. The transverse normal- and shear stresses were analysed along the bottom interface (s2) for two crack propagation length along the core-core interface (dashed line symbolise the crack).

	E-modulus [MPa]	Poisson's ratio
Face sheets	E= 25050	0.30
HP200 (stiff core)	E=250	0.32
H60 (compliant core)	E=42	0.32

Table 1. Elastic properties used in the FE-model.

The FE model is analyzed assuming linear elastic material properties, small nodal displacements and plain strain conditions. Furthermore, the model been meshed with quadratic elements (6- and 8-node elements), with highly refined meshing along the interface of interest (s2, see Figure 1 and Figure 2).

The distributions of the transverse normal- and shear stresses along the interface s2 are graphically presented in Figure 3. Two scenarios have been analyzed; one where the crack has propagated 5mm (pink curve) along the core-core interface, and another where the crack has propagated 15mm (black curve) along the same core-core interface.

It is seen that the stress levels for the crack which has propagated 15 mm are much lower than when the crack has propagated 5mm up along the core-core interface. Accordingly, the ”risk” of initiating new cracks (or further crack propagation) decreases as the crack tip is moved up along the core-core interface.

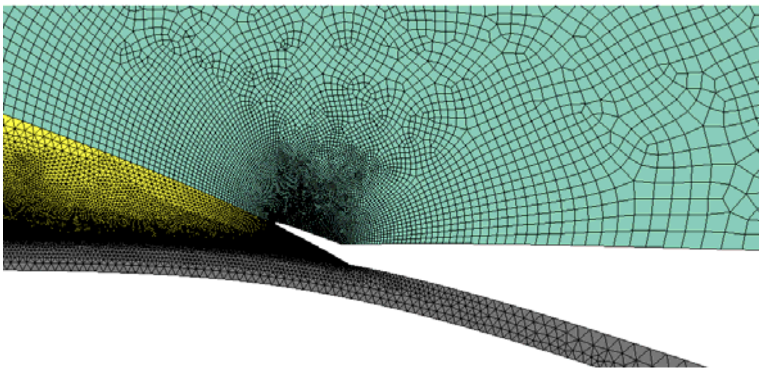

Figure 2: Zoom of finite element mesh in the vicinity of the crack tip along the bottom face-core interface.

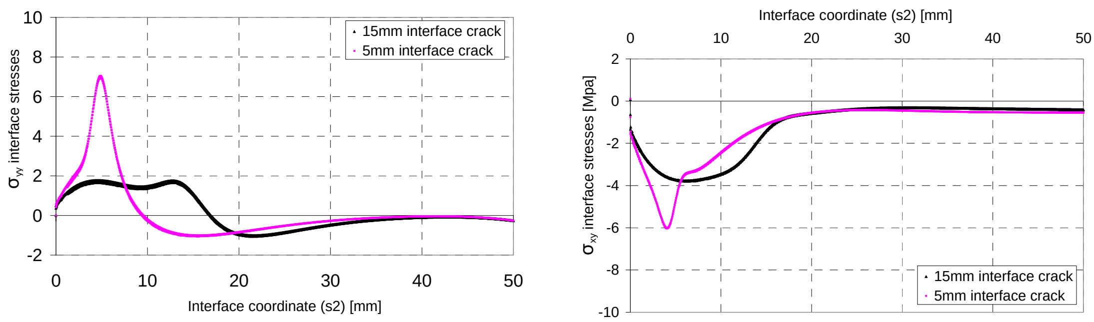

Figure 3: Left: Transverse normal interface stresses for two crack tip positions. Right: Interface shear stresses for the same two crack tip positions.

3 EXPERIMENTAL SETUP

An experimental three point bending quasi static test has been conducted on several sandwich beams with inclined core junctions. The purpose of this test series was to investigate the correlation between the propagation length (s1) along the core junction interface prior to kinking and the core junction angle θ (see Figure 3). The propagation length s1 is measured between points A and B.

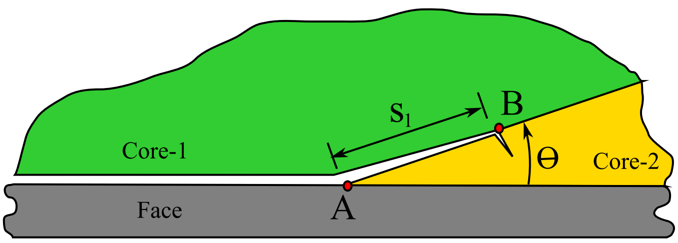

Figure 3: Correlation between the core junction angle (θ) and the propagation length (s1) along the core-core interface.

Twelve specimens were manufactured in four groups with three similar specimens in each group. The four groups differed from each other by varying the core junction angle. The angles studied were 10º, 20º, 30º and 40º. Illustrations of the specimen in each of the four groups are shown in Figure 4.

The specimens had stiffer cores located at the edges and at the mid span in order to redistribute the applied external loads. Between the stiffer core constituents a compliant core was placed. This sequence of varying core densities is commonly seen in practice. One of the compliant core constituents was pre-cracked in order to obtain a well defined starting point of failure (dashed line in Figure 4). This pre-crack was made with a razor blade, which gave a sharp crack tip and an excellent approximation to a "naturally" created crack tip. The sheets of the sandwich beams were made from eight layers of GFRP. Starting from the outer layer at the bottom face sheet the stacking sequence was $[+45,-45,0,90]_S$. The zero direction was chosen to be along the beam length direction.

The core constituents were glued to each other with and Araldite epoxy [13] and cured for 24 hours. The sandwich laminate assembly was finally manufactured using vacuum infusion (VARTM) with an epoxy resin [14]. After the vacuum infusion process the specimens were cured for 24 hours.

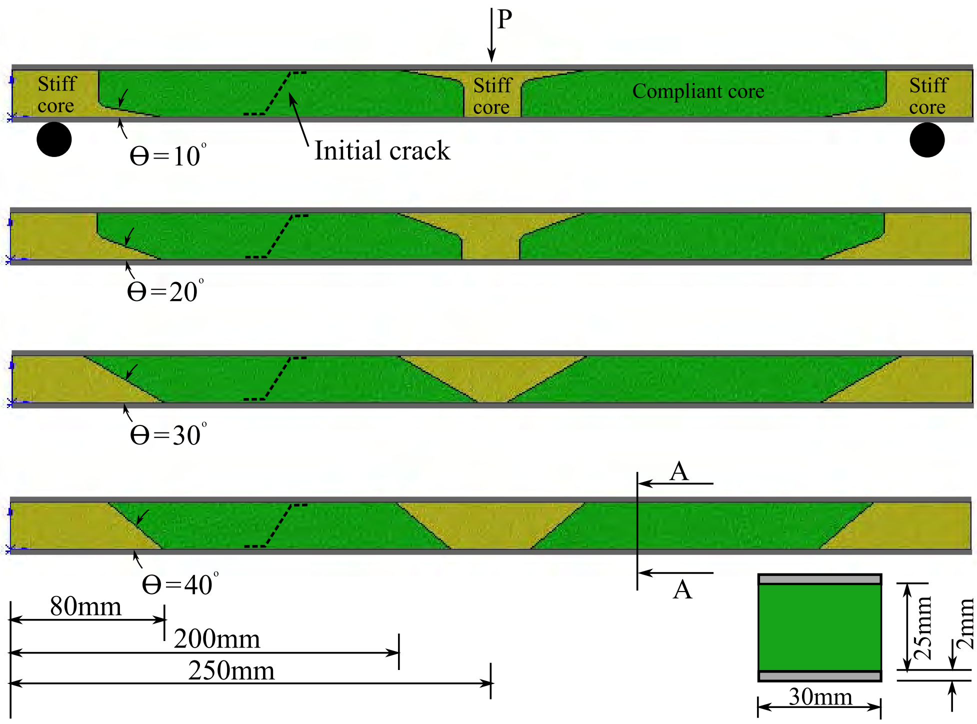

Figure 4: Four sandwich beam configurations tested quasi-statically in three point bending. The four configurations differ from each other by having different core junction angles.

The materials used for the stiff and compliant cores were Divinycell® HP200 and H60, respectively [15]. The estimated properties for the material constituents are given in Table 2.

	E-modulus [MPa]	Poisson's ratio
GFRP [0°]	E_1= 47000, E_2=8000	0.34
HP200 (stiff core)	E=250	0.32
H60 (compliant core)	E=42	0.32

Table 2. Estimated elastic properties for material constituents.

4 RESULTS FROM QUASI STATIC TESTS

The response curves obtained from the tests are shown in Figure 5. The initial part of all curves is approximately linear until the manufactured pre-crack starts to propagate. When this happens there is a sudden load drop. The load level where the pre-crack starts to propagate varies slightly, and an explanation to this could be small discrepancies of the actual size and sharpness of the pre-crack among the specimens. Since this is not the major concern of this investigation it has not been explored further.

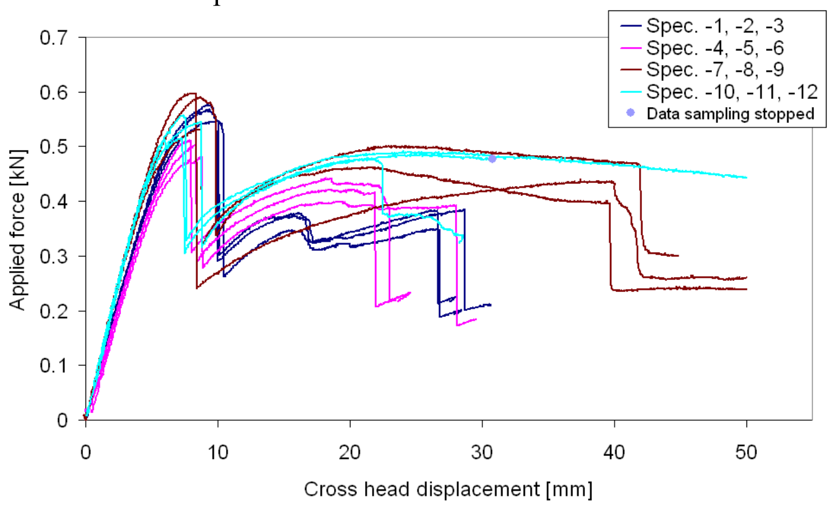

Figure 5: Load vs. displacement curves of the tested specimens. An unintentional stop of the data sampling occurred for specimen 12 – marked with a circular point.

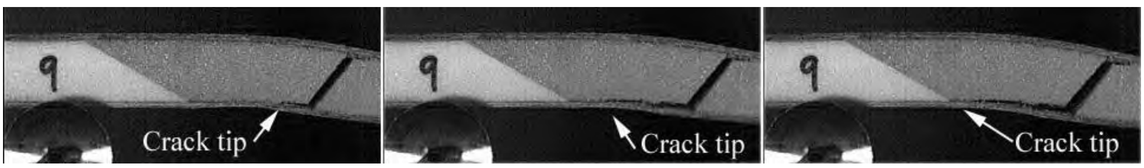

Figure 6: High speed image recordings (6000 fr/sec). In all cases the propagation initiates from the left pre-crack tip and propagates toward the tri-material corner.

The initial propagation of the pre-crack was observed to be very similar for all specimens (see Figure 6). The initial propagation started from the left tip of the pre crack and then propagated toward the tri-material corner, and during this event a major load drop was observed. However, when the crack tip reached the tri-material corner, it appeared that the propagation momentarily stopped. The load was then partly regained, and at a certain load level the crack then again propagated but at a much slower rate/speed.

Two types of propagation sequences were observed. The first and most often occurring sequence is sketched in Figure 7 (A), where the right tip of the pre-crack stays at rest during the whole event. This particular propagation sequence was observed for specimens 1 to 6 and further for specimens 10 and 12. It can be observed from the post mortem pictures in Figure 9. The final loss of load bearing capability occurred for propagation sequence-A when the interface crack (crack segment-2) in Figure 7 (A) kinked out and into the stiffer core, which created crack segments 3 and 4.

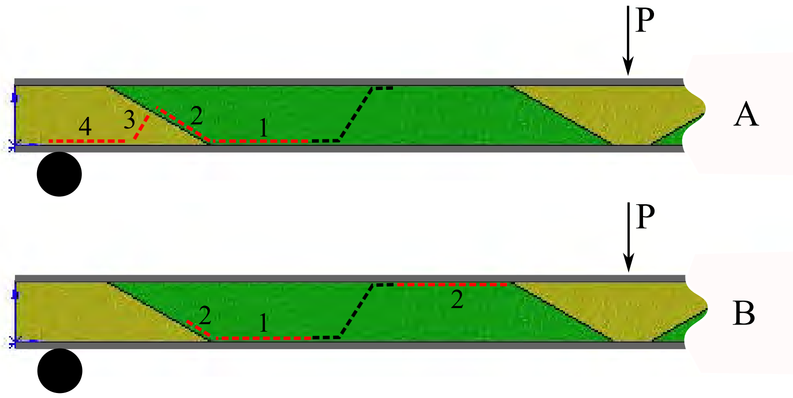

Figure 7 illustrates the two major propagations sequences observed during the experiment. The crack path is divided into segments according to their appearance.

The second propagation sequence occurred for specimens 7 to 9 and number 11 and it is sketched in Figure 7 (B). This propagation sequence differs from the first propagation sequence by not forming any crack kink out of the core interface (interface between the stiff and compliant core). Instead the propagation developed from the right tip of the pre-crack and propagated along the top face sheet toward mid span of the beam. This furthermore led to very large deflections (see Figure 5) for these particular specimens.

Microscopic images of those four specimens that followed propagation sequence-B revealed that they did only propagate a very small distance up along the core-core interface (s1) see Figure 8.

Figure 9 shows post mortem pictures demonstrating the crack formation patterns for all 12 sandwich specimens.

Representative images captured from high speed video recordings of specimens that followed propagation sequence-A is shown in Figure 10 to Figure 12. The images clearly demonstrate that the cracks kinks out of the interface.

The distance along the core-core interface measured from the tri-material corner to the point where the crack kinks out is given in Table 3 (see also Figure 3). Even though the width of the beam (30mm) was relatively small compared to the length of the beam, discrepancies between the measured propagation lengths on the front and back sides of the specimens were observed. Accordingly, the front- and back side measurements were averaged to obtain a single value for each specimen.

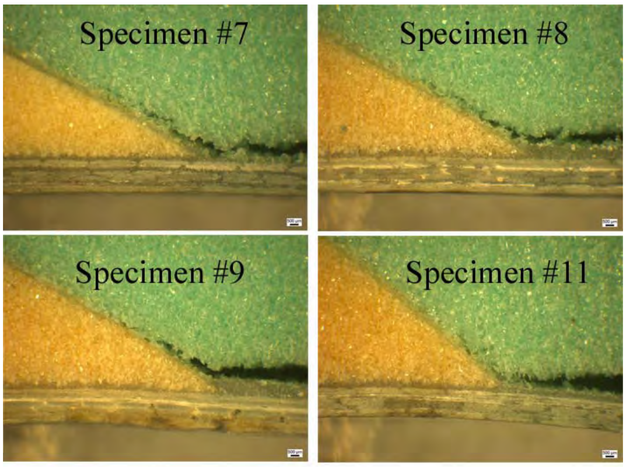

Figure 8. Microscopic images of the four specimens that did not kinked out of the core-core interface (i.e. that followed propagation sequence-B).

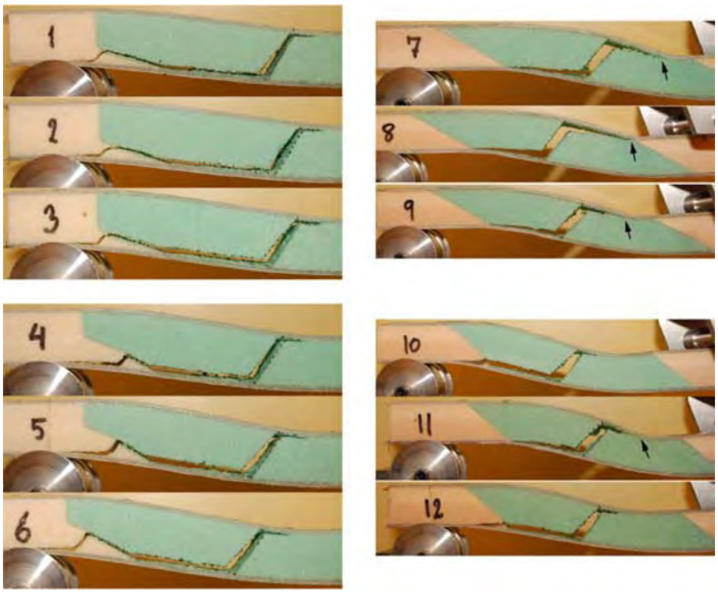

Figure 9: Post mortem pictures of the specimens, which illustrate the crack formation. The black arrow points out those specimens with delamination growth along the top face sheet and core (propagation sequence-B).

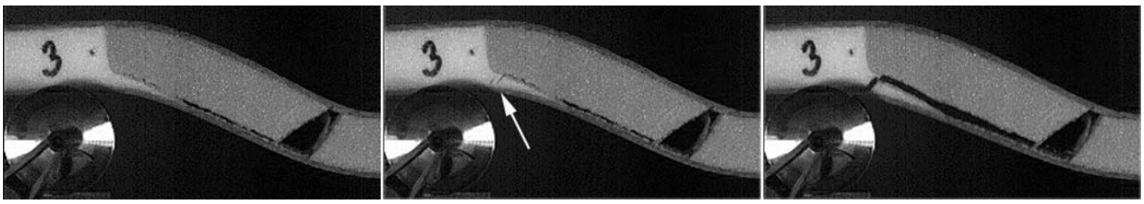

Figure 10: High speed images (6000fr/sec) of typical crack propagation in sandwich beam with a 10º core junction angle (propagation sequence-A).

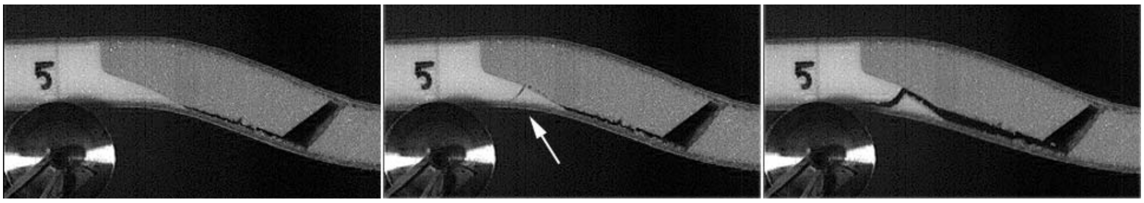

Figure 11: High speed images (6000fr/sec) of typical crack propagation in sandwich beam with a 20º core junction angle (propagation sequence-A).

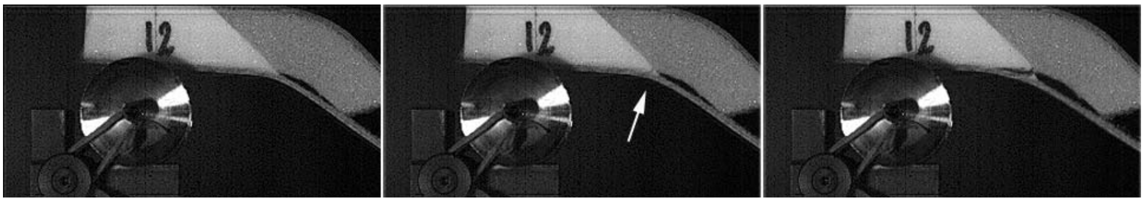

Figure 12: High speed images (6000fr/sec) of typical crack propagation in sandwich beam with a 40º core junction angle (propagation sequence-A).

It is further indicated from Table 3 that there is a correlation between the core junction angle and the propagation length (s1). This has been presented graphically in Figure 13 together with the simulated estimates for the propagation length (s1).

Specimen No.	Core junction angle [º]	Measured propagation length (s1)		
		Front side [mm]	Back side [mm]	Average [mm]
1	10	28.0	29.9	28.9
2	10	25.2	29.5	27.3
3	10	27.6	29.7	28.6
4	20	13.3	23.2	18.2
5	20	18.0	16.4	17.2
6	20	24.3	27.7	26.0
7*	30	6.8	9.0	7.9
8*	30	6.9	6.4	6.7
9*	30	6.0	7.5	6.8
10	40	2.8	0.0	1.4
11*	40	3.4	4.4	3.9
12	40	3.5	3.2	3.4

Table 3: Measured propagation length (s1) for each sandwich specimen. The propagation lengths on the front and back sides of the specimens were measured and averaged. The specimens marked with * followed propagation sequence-B.

Care should be exerted in drawing definite conclusions about the propagation lengths for the specimens that followed propagation sequence-B because the interface cracks did not kink out. However, the estimated propagation lengths are still given in Figure 13 and Table 3 and they should be considered as minimum values for each particular specimen.

The tendency seen from Figure 13 is that the core-core interface crack will tend to propagate easier along a core junction interface with a low inclination angle compared to a core junction interface with a higher inclination angle. This observation correlates very well with the FE simulation results presented in Figure 13 (see also [8]), but it should be noticed that the FE results presented herein are based on an interface toughness law which only has been measured for low mode mixities and extrapolated to higher mode mixities with a trigonometric function.

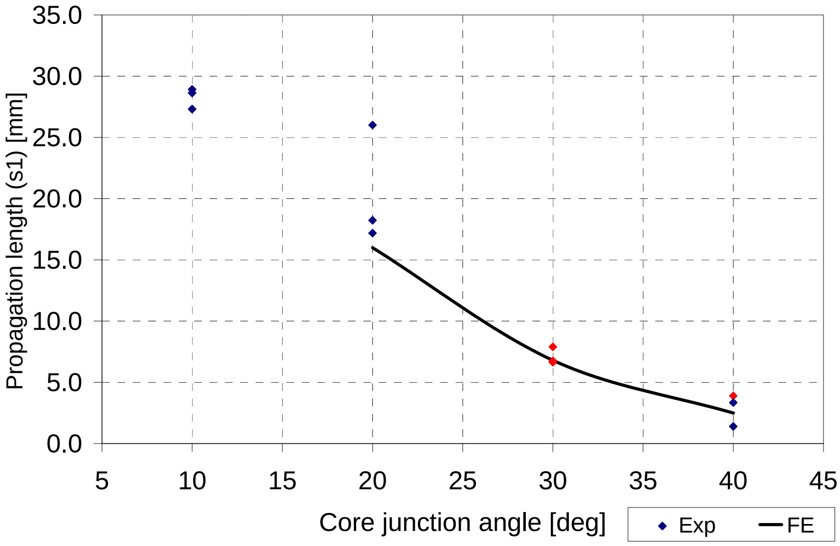

Figure 13: Experimental measurements of core junction angle vs. the propagation length compared with FE simulated values. The experimental measurements marked with red are values from the specimens that followed propagation sequence-B.

9 CONCLUSIONS & DISCUSSION

Quasi static three point bending tests of sandwich beams fabricated with inclined core junction have been performed. Twelve specimens were manufactured and divided into four groups, where the three specimens in each group had the same core junction angle different from the core junction angle of the other two specimen groups. The specimens were pre-cracked with a razor blade in order to achieve a well defined starting point of failure. The specimens were made from Divinycell foam core and GFRP face sheets. Two different crack propagation sequences were observed during the tests; one where the crack propagated up along the core-core interface from where it then kinked down into the stiffer core, and a second sequence where core-core interface crack did not kink out. For both propagation sequences the propagation length along the core-core interface, prior to crack kinking, was measured. Specimens that exhibited the second propagation sequence showed larger deflections than the specimens that followed the first propagation sequence. From the experimental observations and measurements it was observed that a correlation exists between the core junction angle and the crack propagation length measured along the core-core junction interface. Thus, it has been established that the crack can propagate a longer distance along the core-core interface without kinking away from the interface for small core junction angles, whereas steep core junction angles lead to very short crack propagation lengths along the core-core interface.

The experimentally obtained correlation between core junction angle and crack propagation length along the core-core interface has been compared with predictions of finite element analyses (FEA) [8]. The FEA analyses were based on a Linear Elastic Fracture Mechanics approach together with a relation between the stress intensity factors of an interface crack and a kinked crack proposed by He and Hutchinson. An excellent match between the experimental results and the FEA results was observed, but it should be noted, however, that the FEA results presented (see [8] for details) were based on an interface toughness law which was only measured for low mode mixities and then extrapolated to higher mode mixities with a trigonometric function.

ACKNOWLEDGEMENTS

The work presented was supported by:

- The Danish Research Council for Technology and Production Sciences, Grant/Award No. 26-04-0160 "Structural grading - a novel concept for the design of sandwich structures”.
- The Innovation Consortium “Integrated Design and Processing of Lightweight Composite and Sandwich Structures” (abbreviated “KOMPOSAND”) funded by the Danish Ministry of Science, Technology and Innovation and the industrial partners Composhield A/S, DIAB ApS (DIAB Group), Fiberline Composites A/S, LM Glasfiber A/S and Vestas Wind Systems A/S.
- US Navy, Office of Naval Research (ONR), Grant/Award No. N000140710227: “Influence of Local Effects in Sandwich Structures under General Loading Conditions & Ballistic Impact on Advanced Composite and Sandwich Structures”. The ONR program manager was Dr. Yapa Rajapakse.

The support received is gratefully acknowledged.

REFERENCES

1. Grenestedt J, (2001). “Development of a new peel-stopper for sandwich structures”. *Comp Sci Tech*, Vol. 61(11), pp. 1555-1559.
2. Wonderly C, Grenestedt J., (2004), “Dynamic performance of a peel stopper for composite sandwich ship structures”. *J Compos Mater*, Vol. 38(10): pp. 805-831.

3. Kim JH, Lee Y S, Park BJ, Kim DH. (1999), “Evaluation of durability and strength of stitched foam-cored sandwich structures”. *Composite Structures*, Vol. 47(1-4), pp. 543-550.
4. Lascoup B, Aboura Z, Khellil K, Benzeggagh M. (2006), “On the mechanical effect of stitch addition in sandwich panel”. *Comp Sci Tech*, Vol. 66(10), pp. 1385-1398.
5. Jakobsen J., Bozhevolnaya E., Thomsen OT, Jakobsen L. (2006), "Peel Stopper for Sandwich Components" Patent Application 2006-521/01-0184, Aalborg University, Denmark.
6. Jakobsen J, Bozhevolnaya E, Thomsen OT. (2007), “New peel stopper concept for sandwich structures”. *Compos. Sci. Technol.*, Vol. 67 (15-16), pp. 3378-3385.
7. Bozhevolnaya, E., Jakobsen, J. and Thomsen, O.T., “Fatigue Performance of Sandwich Panels with Peel Stoppers”, *Strain – An International Journal for Experimental Mechanics*. Accepted for publication.
8. Jakobsen J., Andreasen J.H., Bozhevolnaya E., (2007), “Crack Kinking of a Delamination at an Inclined Core Junction Interface in a Sandwich Beam”, Submitted for publication.
9. He M.Y. & A. Bartlett, J.H. (1991), “Kinking of a crack out of an interface - role of inplane stress”, *J. American Ceramic Soc.* Vol.74, pp. 767-771.
10. He, M. & Hutchinson, J.W. (1989), “Kinking of a crack out of an interface”, *J Appl Mech Trans ASME,* Vol. 56(2), pp. 270-278.
11. He, M. & Hutchinson, J.W. (1989), “Crack deflection at an interface between dissimilar elastic materials”, *Int J Solids Struct,* Vol. 25(9), pp. 1053-1067.
12. Suo, Z. & Hutchinson, J.W. (1990), “Interface crack between two elastic layers”, *Int J Fract,* Vol. 43(1), pp. 1-18.
13. Huntsman, Araldite® 2011 adhesive data sheet: http://ww1.huntsmanservice.com/tds/Huntsman%20Advanced%20Materials/English/Long/Aral-2011%20_GB_.pdf
14. PRO-SET Resin Infusion Systems data sheet: http://www.wessex-resins.com/proset/pro-set_pdf/PRO-SET_infusion_117_229_238.pdf
15. DIAB Group, Divinycell® H-grade and HP-grade: http://www.diabgroup.com/europe

8th International Conference on Sandwich Structures
ICSS 8
A. J. M. Ferreira (Editor)

Characterizing Sandwich Structures Under Hull Slamming Loading Conditions

Michael L. Silva and Guruswami Ravichandran

California Institute of Technology
Graduate Aeronautical Laboratories, MC 105-50
Pasadena, California 91125-5000, USA
Email: michaels@caltech.edu; ravi@caltech.edu

Key words: Sandwich structures, Experimental Mechanics, Marine craft, Hull slamming

Summary: *The use of sandwich construction is increasing in high speed marine craft due to the high strength to weight capability inherent in sandwich structures. These high speed craft can experience substantial loading at rates much higher than in other sea craft due to the slamming of the hull in rough seas. This hull slamming loading is characterized by periodic yet intense, transient loading. Understanding the fatigue and damage response of sandwich composites to this intense loading is crucial for the design of safe, long lasting marine craft. The objective of this investigation is to analyze and record the evolution of failure mechanisms in sandwich structures due to dynamic high cycle fatigue loading conditions. An experimental facility for simulating the hull slamming conditions has been established. Characteristic loads imparted by a pneumatic hammer along with pulse shaping techniques produce repeatable load pulses simulating hull slamming conditions on panels of sandwich structures of interest such as those with fiber reinforced composite face plates and polymeric foam cores.*

1 INTRODUCTION

The development of recent marine craft has seen the emergence of light-weight designs for high-speed seaborne structures, with novel concepts such as hybrid hulls and catamarans for high speed and long distance missions. These high-speed marine craft could experience a significant number of hull slamming events leading to dynamic high cycle fatigue. The fundamental knowledge gained in this effort will be useful in developing mitigation strategies for hull slamming. It is also anticipated that the proposed research will help in identifying the parameters of significance in developing design rules/maps for selection of candidate material/structural systems for application in the development of new generation of light weight, high-speed marine structures.

High impulsive loading on bows by hull impact remains an area of concern in high-speed ship design. Most studies that have been carried out on slamming have been performed by either by dropping panels or wedges into water [1]. The wedge water entry problem has been studied for many years [2] and of the theoretical pressure distributions have been calculated for such geometries [3].

Though such studies have provided insights concerning scaling laws for local slamming pressures, the mechanisms of load transfer to the structure from slamming and subsequent damage are not clearly understood. In most cases, the structure is considered to be rigid and only limited studies have explored the deformability of the structure due to wet deck slamming. Due to the unpredictability of hull slamming, designing bows to handle impact loading without sacrificing the functionality of the vessel remains difficult. Since hull slamming can lead to catastrophic damage such as complete collapse of the bow structure, we seek to understand the deformation and failure of sandwich structures due to this impulsive loading.

2 EXPERIMENTAL SETUP

The intent of this investigation is to characterize the damage due to repeated hull slamming events, as well as, the influence of foam core thickness and material properties on various failure modes. The response of structural materials used in high-speed marine craft including composites and sandwich structures to wave slamming loads will also be investigated. The experiments will be performed using a specially-designed impact facility that will impart periodic loading, simulating dynamic fatigue conditions. Pulse shaping techniques will be used to generate typical wave slamming profiles [3]. The experimental setup shown in Fig. 1 includes a pneumatic hammer operating under high pressure, which generates repeatable load pulses corresponding to hull slamming conditions as determined from the experiments [4].

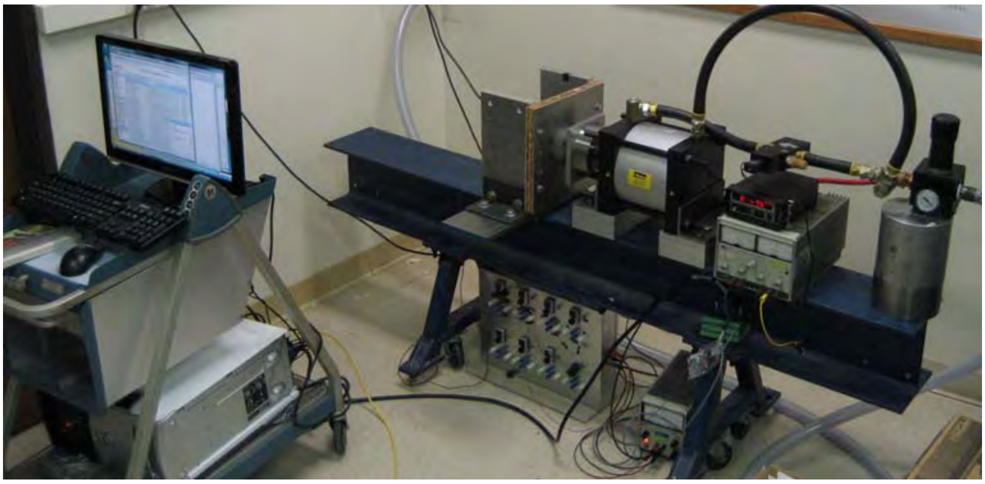

Fig. 1. Hull slamming simulator facility for imposing dynamic loading on sandwich structures.

The dynamic pulsatile loading will be imposed on specimens and panels of materials of interest while being subjected to various states of in-plane stress corresponding to slamming loads (Fig. 2). Due to the transient nature of loading and dissipation due to damage/plasticity, the temperature may increase considerably over ambient temperature and thus affect the material properties and damage evolution. The evolution of damage will be monitored *in-situ* using optical digital image correlation (*DIC*) [5] and thermal imaging (IR camera). We plan to use two high resolution CCD cameras (DIC-1,2) synchronized to record images of the deforming surface and using DIC, we will obtain the complete 3-D displacement field.

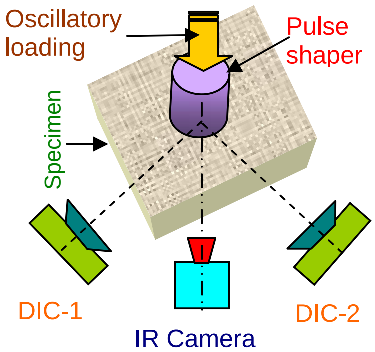

Fig. 2. Schematic of experimental setup for dynamic loading to simulate hull slamming.

Based on the experimental data (loads, deformations), 3-D criteria will be developed for the evolution of damage and failure of materials subjected to repeated loading (dynamic fatigue) conditions as a function of stress state, frequency and amplitude of loading. Of particular interest are the mechanisms of damage and threshold for damage initiation. Residual strength of the sandwich structures will be evaluated at periodic intervals over their life time and will be correlated with the damage accumulation. The experimental will be used to validate the models and simulations of failure due to hull slamming.

The loads representative of the hull slamming events are to be applied to the sandwich structures and their effects evaluated using the non-contact diagnostics and as well as embedded sensors in the structure. Our slamming simulator has been designed and fabricated to apply a desired loading profile a frequencies up to 3 Hz. Though the actual slamming events are of much lower frequency, the ability to rapidly apply cyclic loading provides an opportunity to study material and structural damage in high cycle loading conditions corresponding to hull slamming. A schematic of the setup is shown in Fig. 3. As the valve is opened, the pressurized air is released from one side of the cylinder resulting in a force that is imparted onto the sample. The force generated is measured by a force transducer inline with the piston. The loading corresponding to the slamming event is applied to the structure using an appropriately shaped impactor using the air driven cylinder, which is controlled via a computer program. The impacted structure is monitored using both non-contact optical techniques and strain gages mounted on the sandwich structure.

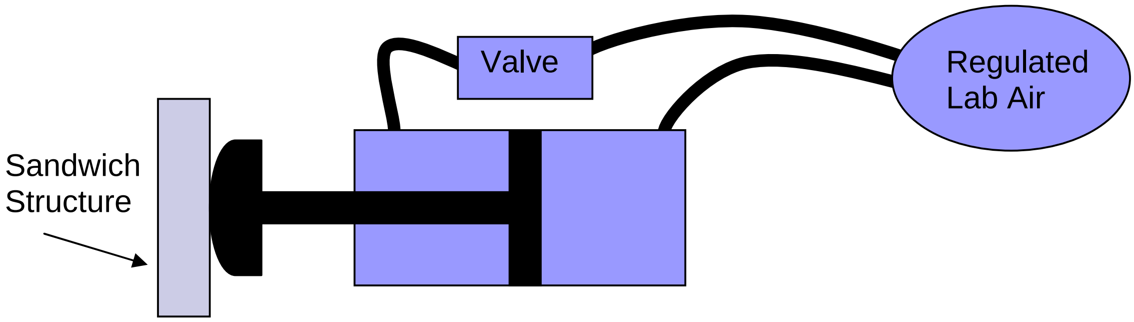

Fig. 3. Schematic of the hull slamming simulator

3 IMPACTOR DESIGN

Utilizing 3-D finite element modeling, the impact head is designed for emulating the magnitude and distribution of the slamming load. Several geometries of impactors have been studied as shown in Fig. 4 along with the resulting pressure distribution along the contact surface. Nylon was chosen as the impactor material since it will deform under loading and allow the pressure to be distributed. Comparing the trapezoidal to the rectangular impactor, the peak pressure increased by a factor of three even though the contact area decreased by a factor of two. The cylindrical impactor gave a peak pressure four times the rectangular impactor. After additional analysis, an appropriate geometry and material combination is chosen to form the impactor for simulating realistic hydroelastic conditions.

The stress distribution for a cylinder impactor can be seen in Fig. 5. The contact surface between the impactor and plate is influenced both by the deformability of the material and the stiffness of the panel. These parameters will also play a role in designing the impactor to apply a load similar to hull slamming.

The design of the hull slamming simulator has been analyzed using displacement based finite elements. The sandwich structure that is subjected to loading consists of two CFRP face plates (0.127 cm thick) and a high density PVC foam core (2.5 cm thick). The load is applied using a rectangular nylon block in the form of pressure of 4.8 MPa, which corresponds to typical hull slamming loads experienced by the marine craft. The boundary conditions simulated correspond to clamped boundaries on all edges. Only a quarter of the geometry is simulated by virtue of symmetry and is highlighted in Fig. 6(a) and the mesh is shown in Fig. 6(b).

The corresponding equivalent (Mises) stress contours are shown for the top and bottom face plate in Fig. 7(a) and (b). The top face plate has a maximum stress of 97.8 MPa while the bottom face plate has a maximum stress of 82 MPa, both of which are well below the failure strength of the CFRP. The locations of the maximum stress are at the edge of the plate in the top face plate and at the center of the bottom face plate. The contours of the equivalent stress in the PVC foam core are shown in Fig. 10. The maximum equivalent stress in the foam core is 5.63 MPa, which occurs at the top side under the short edge of the impactor. These values provide insight into the potential failure sites and modes under hull slamming conditions. Validation studies and detailed investigation are currently in progress.

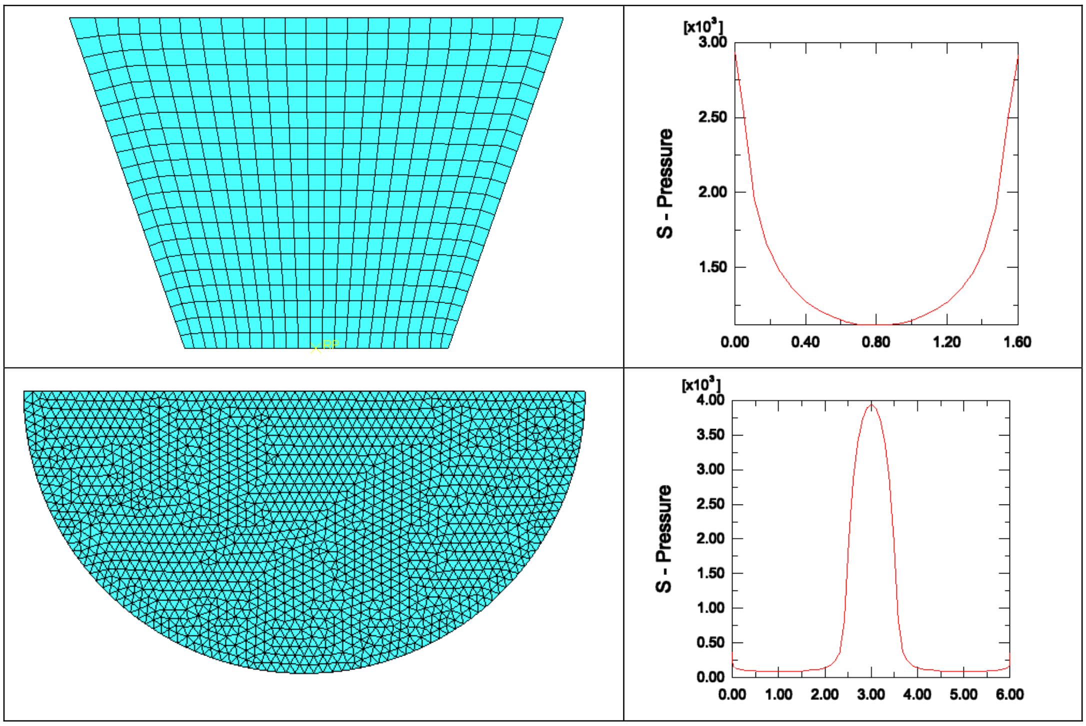

Fig. 4. Pressure distributions along contact edge for various impactor geometries

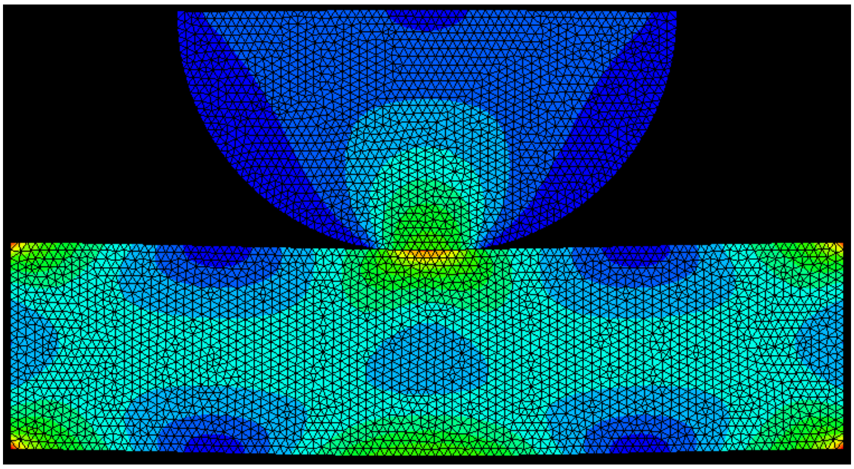

Fig. 5. Equivalent (Mises) stress distribution under a static load with clamped ends.

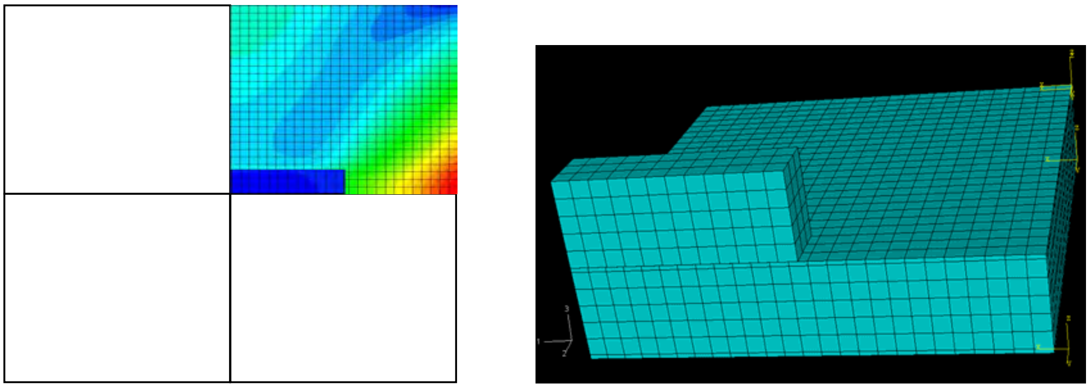

Fig. 6. (a) Plane view of the finite element model showing the impactor and the sandwich structure, (b) 3-D Mesh of the impactor and the sandwich structure.

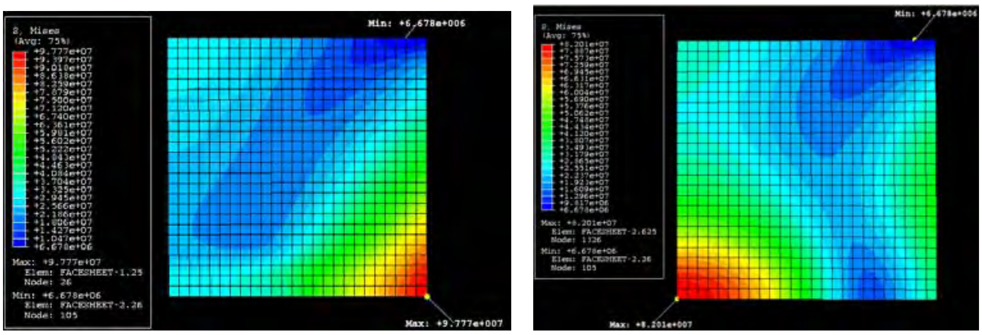

Fig. 7. Equivalent (Mises) stress contours in the (a) top face plate and (b) bottom face plate.

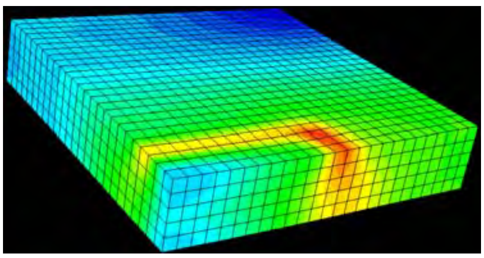

Fig. 8. Equivalent (Mises) stress contours in the PVC foam sandwich core.

4 EXPERIMENTAL OBSERVATIONS

Preliminary testing of a sandwich structure has been preformed and the response monitored using strain gages bonded to the face plates. Several specimens with were fabricated several sandwich structures with various initial debond areas [6]. A typical profile of the loading pulse sequence obtained using the hull slamming simulator is shown in Fig. 9. The loading pulse consists of sharp rise and a gradual fall similar to the load profiles for hull slamming conditions [4].

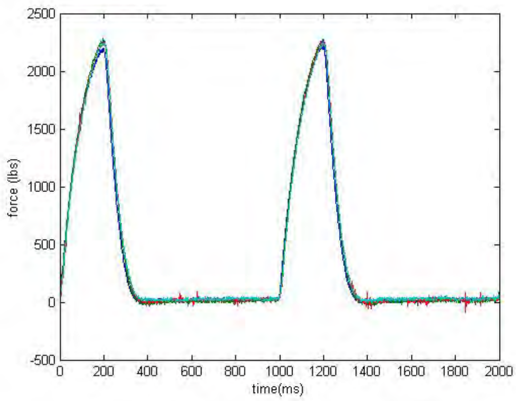

Fig. 9. Typical transient load profile obtained using a hemispherical nylon impactor.

Evolution of strains in the rear face plate was monitored using stain gages bonded to the surface of the sandwich structure. The evolution of strains with increasing number of cycles is shown in Fig. 10 for a sandwich structure with an initial debond (25 mm in diameter) in a central region between the rear face plate and the core. Though the strain signals during loading and unloading remains nearly indistinguishable with progression in the number of loading cycles, there is a clear tendency for the residual strain to increase with time. After loading these structures for an extended period of time, it was found that the residual strain appears to be a good indicator and measure of the delamination.

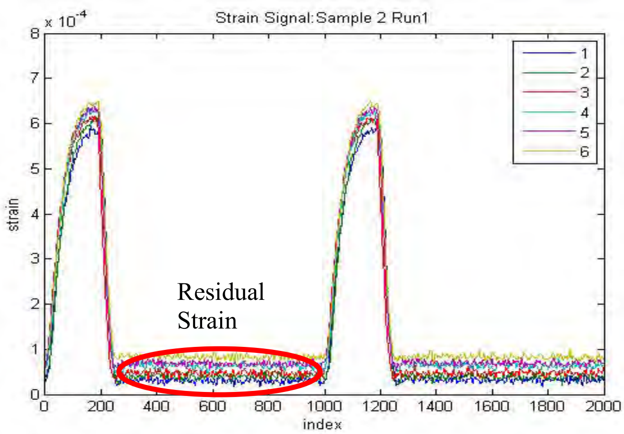

Fig. 10. Sequences of strain profiles at the center of rear face plate in a sandwich structure with an initial debond during hull slamming simulation studies.

5 CONCLUSIONS

A hull slamming simulator has been constructed to study the evolution of damge in sandwich structures under repeated dynamic transient loading conditions. By appropriate selection of impactor material and geometry, the loading pulse can be tailored to match the loading pulses corresponding to actual slamming conditions [4]. The hull simulator provides a unique facility to investigate in detail, the mechanics of damage in sandwich structures under realistic transient loading conditions. Efforts are under way to measure the full field surface deformation of the face plates in real time by implementing the 3D digital image correlation (DIC) technique and tracking the delamination process *in-situ* by imaging the zone of increased temperature due to dissipation using a high resolution infrared thermal camera. The delamination initiation threshold will be characterized and correlated with damage accumulation as a function of pulse duration, frequency and amplitude. The experimental results will be used to guide the development of models for predicting damage under hull slamming conditions experienced by high speed marine craft.

ACKNOWLEDGMENT

The authors gratefully acknowledge the support of the Office of Naval Research through a MURI grant, N00014-06-1-0730 (Dr. Y.D.S. Rajapakse, Program Manager).

REFERENCES

[1] O. M. Faltinsen, “Hydroelastic slamming”, *J. Mar. Sci. Technol.*, 5, 49-65 (2000)

[2] R. Zhao and O. M. Faltinsen, “Water entry of two-dimensional bodies”, *J. Fluid. Mech.*, 246, 593-612 (1993)

[3] O.M. Faltinsen, *Hydrodynamics of High-Speed Marine Vehicles*, Cambridge University Press (2005)

[4] M. Battley and S. Lake, “Dynamic performance of sandwich core materials”, *Proceedings of the 16th International conference on composite materials*, Kyoto, Japan (2007)

[5] M. S. Kirugulige and H. V. Tippur and T. S. Denney “Measurement of transient deformation using digital image correlation method and high-speed photography: application to dynamic fracture”, *Applied Optics*, Vol.46, No. 22, 5083-5096 (2007)

[6] F. Aviles and L. A. Carlsson, “Experimental Study of Debonded Sandwich Panels under Compressive loading”, *J. Sandwich Structures and Materials*, 8, 7-31 (2006)

8th International Conference on Sandwich Structures
ICSS 8
A. J. M. Ferreira (Editor)

For ONR sessions organized by Yapa Rajapakse

A LUMPED-MASS/SPRING MODEL FOR LOCALIZED IMPACT ON SANDWICH STRUCTURES

J. A. Kepler*, A. H. Sheikh* and P. H. Bull*

*Department of Mechanical Engineering
Aalborg University
Pontoppidanstræde 101, 9220 Aalborg East, Denmark
e-mail: jk@ime.aau.dk

Key words: Sandwich panel, Ballistic impact, Numerical model, Lumped mass / spring model, Energy absorption

Summary. *A lumped-mass / spring model has been developed for the simulation of fully penetrating ballistic impact of sandwich panels idealized as an axisymmetric plate. The effect of geometric nonlinearity has been considered in the analysis where the modes of deformation included are: localized face-sheet stretching, core shear compliance, core compressibility and overall bending deformation. The impactor has been idealized as a lumped mass with the incidental velocity of the impactor, connected with the panel through contact springs. For comparison, the model is presented with and without consideration of geometric nonlinearity, in both cases providing temporal and spatial data on deformations and velocities associated with the panel deformation. The simulation results are compared with measured data for energy absorption, obtained through experiments.*

1 INTRODUCTION

Sandwich structures are used extensively in different types of vehicles where the mass is a determining factor in its design. Such vehicles in their civil use are in general exposed to localized impact by small, hard objects like runway debris, railway ballast, hail or some other entity traveling at a considerable relative velocity. For applications (civilian or military) in conflict areas, blast fragments and similar threats are relevant to vehicle design. In some cases, the velocity of the impactor is sufficient for a complete penetration of the panel, and prediction of the penetration process is of obvious interest. Investigations have been carried out in different ways ranging from simple empirical models to sophisticated numerical techniques, depending on the importance and severity of the impact. In this context, commercial codes like LS-DYNA, ABAQUS, PAMCRASH or AUTODYN are capable of predicting the impact process with reasonable accuracy, and some investigations (e.g., [1-4]) have been carried in this direction. However none of these studies have included full penetration of a sandwich panel. Even for impact of monolithic composite laminates, where a number of studies on low velocity impact have been conducted (e.g. [5-14]), a fully penetrating impact process has been addressed by very few investigators (e.g., [15-16]).

Finite-Element simulation of this type of problem requires an extensive computational effort due to the considerable range of discretization of the structural system for precise representation along with other issues related to the problem. Interpretation becomes difficult, in part due to the vast amount of data generated, but also because failure phenomena may be attributed to several distinct physical causes. Finally, the computation time compromises the effectiveness of a sufficiently detailed FE-representation in relation to a panel design process.

Considering these aspects, an attempt has been made to develop a relatively simple, transparent and computationally efficient lumped mass/spring model for the simulation of the present problem. The central idea was initiated in an earlier study [17] where the sandwich panel was idealized as an axisymmetric panel considering only core compliance, and therefore relying on estimates of damage energies and contact force histories. A model developed by Hoo Fatt et al. [18] shares this conceptual basis by representing the panel structural response by a mass-spring system. Another model by Skvortsov et al. [19] employs an analytical scheme of solution for the overall representation of structural energy, but is otherwise similar to the model described in [17].

The enhanced model presented in this paper includes aspects like core compressibility, bending deformation and geometric nonlinearity due to large deformation, thereby being able to provide a prediction of the damage energies and the force history. The impactor has been idealized as a lumped mass with an initial velocity representing the actual impactor incident velocity v_1, connected to the sandwich panel through a number of contact/penalty springs. In the development process, the model has accumulated different features and these may be used in different combinations to test the validity of the modeling assumptions.

2 EXPERIMENTAL INVESTIGATION

The results obtained by the different models in the form of total energy absorption E_t have been compared with those obtained in laboratory tests, using the equipment outlined in figure 1.

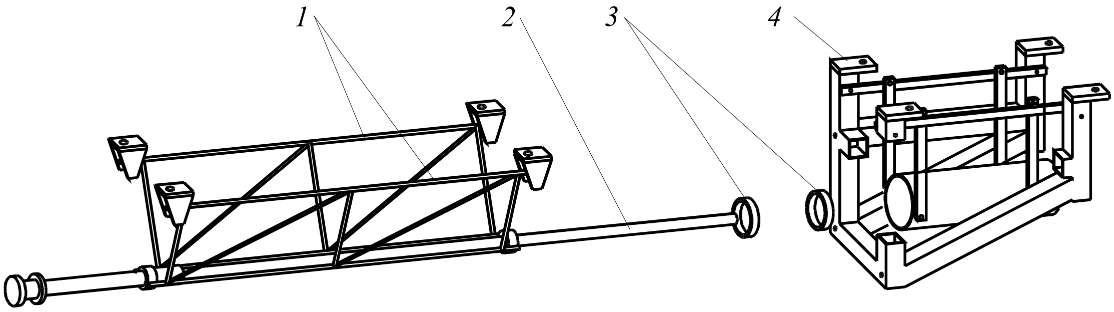

Figure 1: Test equipment : 1 : Gun support, 2 : Gun, 3 : Speed trap,

4 : Specimen support frame with ballistic pendulum

The incidental velocity v_1 of the impactor (mass M) is measured using an optical speed trap placed in front of the gun muzzle while the residual velocity v_2 is measured using a ballistic pendulum placed behind the test panel. With the incidental and residual velocities, the total energy absorption may be obtained as

$$E_t = \frac{1}{2} M \left(v_1^{\,2} - v_2^{\,2} \right) \tag{1}$$

A complete account of the experiments may be found in [20] and [21]. The test specimen configuration was:

Face-sheets: Three layers of 850 g/m^2 non-crimp E-glass [0/90] and one outer layer of 300 g/m^2 CSM, isopolyester matrix, total thickness approximately 3 mm per face-sheet.

Core: PVC foam, 80 kg/m^3, thickness 40 mm

For the present investigation, two test cases using a hemispherical tip impactor (with mass M = 1 kg and diameter Ø = 50 mm) at two different impact velocities v_1 have been selected. The corresponding energy absorptions E_t are given in Table 1.

Table 1: Experimentally measured total energy and the estimated damage energy

Test Case	v_1 [m/s]	v_2 [m/s]	E_T [J]
I	95	68	2170
II	72	39	1820

3 NUMERICAL MODEL DESCRIPTION

In this model the discretized is made in radial as well as thickness direction as shown in Figure 2 where the core is divided into *m* divisions in the thickness direction. The mass of any cell is similarly lumped at its centroid, which is defined as node having two degrees of freedom (movement along radial and vertical directions). In the vertical direction the adjacent nodes are connected through core compression springs while the adjacent nodes in the horizontal direction are connected through springs having stiffness corresponding to radial extension and transverse core shear. Figure 4 shows a representative part of the spring/lumped mass system of the enhanced model. The mass lumped at the typical nodes and stiffness of different springs may be defined as

$$m_{i,j} = 2\pi R_i \Delta \rho_f h_f \qquad j = 1, j = m+2 \tag{2}$$

$$m_{i,j} = 2\pi R_i \Delta \rho_c H / m \quad j \neq 1, j \neq m+2 \tag{3}$$

$$k^{c}_{i,j} = 4\pi R_i \Delta H E_c / m \qquad j = 1, j = m+2 \tag{4}$$

$$k^{c}_{i,j} = 2\pi R_i \Delta H E_c / m \qquad j \neq 1, j \neq m+1 \tag{5}$$

$$k^{r}_{i,j} = 2\pi\, h_f E_f / \ln(R_{i+1}/R_i) \qquad j = 1, j = m+2 \tag{6}$$

$$k^{r}_{i,j} = 2\pi \left(H/m\right) E_c / \ln(R_{i+1}/R_i) \qquad j \neq 1, j \neq m+2 \tag{7}$$

$$k^{s}_{i,j} = 0 \qquad j = 1, j = m+2 \tag{8}$$

$$k^{s}_{i,j} = 2\pi \left(H/m\right) G_c / \ln(R_{i+1}/R_i) \qquad j \neq 1, j \neq m+2 \tag{9}$$

whereG_c is the core shear modulus and E_f and E_c are the elastic moduli of the face and core, respectively. The mass for the clearance zone is proportionately distributed over the nodes located at a distance of R_1 from the centre line (Figure 2).

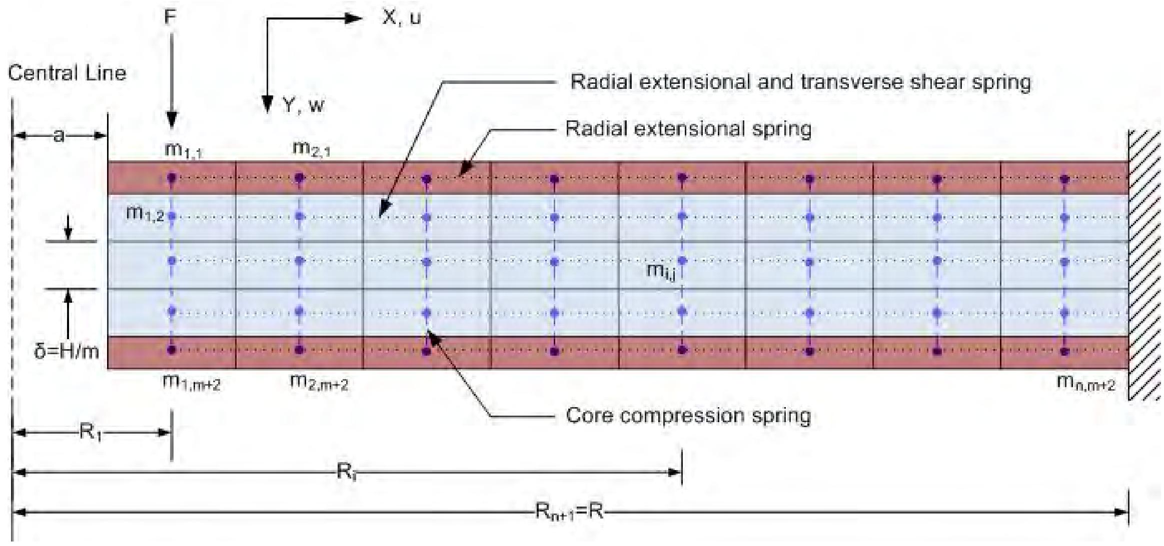

Figure 2: Axisymmetric model of the panel and discretization

Note that the face-sheets are represented only by extensional springs – the individual bending stiffness of the face-sheets is disregarded. Experimental studies have demonstrated that impact-induced delaminations are formed in the initial contact stage; this is indicated in figure 3, where delaminations along the principal directions of stiffness are visible in frames 2 and 3.

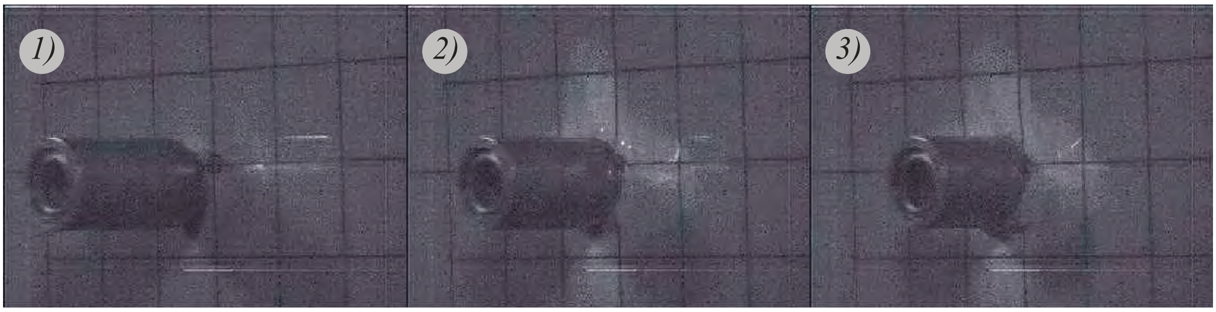

Figure 3: High-speed camera recording of impact on sandwich panel. Panel and impactor were similar to those described in this paper, but at a higher impact velocity (v_1 = 165 m/s). The panel grid spacing is 50 mm, the three frames (1, 2 and 3) are recorded at an interval of 125 µs, and frame 1 corresponds approximately to the instant of initial contact.

In earlier modeling approaches, the impactor/panel interaction was represented by a force history F(t). In the present model, the impactor is idealized as a rigid object and it is represented by a node at its centroid where the mass of the impactor and its initial velocity are assigned at the beginning of the analysis. The interaction of the impactor with the panel is achieved through contact or penalty springs connected to the impactor node and the surrounding nodes at the top face sheet of the panel . The stiffness of a vertical penalty spring connected to the panel node at a radial distance of R_i is taken as follows.

$$k_i^p = 2\pi R_i \Delta H E_c \tag{10}$$

The central clearance a is taken as much less that the radius of the impactor. Moreover, a running check is always kept during the entire analysis to ensure contact between the impactor node and a panel node with their vertical displacement and impactor geometry, which helped to activate a penaty spring at any stage.

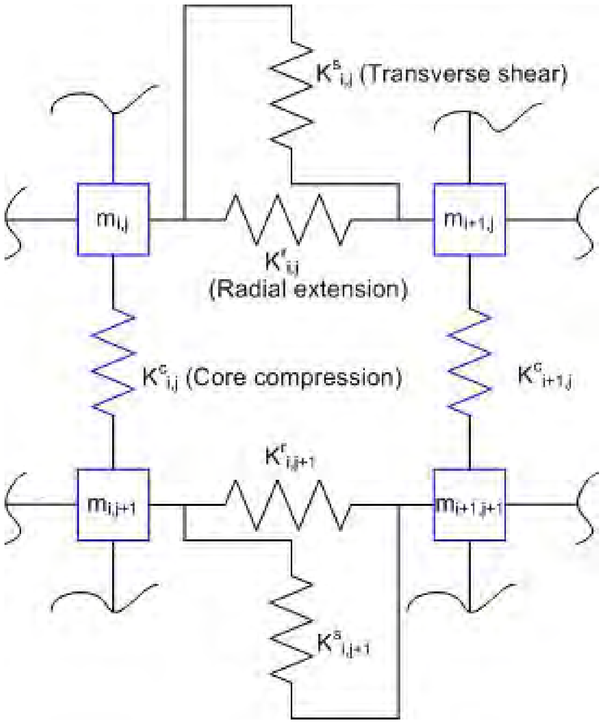

Figure 4: A representative portion of the spring/mass system

Ballistic impact of the kind considered here is by definition localized but still produces large deformation surrounding the impacted region. Thus the effect of geometric nonlinearity is taken into account, based on von Karman's hypothesis. The formulation is based on total Lagrangian technique and the Newton-Raphson iteration technique is used to solve the incremental system of equations as follows.

$$[K_T]\{\delta W\}+[M]\{\ddot{W}\}=\{\delta F\}=\{F\}-\{F_I\} \tag{11}$$

where $[K_T]$ is the tangent stiffness matrix and $\{F_I\}$ is internal force vector, which is evaluated by multiplying secant stiffness matrix with nodal displacement vector and this is carried out at the element level. For a typical horizontal spring having radial extension and transverse shear stiffness the tangent stiffness matrix $[K_T^e]$ and secant stiffness matrix $[K_S^e]$ in the global axis system *X*-*Y* (Figure 2) may be expressed as

$$[K_T^e]=\begin{bmatrix} a & b & -a & -b \\ b & c+d & -b & -c-d \\ -a & -b & a & b \\ -b & -c-d & b & c+d \end{bmatrix} \tag{12}$$

$$\left[K_S^e\right]=\begin{bmatrix} a & b/2 & -a & -b/2 \\ b/2 & c/2+d & -b/2 & -c/2-d \\ -a & -b/2 & a & b/2 \\ -b/2 & -c/2-d & b/2 & c/2+d \end{bmatrix} \tag{13}$$

where $a=k_{i,j}^r$, $b=k_{i,j}^r(w_{i+1}-w_i)/\Delta$, $c=k_{i,j}^r\left\{1.5(w_{i+1},j-w_{i,j})^2/\Delta^2+(u_{i+1,j}-u_{i,j})/\Delta\right\}$ and $d=k_{i,j}^s$. In a linear analysis the displacement dependent stiffness coefficients *b* and *c* become zero where $\left[K_T^e\right]$ and $\left[K_S^e\right]$ leads to a simple linear stiffness matrix $\left[K^e\right]$. For the vertical spring the stiffness matrix in the global axis system *X*-*Y* is as follows.

$$\left[K_T^e\right]=\left[K_S^e\right]=\left[K^e\right]=\begin{bmatrix} 0 & 0 & 0 & 0 \\ 0 & e & 0 & -e \\ 0 & 0 & 0 & 0 \\ 0 & -e & 0 & e \end{bmatrix} \tag{14}$$

where $e=k_{i,j}^c$. This is similarly valid for penalty springs where $e=k_i^p$. The internal force vector of an element may in the global axis system be obtained as

$$\left[F_I^e\right]=\left[K_S^e\right]\left\{W^e\right\} \tag{15}$$

where the nodal displacement vector of an element is $\left\{W^e\right\}^T=\left[u_{i,j}\quad w_{i,j}\quad u_{i+1,j}\quad w_{i+1,j}\right]$ for a horizontal spring and $\left\{W^e\right\}^T=\left[u_{i,j}\quad w_{i,j}\quad u_{i,j+1}\quad w_{i,j+1}\right]$ for a vertical spring. The tangent stiffness matrix $\left[K_T\right]$ and internal load vector $\left\{F_I\right\}$ of the system are obtained by assembling those of all the elements, including penalty springs. Finally the strain energy E_s and kinetic energy E_k of the system are evaluated by summarizing over the spring elements and the mass elements, respectively.

4 COMPARISON OF RESULTS

The numerical model presented above has been used to evaluate the prediction of the penetration process under the assumptions of geometric linearity and geometric nonlinearity (i.e. small or moderately large deformations). The predictions of total energy absorption in the penetration process have been compared to the measured values. In the present numerical modeling, the radius of the panel has been taken as 1.0m, which is sufficient to avoid any interference due to reflection of the overall structural waves from the boundaries. The material properties used for the core (H80 DIAB foam) are: *E* = 80 MPa, *G* = 30 MPa and ρ = 80 kg/m^3 while those of the GFRP face sheets are: *E* = 20 GPa and ρ = 2000 kg/m^3 (the model does not yet handle orthotropic face sheets, and is thus based on the quasi-isotropic equivalent). The panel is discretized using 500 divisions in the radial direction and 10 divisions in the thickness direction of the core. A time step of 1 microsecond has been used for the time integration of the equation system. The energy absorptions predicted by the different models are presented in Table 2 along with those measured in the experiment for the two cases. The different modes used for the simulation are defined as follows.

Model IV: Geometric linearity

Model V: Geometric nonlinearity

(Note: The models were numbered consecutively; models I, II and III were preliminary models, based on a force-history representation of the impactor/panel interaction – these are not treated in further detail in this paper)

Table 2: Experimental and predicted energy absorption by the different models

Test case	Sources	Absorbed energy [J]
I	Model IV	2237
	Model V	2089
	Experiment	2170
II	Model IV	2143
	Model V	2033
	Experiment	1820

In both cases, the models produce results which are within approx. 15% of the measured values. Considering the assumptions of isotropy and the moderate sophistication of the material models, this is satisfactory. Selected deflection results corresponding to test case I are presented in Figures 5 and 6. The figures show the variation of deflection for the top and bottom face-sheets along the radial direction at four different instants (0.2 ms, 0.4 ms, 0.6 ms and 0.8 ms).

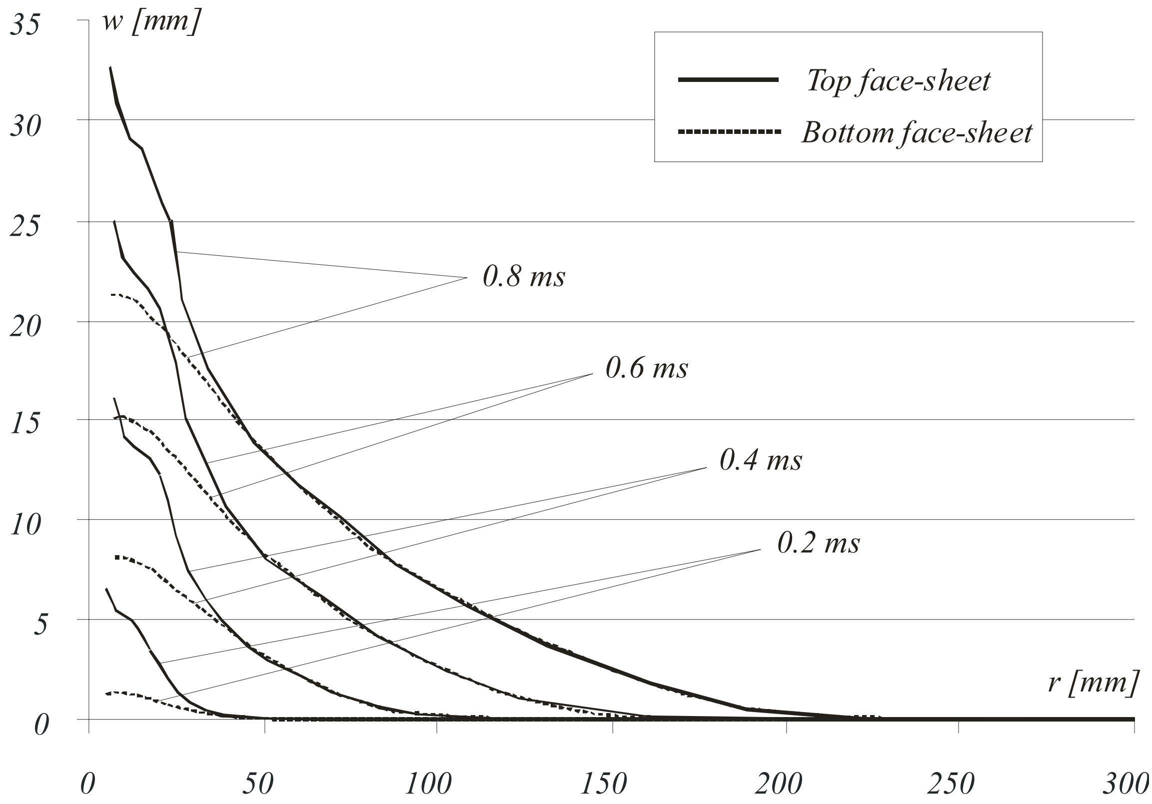

Figure 5: Variation of face-sheet deflections, model IV (linear), at times t = 0.2, 0.4, 0.6, and 0.8 ms

In figure 5, the top face sheet deflection exhibits a pronounced (and unrealistic) peak at small radii 5 mm < r < 10 mm. This effect illustrates the inadequacy of a geometrically linear description near the centre of impact – the total transverse stiffness is significantly underestimated. The region of severe core compression is approximately twice the impactor radius. Outside this region, the compressibility of the core is insignificant.

Figure 6 shows similar results using the nonlinear formulation. Compared with the results from the linear model (figure 5), the maximum deflections for model V are more moderate; this is in good agreement with the expected stiffening effect caused by the membrane reaction as described by a nonlinear model. An additional consequence of the membrane stiffness is that the region of significant core compression extends to about three times the impactor radius.

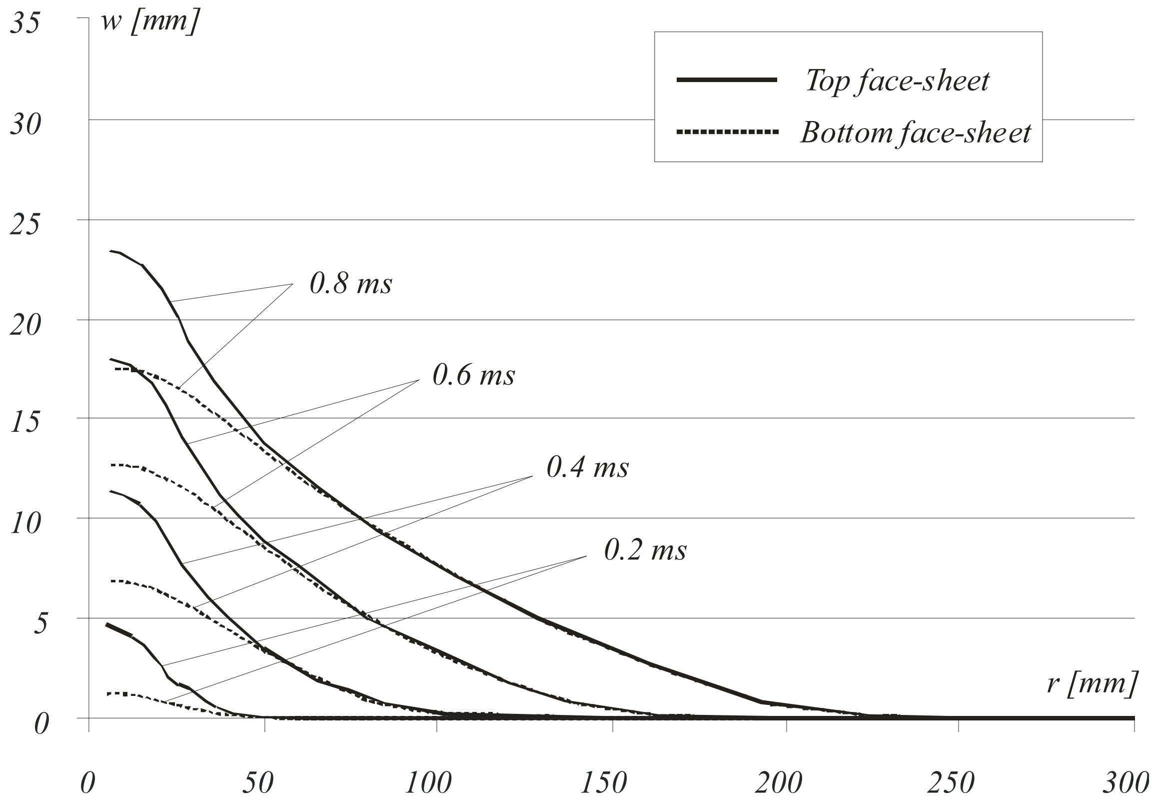

Figure 6: Variation of face-sheet deflections, model V (nonlinear), at times t = 0.2, 0.4, 0.6, and 0.8 ms

5 CONCLUSIONS

The present model has been developed as a conceptually transparent supplement to commercially available finite-element codes. The level of sophistication has deliberately been kept moderate in order to avoid ambiguity in the interpretation of results – as such, the predictive capabilities of the model are still inadequate. A primary aim of the study has been identification of dominant effects, e. g. geometric nonlinearity and core compressibility. As demonstrated, the zone of significant core compression is comparable to the impactor radius, while the membrane effects of the face-sheets extends somewhat further (depending, of course, on the specific parameters).

The discretization used in the specific example is much finer than necessary for convergence – future developments will include separate discretization regions (at larger radii, for example, core compressibility is not an issue, and structural shear and bending deformation will adequately describe the panel response).

A key issue in the programming stage has been numerical stability. The formulation of the contact/penalty springs was adjusted in order to obtain stability in the solution procedure. Unfortunately, this approach renders the model incapable of representing “percussive” impact, which may be physically reasonable under certain conditions.

With the selected discretization, the calculation time was typically less than 10 minutes (on a dual-core PC with 2 GB RAM), which is quite moderate compared to finite-element codes. The model is thereby suitable for parameter studies when designing sandwich panels for protection against penetrating impact.
The modeling of material characteristics is still quite crude, and a key aim for future developments is representation of face-sheet orthotropy and core compression failure.

6 ACKNOWLEDGMENTS

The work presented was supported by:

- The Innovation Consortium "Integrated Design and Processing of Lightweight Composite and Sandwich Structures" (abbreviated "KOMPOSAND") funded by the Danish Ministry of Science, Technology and Innovation and the industrial partners Composhield A/S, DIAB ApS (DIAB Group), Fiberline Composites A/S, LM Glasfiber A/S and Vestas Wind Systems A/S.
- US Navy, Office of Naval Research (ONR), Grant/Award No. N000140710227: "Influence of Local Effects in Sandwich Structures under General Loading Conditions & Ballistic Impact on Advanced Composite and Sandwich Structures". The ONR program manager was Dr. Yapa Rajapakse.

The support received is gratefully acknowledged.

REFERENCES

[1] Aktay L., Johnson A.F. and Holzapfel M. "Prediction of impact damage on sandwich composite panels". *Computation Materials Science*, Vol. 32, No. 3/4, pp 252-260, 2005.

[2] Nguyen M.Q., Jacombs S.S., Thomson R.S., Hachenberg D. and Scott M.L. "Simulation of impact on sandwich structures". *Composite Structures*, Vol. 67, No. 2, pp 217-227, 2005.

[3] Besant T., Davies G.A.O. and Hitchings D. "Finite element modelling of low velocity impact of composite sandwich panels". *Composites Part A*, Vol. 32, No. 2, pp 1189-1196, 2003.

[4] Meo M., Morris A.J., Vignjevic R. and Marengo G. "Numerical simulation of low velocity impact on an aircraft sandwich panels". *Composite Structures*, Vol. 62, No. 3/4, pp 353-360, 2003.

[5] Hou J.P., Petrinic N., Ruiz C. and Hallett S.R. "Prediction of impact damage in composite plates". *Composite Science and Technology*, Vol. 60, No. 2, pp 273-281, 2000.

[6] Williams K.V. and Vaziri R. "Application of a damage mechanics model for predicting the impact response of composite materials". *Computers and Structures*, Vol. 79, No. 10, pp 997-1011, 2001.

[7] Johnson A.F., Pickett A.K. and Rozycki P. "Computational method for predicting impact damage in composite structures". *Composite Science and Technology*, Vol. 61, No. 15, pp 2183-2192, 2001.

[8] Luo R.K., Green E.R. and Morrison C.J. “An approach to evaluate the impact damage initiation and propagation in composite plates”. *Composites: Part B*, Vol. 32, No. 6, pp 513-520, 2001.
[9] Guan Z. and Yang C. “Low-velocity impact and impact process of composite laminates”. *Journal of Composite Materials*, Vol. 36, No. 7, pp 851-871, 2002.
[10] Lee Y.J. and Huang C.H. “Ultimate strength and failure process of composite laminated plates subjected to low-velocity impact”. *Journal of Reinforced Plastics and Composites*, Vol. 22, No. 12, pp 1059-1081, 2003.
[11] de Moura M.F.S.F. and Goncalves J.P.M**.** “Modelling the interaction between matrix cracking and delamination in carbon-epoxy laminates under low velocity impact”. *Composite Science and Technology*, Vol. 64, No. 7/8, pp 1021-1027, 2004.
[12] Lua J. and Gregory W**.** “Development of a dynamic failure prediction tool for marine composite structure”. *Journal of Applied Mechanics, ASME*, Vol. 256, No. 7, pp 299-308, 2005.
[13] Iannucci L. “Progressive failure modelling of woven carbon composite under impact”. *International Journal of Impact Engineering*, Vol. 32, No. 6, pp 1013-1043, 2006.
[14] Zhang Y., Zhu P. and Lai **X**. “Finite element analysis of low-velocity impact damage in composite laminated plates”. *Material and Design*, Vol. 27, No. 6, pp 513-519, 2006.
[15] Silva M.A.G., Cismasiu C. and Chiorean C**.G**. “Numerical simulation of ballistic impact on composite laminates”. *International Journal of Impact Engineering*, Vol. 31, No. 3, pp 289-306, 2005.
[16] Grujicic M., Pandurangan B., Koudela K.L. and Cheeseman B.A. “A computational analysis of the ballistic performance of light-weight hybrid composite armors”. *Applied Surface Science*, Vol. 253, No. 2, pp 730-745, 2006.
[17] Kepler J.A. and Hansen M.R. "Numerical modeling of sandwich panel response to ballistic loading". Proceedings of the 7th International Conference on Sandwich Structures, Aalborg, Denmark, 2005.
[18] Hoo Fatt, M.S. and Sirivolu, D. "Impact Perforation of Composite Sandwich Panels". Proceedings of the16th International Conference on Composite Materials, Kyoto, Japan, 2007.
[19] Skvortsov, V., Kepler J.A. and Bozhevolnaya, E.”Energy partition for ballistic penetration of sandwich plates”. *International Journal of Impact Engineering*, Vol. 28, 2003.
[20] Kepler J.A. ”Impact penetration of sandwich panels at different velocities – an experimental study: part I: parameters and results”. *Journal of Sandwich Structures and Materials*, Vol. 6, No. 4, 2004.
[21] Kepler J.A. ”Impact penetration of sandwich panels at different velocities – an experimental study: part II: interpretation of results and modeling”. *Journal of Sandwich Structures and Materials*, Vol. 6, No. 5, 2004.

8th International Conference on Sandwich Structures
ICCS 8
A. J. M. Ferreira (Editor)

For ONR sessions organized by Yapa Rajapakse

FAILURE AND FATIGUE OF SANDWICH STRUCTURES WITH CORE JUNCTIONS

Martin Johannes, Elena Bozhevolnaya and O.T. Thomsen

Department of Mechanical Engineering
Aalborg University
Pontoppidanstræde 101, 9220 Aalborg, Denmark
e-mail: maj@ime.aau.dk, web page: http://www.me.aau.dk

Key words: Sandwich structures, Core junctions, Local effects, Failure, Fatigue.

Summary: *The paper concerns the failure and fatigue associated with local effects occurring in the vicinity of junctions between different core materials in sandwich beams subjected to transverse shear loading. It is known from analytical and numerical modelling that these effects display themselves by an increase of the bending stresses in the faces as well as the core shear and transverse normal stresses at the junction between the different core materials. However, their influence on the failure behaviour is not fully understood, and there are indications that the present models, which are based on the assumption of linear elastic material behaviour, overestimate the importance of the local effects with respect to failure initiation. The present paper presents preliminary results of an ongoing experimental study on the failure and fatigue of sandwich structures with core junctions. The local effects were studied both under quasi-static and fatigue loading conditions for typical types of sandwich beams with glass-fibre reinforced polymer (GFRP) face sheets and core junctions between polymer foams of different densities and rigid aluminium. In contrast to preliminary studies using similar specimen types and loading conditions, and to previous studies with in-plane tensile loading, the experiments did not show an influence of the local effects on the quasi-static failure behaviour or on the fatigue failure. The observed failure was due to core shear in areas that are supposedly unaffected by the local effects and thus not different to failure of a sandwich beams without core junctions. However, further experiments with an increased stiffness mismatch at the junction, different sandwich geometries and with more fatigue load levels have to be performed before a final conclusion can be made.*

1 INTRODUCTION

Sandwich structures have gained an important role in lightweight construction as they can outperform structurally equivalent monolithic structures for most load cases. However, difficulties arise when local effects disturb the uniform distribution of stresses in the constituents of the sandwich structure. These local effects occur due to discontinuities such as changes of geometry or material properties, or when localised external loads are applied. It is well known that in the vicinity of sub-structures in sandwich panels, e.g. local to joints, core junctions or inserts, stress concentrations are present. These may initiate local failure processes which lead to global failure of the whole sandwich structure [1].

In the case of local effects that are caused by the mismatch of the elastic properties of the adjoining materials at core junctions, local face sheet bending and local tension/compression of the core occur. This is accompanied by an increase of the in-plane stresses in the sandwich faces and stress concentrations with respect to the shear and through-the-thickness stresses in the adjacent cores. For the transverse shear load case these stress concentrations, which are induced by the geometric and material discontinuities at the core junction, compete with the inherent peak core shear stresses present in the core mid section about being the most critical in terms of causing failure. The effect of the discontinuities on the stress distribution has been analytically and numerically modelled for the linear elastic range, and the predicted face deformations have been verified experimentally by taking local strain measurements [2-4]. With respect to the failure behaviour, however, it is considered that the influence of nonlinear behaviour of the constituent materials and the high stress gradients close to the junction are important factors.

The failure prediction concerning sandwich beams with core junctions under quasi-static transverse shear loading conditions was addressed in [5-7]. Experiments showed that the local stress concentrations at core junctions pose a risk of premature failure, but also that there are difficulties in establishing appropriate criteria for assessing the role of the stress concentrations caused by the local effects.

Under fatigue loading conditions the local effects can have an influence on the failure behaviour as well. This was shown both for tensile in-plane loading [6] and for three-point bending loading [8]. For the case of in-plane tensile loading it was clearly shown that core junctions in sandwich beams can lead to accumulation of damage at the core junction and a reduced fatigue life. For the case of three-point bending loading the experimental study in [8] compared different types of core junctions in sandwich beams using a conventional butt junction and optimised designs and revealed differences in their fatigue lives. However, open questions remained, such as where the failure actually initiated, how the fatigue life of the sandwich with core junction relates to a comparable reference sandwich panel without core junctions, how the stiffness ratio of the cores at the junction influences the fatigue behaviour, and whether the influence of local effects on the fatigue failure behaviour changes with the level of the fatigue loading. Further, the number of specimens used in [8] was not sufficient to draw definitive conclusions.

High-speed video recordings of more recent three-point bending fatigue tests with similar sandwich beam specimens [9] showed that failure initiation occurred as core shear failure in the weaker of the two foam cores. This is the “nominal” failure mode of a sandwich beam without discontinuities under transverse shear loading, as described in more detail e.g. in [10] for four-point bending loading tests. As there is no immediate physical causality between such core shear failures and differences in fatigue life due to different core junction shapes as reported in [8], a larger scale fatigue test series is necessary to allow for a statistical treatment and examination of a possible correlation. Further, high-speed video recordings are used to document the failure observed for each single fatigue test. The purpose is to seek a physical explanation of the reported phenomena, and to relate the findings from the fatigue tests to results from associeted quasi-static tests. The study compares various core junction designs and a reference sandwich without a core junction. The fatigue life is evaluated over a range of loads to determine Wöhler-curves and to derive a fatigue damage accumulation law for the considered sandwich configurations. The ultimate aim is to propose a generalised damage accumulation law for sandwich structures with core junctions.

The current paper presents preliminary results of the ongoing study. The focus of the initial experiments described in this paper was to compare the effect of different stiffness ratios of the materials that form the core junctions on the failure and fatigue behaviour.

2 SANDWICH TEST SPECIMENS

Three sandwich beam specimen configurations have been considered in the experimental investigation. All configurations of sandwich beams contained 2 mm thick GFRP face sheets and a 25 mm thick core layer. The GFRP consisted of 4 layers of a bidirectional stitched non crimp fabric with an areal weight of 650 g/m^2 using a symmetric and balanced $[0/90]_{2S}$ lay-up. The core layer of configurations 1 and 2 contained two different core materials in three sections as shown in Figure 1, forming two core junctions between the different cores. Configuration 3 contained only one core material; this was meant as a reference specimen type without a core junction. The width of the sandwich beams was 30 mm in all cases.

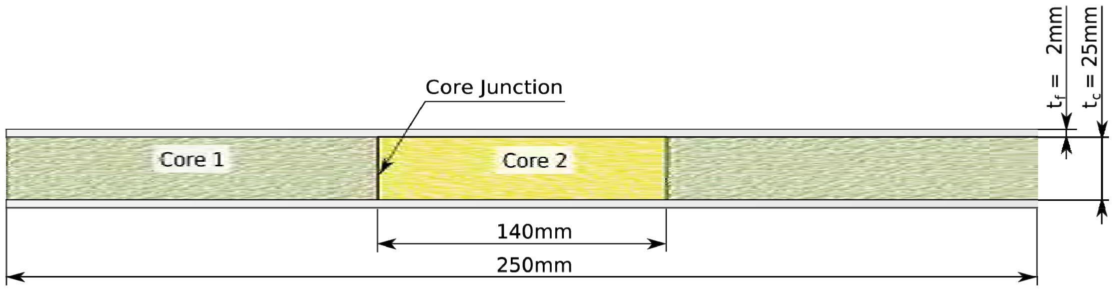

Figure 1: Schematic of a sandwich beam specimen with core junctions

The considered sandwich configurations are specified in Table 1. The table also shows the associated stiffness ratios, i.e. the ratio of the shear moduli of the core materials that determine the magnitude of the local effects at the junction [4].

Config.	Core material 1	Core material 2	Core junction shape	Core stiffness ratio G_{core1} / G_{core2} [MPa/MPa]
1	Divinycell H60	Divinycell H200	Butt junction	22 / 90 [11]
2	Divinycell H60	Aluminium	Butt junction	60 / 27000 [11-12]
3	H60		No junction	(1/1)

Table 1: Considered sandwich configurations

The specimens were produced by liquid resin vacuum infusion. The lay-up of the face sheets was placed on the laminating table, a previously manufactured core plate was placed on the lay-up of the lower face, and the lay-up of the upper face was placed on top of the core layer. The core plate consisted of the three core materials stated in Table 1. The whole lay-up was bagged and by a one-step vacuum infusion process a sandwich plate was produced, from which sandwich specimens were cut and then machined to their final width.

3 EXPERIMENTAL WORK – QUASI-STATIC TESTS

Quasi-static tests to failure were carried out to assess the influence of the local effects on the static failure behaviour and to get the relevant load levels for the fatigue tests. The tests were carried out on a Schenck Hydropuls servohydraulic test machine using a three point bending set-up. The set-up consisted of a lower fixture with two rollers and an upper fixture with a loading bolt. The specimen was centred with respect to the loading bolt; the span between the rollers was set to 440 mm. Small polymer tabs were attached to the specimen at the support points to avoid local indentation failure. The tests were carried out on a Schenck Hydropuls servohydraulic test machine and run in displacement-controlled mode at a constant displacement rate of 6 mm/min. Four specimens of each configuration were tested at room temperature. The load and crosshead displacement data were recorded and high-speed video recordings were taken of the tests. Figure 2 shows load-displacement curves from the tests.

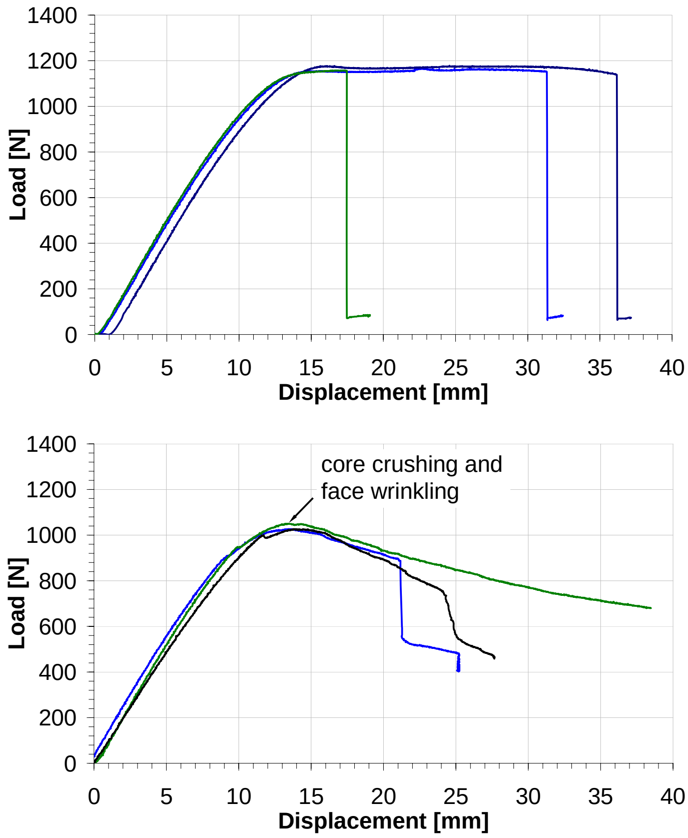

Figure 2: Load displacement curves from the quasi-static tests.
Top: Typical deformation and failure behaviour (config. 3 with thick tab at central loading point).
Bottom: Failure by local indentation and face wrinkling (config. 3 with small polymer tab only).

The top chart of Figure 2 shows a deformation behaviour that is representative for practically all the tests. After an initial linear stage the specimen deformation continues at a constant load until failure occurs at very high displacements. The curves were obtained with specimen configuration 3 using a relatively thick tab of H200 foam at the central loading bolt in addition to the small polymer tabs that were used in all other tests. Configurations 1 and 2 showed similar deformation behaviour, and there was no need for an additional thick tab due to the relatively stiff core inserts in these configurations. The bottom chart shows the behaviour of configuration 3 when using only the small polymer tab at the central loading bolt. The high compressive stresses at this point lead to core crushing and subsequent face wrinkling. Alternatively, a medium sized foam tab was used which also lead to local face failure. It was thus decided to evaluate only those tests of configuration 3 where the thick tab was used, and to use the same set-up also in the fatigue tests. The average maximum load from the load-displacement curves of each specimen configuration was used as a basis to calculate the loads for the fatigue tests.

Figure 3 shows images of the high-speed video recordings showing the failure of a specimen of configuration 3 with only the small polymer tab (upper left), the medium sized foam tab (lower left) and with the big foam tab (upper right), respectively, and of a specimen of configuration 1 with an H60/H200 core junction. It can be seen that the big tab changes the deformation behaviour, as it suppresses the local indentation at the beam centre. This raises the question of what is the best set-up to allow for a comparison of sandwich beams without core junction with sandwich beams with a core junction. It has to be noted that the length of the big foam tab is smaller than the length of the stiff middle section in the beams with core junction so that no extra stiffness is introduced relative to those beams. The video recordings were taken at a frame rate of 1000 frame per second, and neither for configuration 1 nor for configuration 2 there was evidence that failure was associated with the core junction. Except for those tests of configuration 3 that were carried out without the big tab all specimens failed in core shear.

Config. 3 without foam tab

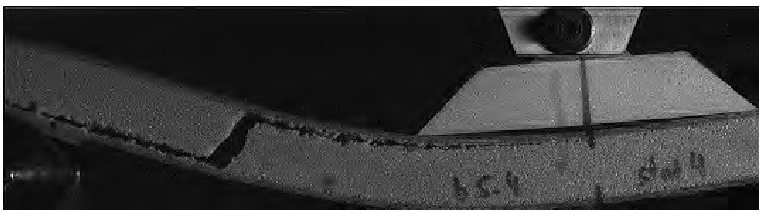

Config. 3 with big foam tab

Config. 3 with medium foam tab

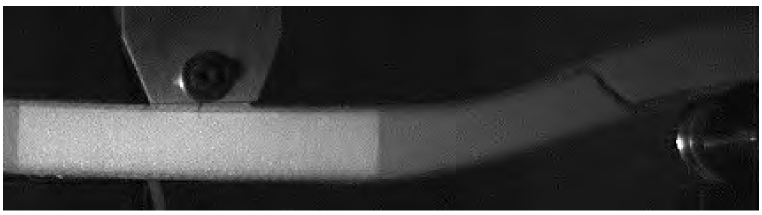

Config. 1

Figure 3: Images of typical failure behaviour in the quasi-static tests

4 EXPERIMENTAL WORK – FATIGUE TESTS

The main objective of the fatigue tests was to examine whether it is possible to observe and record a failure behaviour that is associated with the local effects at the core junction. Further it should be examined if there is a change in fatigue life from a specimen without core junction to a specimen with core junction, or from a core junction with low stiffness ratio to one with a higher stiffness ratio, respectively.

The fatigue tests were run in load-control with the same set-up as used in the quasi-static tests. The loading was sinusoidal with a loading ratio $R=F_{fat,min}/F_{fat,max}=0.1$ and a frequency of 3 Hz for all the tests. Special care was taken to ensure an approximately constant room temperature throughout the tests by means of an air-conditioning system. It is known from initial experiments and from literature [10] that a temperature variation of more than 5-10°C can greatly alter the fatigue life of the Divinycell foams and specimens made thereof. Four specimens of each configuration were tested in fatigue, and the peak and valley load and displacement data were recorded. The high-speed video camera was set-up to be triggered when a certain displacement limit was exceeded so that it would record the final failure of the specimen. Several attempts were made to track also initial fatigue failure and damage formation. However, as it is very small cracks or irregularities generally forming in the areas of maximum shear (between the centre loading bolt and the outer support rolls) in the centreline of the sandwich beam (the "fracture process zone", as described in [10]), it was impossible to correlate this initial failure to a change in displacement. In fact, the reduction in stiffness during the test was very small until the small initial cracks form a macroscopic horizontal crack. The final failure occurs when this crack kinks towards the face sheets and propagates rapidly along the face/core interface. The last stage of failure from macro-crack formation to final failure happens within a very short time (less than 5% of the fatigue life). The high-speed video recording captures the shearing of the accumulated macro-crack and the final failure, but the resolution is not sufficient to identify any small initial cracks. However, it is believed that there is an indication whether there is a connection between the local effects at the core junction and the location where the macro-crack is formed and where the crack-kinking takes place.

Figure 4 shows images of the high-speed video recordings showing the typical final failure of specimen configurations 1 to 3. The images of the final failure correspond to the failure behaviour as described above and in more detail in [10]. The size of the fracture process zone is related to the area of maximum shear stresses and thus dependent on the loading conditions [10]. For the given specimen type and loading conditions it has about constant size. It should be noted, though, that care has to be taken when measuring the size on the failed specimens. Although not common, it can be seen in the middle picture of Figure 4 that it is also possible that the cracks do not kink away from the end of the fracture process zone, but from a place within, so that the length between the kinked cracks does not necessarily correspond to the size of the fracture process zone.

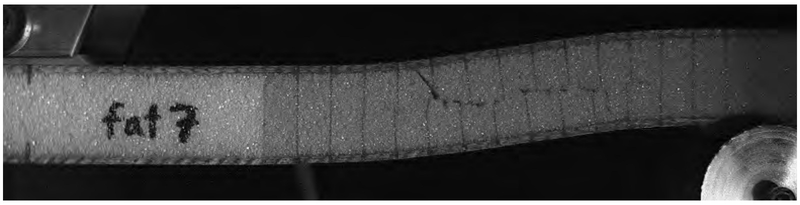

Configuration 1: H60-H200 core junction

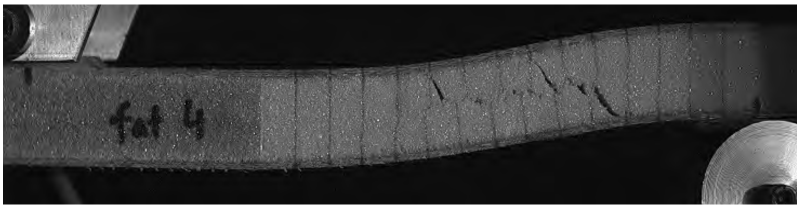

Configuration 2: H60-aluminium core junction

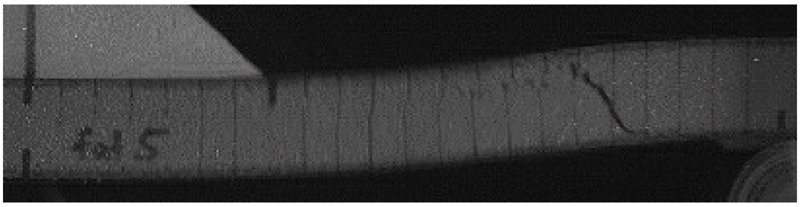

Configuration 3: only H60 foam - no core junction

Figure 4: Images of typical final failure behaviour in the fatigue tests (Configs. 1-3).

Judging from the failure pictures it has to be concluded that for the examined sandwich configurations failure was not associated with local effects at the core junctions. This means that unlike to other tests with in-plane tensile loading [6-7] it is not apparent that the local stress concentrations at the junctions influence the failure behaviour under the three point bending (transverse shear) conditions investigated herein. A summary of the observed fatigue lives is given in Table 2.

Config.	Load level $F_{fat,max}/F_{stat,max}$	Average fatigue life [cycles]	Standard deviation [cycles]	Failure mode
1	0.50	494 591	15515 (3%)	Core shear failure
	0.60	297 250	32739 (11%)	Core shear failure
	0.75 (batch 1)	29 658	7506 (25%)	Core shear failure
	0.75 (batch 2)	31 790	11271 (35%)	Core shear failure
2	0.50	479 787	84738 (18%)	Core shear failure
	0.75	22 985	6352 (28%)	Core shear failure
3	0.75	58 674	11629 (20%)	Core shear failure

Table 2: Fatigue test results

Table 2 shows an interesting tendency in the recorded fatigue lives. At the same load level $F_{fat,max}/F_{stat,max}$ the fatigue lives of the specimens with core junction are shorter than those recorded for the specimens without a core junction. Moreover, the recorded fatigue lives of the specimens with a higher stiffness ratio at the core junction are lower than the ones with a lower stiffness ratio. This could indicate a correlation between the stress concentrations at the core junctions and the fatigue life. However, unlike in the study where such a correlation was proposed [8], and where optimised and thus only slightly changed core junction shapes were examined, the change in design of the specimens in this paper also caused a change in the overall stiffness of the specimens. A direct comparison, in particular of configurations 1 and 2, respectively, with configuration 3, is therefore not possible. A change of the set-up to a four point bending test could improve the validity of the comparison.

In continuation of the initial stages of the study reported herein, more specimens will be tested to allow for a thorough statistical treatment. Due to the limited amount of data it is also omitted to construct Wöhler-curves at the current point.

An open question that has not been raised in detail in previous studies is the influence of the specimen quality on the fatigue life. This is linked to the variability of the manufacturing procees, which in this case was vacuum infusion. The overall specimen quality in this study can be considered as good. However, there are still variations in the average static failure load from one specimen batch to the other. To compensate for this, quasi-static tests were carried out for each batch before determining the absolute fatigue load. There were two specimen batches of configuration 1 that differed in the average static failure load by about 15%, but as can be seen from Table 2 they yielded about the same fatigue life at the same load level. As a further improvement of the statistical treatment the manufacture of different specimen configurations in the same specimen batch could be an option.

5 CONCLUSIONS

This paper has presented preliminary results of an ongoing experimental study on the failure and fatigue of sandwich structures with core junctions subjected to transverse shear loading. The local effects were studied both under quasi-static and fatigue loading conditions for typical types of sandwich beams with glass-fibre reinforced plastic (GFRP) face sheets and core junctions between polymer foams of different densities and rigid aluminium. In contrast to preliminary studies using similar specimen types and loading conditions, and to previous studies with in-plane tensile loading, the experiments did not show an influence of the local effects on the quasi-static failure behaviour or on the fatigue failure. The observed failure was due to core shear in areas that are supposedly unaffected by the local effects and thus not different to failure of a sandwich without core junctions. However, further experiments with an increased stiffness mismatch at the core junction, different sandwich geometries and with more fatigue load levels have to be performed before a final conclusion about the influence of local effects on the failure and fatigue can be made.

ACKNOWLEDGEMENTS

The work presented was supported by:

- The Innovation Consortium “Integrated Design and Processing of Lightweight Composite and Sandwich Structures” (abbreviated “KOMPOSAND”) funded by the Danish Ministry of Science, Technology and Innovation and the industrial partners Composhield A/S, DIAB ApS (DIAB Group), Fiberline Composites A/S, LM Glasfiber A/S and Vestas Wind Systems A/S.

- US Navy, Office of Naval Research (ONR), Grant/Award No. N000140710227: "Influence of Local Effects in Sandwich Structures under General Loading Conditions & Ballistic Impact on Advanced Composite and Sandwich Structures". The ONR program manager was Dr. Yapa Rajapakse.

The support received is gratefully acknowledged.

REFERENCES

[1] D. Zenkert, *An Introduction To Sandwich Construction*, EMAS, London (1997).

[2] E. Bozhevolnaya, O.T. Thomsen, A. Kildegaard and V. Skvortsov, "Local effects across core junctions in sandwich panels", *Composites Part B: Engineering*, 34, 509-517 (2003).

[3] E. Bozhevolnaya and O.T. Thomsen, "Structurally graded core junctions in sandwich beams: Quasi static loading conditions", *Composite Structures*, 70, 1-11 (2005).

[4] E. Bozhevolnaya and A. Lyckegaard, "Local effects at core junctions of sandwich structures under different types of loads", *Composite Structures*, 73, 24-32 (2006).

[5] A. Lyckegaard, E. Bozhevolnaya and O.T. Thomsen, "Stress analysis and prediction of failure in structurally graded sandwich panels", *In Proceedings of the 16th European Conference on Fracture (ECF-16)*, 557-558 (2006).

[6] M. Johannes, E. Bozhevolnaya and O.T. Thomsen, "Examination of the Influence of Local Effects on Sandwich Beam Failure Characteristics", *In Proceedings of the 12th European Conference on Composite Materials (ECCM-12)*, 565-566 (2006).

[7] J. Jakobsen, M. Johannes and E. Bozhevolnaya, "Failure Prediction of In-Plane Loaded Sandwich Beams with Core Junctions", *Composite Structures*, 82, 194-200 (2007).

[8] E. Bozhevolnaya and O.T. Thomsen, "Structurally graded core junctions in sandwich beams: Fatigue loading conditions", *Composite Structures*, 70, 12-23 (2005).

[9] J. Jakobsen, E. Bozhevolnaya and O.T. Thomsen, "Quasi-static testing of new peel stopper design for sandwich structures", *In Proceedings of the 13th International Conference on Experimental Mechanics (ICEM-13)*, (2007).

[10] M. Burman and D. Zenkert, "Fatigue of foam core sandwich beams - 1: Undamaged specimens", *International Journal of Fatigue*, 19, 551-561 (1997).

[11] DIAB AB, Sweden, Divinycell® Technical Manual H-grade, (2003).

[12] Matweb Online Materials Information Resource, www.matweb.com [viewed 01/02/2008]

8th International Conference on Sandwich Structures
ICSS 8
A. J. M. Ferreira (Editor)

KINKING OF INTERFACIAL CRACKS IN SANDWICH BEAMS

E. E. Gdoutos and V. Balopoulos
School of Engineering
Democritus University of Thrace
GR-671 00 Xanthi, Greece

Key words: Sandwich beams, Debonding, Foam cores, Finite elements, Linear elastic fracture mechanics, Strain energy release rate.

Summary. *Debonding between core and facings is a common failure mode of sandwich structures that can severely damage the load-carrying capacity of the structure. The objective of this work is to study the effect of debonding in double cantilever beam specimens made of aluminum facings and PVC foam cores. The configuration follows the standard ASTM D5528-94a peel test. Four PVC foam core materials under the commercial name Divinycell H with densities 60, 80, 100, and 250 kg/m*^{3} *are considered. In each case debonding is introduced between the core and the adhesive at the loaded facing of the beam. Linear elastic fracture mechanics is used to model interfacial crack growth and crack kinking into the core. Due to the different mechanical properties of the adjoining materials mixed-mode loading conditions dominate in the neighborhood of the crack tip. Results for the stress and displacement fields are obtained using a finite element computer code. The energy release rate and both opening- and sliding-mode stress intensity factors for interfacial and core cracks are calculated and found that they can be approximated as linear functions of crack length. From results of stress intensity factors in conjunction with the maximum circumferential stress criterion it was obtained that for weak interfaces debonding grows along the interface. On the contrary, for strong interfaces, crack kinks into the core, followed by rapid curving. After a small initial curved depth* h_∞ *the crack becomes parallel to the interface. It was obtained that* h_∞ *is inversely proportional to the modulus of elasticity of the core material and independent of the core thickness.*

1. INTRODUCTION

Sandwich structures are composed of dissimilar materials and exhibit various failure modes including facing compression or tension failure, core shear failure, compression facing wrinkling, indentation failure and debonding between the core and the facings. Failure modes can be caused by accidental overloads of the structure or by initial defects. Sandwich structures offer improved stiffness and strength to weight ratios compared to monolithic materials. Furthermore, they present excellent thermal and acoustic insulation properties. They have found wide applications in weight-sensitive structures where the main loads are flexural.

A thorough investigation of failure modes of composite sandwich structures made of carbon/epoxy facings and PVC foam core materials was performed by Daniel and Gdoutos [1-5]. Debonding between core and facings is a serious failure mode of sandwich structures. It can be modeled as an interface crack between dissimilar materials and studied by linear elastic fracture mechanics (LEFM) [6, 7]. Zenkert [8] applied LEFM to analyze the facings to core debonding in sandwich structures. Carlsson and Prasad [9 – 11] studied the mixed-mode fracture in a sandwich plate for different loadings on the debonding sandwich facing. A comprehensive study of the facing to core debonding was performed by Ratcliffe and Cantwell [12]. Østergaard et al [13] measured the interface toughness in sandwich double cantilever beams made of glass/polyester facings and PVC cores and found that it strongly depends on the mode mixity. Berggreen et al [14] developed a numerical model based on finite elements for the prediction of debonding between facing and core in foam core sandwich structures. Grau et al [15] determined the interfacial fracture toughness in composite sandwich panels made of graphite/epoxy facings and an aramid fiber/phenolic resin honeycomb core. They found that the interfacial fracture toughness increases as much as 70% as the shear component increases, which leads to an overestimation of the load carrying capacity of debonded sandwich panels.

In the present work we consider a sandwich double cantilever beam (*DCB*) specimen made of aluminum facing and foam core with initial debonding in the form of an interfacial crack (Figure 1). The growth behavior of the interfacial crack is studied by a finite element analysis coupled with failure criteria. The fundamentals of interfacial crack propagation in linear elastic fracture mechanics (LEFM) are first presented. Then, we describe the materials and the geometry of the sandwich DCB specimen and its discretization. From the finite element analysis we obtain results for the strain energy release rate and the opening- and sliding-mode stress intensity factors for the interfacial crack. These results are coupled with the maximum circumferential stress criterion [16] to obtain the crack growth behavior in the core. Results for the dependence of the crack growth path in the core are obtained as a function of the stiffness of the core. It was found that for weak interfaces debonding grows along the interface, while for strong interfaces crack kinks into the core, followed by rapid curving. After a small initial curved depth h_∞ the crack becomes parallel to the interface. It was obtained that h_∞ is inversely proportional to the modulus of elasticity of the core material and independent of the core thickness.

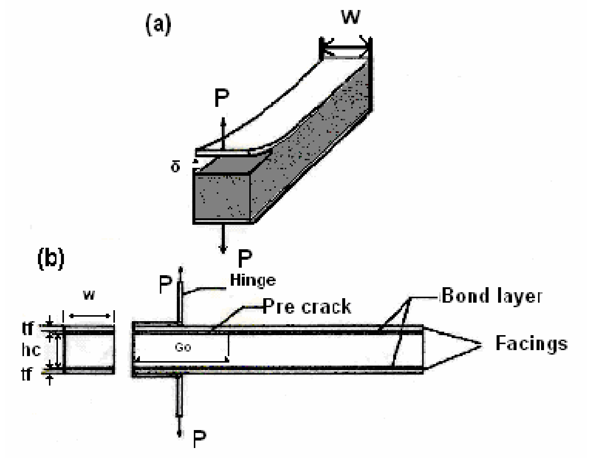

Figure 1: Sandwich peel test specimen.

2. INTERFACIAL CRACKS

Consider an interfacial crack between two dissimilar materials, 1 and 2 (Figure 2). We briefly present the fundamentals of fracture mechanics of interfacial cracks [17-20]. In elastic problems of bimaterial bodies two parameters α and β ($j \in \{1,2\}$), that express the mismatch of the elastic properties of the adjoining materials, are defined by [21]:

$$\left.\begin{aligned} \alpha &= \frac{\overline{E}_1 - \overline{E}_2}{\overline{E}_1 + \overline{E}_2} \\ \beta &= \frac{G_1(\kappa_2 - 1) - G_2(\kappa_1 - 1)}{G_1(\kappa_2 + 1) + G_2(\kappa_1 + 1)} \end{aligned}\right\}, \text{ where } G_j = E_j \big/ 2(1+\nu_j) \text{ and } \left\{\begin{aligned} &\overline{E}_j = E_j \big/ \left(1-\nu_j^2\right),\ \kappa_j = 3 - 4\nu_j \text{ for plane strain} \\ &\overline{E}_j = E_j\,, \kappa_j = (3-\nu_j)\big/(1+\nu_j) \text{ for plane stress} \end{aligned}\right. \quad (1)$$

The singular normal and shear stresses, σ_{yy} and τ_{xy}, and the opening and sliding displacements of the crack faces δ_x and δ_y, along the crack axis are given by [7]:

$$\sigma_y + \mathrm{i}\tau_{xy} = \frac{K r^{\mathrm{i}\varepsilon}}{\sqrt{2\pi r}} \text{ and } \delta_y + \mathrm{i}\delta_x = \frac{4\left(1/\overline{E}_1 + 1/\overline{E}_2\right)}{(1+2\mathrm{i}\varepsilon)\cosh(\pi\varepsilon)}\sqrt{\frac{r}{2\pi}} K r^{\mathrm{i}\varepsilon}, \text{ where } K = K_1 + \mathrm{i}K_2 \text{ and } \varepsilon = \frac{1}{2\pi}\ln\left(\frac{1-\beta}{1+\beta}\right) \quad (2)$$

In the above equation K is the complex stress intensity factor and K_1 and K_2 are the opening-mode and sliding-mode stress intensity factors. Note that the displacement field has an oscillatory term $r^{\mathrm{i}\varepsilon}$ which leads to overlapping of the crack faces in a very small area near the crack tip. For most practical applications β is small and it can be assumed equal to zero. Under such circumstances no overlapping of the crack faces takes place.

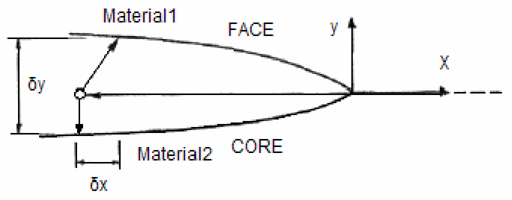

Figure 2: Interfacial crack between two dissimilar materials.

Thus, the singular stress and displacement fields in the neighborhood of the interfacial crack are proportional to [7]

$$\{\sigma_y, \tau_{xy}\} = \frac{\{K_{\mathrm{I}}, K_{\mathrm{II}}\}}{\sqrt{2\pi r}} \quad \text{and} \quad \{\delta_y, \delta_x\} = \frac{4\left(1/\overline{E}_1 + 1/\overline{E}_2\right)\sqrt{r}}{\sqrt{2\pi}}\{K_{\mathrm{I}}, K_{\mathrm{II}}\} \tag{3}$$

The strain energy density is given by [7]

$$G_{\mathrm{int}} = \frac{1}{2}\left[\frac{1}{\overline{E}_1} + \frac{1}{\overline{E}_2}\right](K_{\mathrm{I}}^2 + K_{\mathrm{II}}^2) \tag{4}$$

For similar materials ($\overline{E}_1 = \overline{E}_2 = \overline{E}$) Eq. (4) gives the value of the strain energy release rate for a crack in a monolithic elastic material as:

.
$$G_{\mathrm{vol}} = \frac{K_{\mathrm{I}}^2 + K_{\mathrm{II}}^2}{\overline{E}} \tag{5}$$

The interfacial crack may propagate along the interface or kink into one of the adjoining materials. The angle of initial crack propagation, Ω, is given, according to the maximum tangential (hoop) stress criterion [16], by:

$$\Omega = 2\tan^{-1}\left(\frac{\sqrt{1 + 8\left(K_{\mathrm{II}}/K_{\mathrm{I}}\right)^2} - 1}{4K_{\mathrm{II}}/K_{\mathrm{I}}}\right) \tag{6}$$

Kinking of the interfacial crack into the core occurs when the following inequality is satisfied:

$$\left(\frac{\max\limits_{\Omega} G}{G_{\mathrm{I,cr}}}\right)_{\mathrm{core}} > \left(\frac{G}{G_{\mathrm{cr}}(\gamma)}\right)_{\mathrm{int}} \tag{7}$$

The critical strain energy release rate for the core material in mode I, $G_{\mathrm{I,cr}}$, and the critical interfacial strain energy release rate ,$G_{\mathrm{cr}}(\gamma)$, as function of mode mixity, are determined experimentally. They are characteristic parameters of the core and the interface, respectively. On the other hand, the values of energy release rate for crack growth in the core and along the interface depend on the applied loads and the geometry of the sandwich plate, and are determined numerically.

3. SIMULATION OF CRACK PROPAGATIONS

We consider a sandwich double cantilever beam (*DCB*) specimen of length 152.4 mm (6 in) and width 25.4 mm (1 in) loaded by a concentrated load at a distance 25.4 mm (1 in) from its end (Figure 1). The beam is made of aluminum 2024 T3 facings of thickness 1 mm and a PVC foam (Divinycell H) core of thickness 25.4 mm (1 in). The core is bonded to the facings by of epoxy adhesive (Araldite AV 138M paste with HV998 hardener [22]) of thickness 0.3 mm. Four different PVC core materials, H60, H80, H100, and H 250, with densities 60, 80, 100 and 250 Kg/m^3 were studied [23]. Material properties are given in Table 1. All Divinycell core materials are considered as linear elastic and isotropic. The specimen configuration follows that proposed by Prasad and Carlsson [10, 11], which is similar to the standard ASTM D5528-94a test [24]. An interfacial crack of length 51.1 mm is introduced between the core and the adhesive at the loaded end of the specimen. Propagation of the interfacial crack is studied under condition of plane strain.

Modeling and analysis is performed using a computer program developed by the Fracture Group of Cornell University under the commercial name FRANC 2D [25]. The initial meshing, the fracture toughness parameters ($K_{\mathrm{I,cr}}$, $G_{\mathrm{int,cr}}(\gamma)$) and the initial crack configuration are first introduced. Then, as the crack propagates FRANC 2D removes automatically the affected portions of the mesh, places a new rosette of appropriate size around the new crack tip and performs local re-meshing semi-automatically. The elastic stress and displacement fields and the stress intensity factors are obtained, and the preferred direction of crack propagation is calculated based on the maximum circumferential stress criterion [16]. The crack tip is then moved to its new location by a user-specified increment.

Table 1. Material properties.

Materials	t (mm)	E (GPa)	ν	$\bar{E}$ (GPa)	$G_{Int,cr}$ (Nmm/mm^2)	$G_{I,cr}$ (Nmm/mm^2)
Al2024T3	1.00	62.30	0.33	69.95		
AralditeAV138M	0.30	4.700	–0.22	4.939		
Divinycell H60	25.40	0.056	0.26	0.059	0.28	0.10
Divinycell H80	25.40	0.080	0.29	0.087	0.45	0.22
Divinycell H100	25.40	0.100	0.25	0.107	0.78	0.30
Divinycell H250	25.40	0.280	0.30	0.308	1.55	1.00

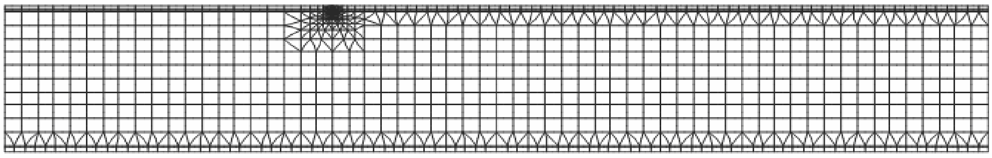

Figure 3: Initial meshing.

The model of the sandwich DCB specimen is shown in Figure 3. It is composed of seven topological regions. Each region is divided into regular and transition sub-regions. Sub-region boundaries are then subdivided into segments of appropriate number and proportions, and meshing is done automatically by boundary extrapolation, using Q8 and T6 elements for regular and transition sub-regions, respectively. The initial model contains 1501 elements (986 Q8 and 515 T6), of which 282 discretize the upper face, 114 the upper layer of adhesive, 97 the lower layer of adhesive, 97 the lower facing and 911 the core.

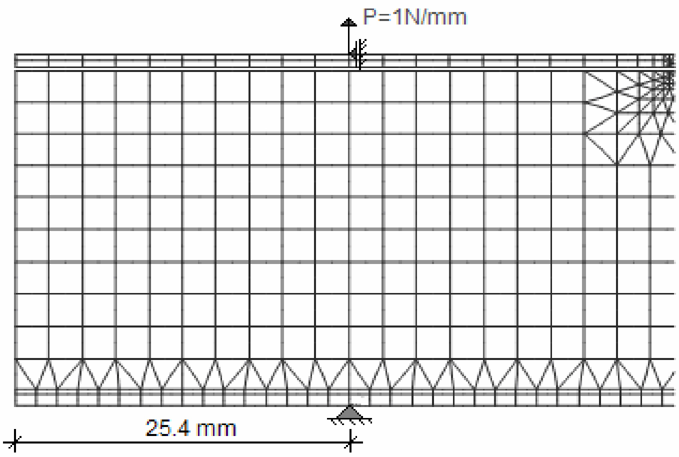

Figure 4: Finite element discretization and loading.

Figure 4 shows the mesh part of the specimen with the applied concentrated load and the interfacial crack. The interfacial crack has an initial length of 25.4 mm and depth of 0.3 mm, and is introduced between the upper layer of adhesive and the core. It is surrounded by a two-layer octagonal rosette, which is surrounded by a local T6 transition mesh. The internal layer covers 30% of the rosette radius and is made of triangular square-root-singular elements (degenerate quarter-point Q8, [25]), whereas the external layer covers 70% of the radius and is made of trapezoidal Q8 elements. The ability of FRANC 2D to work with square-root-singular elements is of major importance since it can model the inverse square root singularity in the neighborhood of the crack tip.

The initial model is analyzed based on Eq. (3) (for $\beta = \varepsilon = 0$) to obtain the initial stress intensity factors (SIFs) by means of the displacement correlation method, which works correctly both for interfacial and core cracks. In the case of three-noded edges of square-root singular elements, the stress intensity factor is given by [26]:

$$\boldsymbol{K} = K_{\mathrm{II}}\boldsymbol{e}_1 + K_{\mathrm{I}}\boldsymbol{e}_2 = \frac{\sqrt{2\pi}\,\overline{E}}{4\sqrt{l}}\left(4\Delta\boldsymbol{u}_{1/4} - \Delta\boldsymbol{u}_1\right) \tag{8}$$

where $\Delta\boldsymbol{u}$ is the vector of relative crack flank displacements. On the basis of the SIFs obtained, FRANC 2D identifies the three directions of propagation (along the interface, into the core, or into the adhesive) and computes the associated energy release rates. Then Eq. (7) is used to determine whether the crack will propagate in the facing, the adhesive or the core.

The PVC-foam core is porous and has very strong chemical affinity with the epoxy adhesive. Thus, the critical interfacial energy release rate, $G_{\mathrm{int,cr}}$, is expected to be greater than the that for crack propagation in the core, $G_{\mathrm{I,cr}}$. In fact, experimental values reported in [27] suggest $G_{\mathrm{int,cr}} \sim 2G_{\mathrm{I,cr}}$ (Table 1), so that for any initial interfacial length, the crack kinks into the core. In view of these observations, we consider two sequences of configurations (trajectories) for each model:

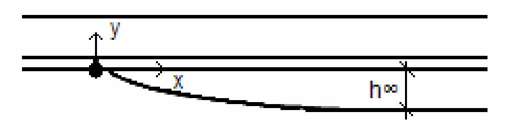

Figure 5. Curved interfacial crack propagation in the core.

- a natural trajectory, where the crack kinks into the core (subsequent propagation according to the maximum circumferential stress criterion), and
- an artificial trajectory, where the crack is forced to stay on the interface, by introducing artificially low values for $G_{\mathrm{int,cr}}$.

The natural trajectory near the kink is followed in very small crack increments, since it exhibits high curvature. In both cases the crack is simulated for values of the distance from the crack tip, x, up to 25.4 mm (1 in), where x is measured from the lower re-entrant corner as shown in Figure 5.The results obtained for the artificial trajectory serve as reference values and a basis for comparisons.

4. NUMERICAL RESULTS AND DISCUSSION

For the prediction of the crack trajectory we use the interface toughness values for normal adhesion (Table 1). It is obtained that first the interfacial crack kinks into the core and then curves back toward the interface (Figure 6). For intermediate values of the distance x from the crack tip (3 mm< x <30 mm), we obtain the following results:

- the crack after a at a small depth h_∞ becomes parallel to the interface (as shown in Figure 5)

- $K_{\mathrm{I,int}}$, $K_{\mathrm{II,int}}$, and $K_{\mathrm{I,core}}$ vary linearly with the distance x from the crack tip linear in x (Figure 7), and
- G_{int} and G_{core} vary linearly with x and are almost independent of the core properties (Figure 8).

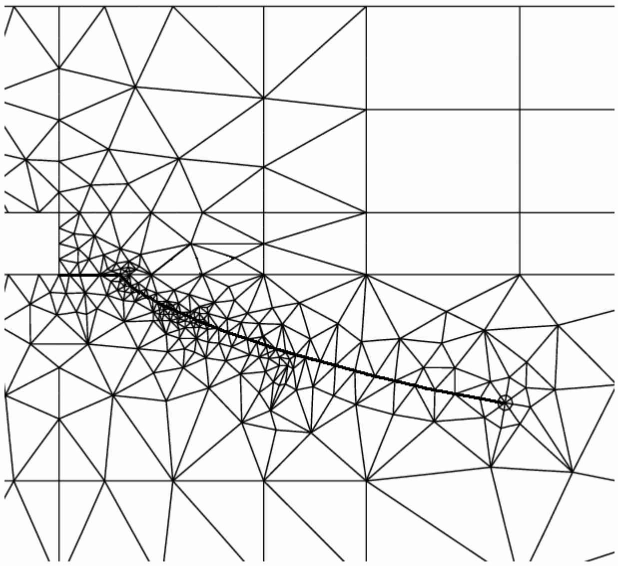

Figure 6: Initial crack path trajectory.

Regarding the sub-interfacial crack propagation into the core we observe that the crack becomes parallel to the interface at a constant depth h_∞. An explanation of the constant value of h_∞ and the linear variation of stress intensity factors with the distance from the crack tip x can be obtained by noting that the debonded part of the specimen (above the crack) can be considered as a thin cantilever beam ($l/d \sim 25$), elastically supported by the foam core, and subjected to a dominant bending moment varying linearly with x and to a relatively small (constant) shear force. Thus, the near-tip stress field is linearly proportional to x and, hence, the crack propagates in a self-similar manner parallel to the interface. The strain energy release rate can be determined by differentiating the work of the applied load with respect to the distance from the crack tip and is constant during crack propagation.

The core stiffness appears to be the main factor that influences the value of the asymptotic depth h_∞. Indeed, it can be obtained from Table 2 that the product $\overline{E}h_\infty$ is almost constant and equal to *60 N/mm* for the three PVC foam materials H60, H80 and H250. For H100 it takes the value *70 N/mm*. Thus, the depth h_∞ is inversely proportional to the modulus of elasticity of the core material.

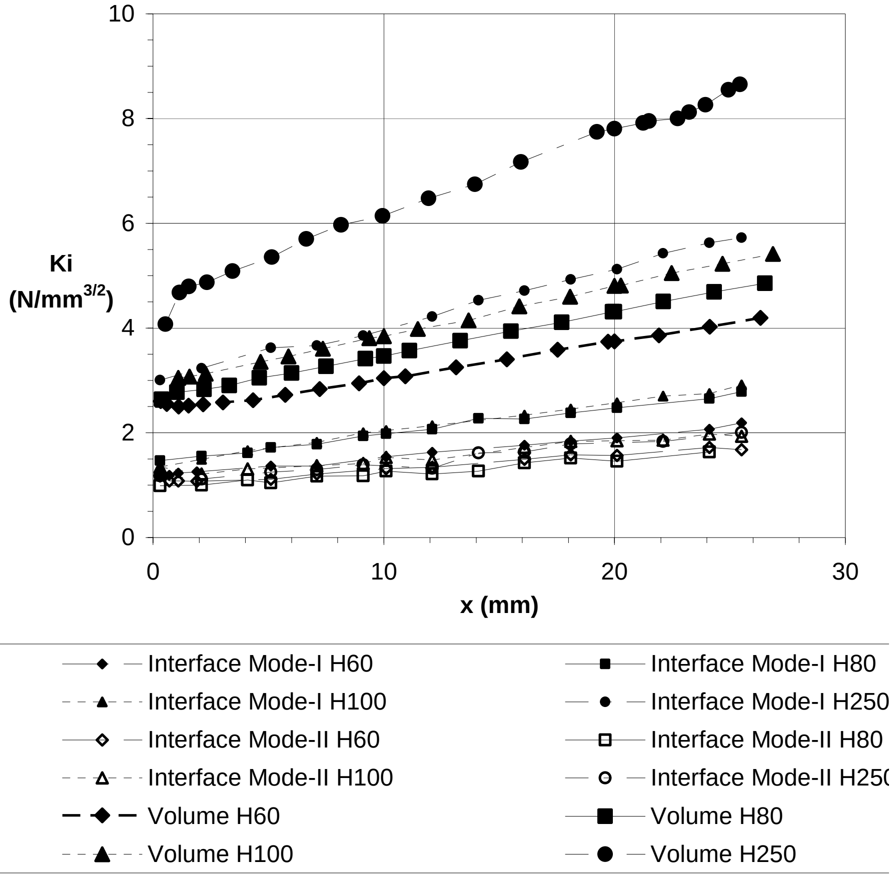

Figure 7: Dependence of the SIFs on the distance from the crack tip.

Table 2. Values of critical distance h_∞ and strain energy release rates.

	$\overline{E}$ (GPa)	h_∞ (mm)	$\overline{E}h_\infty$ (N/mm)	$G_{\text{core}}(x) \simeq \zeta_0 + \zeta_1 x + \zeta_2 x^2$			$\left.\frac{G_{\text{core}}}{G_{\text{int}}}\right\rvert_{3\text{mm}}$	$\left.\frac{G_{\text{core}}}{G_{\text{int}}}\right\rvert_{30\text{mm}}$
				$\zeta_0 * 10^2$	$\zeta_1 * 10^3$	$\zeta_2 * 10^5$		
H 60	0.059	1.01	59.6	9.4	5.4	7.7	2.3	2.3
H 80	0.087	0.70	60.9	8.0	5.1	8.1	2.3	2.3
H 100	0.107	0.65	69.6	8.0	5.1	8.1	2.5	2.4
H 250	0.308	0.20	61.6	6.7	4.8	8.7	2.0	2.0

5. CONCLUSIONS

An investigation of the debonding of the facing from the core in sandwich structures with relatively soft brittle core materials (PVC foams) and stiff facings (aluminum) under a concentrated load pertaining to the standard “peel test” (ASTM D5528-94a) was undertaken. Under such conditions and for a critical applied load, debonding propagates along the interface only when the adhesion between the interface and the core is weak. Otherwise, the crack kinks into the core and after a small initial curved path it propagates parallel to the interface at a depth h_∞. The value of h_∞ is inversely proportional to the modulus of elasticity of the core. This behavior is independent of the core thickness, which is an order of magnitude larger than the thickness of the facing and the adhesive. Away from boundary effects (e.g., concentrated loads, beam supports, crack kinking, etc.) both stress intensity factors and strain energy release rate can be approximated as linear functions of the crack length.

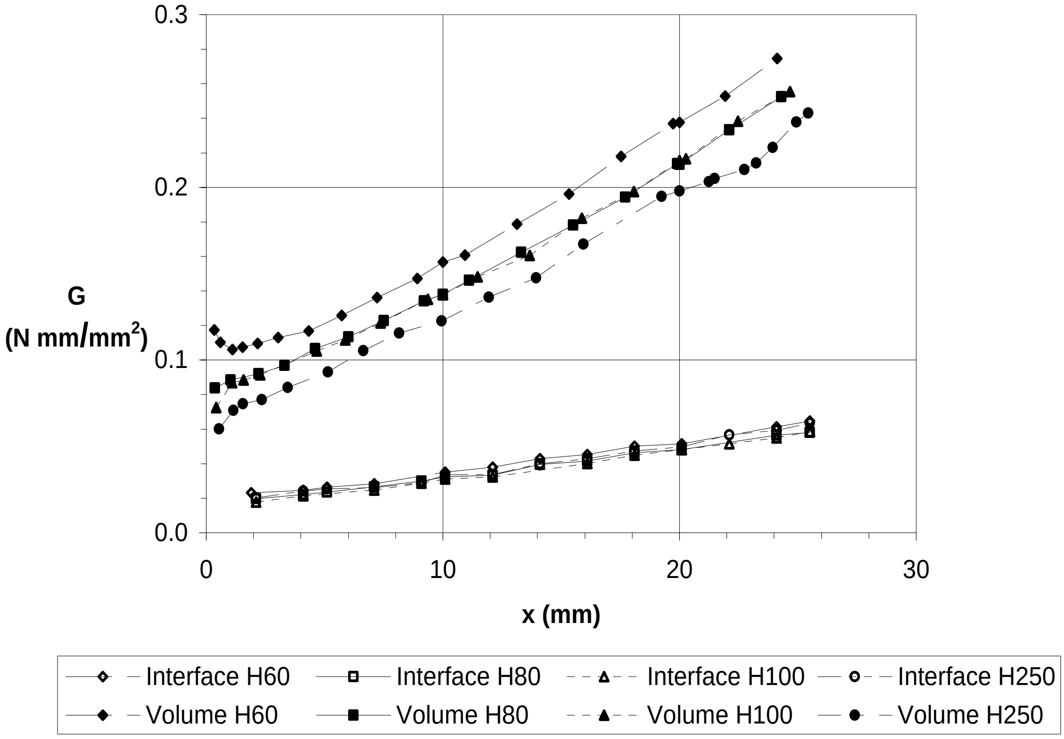

Figure 8: Dependence of the energy release rates on the distance x from the crack tip.

REFERENTES

1. E.E. Gdoutos, I.M. Daniel, and K.-A. Wang, "Indentation failure in composite sandwich structures," *Exp. Mech.*, 42, 426-431, 2002.
2. I.M. Daniel, E.E. Gdoutos and K.-A. Wang, "Failure of composite sandwich beams," *Adv. Comp. Letters*, 11, 49-57, 2002.

3. I.M. Daniel, E.E. Gdoutos, K.-A. Wang and J.L. Abot, "Failure modes of composite sandwich beams," *Int. J. Damage Mech.*, 11, 309-334, 2002.
4. J.L. Abot, I.M. Daniel, and E.E. Gdoutos, "Failure mechanisms of composite sandwich beams under impact loading," *Proc. 14th Europ. Conf. Fract.,* Cracow, September 8-13, 2002, edited by A. Neimitz et al, Vol. I, 13-19, 2002.
5. E.E. Gdoutos, I.M. Daniel and K.-A. Wang, "Compression facing wrinkling of composite sandwich structures," *Mech. Mater.*, 35, 511-522, 2003.
6. E.E. Gdoutos, *"Fracture Mechanics Criteria and Applications,"* Kluwer Academic Publishers, (1990).
7. E.E. Gdoutos, *"Fracture Mechanics – An Introduction,"* Second Ed., Springer, (2005).
8. D. Zenkert, "Strength of sandwich structures with interface debondings," *Compos. Struct.,* 17, 331-350, 1991.
9. L.A. Carlsson and S. Prasad, "Interfacial fracture of sandwich beams," *Engng Fract. Mech.*, 44, 581–590 (1993).
10. S. Prasad and L.A. Carlsson, "Debonding and crack kinking in foam core sandwich beams ─ I. Analysis of fracture specimens," *Engng Fract. Mech.*, 47, 813–824 (1994).
11. S. Prasad and L.A. Carlsson, "Debonding and crack kinking in foam core sandwich beams ─ II. Experimental investigation," *Engng Fract. Mech.*, 47, 825–841, (1994).
12. J. Ratcliffe and W.J. Cantwell, "Center notch flexure sandwich geometry for characterizing skin-core adhesion in thin-skinned sandwich structures," *J. Reinf. Plast. Comp.*, 20, 945-970, 2001.
13. R.C. Østergaard, B.F. Sørensen and P. Brøndsted, "Measurement of interface fracture toughness of sandwich structures under mixed mode loadings," *J. Sand. Struct. Mat.*, 9, 445-466, 2007.
14. C. Berggreen, B.C. Simonsen and K.K. Borum, "Experimental and numerical study of interface crack propagation in foam-cored sandwich beams," *J. Comp. Mater.,* 41, 493-520, 2007.
15. D.L. Grau, X.S. Qiu and B.V. Sankar, "Relation between interfacial fracture toughness and mode-mixity in honeycomb core sandwich composites," *J. Sand. Struct. Mat.*, 8, 187-203, 2006.
16. F. Erdogan and G.C. Sih, "On the crack extension in plates under plane loading and transverse shear," *J. Bas. Engng,* 85, 519–527 (1963).
17. J.W. Hutchinson, M.E. Mear, and J.R. Rice, "Crack paralleling an interface between dissimilar materials," *J. Appl. Mech.*, 54, 828–832 (1987).
18. J.R. Rice, "Elastic fracture mechanics concepts for interface cracks," *J. Appl. Mech.*, 55, 98–103 (1988).
19. M.-Y. He and J.W. Hutchinson, "Kinking of a crack out of an interface," *J. Appl. Mech.*, 56, 270–278 (1989).

20. D.A. Zacharopoulos, E.E. Gdoutos and A. Bekiaris, "Crack kinking along a bimaterial interface," in *Procs 1st Hellenic Conf. Composite Mater. & Struct.,* Xanthi, Greece, I, 192-207 (1997).
21. J. Dundurs, "Edge-bonded dissimilar orthogonal elastic wedges under normal and shear loading," *J. Appl. Mech*., 3, 650–652 (1969).
22. Arardite Technical manual for "Adhesive AV 138M with Hardener HV 998"
23. DIAB International AB, Divinycell Grade H Technical Manual, (2003).
24. ASTM Standard D5528-94a. "Standard test method for mode-I interlaminar fracture toughness of unidirectional fiber-reinforced polymer matrix composites," *ASTM Annual Book of ASTM Standard* 15.03, 283–292, American Society for Testing and Materials (1999).
25. A. Ingraffea, and P. Wawrzynek, User's guide for FRANC2D Version 3.1, www.cfg.cornell.edu (1993).
26. K. Weiler, "Edge-based data structures for solid modeling curved-surface environments," *IEEE Comp. Graph. & App.,* 5, 21–40 (1985).
27. K. Shivakumar, H. Chen, and A.S. Smith, "An evaluation of data reduction methods for opening mode fracture toughness of sandwich panels," *J. Sandwich Struct. & Mater.,* 7, 77–90 (2005).

8th International Conference on Sandwich Structures
ICCS 8
A. J. M. Ferreira (Editor)

For ONR sessions organized by Yapa Rajapakse

EVALUATION OF THE STRESSES AT CORE JUNCTIONS IN SANDWICH STRUCTURE USING THERMOELASTIC STRESS ANALYSIS

M. Johannes*, J. M. Dulieu-Barton† E. Bozhevolnaya*, O.T. Thomsen*

*Department of Mechanical Engineering, Aalborg University
Pontoppidanstræde 101, 9220 Aalborg East, Denmark

†School of Engineering Sciences, University of Southampton, UK
e-mail: janice@soton.ac.uk

Key words: Sandwich structures, Core junctions, Local effects, Thermoelastic stress analysis (TSA).

Summary: *Local effects at core junctions in sandwich structure are assessed experimentally using thermoelastic stress analysis. It is shown that non-adiabatic effects have significant effects on the thermoelastic response from thin aluminium face sheets. It is demonstrated that an experimental model can be constructed that eliminates the non-adiabatic behaviour. It is shown that TSA can obtain accurate data from a sandwich beam loaded in transverse shear via three point bending.*

1 INTRODUCTION

Sandwich structures are designed so that the face sheets are loaded in a membrane stress state and the core carries the shear stresses. Difficulties arise when local effects disturb the uniform distribution of stresses. The local effects occur because of discontinuities in the structure such as changes of geometry or material properties, or when localised external loads are applied. It is well-known that in the vicinity of sandwich sub-structures, e.g. joints, stiffeners or inserts, stress concentrations are present. These may initiate local failure processes which lead to global failure of the whole structure [1]. In this paper the substructure is represented simply by junctions of cores with different stiffness. Here the local effects are caused by the mismatch of the elastic properties of the adjoining materials at the core junctions; local bending of the face sheets is induced, along with local tension or compression of the adjacent cores. Depending on the loading this is accompanied by an increase of the in-plane stresses in the sandwich faces sheets and a variation of the shear and through the thickness stresses in the adjacent cores. The effect of such a discontinuity on the stress distribution has been the object of previous research [2-4], and analytical and numerical models are available for the linear elastic range. The present paper investigates discontinuities in aluminium and glass-fibre reinforced polymer (GFRP) face sheet foam core sandwich construction using a full-field non-contact experimental analysis technique known as thermoelastic stress analysis (TSA) [5]. The paper focuses on the stresses developed in the face sheets when the sandwich structure is subjected to a transverse shear loading.

A detailed description of TSA and its application is provided in the following section of the paper. TSA was chosen primarily for this work as it can provide high resolution stress data directly from the component under investigation. The technique employs a sensitive infra-red photon detector that can measure the small temperature change induced by an elastic stress change in the structure. High resolution data collection is particularly important in this application, as the discontinuity in the core material causes sharp changes in the stresses in the face sheets, which are localised over a small area close to the core junction. Furthermore with TSA there is no need to attach sensors or apply coatings which may modify the behaviour of the sandwich material. Previous work [6] has shown that TSA was unable to detect with any accuracy the stress change that occurred in an aluminium alloy face sheet in the neighbourhood of a core junction. In developing the theory for TSA it is assumed that the small temperature change occurs adiabatically. This assumption breaks down in materials with relatively high thermal conductivity, particularly in areas of high stress gradient such as in the vicinity of the core junctions in the aluminium alloy face sheets. As TSA is a useful tool it was decided that an experimental model should be constructed that eliminates the non-adiabatic behaviour. The design of the experimental model and the considerations that were required to accurately model the aluminium alloy structure are described and validated using FEA. The calibration techniques for the face sheet materials that facilitate quantitative TSA are provided along with a description of the experimental arrangements to obtain the TSA from the face sheets. The results show that it is possible to accurately model the structure, and that TSA can be used to accurately determine the stresses induced in the neighbourhood of core junctions.

2 THERMOELASTIC STRESS ANALYSIS -THEORY

Thermoelastic Stress Analysis (TSA) is a well established technique for the evaluation of stresses in engineering components. Most quantitative studies have concentrated on isotropic materials and the underlying theory has been reviewed and discussed in many reference sources. Essentially an infra-red detector is used to measure the small temperature change associated with the thermoelastic effect and is related to the changes in the sum of the principal stresses on the surface of the material, $\Delta(\sigma_1 + \sigma_2)$, as follows:

$$\Delta T = -\frac{\alpha T_0}{\rho C_p}\Delta(\sigma_1 + \sigma_2) \tag{1}$$

where α is the coefficient of linear thermal expansion, T_0 is the absolute temperature, ρ is the density, C_p is the specific heat at constant pressure and the subscripts 1 and 2 denote the *directions of the principal stresses*.

The quantity $\alpha/\rho C_p$ given in equation (1) is known as the thermoelastic constant. The output from the detector is termed the 'thermoelastic signal', S, and is related to the changes in the sum of the principal stresses on the surface of the material using the following expression:

$$\Delta(\sigma_1 + \sigma_2) = AS \tag{2}$$

where A is a calibration constant dependent on the thermoelastic constant of the material.

Equation (2) is valid for any linear elastic, isotropic, homogeneous material, assuming that the thermoelastic temperature change takes place under adiabatic conditions, which are achieved by the application of a cyclic load. Techniques for obtaining the calibration constant for isotropic materials are well established; some common approaches have been described and assessed in [7]. These involve either measuring the surface strains and relating them to the stresses or using a calibration test specimen with a known stress field. The simple thermoelastic theory devised for an isotropic body is not valid for orthotropic composite materials when the following equation is used [8]:

$$(\alpha_1 \Delta\sigma_1 + \alpha_2 \Delta\sigma_2) = A^* S \tag{3}$$

where A^* is a further calibration constant and here the subscripts 1 and 2 denote the *principal material directions* of the surface lamina.

In practice, heat diffusion will occur and limit the validity of the assumption of adiabatic conditions, particularly in components with regions containing high stress gradients, such as those found local to the core junctions. The likelihood of non-adiabatic behaviour is increased in materials with a high thermal conductivity, e.g. metallic materials. To examine the effect of heat conduction in TSA a generalised form of the heat conduction equation can be used. This can be written in terms of the first stress invariant, σ_I, for an isotropic material as follows [9]:

$$\frac{\partial T}{\partial t} = -\frac{1}{\rho C_p}\left[\alpha T_0 \frac{\partial \sigma_I}{\partial t} + k\nabla^2 T\right] \tag{4}$$

where k is the thermal conductivity, and T is the absolute temperature at a point in time, t.

Equation (4) is a function of the material properties and the cyclic loading frequency (i.e. time). The first term in the bracket on the right side of equation (4) corresponds to the locally generated heat due to the temporal change of stress. The second term is the local heat conduction due to a spatial change in temperature resulting from a stress gradient in the component. Clearly in situations where the thermal conductivity is zero or there is no temperature (stress) gradient, adiabatic conditions can be achieved. In other cases if the cyclic loading frequency is such that the first term is large in comparison with the second then practically adiabatic behaviour can be obtained. In this case equation (4) can be integrated over the period of the stress change to give the relationship in equation (1). However, in studies where $\nabla^2 T$ and/or k are significant, adiabatic conditions may not be achieved at practical loading frequencies. From some simple calculations based on heat conduction alone it was concluded that to achieve adiabatic behaviour in specimens with aluminium face sheets the loading frequency would have to be set to such a high level that would not be achievable in practice with a standard servo-hydraulic test machine. Therefore it was considered necessary to construct an experimental model made from low conductivity polymers to enable the application of TSA to sandwich structures with high conductivity face sheets.

Most of the previously reported TSA work used either the SPATE or the Deltatherm systems. In the current work a Silver 480M system, fitted with a 27 mm lens, manufactured by Cedip Infrared Systems, is used. This system contains two overlaid 320 x 256 detector element indium antimonide (InSb) infra-red detector arrays and two corresponding sets of internal buffers that enable sequential data storage; the arrays are used alternately, one capturing data while the other transfers data to its internal buffer. The maximum frame rate is 383 Hz, which is dictated by the data transfer and processing chain. Each detector element voltage output is digitised independently by a designated processor housed in the camera unit and then sent to the computer as a digital signal and output in units of 'digital level' (DL). The routine used by the Cedip system for processing the DL thermal data into *S*, the thermoelastic signal (see equations (2) and (3)), uses a reference signal from the load cell of the test machine and a fast Fourier transform to obtain the magnitude and phase angle of the DL output of each detector element with respect to the reference signal. Regions of tension or compression can be identified from the phase data by comparing the phase of a region of interest with that of a region of known tension or compression. To manipulate the raw data into stress data where positive and negative regions are identified, the data were exported and processed independently using Matlab.

3 EXPERIMENTAL MODEL

In the experimental work four types of sandwich specimens are studied. These types are identified by the face sheet materials as follows: (1) aluminium alloy, (2) PMMA, (3) GFRP-CSM (chopped strand mat), (4) GRFP-NCF (non-crimp fabric in quasi isotropic configuration). All four types have various configurations of core materials consisting of aluminium alloy, PMMA, two densities of polymer foam and polyurethane rubber foam. The type 2 and type 3 specimens are used primarily to model the type 1, and type 4 is used to provide realistic examples with GRFP face sheets. The specimens contained five core sections arranged in a symmetric manner, as shown in Figure 1. Two different core junctions are formed between the core sections. For specimen types 1 and 4 the length of core 1 was 90 mm, for specimen types 2 and 3 it was 100 mm. The face thickness, t_f, varied depending on the face sheet material; the thickness of the core, t_c, was 25 mm for all sandwich types.

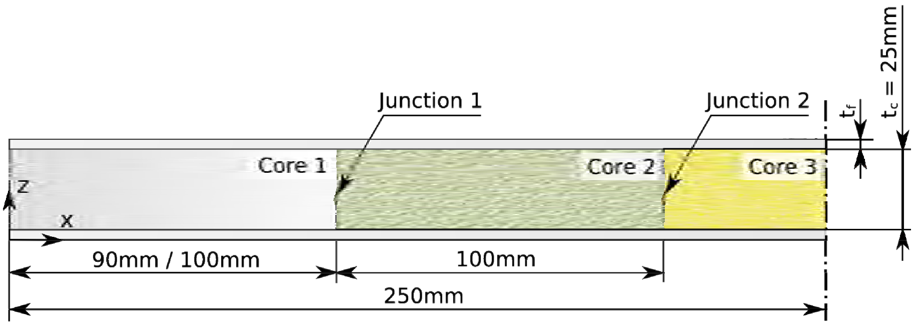

Figure 1: Schematic of a sandwich beam specimen
(specimen is symmetrical about centre line so only half is shown)

To develop an effective experimental model for the sandwich type 1 with aluminium face sheets, it is essential that the material modular ratios between the core materials and the face sheets are of the order of those of the original structure, as these determine the extent of the local effects [2-4]. Therefore a variety of materials were considered to produce the model. The candidate sandwich constituent materials and their properties are listed in Table 1. GFRP-CSM denotes glass-fibre reinforced plastic comprising an epoxy resin reinforced with chopped strand mat; GRFP-NCF also comprises an epoxy resin but is reinforced with a non-crimp fabric in quasi isotropic configuration as indicated in Table 1. The Rohacell 51WF and 200WF are PMI polymer foams of different densities and hence different mechanical properties, the Dynathane material is a very compliant closed cell PU rubber foam. As accurate Young's modulus values are essential for developing the experimental model they were measured in tensile tests using a long gauge extensometer according to ISO 527. A summary of the materials used to produce the four specimen types is given in Table 2.

Material	Young's modulus [MPa]	Poisson's ratio
Aluminium alloy 7075-T6	71700	0.32
PMMA (Degussa Plexiglas XT)	3100	0.41
GFRP-CSM	13000	0.30
GFRP-NCF, $[0/+45/90/-45\ /\ +45/90/-45/0]_2$	19200	0.29
Rohacell 51WF	75 [10]	0.32 [11]
Rohacell 200WF	350 [10]	0.38 [11]
Dynathane 1000 (PU rubber foam)	5.5	0.22

Table 1: Material properties of the sandwich constituents

Type	Face Material	t_f [mm]	width [mm]	Core Material 1	Core Material 2	Core Material 3
1	Aluminium alloy	1.0	45.6	Aluminium alloy	Rohacell 51WF	Rohacell 200WF
2	PMMA	1.5	47.2	PMMA	Dynathane 1000	Rohacell 51WF
3	GFRP-CSM	1.2	46.8	PMMA	Dynathane 1000	Rohacell 51WF
4	GFRP-NCF	2.8	49.0	Aluminium alloy	Rohacell 51WF	Rohacell 200WF

Table 2: Specimen configurations

To produce an experimental model of the sandwich specimen with aluminium face sheets, PMMA was used to model the face sheets, as PMMA has a low thermal conductivity. The PMMA also has a smooth surface and a relatively high thermoelastic constant, so it will provide a high and relatively noise free thermoelastic signal. Moreover PMMA is readily available and easy to machine to the desired shape. In combination with solid PMMA for core 1, PU rubber foam for core 2 and Rohacell 51WF foam for core 3 this yields a model specimen with stiffness ratios as given in Table 3. E_{face}/E_{core1} is identical and a trivial matter to achieve. However identifying materials for core 2 and core 3 that give the exact modular ratios between the face sheet and the core is not straightforward. To achieve a modular ratio of 956 between the face sheet and core 2 a material with a Young's modulus of 3.24 MPa would be required. Such materials exist but were not readily available in the form necessary to produce the sandwich core. Also at these low modulus values material properties cannot be guaranteed and it was considered that the Dynathane 1000 with a modulus of 5.5 MPa was a good compromise. Similar consideration was given to the modular ratio between the core 3 and the face sheet. Here it was decided to use Rohacell 51WF which gave an E_{face}/E_{core3} ratio of 41 as compared to a required value of 205. To achieve the correct modular ratio, a Young's modulus of 15.1 MPa would be required and there was not a material available in an appropriate form with this modulus; in fact the Rohacell 51WF was the material with the lowest modulus in the appropriate form. These compromises also produce similar mismatch in the modular ratios of the core materials.

Type	E_{face}/E_{core1}	E_{face}/E_{core2}	E_{face}/E_{core3}	E_{core1}/E_{core2}	E_{core3}/E_{core2}
1	1	956	205	956	4.7
2	1	564	41	564	14
3	4.2	2364	173	564	14
4	0.3	256	55	956	4.7

Table 3: Modular ratios of face sheet and core materials

To assess the influence of the face sheet surface structure on the TSA signal quality and the achievable spatial resolution, specimens using GFRP-CSM and GFRP-NCF face sheets were designed. As with the PMMA face sheet material non-adiabatic behaviour will not have a significant effect in the sandwich structures with GFRP face sheets. Specimen type 3 represents a second model and permits a comparison with types 1 and 2 with respect to the thermoelastic signal from different materials and surfaces. In this case making core 1 from the same material as the face sheets was not considered, as controlling the resin cure and achieving sufficient infiltration of a thick laminate to produce identical material properties to that of a thin laminate during an infusion process is not viable. Therefore it was decided to use the PMMA as core 1. The Dynathane was chosen as the core 2 material to produce an E_{face}/E_{core2} that was 40% greater than that required compared to 40% less in specimen type 2. For this specimen type the use of Rohacell 51WF as the core 3 material produced an E_{face}/E_{core3} much closer to that of specimen type 1a than that of specimen type 2. Type 4 was chosen to model stiffness ratios resembling those of commonly used sandwich structures where a stiffer core section or insert is used for a local increase of stiffness and strength, e.g. in order to introduce a load. Following the discussions in the previous section, non-adiabatic behaviour will not have a significant effect in the sandwich structures with GFRP face sheets; here it is the peculiarities of the non-homogenous surface of the composite face sheet that is of interest.

Two techniques were employed to manufacture the sandwich specimens. For type 1 and 2, aluminium or PMMA strips, respectively, were bonded to previously manufactured core layers consisting of the three core materials as described in Table 2. For all bonds, an Araldite® 2011 epoxy adhesive was used. To bond the face sheet strips to the core layer, the specimens were stacked and a uniform pressure applied to all specimens simultaneously. After curing of the resin, the specimens were brought to their final shape by machining them along the edges to their final width, which is provided in Table 2. The type 3 and 4 specimens were produced by liquid resin vacuum infusion. The lay-up of the face sheets in type 3 consisted of 3 layers of chopped strand mat with an areal weight of 300 g/m^2. Additionally, four extra layers of a very fine chopped strand mat with an areal weight of 30 g/m^2 were used on top to create a smoother surface. The lay-up of the face sheets in type 4 consisted of 4 layers of a quadric-directional quasi-isotropic stitched non-crimp fabric with an areal weight of 850 g/m^2. A previously manufactured core plate was placed on the lay-up of the lower face, and the lay-up of the upper face was placed on top of the core layer. The core plate consisted of the three core materials stated in Table 2. The whole lay-up was bagged and by a one-step vacuum infusion process a sandwich plate was produced, from which sandwich specimens were cut and then machined to their final width as given in Table 2.

4 LOADING ARRANGEMENTS

A transverse shear loading was realised using a three point bending jig as shown in Figure 2. The specimens were simply positioned on rollers and a central load applied *via* a third roller. In this configuration, with the test rig mounted on the bed of an Instron 8800 series servo-hydraulic test machine equipped with a 10 kN load cell it was impossible to view the face sheet directly with the infra-red detector as there was simply insufficient space. Therefore it was necessary to employ a mirror tilted at 45^o to the face sheet and mounted on the test machine bed as shown in Figure 2. This set-up permitted observation of the lower face sheet. Any signal attenuation as a result of using the mirror was accounted for by including the mirror in the calibration procedure (see below) and was minimised by using a front coated mirror.

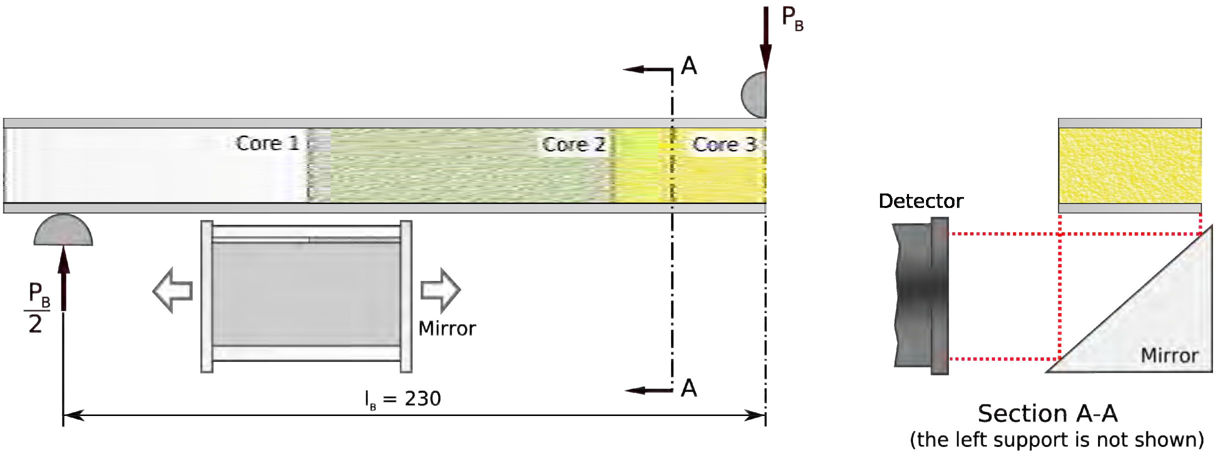

Figure 2: Test set-up for the TSA of the transverse shear loading

5 VERIFICATION OF EXPERIMENTAL MODEL

Prior to manufacturing the test specimens, FEA was used to reassure that the chosen sandwich configurations given in Table 2 were suitable experimental models. The basis of the assessment was that the sandwich model configurations 2 and 3 produce a local stress magnitude and spatial extension, which is similar to that with the aluminium face sheets. An idealised two dimensional finite element model of a sandwich beam with core junctions was used to calculate the global and local stresses numerically. The FEA was carried out using ANSYS. The FEA model has been used in previous studies [6] and proven to provide accurate results for the face sheet deformations, validated with strain gauge measurements [3]. The material properties used in the FEA are given in Table 1. All materials were assumed to be isotropic and linear elastic. The isotropic assumption of is fully valid for the aluminium and the PMMA and approximately valid for the polymer foams. It is a simplification for the GFRP face sheets, but considered as reasonable with respect to the nominal membrane stress state in the sandwich face sheets and the quasi-isotropic lay-up of the composite. The finite element calculations were based on the assumption of plane stress. A comparison of the FEA data from the face sheet surface and the interface between the face sheet and the core at the core junctions for sandwich types 1, 2 and 3 is given in Figure 3. Here the stress in the ‘x-direction’ is plotted, which is along the length of the specimen with the origin at the left end as shown in Figure 1. It can be seen that the magnitude and spatial extension of the local effects of the model specimens are very similar to those of type 1. Specimen type 2 gives practically identical stresses to type 1. This shows that the specimen 2 makes a reasonable experimental model for specimen type 1. Specimen 3 does not provide a good model but will be studied experimentally to assess the effect of surface finish on the TSA data.

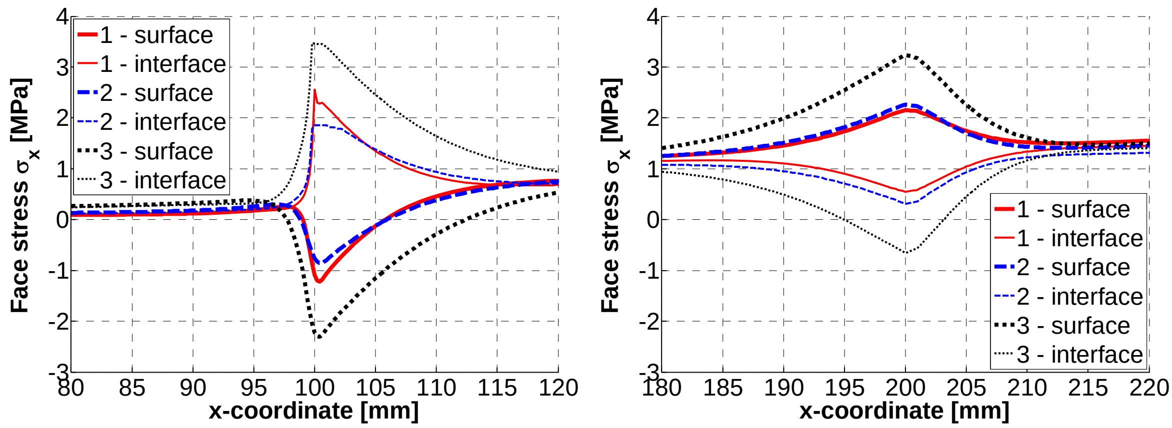

Figure 3: FEA of sandwich specimen; left: junction 1; right: junction 2

6 THERMOELASTIC CALIBRATION OF FACE SHEET MATERIALS

To convert the thermoelastic signal, S, into stress data it is necessary to define the calibration constants A and A^*, as given in equations (2) and (3). The standard procedure is to determine A and A^* experimentally. Therefore a set of calibration test specimens was used for obtaining the calibration constant of each of the face sheet materials in the form of rectangular plane coupons of 500 mm long x 30 mm wide and of the same thickness as the face sheets. The coupons were then gripped directly in the jaws of an Instron 8800 servo-hydraulic test machine and subjected to a cyclic tension-tension loading. In this loading mode σ_2 is eliminated in the face sheet materials for specimen types 1, 2 and 3, as these materials are isotropic. In specimen type 4 with the NCF face sheet with quasi-isotropic lay-up, where equation (3) applies, there is the possibility that σ_2 (the stress in the surface ply transverse to the 0° fibre orientation) is finite. It is considered that the Poisson’s ratio effects will be small because of the quasi-isotropic lay-up and it is reasonable to assume that the second bracketed term in equation (3) can be neglected. Therefore it is possible to determine the quantity $A^*/\alpha_1=A^{**}$ experimentally, and to use this as a calibration constant. To assess the effect of using the mirror in the experimental set up the calibration constants were derived with and without the mirror.

Table 4 gives the mean stress, stress range and loading frequencies used in the calibration tests. Two specimens of each set were used for the calibration and the different mean stresses, stress ranges and loading frequencies were used to obtain a calibration constant value. In Table 4 A and A_M denote the calibration constant without and with the mirror, respectively. The values of A, A^{**}, A_M and A_M^{**} were obtained by taking the area mean of the thermoelastic signal in each data set. The derived calibration constants showed no dependence on the mean stress, stress amplitude or frequency within the range of parameters given in Table 4. Therefore a mean of the values derived from each test was obtained to give the A, A^{**}, A_M and A_M^{**} given in Table 4. The associated coefficients of variation are given in brackets in the table and show that the maximum variation was given by the NCF material. It should be noted, though, that as each value for the calibration constant is a mean of all the calibration tests carried out (either with or without the mirror) for that particular material, any scatter resulting from a non-homogeneous surface will not be reflected in the coefficients of variation given in Table 4. It should also be noted that the stresses for the GFRP are the overall average stresses in the specimen and not the surface layer stress; this complies with the FEA, as the face sheets were modelled as a homogeneous material. The use of the mirror has little effect on the calibration, although remarkably in one case it provides a lower calibration constant than direct viewing; this could be attributed to small variations in the specimen and mirror temperature. This was not regarded as an important influencing factor so the A_M and A_M^{**} values were used to calibrate the data obtained from the test on the sandwich structure described in the next section.

Material	Mean stress [MPa]	Stress range [MPa]	Frequency [Hz]	A, A^{*} [MPa/DL]	A_M, A_M^{**} [MPa/DL]
Aluminium alloy	20.0, 40.0	10.0, 20.0	10, 30, 50	6.06 (5.3%)	6.45 (2.5%)
PMMA	5.4, 10.8	3.2, 6.4	6, 10	1.31 (6.1%)	1.33 (3.8%)
GFRP-NCF	10.0, 20.0	5.0, 10.0	6, 10	5.63 (11.2%)	5.35 (9.9%)
GFRP-CSM	10.0, 20.0	5.0, 10.0	6, 10	3.74 (3.7%)	3.87 (6.7%)

Table 4: Calibration constants

7 THERMOELASTIC STRESS ANALYSIS-RESULTS

In this section of the work the TSA data collected using the set-up shown in Figure 2 is compared with FEA data produced in the same manner as that described in section 5. In comparing the FEA results with the TSA, the normal stress in the x-direction, σ_x, on the surface of the face sheets obtained from the FEA is practically identical to the first stress invariant, i.e. $(\sigma_1 + \sigma_2) = (\sigma_x + \sigma_y)$ obtained from the TSA, where σ_1, σ_2 are the principal stresses on the surface. This is because a plane stress state exists on the surface and the out-of-plane normal stress component, σ_z, is zero. In the 2D model the y-direction normal stress, σ_y, is zero. In the experimental work this may be non-zero, but can be assumed to be negligible, apart from some minor Poisson's ratio effects which are not taken into account in the FEA. Therefore the FEA results for σ_x are in a form practical for comparison to the TSA results.

The type 1 specimens were loaded at a level of 200±100 N with frequencies of 10, 40 and 60 Hz. Specimen type 2 was loaded at a level of 40±25 N with a frequency of 6 Hz, specimen type 3 was loaded at a level of 50±25 N with a frequency of 10 Hz, and specimen type 4 was loaded at a level of 200±150 N with a frequency of 10 Hz. Full-field thermoelastic data were obtained using the Silver 480M system using a frame rate of 269 Hz with each data set containing 1000 frames, which corresponds to a recording time of about 3.7s. As the camera had to be moved to collect data sets from the vicinity of each core junction, marks on the specimen provided points of reference to create scaling vectors that allowed the two data sets to be joined accurately. The full-field data were interrogated to provide line plots along the x-axes of the specimen. To reduce noise an averaging procedure was developed so that the data from the entire evaluation area shown could be used. As the data across the width of the specimen is uniform, individual pixel data were averaged and these average values plotted to give a single averaged value at each x position in the evaluation area. After this the calibration constants derived in the previous section were applied as appropriate to the data. Figure 4 shows the TSA line data from the face sheets through the two core junctions along with the results from the FEA.

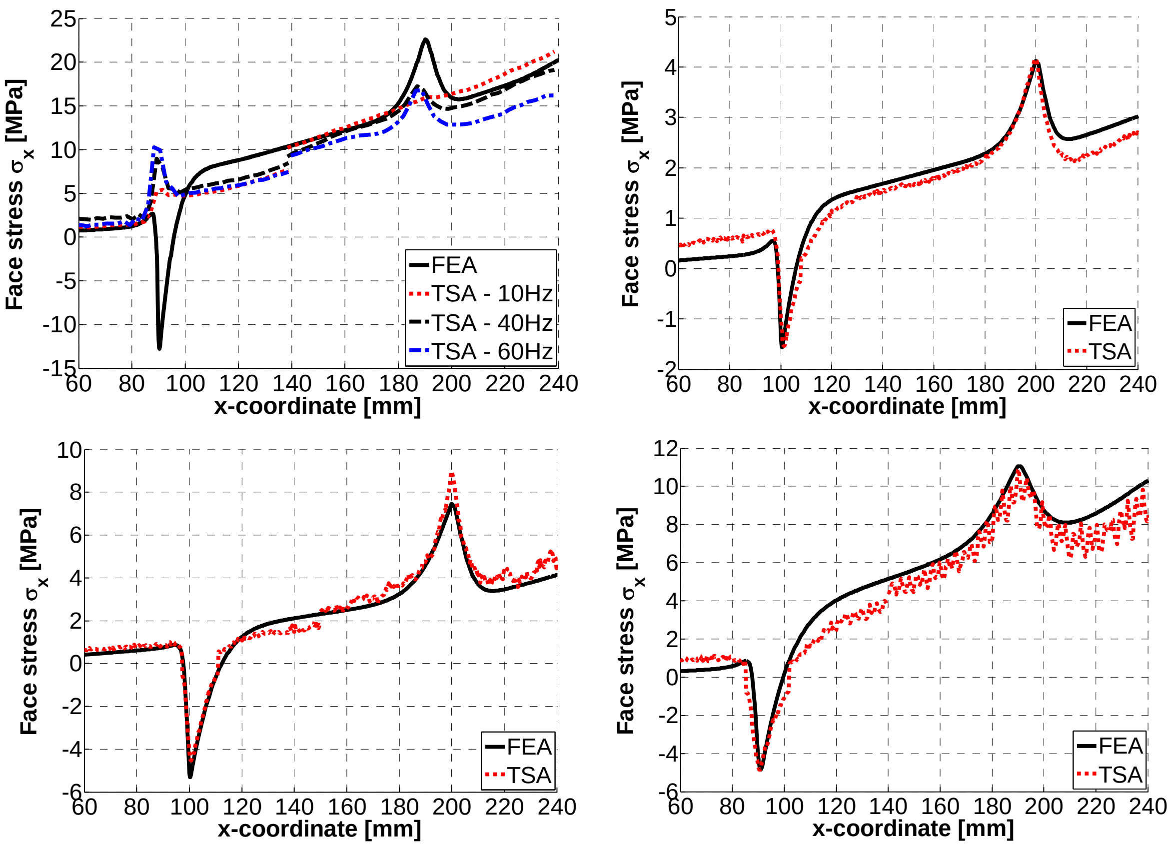

Figure 4: TSA and FEA results obtained for the 4 specimen types;
top left: type 1; top right: type 2; bottom left: type 3; bottom right: type 4

For the type 1 specimen with the aluminium face sheets Figure 4 shows that the TSA and the FEA show reasonably good correspondence in the areas away from the discontinuities. However, the local effects predicted by the FEA for the face surface are not captured by the TSA. There is a peak in the stresses from TSA at both junctions, but the shape of the stress variation does not match the FEA and there is a difference in magnitude. A comparison of Figure 4 and with Figure 3 shows that the TSA data rather follow the FEA data from the face/core interface. The effect is apparent at the three loading frequencies but is changing. This is a clear sign that adiabatic conditions have not been achieved. Moreover the corresponding phase data showed a non-uniform profile also indicating that adiabatic conditions had not been achieved and hence justifying the requirement for an experimental model. For specimen type 2 with the PMMA face sheet the TSA data show excellent agreement with the FEA data. The peak stresses at both the core junctions correspond exactly with the TSA. The distribution of the stresses is practically identical. However, the agreement on either side of the core junctions is not as exact. For the type 3 specimen the FEA and TSA are in practically perfect agreement. Here some influence of the inhomogeneous surface can be seen as noise in the data. However, for the transverse shear loading there is virtually no in-plane specimen movement, and any variations in the surface finish would have little effect. For the type 4 specimen with NCF face sheets the agreement between TSA and FEA is excellent, as with specimens 2 and 3. Here the scatter in the data is more than that for the specimen with the CSM face sheets, possibly caused by the undulating surface of the NCF, resulting from the stitching of the fabric layers.

8 CONCLUSIONS

The work in this paper has shown that TSA can be applied in a quantitative manner to sandwich structures. The purpose of the work was to examine the effect of discontinuities in the stress field using the technique in the sandwich face sheets at core junctions. The experimental work showed that non-adiabatic effects pose a major obstacle when examining the stress variations in thin metal sandwich face sheets (aluminium in particular) where large stress gradients are present. It was shown that non-adiabatic effects do not occur for materials of low thermal conductivity as for example plastics or glass fibre reinforced plastics. A model sandwich specimen with comparable stress concentrations using PMMA face sheets was used to demonstrate that high stress gradients can be detected using TSA. For a range of sandwich types with GFRP face sheets it was demonstrated that TSA can be used successfully to assess the stress field at core junctions.

ACKNOWLEDGEMENTS

The work presented was supported by the Innovation Consortium "Integrated Design and Processing of Lightweight Composite and Sandwich Structures" (abbreviated "KOMPOSAND") funded by the Danish Ministry of Science, Technology and Innovation and the industrial partners Composhield A/S, DIAB ApS (DIAB Group), Fiberline Composites A/S, LM Glasfiber A/S and Vestas Wind Systems A/S.

Moreover, the work was supported by the US Navy, Office of Naval Research (ONR), Grant/Award No. N000140710227: “Influence of Local Effects in Sandwich Structures under General Loading Conditions & Ballistic Impact on Advanced Composite and Sandwich Structures”. The ONR program manager was Dr. Yapa Rajapakse.

The polymer foam core materials used in the experimental work were provided by Röhm GmbH & Co. KG. The support received is gratefully acknowledged.

The experimental work presented herein was conducted during the period of a 6 month stay of the first author with the Fluid Structure Interactions Group at the School of Engineering Sciences, University of Southampton, UK. The kind hospitality of the School of Engineering Sciences and access to its experimental facilities is gratefully acknowledged.

REFERENCES

[1] Zenkert, D., *An Introduction to Sandwich Construction*, 1997 (EMAS, London).

[2] Bozhevolnaya, E., Thomsen, O.T., Kildegaard, A. and Skvortsov, V., Local effects across core junctions in sandwich panels, *Composites. Part B: Engineering*, 34, 509-517 (2003).

[3] Bozhevolnaya, E., Lyckegaard, A. and Thomsen, O.T., Localized effects across core junctions in sandwich beams subjected to in-plane and out-of-plane loading, *Applied Composite Materials*, 12, 135-147 (2005).

[4] Bozhevolnaya, E. and Lyckegaard, A., Local effects at core junctions of sandwich structures under different types of loads, *Journal of Composite Structures*, 73(1), 24-32 (2006).

[5] Dulieu-Barton, J. and Stanley, P., Development and applications of thermoelastic stress analysis, *Journal of Strain Analysis for Engineering Design*, 33, 93-104 (1998).

[6] Johannes, M., Dulieu-Barton, J.M., Bozhevolnaya, E. and Thomsen, O.T., Thermoelastic stress analysis of sandwich structures with core junctions, *Proceedings of 13th International Conference on Experimental Mechanics*, Alexandroupolis, Greece, 8pp on CD, (2007).

[7] Dulieu-Smith, J.M., Alternative calibration techniques for quantitative thermoelastic stress analysis, *Strain*, 1995, 31, 9-16 (1995).

[8] Stanley P. and Chan W.K., The application of thermoelastic stress analysis to composite materials, *Journal of Strain Analysis for Engineering Design*, 23, 137-142 (1988).

[9] Biot, M.A., Thermoelasticity and irreversible thermodynamics, *Journal of Applied Physics*, 27, 240-253 (1956).

[10] Degussa, Röhm GmbH & Co. KG, Rohacell Data CD, 2006.

[11] Personal communication with Degussa, Röhm GmbH & Co. KG, Germany.

8th International Conference on Sandwich Structures
ICSS 8
A. M. Ferreira (Editor)

AUXETIC PVC FOAM AS A CORE MATERIAL FOR SANDWICH PANELS

Fu-pen Chiang[1], Gunes Uzer[2]

[1] SUNY Distinguished Professor& Chair,
[2] Graduate Student
Dept. of Mechanical Engineering
Stony Brook University
Stony Brook, NY 11794-2300
Fu-Pen.Chiang@sunysb.edu

Key words: Auxetic Material, Speckle Photography, Full-field Measurement, Foam Composite

Summary. *An auxetic material has the unusual property of having a negative Poisson's ratio. Thus when loaded in uniaxial tension, it expands rather than shrinks laterally. Manmade auxetic material was first manufactured by Lakes in 1987. In this paper we present the process of converting an ordinary PVC foam into an auxetic foam. We then proceed to characterize the mechanical properties of the resulting material. Auxeticity can be one dimensional or multidimensional. And the degree of auxeticity is a function of the volumetric reduction from the original material. The larger the volumetric reduction, the larger the negative Poisson's ratio. Compared with the original foam, an auxetic foam will have a larger strain to failure but a smaller stiffness in direction of compression.*

1 INTRODUCTION

Poisson's ratio is defined as the ratio of the transverse normal strain divided by the longitudinal strain for a uniaxial loaded specimen. In general materials shrink transversely when stretched; therefore the Poisson's ratios of these materials are positive. However, a novel material which was named negative Poisson's ratio foam (also called auxetic foam, anti-rubber, dilatational, etc.) was manufactured by Lakes [1]. When loaded in uniaxial tension, it expands rather than shrinks laterally. An auxetic material has many advantages over the conventional as a possible ship building material. An auxetic thin plate deflects much less than a conventional plate for a given load [2]. It reduces acoustic noise due to its lower cut-off frequency [3]. It resists better indentation and low velocity impact damages [4, 5]. When bent it deforms synclastically rather than anticlastically thus rendering it ideally suitable for forming into convex-convex surfaces [6]. Furthermore it resists shear failure due to the resulting large shear.

This interesting behavior of auxetic cellular solids results from the unusual microscopic characteristics called "re-entrant structure", as illustrated in Fig.1 (From No.1 to

No.4, the specimen was sequentially loaded). Once the specimen is stretched, these re-entrant structures will unfold in all directions, hence the specimen will expand laterally.

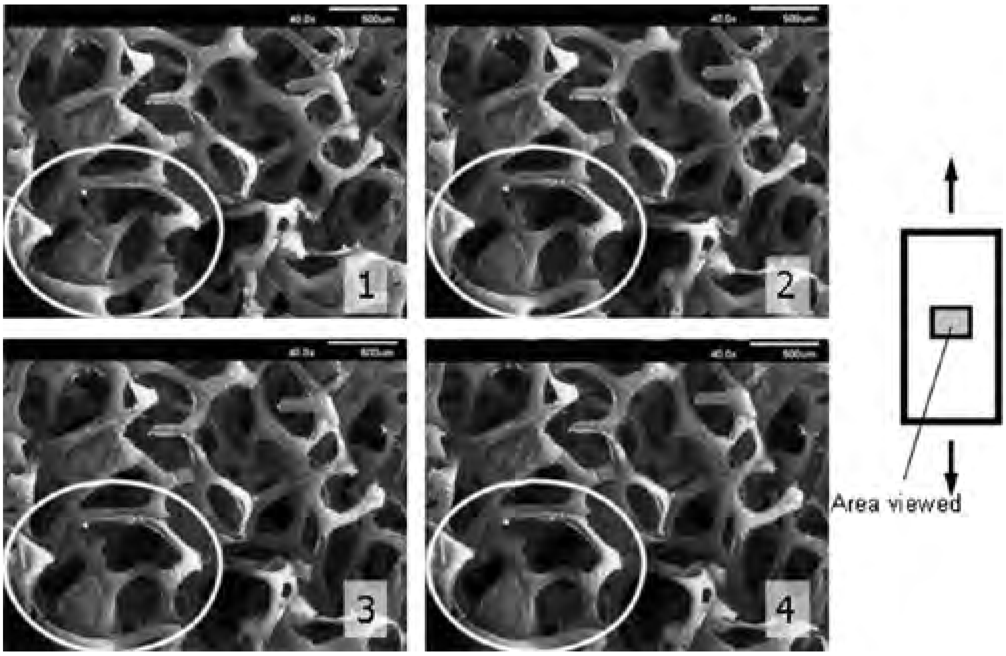

Fig.1. Microscopic Images of Auxetic Foam

2 DIGITAL SPECKLE PHOTOGRAPHY

The technique we use [7-9], while it is similar in principle to digital image correlation (DIC) scheme, the algorithm is quite different. We use a two-step Fourier transformation process to yield the displacement vector distribution of a cluster of digitized speckles via FFT (Fast Fourier Transform). The digital speckle patterns are first divided into subimages with 32x32 pixel arrays or other pixel arrays. Let $h_1(x,y)$ and $h_2(x,y)$ be the complex amplitudes of the light disturbance of a generic speckle subimage pair, before and after deformation, respectively, and

$$h_2(x,y) = h_1\left[x - u(x,y), y - v(x,y)\right], \qquad (1)$$

where u and v are the displacement components, averaged over the subimage area, along the x and y directions respectively. A first step FFT is applied to both h1 and h2 resulting

$$H_1(f_x, f_y) = \Im\{h_1(x,y)\}, \qquad (2)$$
$$H_2(f_x, f_y) = \Im\{h_2(x,y)\}.$$

Then, a numerical "interference" between the two speckle patterns is performed at the spectral domain, i.e.

$$F(f_x,f_y)=\frac{H_1(f_x,f_y)H_2^*(f_x,f_y)}{\left|H_1(f_x,f_y)H_2(f_x,f_y)\right|}=\exp\{j[\phi_1(f_x,f_y)-\phi_2(f_x,f_y)]\} \quad (3)$$

where $\phi_1(f_x,f_y)$ and $\phi_2(f_x,f_y)$) are the phases of $H_1(f_x,f_y)$ and $H_2(f_x,f_y)$, respectively. It is seen that

$$\phi_1(f_x,f_y)-\phi_2(f_x,f_y)=2\pi(uf_x+vf_y) \quad (4)$$

Finally, the halo function is obtained by another FFT resulting

$$G(\xi,\eta)=\Im\{F(f_x,f_y)\}=\overline{G}(\xi-u,\eta-v) \quad (5)$$

which is an expanded impulse function located at (u, v). By detecting the crest via computer search of this impulse function, the displacement vector is determined. Every subimage pair is "compared" this way resulting in an array of displacement vector map. From which strains can be calculated using an appropriate strain displacement relation

3 EXPERIMENTS AND RESULTS

To demonstrate and study this unusual material, an auxetic foam was fabricated from a conventional PVC foam (H45-Blue). A 50x85x95 mm foam block with 44.4 kg/m^3 density was first cut and then compressed in all 3 dimensions using an aluminum mold. After that, the aluminum mold was heated up slightly above the softening point (approximately150^{o}C) and kept at this temperature for about 15 minutes. Finally, the aluminum mold was cooled down to the ambient temperature and the auxetic foam was made. Fig. 1 shows the manufacturing scheme and the microstructures of the foam as-received and after processing.

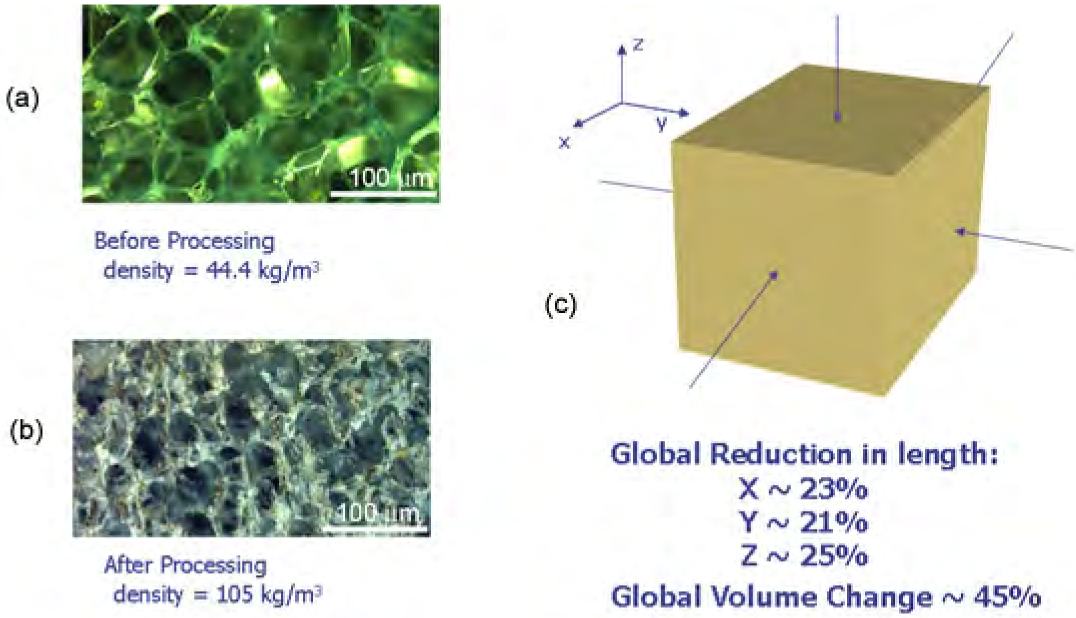

Fig.2. Microscopic images of foam material (a) as-received, (b) after processing (c) schematic of the manufacturing process of auxetic foam

As illustrated in Fig. 2(b), after compression and heat treatment, the foam cells become smaller and crushed inward. Density of the processed specimen was 105 kg/m^3 as compared to the original 44 kg/m^3. Global reduction of the fabricated foams was about 45%. Using the current design, compressing the specimens evenly and simultaneously in all directions was not possible. We compressed the specimens sequentially in all three directions (x, y, and z, respectively) with incremental amounts of compression. The macro deformations of the specimens were determined by employing a 10mm x 10mm grid printed onto specimen surface before the compression process. Local volume change varies from ~ 47 to 82%. Volume change is higher on the faces of the block and becomes smaller towards the middle. A thin layer of material at all faces that were in contact with the mold tends to be denser. These layers were shaved off. The core then was cut into coupon specimens for uniaxial loading as shown in Fig. 3. A digital optical microscope (VHX-100) was used to record the speckle pattern as the load is being applied by a servo controlled stage at a constant rate of displacement. Fig. 3 depicts the basic test setup and viewing area under microscope.

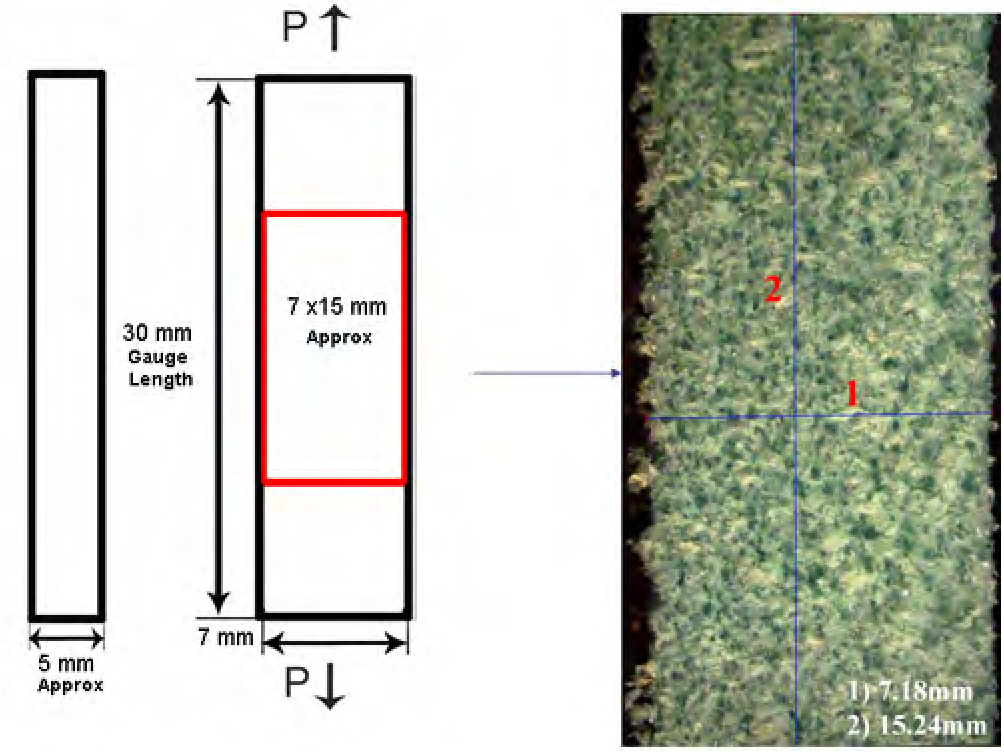

Fig.3. Auxetic foam specimen: (a) Dimensions of the coupon. (b) Microscopic picture of the specimen surface at 20x.

The resulting specklegrams were analyzed with the CASI (Computer Aided Speckle Interferometry) algorithm as described in the previous section. Fig. 4 shows a typical specimen and resulting displacement fields. It can be seen clearly from the vector field that with increasing load, specimen expands in both directions without much rotation and assumes auxetic behavior.

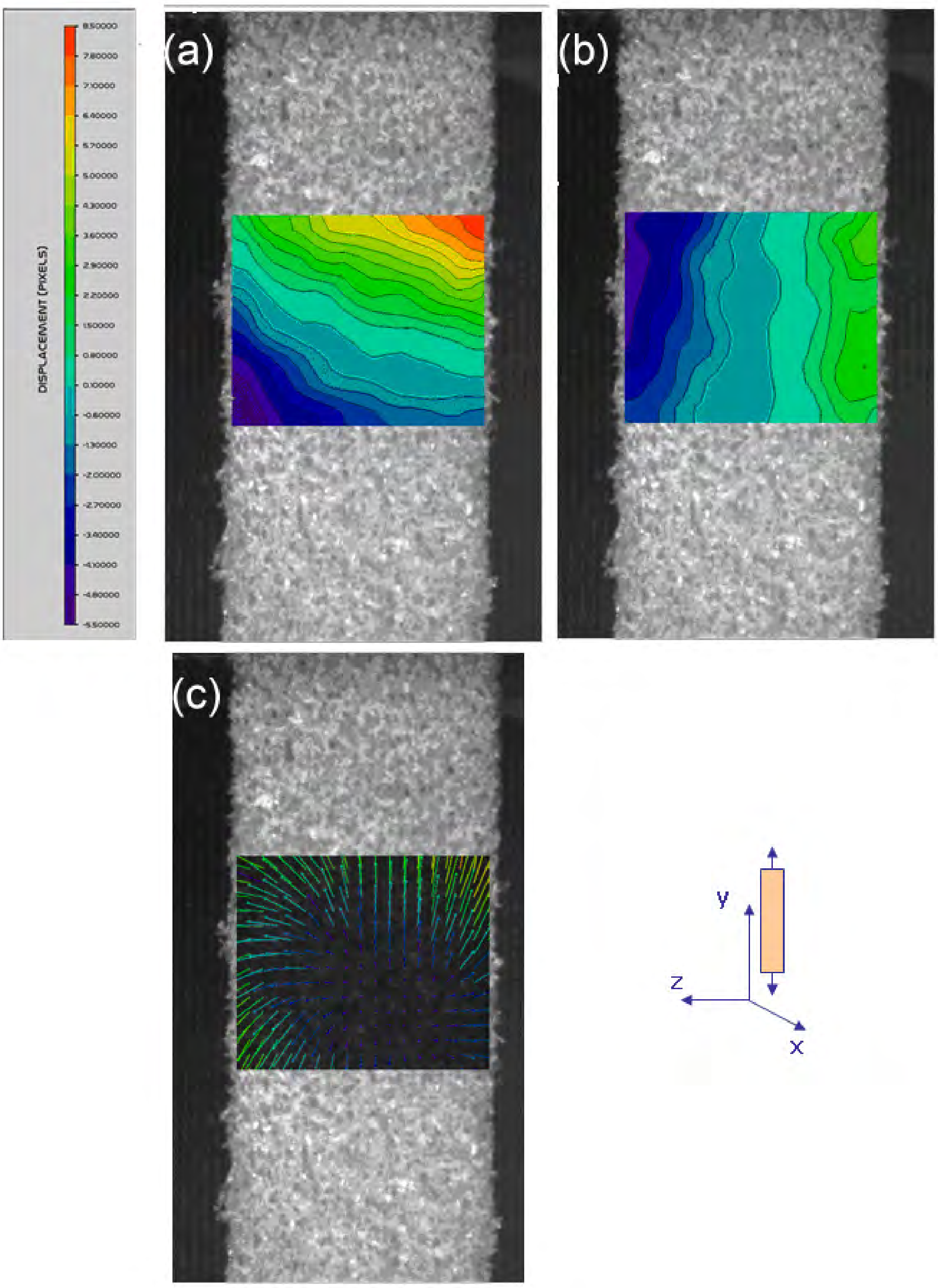

Fig.4. An example of displacement fields obtained by CASI. (a) v field, (b) u field, (c) total displacement vector.

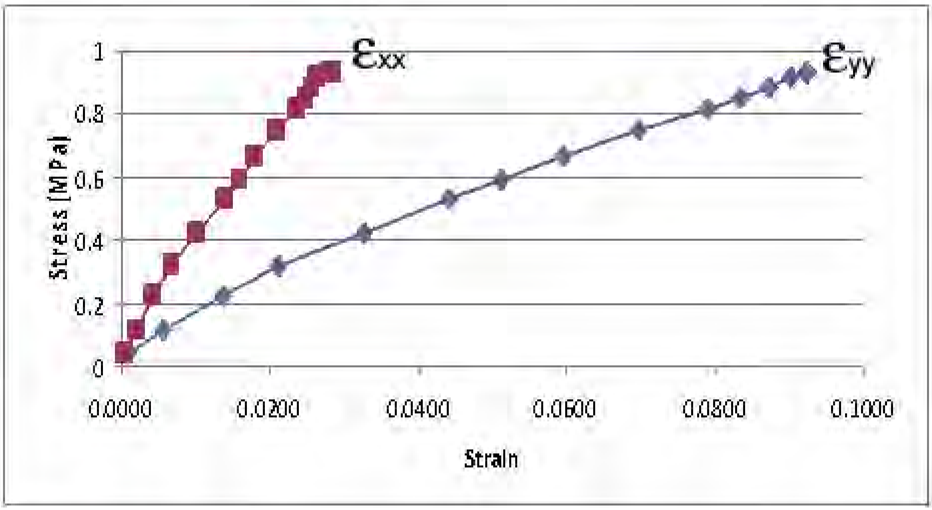

Fig.5. Stress-strain curve of a typical specimen.

The stress- strain curve (using the average strain of the entire specimen) was plotted as shown in Fig.5. It is seen that under the uniaxial tensile load, the transverse strain is positive rather than negative, demonstrating the auxetic behavior.

Poisson's ratio values are not constant values. As shown in Fig.6 as the tensile strain increases the Poisson's ratio value become smaller. We also found that degree of auxeticity is related to the volumetric compression of the material. The larger the volumetric compression the larger the Poisson's ratio. Fig. 7 depicts the obtained Poisson's ratio values versus volumetric change. The values on the plots are the average Poisson's ratio values for the specimens.

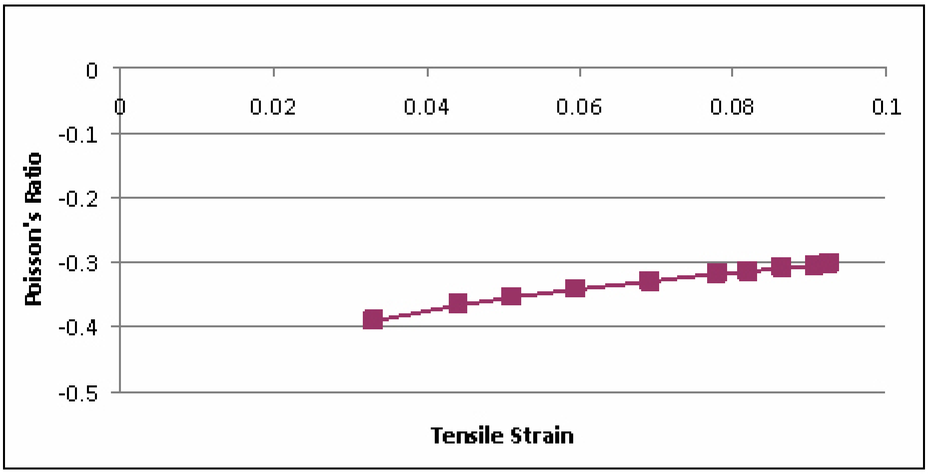

Fig.6. The resulting Poisson's ratio values.

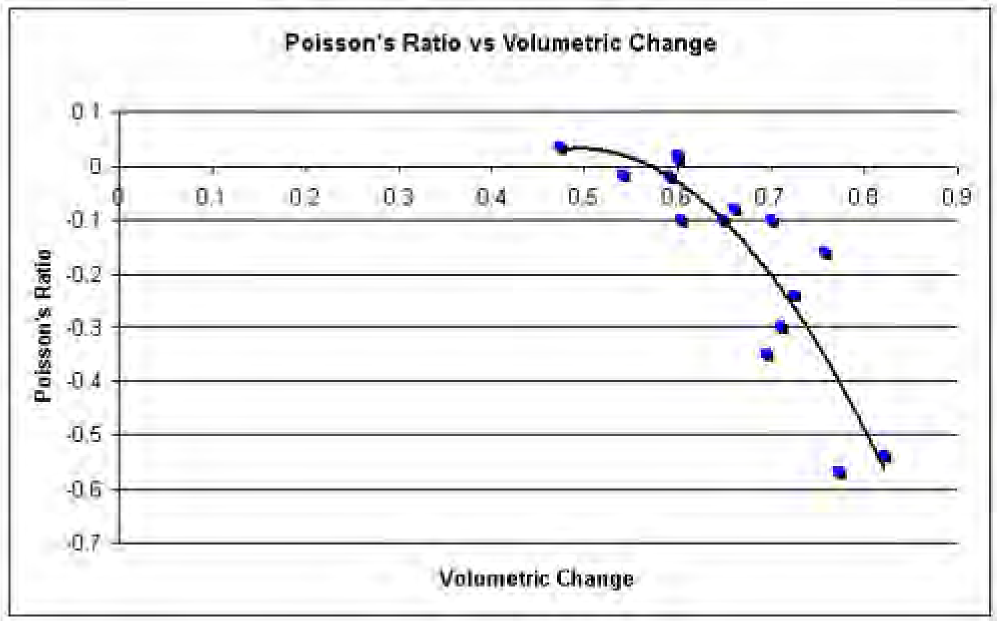

Fig.7. Poisson's ratio as a function of volumetric change.

4 CONCLUSIONS

We have successfully converted by sequential triaxial compression and heating an ordinary PVC (H45-Blue) foam (with the original Poisson's ratio 0.3) into an auxetic foam with Poisson's ratio chnages up to -0.6. The Digital Speckle Photography (DSP) Technique can be efficiently applied to map full-field deformation of foam material. We find that the Poisson's ratio decreases in absolute volume when the stress increases. Furthermore the degree of auxeticity is a function of volumetric reduction of the original material. The larger the volumetric reduction of the original material, the larger the auxeticity of the resulting foam.

ACKNOWLEDGEMENTS

The work reported have supported by grant from the Office of Naval Research (ONR) No: N000140410357. We gratefully thank Dr. Yapa Rajapakse the manager of ONR's Solid Mechanics Program for his support and encouragement.

REFERENCES

[1] Lakes, R.S., "Foam structures with a negative Poisson's ratio." *Science*, Vol. 235: pp 1038-1040, 1987.

[2] Evans, K. E. "Auxetic polymers: a new range of materials." *Endeavour, New Series* Vol. 15 No. 4: pp 170-174, 1991.

[3] Chen, C. P. and Lakes, R. S. "Dynamic wave dispersion and loss properties of conventional and negative Poisson's ratio polymeric cellular materials." *Cellular Polymers*

Vol. 8, No.5: pp 343-359, 1989.

[4] Scarpa, F., J. R. Yates, et al. "Dynamic crushing of auxetic open-cell polyurethane foam." *Proceedings of the Institution of Mechanical Engineers, Part C: Journal of Mechanical Engineering Science* Vol. 216, No.12: pp1153-1156, 2002.

[5] Scarpa, F., L. G. Ciffo, et al. "Dynamic properties of high structural integrity auxetic open cell foam." *Smart Materials and Structures* Vol. 13, No.1: pp 49-56, 2004.

[6] Whitty, J. P. M., Alderson, A., Myler, P., and Kandola, B. "Towards the design of sandwich panel composites with enhanced mechanical and thermal properties by variation of the in-plane Poisson's ratios." *Composites Part A: Applied Science and Manufacturing* Vol. 34 No. 6 SPEC: pp525-534, 2003.

[7] Chen D.J., Chiang F.P"Computer-aided speckle Interferometry using spectral amplitude fringes". *Appl Opt*, 32,225–236, 1993.

[8] Chen D.J, Chiang F.P, Y.S. Tan and H.S. Dan "Digital speckle displacement using complex spectrum method" *Appl Opt*, 32(11), 1839–1849, 1993.

[9] Chiang F.P., "Evolution of the White Light Speckle Method and Its Application to Micro/Nanotechnology and Heart Mechanics", Optical Engineering, 42(5), pp. 1288-1292, 2003.

8th International Conference on Sandwich Structures
ICSS 8
A. J. M. Ferreira (Editor)

SPECTRAL AND PERTURBATION ANALYSIS OF SANDWICH BEAMS WITH A NOTCH DAMAGE

Nicoleta Apetre[⋆], **Massimo Ruzzene**[⋆], **Sathya Hanagud** [⋆]
and
S. Gopalakrishnan[†]

[⋆]School of Aerospace Engineering
Georgia Institute of Technology
270 Ferst Drive, Atlanta GA, 30332, USA
e-mail: nicole.apetre@gatech.edu

[†]Department of Aerospace Engineering, Indian Institute of Science, Bangalore 560 012, India
e-mail: krishnan@aero.iisc.ernet.in

Key words: Damaged sandwich structures, Notched sandwich structures, Spectral Finite Element method, Perturbation techniques.

Summary. *The influence of damage on waves propagating in sandwich structures is investigated through a numerical model formulated by combining Spectral Finite Elements and Perturbation Techniques. The dynamic behavior of sandwich beams is described based on Mead and Markus assumptions. Damage is modeled as a small, localized reduction of one face sheet thickness which allows the application of perturbation theory. Numerical examples in the time domain are presented to illustrate the model capabilities.*

1 INTRODUCTION

The first step in deriving models for damage detection in structures is the study of the damage influence on structures characteristics. Because sandwich structures offer several advantages over other continuous or laminated plate structures, it is important to develop models that describes the effect of damages such as cracks, delaminations and disbands on structures features. Guided waves, such as Lamb waves, show sensitivity to a variety of damage types and have the ability to travel relatively long distances within the structure under investigation. For this reason, Guided Ultrasonic Waves (GUWs) are particularly suitable for Structural Health Monitoring (SHM) applications, which may employ a built-in sensor/actuator network to interrogate and assess the state of health of the structure [1, 2, 3]. Alternatively, full wavefield measurements can be obtained through scanning Laser Vibrometers, which allow the implementation of strain energy-based damage measures [4], and of frequency/wavenumber filtering techniques for improved damage visualization [5].

Cellular materials with constant or continuously varying density or pore size (porosity) are a class of materials that can be used as core in sandwich structures. Recently, engineered cellular materials are made using polymers, metals, and ceramics. They are widely used as thermal and acoustic insulations, or as absorbers of kinetic energy from impacts. The cellular/foamed materials are qualitatively and quantitatively investigated in a large number of publications. Among those, two books are worth mentioning: Ashby et. al. [6] design guide for metal foams (contains processing techniques, characterization methods, design and applications) and Gibson and Ashby [7], a monograph on cellular solids. Although cellular materials are highly heterogeneous, it will be useful to idealize them as continua in order to obtain closed-form solutions to some fundamental solid mechanics problems.

Spectral Finite Element Method (SFEM), which is a very similar method with the Finite Element Method, but it is formulated in the frequency domain, gives very accurate solution for the dynamic analysis of structures because it is based on the exact dynamic stiffness matrix by using the exact shape functions [8]. Consequently SFEM implementation doesn't require any structural discretization to improve the solution accuracy - longer and fewer elements are needed. A review of the SFEM in structural dynamics is presented in [9].

Apetre et. al. [10] investigate the influence of damages on waves propagation in beams based on the first order theory which couples bending and axial behavior, thus allowing the prediction of mode conversion phenomena. This paper continues the previous work ([10]) presenting the application of SFEM in conjunction with the perturbation analysis of damaged sandwich beams. Damage is modeled as a thickness reduction of small extent of top face sheet, which allows the introduction of a perturbation parameter ϵ. The application of perturbation techniques yields a set of differential equations, corresponding to increasing orders of ϵ, which are solved through the application of SFEM. The paper is organized as follows. The brief introduction presented in this section is followed by the derivation of the governing equations for the notched sandwich beam based on Hamilton principle and perturbation techniques (Section 2). Section 3 presents the methodology followed to solve the perturbation equations through SFEM, while Section 4 presents numerical results in both time domain and frequency domain obtained from the analysis in order to illustrate the effect of the considered type of damage on the dynamic behavior of the beam. Finally, Section 5 summarizes the main results of the work and outlines current and future research directions.

2 PERTURBATION EQUATIONS FOR A SANDWICH BEAM WITH A NOTCH DAMAGE

The dynamic behavior of the notched sandwich beam shown in Figure 1 is described by a set of governing equations derived through Hamilton principle. The defect is modeled as a reduction in top face sheet thickness of depth h_d, extending over a length Δl, placed at the distance x_d. According to Figure 1(a), $x \in [0, L]$ denotes the horizontal coordinate, whereas the vertical coordinate z varies in the following interval:

$$z \in \left[-\left(\frac{h_2}{2} + z_0 + h_3 \right), \;\; \frac{h_2}{2} - z_0 + h_1(1 - \varepsilon \gamma_d(x)) \right] = [-h_b \;\; h_t(x)] \tag{1}$$

where h_1 and h_3 are the thicknesses of the face sheets, h_2 is the thickness of the core, z_0 is the neutral axis location, $\varepsilon = \frac{h_d}{h_1}$, and where $\gamma_d(x)$ is a damage function defined as:

$$\gamma_d(x) = H\left(x - (x_d - \Delta l)\right) - H\left(x - x_d\right) \tag{2}$$

with H denoting the Heaviside function.

It is assumed that the shear modulus of the face sheets material is significantly higher than the one of the core, so Mead and Marcus theory [11] can be used. The elastic and isotropic face sheets do not suffer shear deformation normal to the plate surface and only undergo longitudinal strain. Normal strains in the core are neglected as it is assumed that is subject to shear strain only. From the beam geometry of Figure 1(b), the shear strain in the core can be expressed as:

$$\gamma = \frac{1}{h_2}(u_1 - u_3 + hw_{,x}) \tag{3}$$

where u_1 and u_3 are the longitudinal deflections of the two face sheets, $w_{,x}$ denotes the slope of the deflection line, and the parameter h is defined as:

$$h = h_2 + \frac{h_1 + h_3}{2}. \tag{4}$$

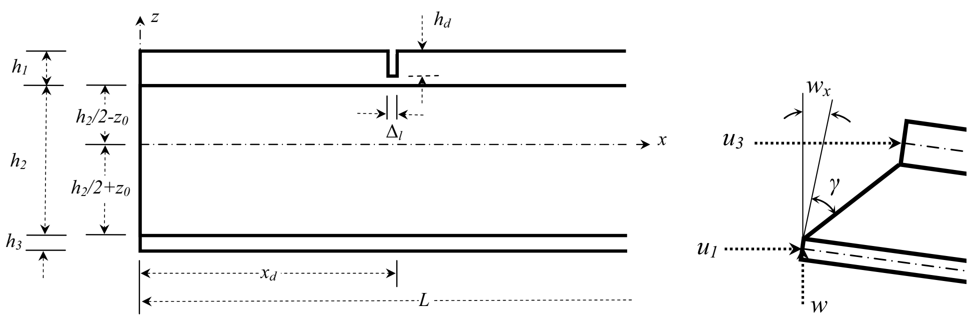

(a) (b)

Figure 1: Undeflected and delfected configurations of a sandwich beam

The longitudinal deflection u_2 of the core can be given in terms of the displacements, as:

$$u_2 = \frac{1}{2}\left(u_1 + u_3 + \frac{h_1 - h_3}{2} w_{,x}\right) \tag{5}$$

The strain energy of the sandwich beam includes the extension of the face sheets, the core shear deformation and the bending of the entire cross section:

$$U = \frac{1}{2}\int_0^L E_1 A_1(x) u_{1,x}^2 dx + \frac{1}{2}\int_0^L E_3 A_3 u_{3,x}^2 dx + \frac{1}{2}\int_0^L G A_2 \gamma^2 dx + \frac{1}{2}\int_0^L D_t(x) w_{,xx}^2 dx \tag{6}$$

where E_i is the Young's modulus of ith layer ($i = 1, 2, 3$), A_i is cross sectional area of ith layer, D_t is the bending rigidity of the beam and G_2 is the shear modulus of the core. Because of the notch presence, the area of top face sheet and the bending rigidity is a function of longitudinal coordinate, x.

The kinetic energy is:

$$T = \frac{1}{2}\int_0^L m_1(x)\dot{u}_1^2 dx + \frac{1}{2}\int_0^L m_3\dot{u}_3^2 dx + \frac{1}{2}\int_0^L m_2\dot{u}_2^2 dx + \frac{1}{2}\int_0^L m(x)\dot{w}^2 dx \tag{7}$$

where m_i is the mass per unit length of the ith layer, and m is the total mass per unit length of the sandwich beam.

The work of the external forces is

$$\begin{aligned} V = &-\int_0^L \big[n_1(x,t)u_1 + n_3(x,t)u_3 + q(x,t)w + \tilde{m}(x,t)w_{,x}\big]dx \\ &-\sum_{j=1}^{N}\int_0^L \big[N_{1j}(t)u_1 + N_{3j}(t)u_3 + Q_j(t)w + M_j(t)w_{,x}\big]\delta(x - x_j)dx \end{aligned} \tag{8}$$

where, for simplicity we assume that the loads are applied along the reference planes of the face sheets and core. Also in equation (8), $n_i(x,t)$ ($i = 1, 3$) and $q(x,t)$ respectively denote axial and transverse distributed external loads, $\tilde{m}(x,t)$ denotes a bending moment distribution, while $N_{ij}(t)$, $Q_j(t)$ and $M_j(t)$ are external concentrated longitudinal and vertical loads, and bending moment applied at N locations $x = x_j$. Finally δ is the Dirac delta function.

Applying Hamilton's principle:

$$\int_{t_1}^{t_2} \delta(U - T + V)dt = 0 \tag{9}$$

where δ is the first variation, t denotes time and t_1, t_2 define the integration time limits, the following differential system is obtained:

$$\mathbf{M}_1\ddot{\mathbf{U}} + \mathbf{M}_2\ddot{\mathbf{U}}_{,x} + \mathbf{M}_3\ddot{\mathbf{U}}_{,xx} + \mathbf{M}_4\mathbf{U} + \mathbf{M}_5\mathbf{U}_{,x} + \mathbf{M}_6\mathbf{U}_{,xx} + \mathbf{M}_7\mathbf{U}_{,xxx} + \mathbf{M}_8\mathbf{U}_{,xxxx} = \mathbf{F}(x,t) \tag{10}$$

where $\mathbf{U}(x,t) = [u_1(x,t)\ u_3(x,t)\ w(x,t)]^T$ and the matrices $\mathbf{M}_i$ are defined as:

$$\mathbf{M}_1 = \begin{bmatrix} m_1(x) + \frac{m_2}{4} & \frac{m_2}{4} & 0 \\ \frac{m_2}{4} & m_3 + \frac{m_2}{4} & 0 \\ -\frac{m_2 h_{1,x}}{8} & \frac{m_2 h_{1,x}(x)}{8} & m(x) \end{bmatrix} \quad \mathbf{M}_2 = \frac{m_2(h_1(x) - h_3)}{8}\begin{bmatrix} 0 & 0 & 1 \\ 0 & 0 & 1 \\ -1 & -1 & h_{1,x}(x) \end{bmatrix} \tag{11}$$

$$\mathbf{M}_4 = \frac{GA_2}{h_2^2}\begin{bmatrix} 1 & -1 & 0 \\ -1 & 1 & 0 \\ -h_{,x}(x) & h_{,x}(x) & 0 \end{bmatrix} \quad \mathbf{M}_5 = \frac{GA_2 h(x)}{h_2^2}\begin{bmatrix} E_1A_1(x)\frac{h_2^2}{GA_2 h(x)} & 0 & 1 \\ 0 & 0 & -1 \\ -1 & 1 & 2h(x)h_{1,x}(x) \end{bmatrix} \tag{12}$$

$$
\begin{aligned}
\mathbf{M}_3 &= \text{diag}[0\ 0\ \ -\frac{m_2(h_1(x)-h_3)}{16}] \\
\mathbf{M}_6 &= \text{diag}\left[-E_1A_1(x)\ \ -E_3A_3\ D_{t,xx}(x)-\frac{GA_2h^2(x)}{h_2^2}\right] \\
\mathbf{M}_7 &= \text{diag}[0\ 0\ 2D_{t,x}(x)] \\
\mathbf{M}_8 &= \text{diag}[0\ 0\ D_t(x)]
\end{aligned}
\tag{13}
$$

and where the force vector is:

$$
\mathbf{F}(x,t)=\left\{\begin{array}{c}
n_1(x,t)+\sum_{j=1}^{N}N_{1j}(t)\delta(x-x_j) \\
n_3(x,t)+\sum_{j=1}^{N}N_{3j}(t)\delta(x-x_j) \\
q(x,t)-\tilde{m}_{,x}(x,t)+\sum_{j=1}^{N}Q_j(t)\delta(x-x_j)+\sum_{j=1}^{N}M_j(t)(\delta(x-x_j))_{,x}
\end{array}\right\}
\tag{14}
$$

Equations (10) can be conveniently expressed in the frequency domain through the Fourier Transform (FT) of the applied generalized loads $\mathbf{F}(x,t)$, which can be expressed as:

$$
\mathbf{F}(x,t)=\sum_k \hat{\mathbf{F}}_k(x,\omega_k)e^{i\omega_k t}
\tag{15}
$$

where $i=\sqrt{-1}$, and $\hat{\mathbf{F}}_k(x,\omega_k)$ denotes the harmonic component of the generalized load at frequency ω_k [8]. Accordingly, the beam's displacements can be written as:

$$
\mathbf{U}(x,t)=\sum_k \hat{\mathbf{U}}_k(x,\omega_k)e^{i\omega_k t}
\tag{16}
$$

where $\hat{\mathbf{U}}_k(x,\omega_k)$ are the displacements corresponding to the k-th harmonic component of the load. For simplicity, in the remainder of the paper, the subscript k is dropped so that the following notation is adopted $\omega_k=\omega$, $\hat{\mathbf{U}}_k(x,\omega_k)=\hat{\mathbf{U}}(x,\omega)$.

Next, displacements of the sandwich beam in the reference plane are considered as perturbations (over the small parameter ε) of the displacements of the undamaged beam ([12] and [13]):

$$
\hat{\mathbf{U}}(x,\omega)=\hat{\mathbf{U}}^{(0)}(x,\omega)-\varepsilon\hat{\mathbf{U}}^{(1)}(x,\omega)+\mathcal{O}(\varepsilon^2)
\tag{17}
$$

Also, based on the beam geometry, the thickness of the top face sheet is $h_1(x)=h_1(1-\varepsilon\gamma_d(x))$ and all the system matrices can be expanded as: $\mathbf{M}_k(x)=\mathbf{M}_k^{(0)}-\varepsilon\mathbf{M}_k^{(1)}(x)$ for $k=1,...,8$

Replacing (15)-(17) into the differential system (10) and collecting the coefficients of ε^0 and ε^1 yields the following set of differential equations:

$$
\varepsilon^0:\ \mathbf{M}_8^{(0)}\hat{\mathbf{U}}^{(0)}_{,xxxx}+\left[\mathbf{M}_6^{(0)}-\omega^2\mathbf{M}_3^{(0)}\right]\hat{\mathbf{U}}^{(0)}_{,xx}+\left[\mathbf{M}_5^{(0)}-\omega^2\mathbf{M}_2^{(0)}\right]\hat{\mathbf{U}}^{(0)}_{,x}+\left[\mathbf{M}_4^{(0)}-\omega^2\mathbf{M}_1^{(0)}\right]\hat{\mathbf{U}}^{(0)}=\hat{\mathbf{F}}^{(0)}
\tag{18}
$$

$$\varepsilon^1: \ \mathbf{M}_8^{(0)}\hat{\mathbf{U}}^{(1)}_{,xxxx} + \left[\mathbf{M}_6^{(0)} - \omega^2\mathbf{M}_3^{(0)}\right]\hat{\mathbf{U}}^{(1)}_{,xx} + \left[\mathbf{M}_5^{(0)} - \omega^2\mathbf{M}_2^{(0)}\right]\hat{\mathbf{U}}^{(1)}_{,x} + \left[\mathbf{M}_4^{(0)} - \omega^2\mathbf{M}_1^{(0)}\right]\hat{\mathbf{U}}^{(1)} = \hat{\mathbf{F}}^{(1)} \tag{19}$$

where $\hat{\mathbf{F}}^{(0)}(x,\omega)$ is the applied load and $\hat{\mathbf{F}}^{(1)}(x,\omega)$, due to the notch presence, is defined as:

$$\hat{\mathbf{F}}^{(1)} = -\mathbf{M}_8^{(1)}\hat{\mathbf{U}}^{(0)}_{,xxxx} - \mathbf{M}_7^{(1)}\hat{\mathbf{U}}^{(0)}_{,xxx} - \left[\mathbf{M}_6^{(1)} - \omega^2\mathbf{M}_3^{(1)}\right]\hat{\mathbf{U}}^{(0)}_{,xx} - \left[\mathbf{M}_5^{(1)} - \omega^2\mathbf{M}_2^{(1)}\right]\hat{\mathbf{U}}^{(0)}_{,x} - \left[\mathbf{M}_4^{(1)} - \omega^2\mathbf{M}_3^{(1)}\right]\hat{\mathbf{U}}^{(0)} \tag{20}$$

Equations (18), (19) can be solved for an assigned set of loads in terms of the unknown displacements $\hat{\mathbf{U}}^{(0)}(x,\omega)$ and their first order perturbation $\hat{\mathbf{U}}^{(1)}(x,\omega)$. Next section presents a general method to solve these equations.

3 SPECTRAL FINITE ELEMENT DISCRETIZATION

The equation for the ε^0 term corresponds to the governing equation for the undamaged beam, the first order perturbation equation has the same form and features an applied generalized load that is a function of the solution of the ε^0 equation. A common strategy for the solution of the two equations (equations (18),(19)) deriving from the expansion of the beam's displacements in terms of the perturbation parameter can be adopted based on their formally identical form. Each of the equations can in fact be written in the following matrix form:

$$\mathbf{T}_4\mathbf{W}_{,xxxx}(x,\omega) + \mathbf{T}_2\mathbf{W}_{,xx}(x,\omega) + \mathbf{T}_1\mathbf{W}_{,x}(x,\omega) + \mathbf{T}_0\mathbf{W}(x,\omega) = \mathbf{F}(x,\omega) \tag{21}$$

We consider an element j of length L_j that connects two nodes. The behavior of each node is described by 4 degrees of freedom, so that the element's vector of degrees of freedom is defined as $\mathbf{d}_j(\omega) = \{\hat{u}_1(0,\omega),\ \hat{u}_3(0),\ \hat{w}(0),\ \hat{w}_{,x}(0),\ \hat{u}_1(L_j),\ \hat{u}_3(L_j),\ \hat{w}(L_j),\ \hat{w}_{,x}(L_j)\}^T$. The displacement $\mathbf{W}(x,\omega)$ within element j is obtained as an interpolation of the nodal degrees of freedom $\mathbf{d}_j$:

$$\mathbf{W}(x,\omega) = \mathbf{N}_j(x,\omega)\mathbf{d}_j(\omega) \tag{22}$$

where $\mathbf{N}_j(x,\omega)$ is the matrix of the dynamic shape functions which is obtained from the solution of the homogeneous governing equation

$$\mathbf{N}_j(x,\omega) = \boldsymbol{\Theta}(\omega)\mathbf{G}(x,\omega)\mathbf{T}_j^{-1}(\omega) \tag{23}$$

where $\Theta(\omega)$ is the matrix of eigenvectors, $\mathbf{G}(x,\omega) = \text{diag}[e^{i\lambda_k x}]$ is a diagonal matrix, λ_k is the kth eigenvalue and where the matrix $\mathbf{T}$ is defined as:

$$\mathbf{T} = \begin{bmatrix} \Theta(\omega)\mathbf{G}(0,\omega) \\ \Theta(\omega)\mathbf{G}(0,\omega)_{,x} \\ \Theta(\omega)\mathbf{G}(L_j,\omega) \\ \Theta(\omega)\mathbf{G}(L_j,\omega)_{,x} \end{bmatrix} \tag{24}$$

The dynamic shape functions provide the exact displacement variation along the beam if the external loads are concentrated at the nodal locations [8]. In the case considered here, it can be shown that the generalized load in the first order perturbation equations reduces to a concentrated nodal load if a node is placed at the damage location. Accordingly, the solution of homogeneous beam equations and proper description of nodal loads corresponding to the presence of damage based on the formulation presented above can be used to obtain exact dynamic shape functions and accurate representations of the beam's displacements in the frequency range corresponding to the applied load. This approach can also be applied when loads are generally distributed along the element length. In this case, the dynamic shape functions do not reproduce exactly the displacement field within the element, and some approximation is introduced. The application of nodes at damage and load locations do not cause a dramatic increase in the computational time, and the presented modeling approach still represents an efficient tool for the analysis of wave propagation in the considered class of damaged structures. Refinements of the formulation, allowing the accurate representation of general load distributions and of damage locations within the element, are under development and will be discussed in future papers.

The element's vector of degrees of freedom $\mathbf{d}_j(\omega)$ is obtained from the following algebraic equation:

$$\mathbf{K}_j(\omega)\mathbf{d}_j(\omega) = \mathbf{f}_j(\omega) \tag{25}$$

where $\mathbf{K}(\omega)_j$ is the element stiffness matrix at frequency ω, defined based on the weak formulation as:

$$\begin{aligned}\mathbf{K}_j(\omega) = \int_0^{L_j} \Big\{ & \mathbf{N}_{j,xx}^T(x,\omega)\mathbf{T}_4\mathbf{N}_{j,xx}(x,\omega) - \mathbf{N}_{j,x}^T(x,\omega)\mathbf{T}_2\mathbf{N}_{j,x}(x,\omega) \\ & + \mathbf{N}_j^T(x,\omega)\mathbf{T}_1\mathbf{N}_{j,x}(x,\omega) + \mathbf{N}_j^T(x,\omega)\mathbf{T}_0\mathbf{N}_j(x,\omega) \Big\} dx\end{aligned} \tag{26}$$

and where $\mathbf{f}$ is the vector of applied nodal loads:

$$\mathbf{f}_j(\omega) = \int_0^{L_j} \mathbf{N}_j^T(x,\omega)\mathbf{F}(x,\omega)dx \tag{27}$$

4 NUMERICAL EXAMPLES

In this section, the developed technique is applied to evaluate longitudinal and transverse wave propagation in damaged beams based on two examples. The first example considers a clamped-free sandwich beam with a notch at $x_d = L/2$ and a vertical load at $x_f = L$. The beam is modeled using 2 spectral elements as shown in Figure 2(a). The beam has length $L = 2$ m, core thickness $h_2 = 4 \times 10^{-3}$ m, face sheets thickness $h_1 = h_3 = 3 \times 10^{-3}$ m and width $b = 50 \times 10^{-3}$ m. The material of face sheets is aluminum (Young's modulus $E_1 = E_3 = 70$ GPa, density $\rho_1 = \rho_3 = 2700$ kg/m^3, Poisson's ratio $\nu_1 = \nu_3 = 0.33$), whereas the mechanical properties of the core are: Young's modulus $E_2 = 70$ MPa, density $\rho_2 = 724$ kg/m^3, Poisson's ratio $\nu_2 = 0.4$ The notch is of length $\Delta l = 5 \times 10^{-3}$ m and depth $h_d = h_1/4$. The considered excitation is a 4-cycles sinusoidal burst at 50 kHz modulated by a Hanning window (Figure 2(c)), applied at x_f in the longitudinal direction.

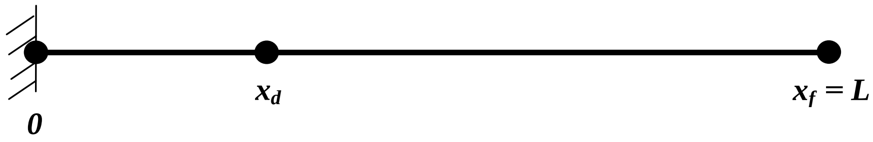

(a)

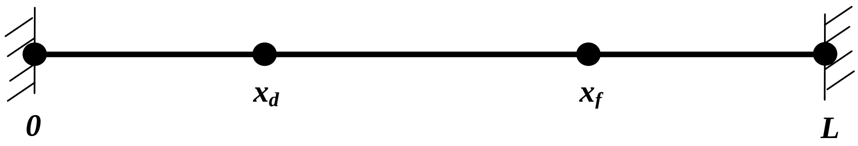

(b)

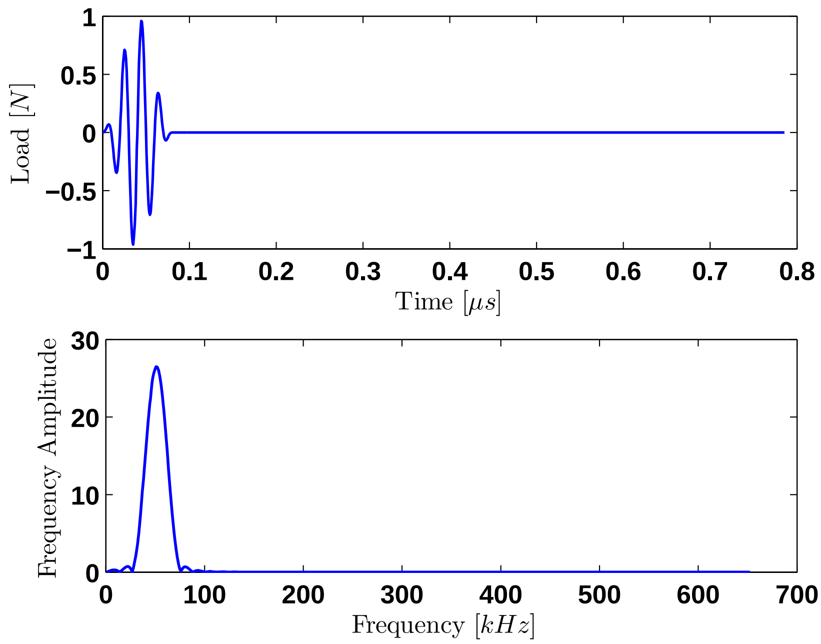

(c)

Figure 2: Schematic of (a) the clamped-free beam and (b) the simply-supported beam with a load at x_f, and a notch at x_d modeled using two spectral elements; (c) Modulated sinusoidal pulse load in time and frequency domain.

The sandwich beam wavenumbers with respect to the frequencies and the Euler-Bernoulli beam theory wavenumbers and the axial displacement wavenumbers are plotted in Figure 3: because of the Mead and Marcus theory [11] assumptions, the wavenumbers are very similar.

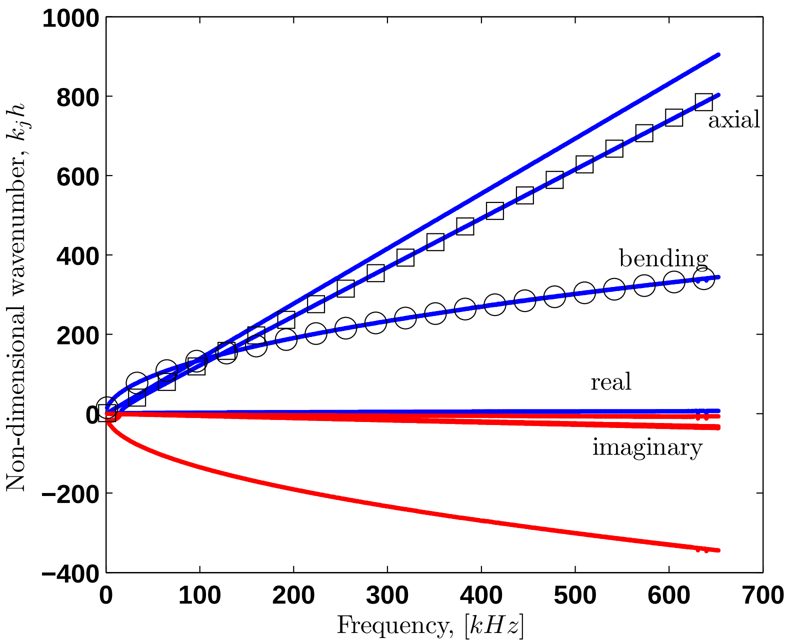

(a)

Figure 3: Spectrum relation for the sandwich beam (continuous line) and for the Euler-Bernoulli beam theory (circles) and axial displacement (squares)

Figure 4 presents 3D surfaces of the displacements (as functions of time and longitudinal coordinate) whereas Figure 5 presents snapshots of displacements variations along the beam length at three instants of time. The axial displacements in the face sheets are plotted in the subplots (a) and (b) and the transversal displacement is plotted in subplot (c). A longitudinal load causes a longitudinal wave and a transverse wave to propagate from the tip of the beam. When the waves reach the notch (in this case at $x = L/2$), they are partially reflected and partially converted. The problem is coupled both because of the sandwich beam geometry and because of the notch presence.

In order to study the influence of boundary conditions a second example considers a simply-supported sandwich beam with a notch at $x_d = 0.66$ and a transverse load at $x_f = 1.33$. The same geometry and material properties as for the previous problem are assumed. In this case the notch depth is $h_d = h_1/4$. As in the previous case Figure 6 presents 3D surfaces of the displacements (as functions of time and longitudinal coordinate) whereas Figure 7 presents snapshots of displacements variations along the beam length at three instants of time. From

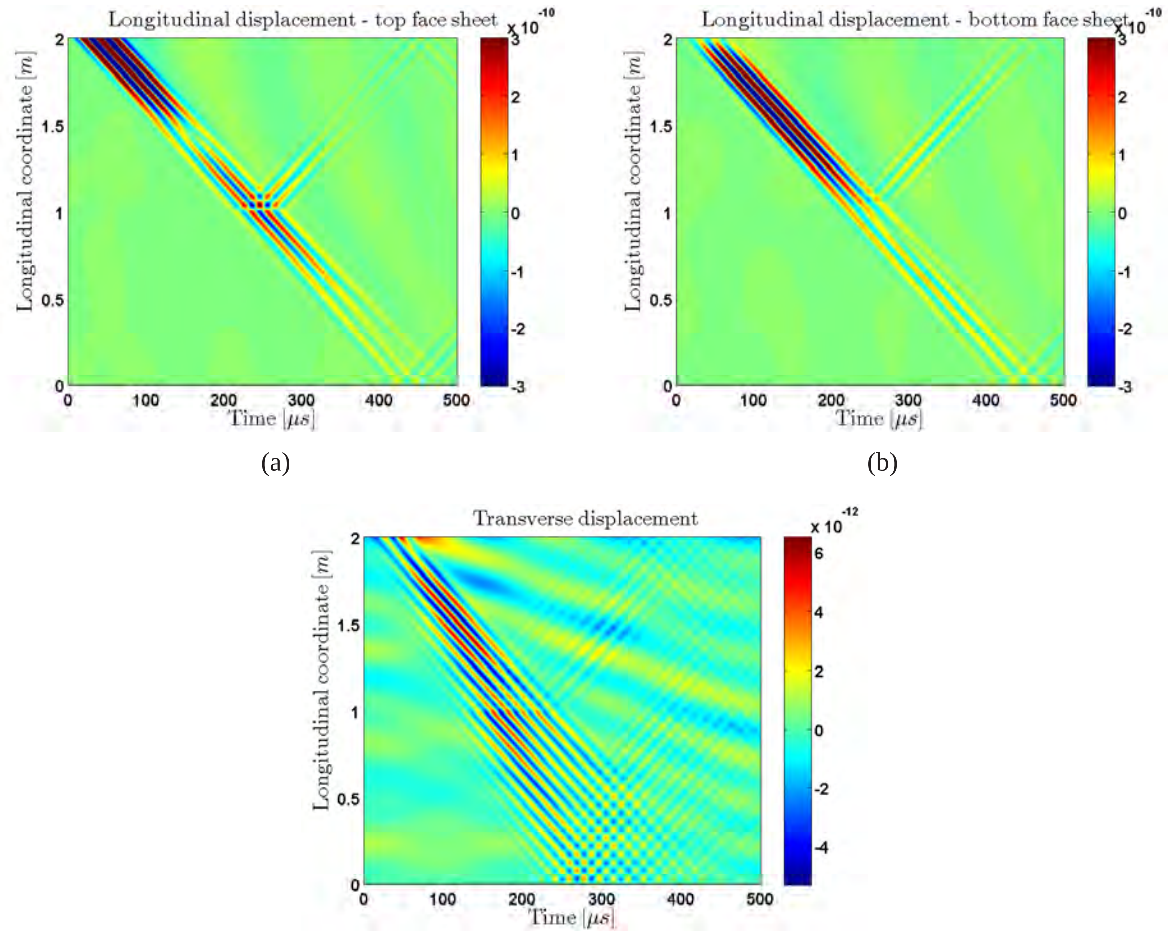

(a) (b)

(c)

Figure 4: Displacements as function of time and longitudinal coordinate (a) Longitudinal displacement in the top face sheet; (b) Longitudinal displacement in the bottom face sheet and (c) Transverse displacement. The length of the notch is $\Delta l = 0.05$m.

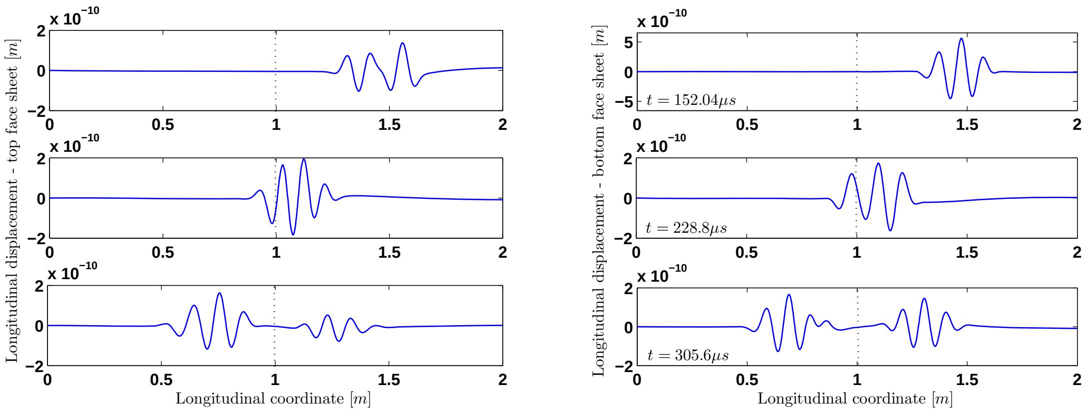

Figure 5: Longitudinal displacements in the face sheets as function of time and longitudinal coordinate (a) Longitudinal displacement in the top face sheet; (b) Longitudinal displacement in the bottom face sheet. The length of the notch is $\Delta l = 0.05$m. The dotted line shows the damage location

the Figure 7 we can conclude that the transverse load produces both transverse and longitudinal waves that are propagating and are partially reflected at the damage location.

5 CONCLUSIONS

The dynamic behavior of the sandwich beams with a notch is investigated through the perturbation techniques. The governing equations of a sandwich beam are derived using Hamilton principle. Spectral element formulation based on the exact dynamic stiffness matrix is used to determine the solution. The results show reflections of the waves and coupling between the longitudinal and transversal displacements and velocities due to both sandwich beam and the notch presence. Future work will include a model validation, a parametric study of the damage geometry, and an extension to different types of damages (delamination, corrosion). Also a damage indicator which locates, quantifies and classifies the damage is in progress and will be presented in the future work.

REFERENCES

[1] Staszewski, W.J., Boller, C., Tomlinson, G.,*Health Monitoring Of Aerospace Structures. Smart Sensors And Signal Processing*, Wiley & Sons Ltd., 2004.

[2] Rose, J.L. A Baseline and Vision of Ultrasonic Guided Wave Inspection Potential *Journal of Pressure Vessel Technology*, Vol. 124, pp. 273-282.

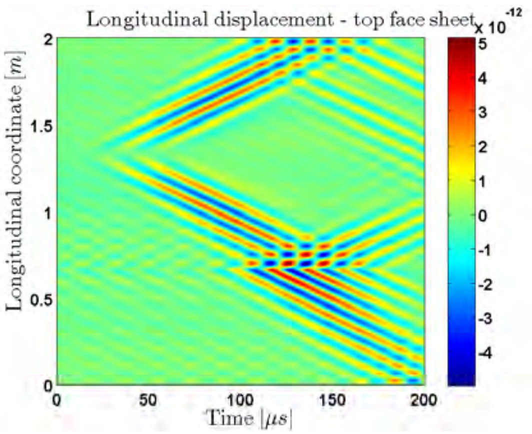

(a)

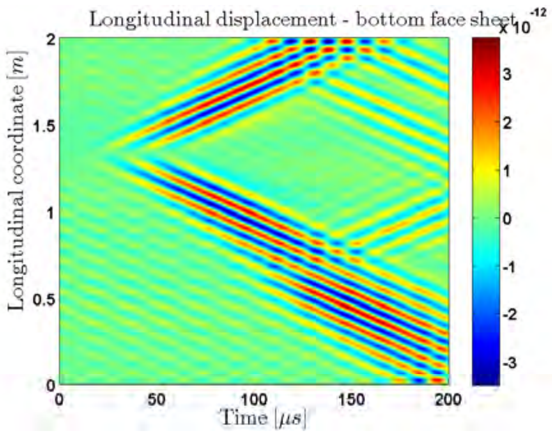

(b)

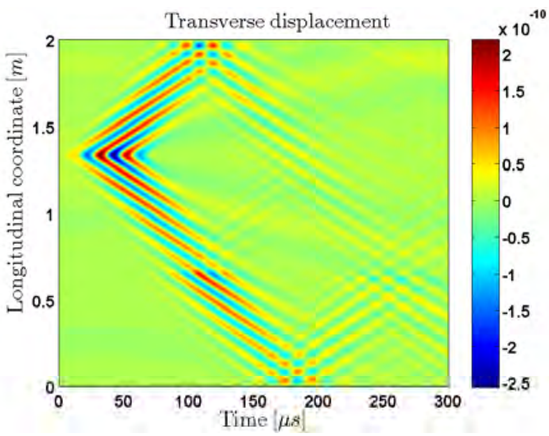

(c)

Figure 6: Displacements as function of time and longitudinal coordinate (a) Longitudinal displacement in the top face sheet; (b) Longitudinal displacement in the bottom face sheet and (c) Transverse displacement. The length of the notch is $\Delta l = 0.01$m.

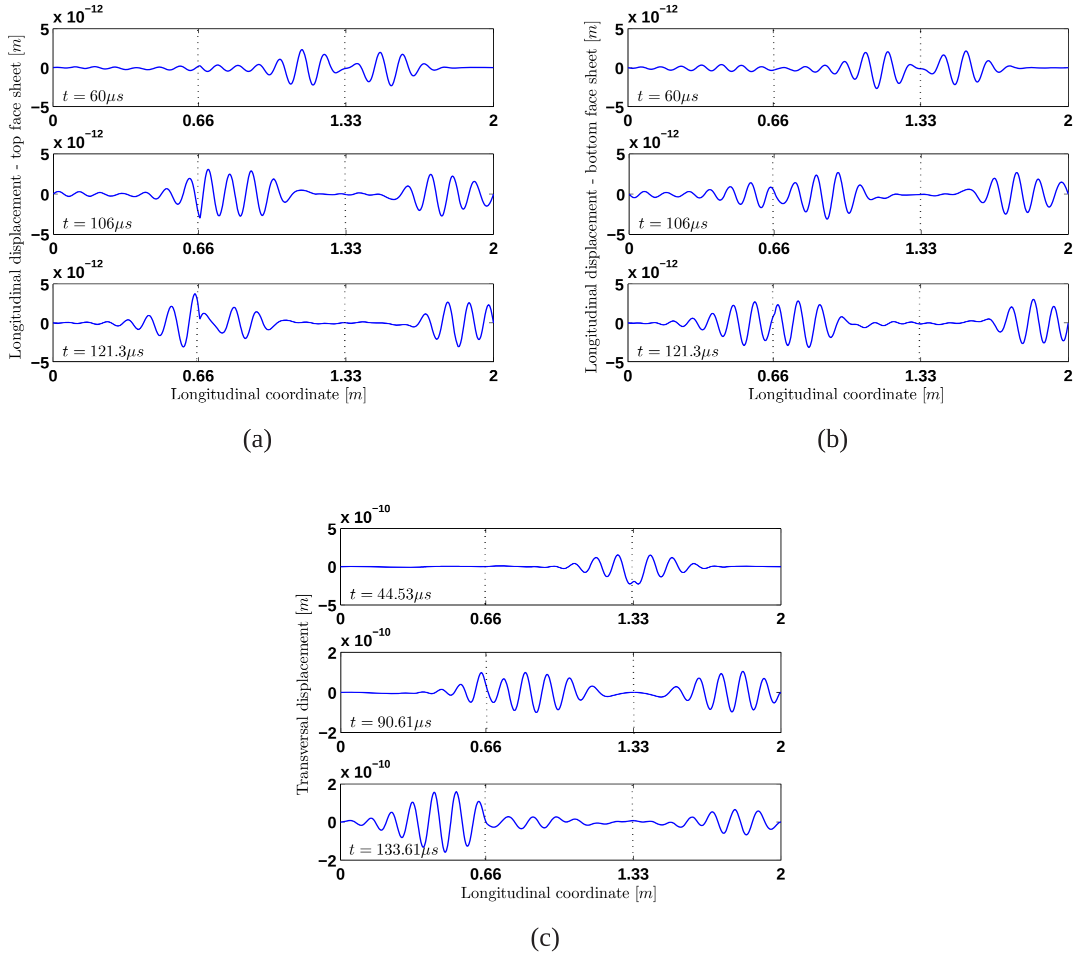

Figure 7: Displacements as function of time and longitudinal coordinate (a) Longitudinal displacement in the top face sheet; (b) Longitudinal displacement in the bottom face sheet and (c) Transverse displacement. One dotted line shows notch location $x_d = 0.66$m whereas the second dotted line shows load location $x_d = 1.33$m.

[3] Giurgiutiu, V., Tuned Lamb Wave Excitation and Detection With Piezoelectric Wafer Active Sensor of Structural Health Monitoring. *Journal of Intelligent Material Systems and Structures*, Vol. 16, No. 4, April 2005, pp. 291-305.

[4] Sharma,V., Ruzzene,M. , Hanagud,S. 2006. Damage index estimation in beams and plates using laser vibrometry. *AIAA Journal*, 44, 919-923.

[5] Ruzzene M. Frequency/wavenumber Filtering For Improved Damage Visualization *Smart Materials and Structures*, In press, November 2007.

[6] Ashby, M., Evans, A., Fleck, N., Gibson, L.J., Hutchinson, J.W., Wadley, H.G., 2000. *Metal Foams: A Design Guide, Boston, Butterworth Heinemann*.

[7] Gibson, L.J., Ashby, F., 1997. *Cellular Solids: Structure and Properties*, Cambridge, Cambridge University Press.

[8] J.F. Doyle,1997. Wave Propagation in Structures. Springer-Verlag, New York.

[9] Lee, U., Kim, J., Leung, A.Y.T., 2000. The Spectral Element Method in Structural Dynamics. The Shock and Vibration Digest 32(6), 451-465.

[10] Apetre,N., Ruzzene, M., Hanagud, S., Gopalakrishnan, S.. Spectral and Perturbation Analysis of First Order Beams with Notch Damage. Accepted for publication to the *Journal of Applied Mechanics*. August 2007.

[11] Mead, D.J. and Markus, S.The forced vibration of a tree layer, damped sandwich beam with arbitrary boundary conditions. *Journal of Sound and Vibration*, **10**, 163-175, 1969.

[12] H. Luo, S. Hanagud, 1997. An integral equation for changes in the structural characteristics of damaged stuctures, International Journal of Solids and Structures, 34. (35-36), 4557-4579

[13] Lestari, W., 2001. Damage of Composite Structures: Detection Technique, Dynamic Response and Residual Strength, PhD Thesis, Georgia Institute of Technology.

8th International Conference on Sandwich Structures
ICSS 8
A. J. M. Ferreira (Editor)

FRACTURE MECHANICS ANALYSIS OF A MODIFIED TSD SPECIMEN

Christian Berggreen[*] and Leif A. Carlsson[†]

[*] Department of Mechanical Engineering
Technical University of Denmark
Nils Koppels Allé, Building 403, DK-2800 Kgs. Lyngby, Denmark
e-mail: cbe@mek.dtu.dk, web page: http://www.mek.dtu.dk

[†] Department of Mechanical Engineering
Florida Atlantic University
777 Glades Road, Boca Raton, FL 33431, USA
e-mail: carlsson@fau.edu, web page: http://www.me.fau.edu

Key words: Sandwich structures, Fracture mechanics, Interfaces, Mixed mode loading.

Summary. *The Tilted Sandwich Debond (TSD) specimen has been recognized as a viable candidate for characterization of the face/core fracture resistance. Analysis, however, shows that the range of phase angles that can be realized by altering the tilt angle is quite limited. A parametric study however shows that a way to extend the mode-mixity span of the TSD specimen is to reinforce the loaded upper face with a stiff metal plate. In this way, the range of phase angles is extended to a practical range. Guidelines on selection of thicknesses of the reinforcement, and design considerations for further modifications are provided.*

1 INTRODUCTION

The Tilted Sandwich Debond (TSD) specimen, shown in Fig. 1, was introduced as a debond test for foam cored sandwich specimens in 1999 by Li and Carlsson [1]. The specimen is tilted which means that the debonded face will be subject to an axial load, P_A, in Fig. 1, in addition to the normal load, P_N ($P_A = P \sin\theta$, $P_N = P \cos\theta$). The axial load was initially thought to promote a negative shear stress at the crack tip that would mitigate the shear stress due to the bimaterial interface and counter the tendency for the crack to kink down into the core, Fig. 2. Testing of foam cored sandwich specimens, however, showed that the crack initially kinked down into the core (although the crack returned to the upper face/core interface as the crack propagated further) [1]. Experimental test results at different tilt angles revealed similar fracture resistance curves (R-curves) and subsequent analysis [2] revealed that the phase angle for a typical TSD specimen remains quite unaffected by the tilt angle.

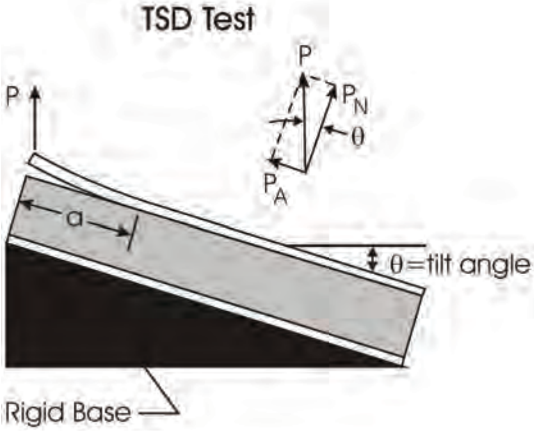

Figure 1: Schematic representation of the conventional TSD specimen.

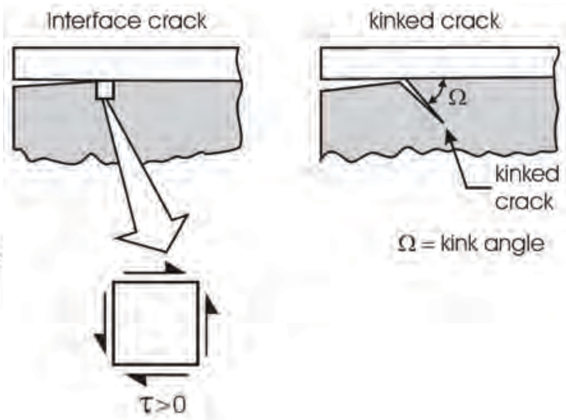

Figure 2: Illustration of crack kinking into the core under positive shear at the crack tip.

It is generally recognized that the fracture toughness for propagation of an interface crack between two dissimilar materials depends on the mode-mixity often expressed as a "phase angle", ψ, defined by the inverse tangent of the ratio between the mode II and mode I stress intensity factors ($\psi_R = arctan(K_{II}/K_I)$). Pure mode I corresponds to $\psi_R = 0$, while pure mode II corresponds to $\psi_R = \pm 90$[1]. Consequently, a large magnitude of the phase angle indicates a mode II dominated loading.

It should be pointed out that generally positive shear ($K_{II} > 0$), associated with a positive shear stress ahead of the crack tip, see Fig. 2, tends to promote kinking of the crack into the core [3,4]. Conversely, a negative shear stress, $\tau < 0$, will generally promote interface growth, although cases have been reported where negative shear leads to crack kinking into the face sheet [5,6]. The face sheets in the specimens examined by Berggreen, et al. [5] and Lundsgaard-Larsen, et al. [6] were composite laminates. For metal faces kinking is not possible.

A full characterization of debond failure requires testing over a wide range of mode-mixities. A very intriguing test method has been devised by Sørensen et al. [7] for monolithic composites and later applied for sandwich by Østergaard et al. [8] and modified by Lundsgaard-Larsen, et al. [9], where the ends of a DCB specimen are loaded by moments where the directions of the moments and their relative magnitudes can be varied. This test is denoted "DCB-UBM" where UBM represents "unequal bending moments". This method, furthermore, produces stable crack growth if run under displacement control since the crack loading does not change with crack length. Despite the many advantages with this test, it requires a very tall test frame and quite complex fixturing and instrumentation. Hence, there is need for a more simple mixed mode test for sandwich specimens.

[1] Given here as the reduced formulation (subscript "R"), thus assuming the oscillatory index $\varepsilon = 0$, and designating the stress intensity factors K_I and K_{II} with roman subscripts.

Preliminary finite element analysis of the TSD specimen by the 1st author revealed that the mode-mixity changed with the thickness of the upper loaded face sheet, and it was also found that the sensitivity to tilt angle increased with increasing face thickness. This finding justified more in-depth analysis, and it is the objective of this paper to provide analysis and guidelines for designing a modified TSD specimen for a desired phase angle range.

2 SOLUTIONS FOR INTERFACE CRACKS

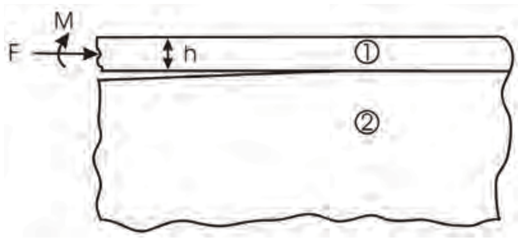

Figure 3: Face sheet (1) subject to edge loads supported by an infinite core (2).

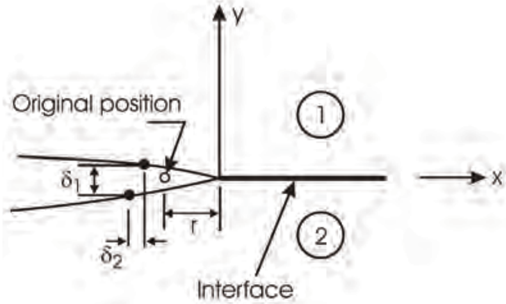

Figure 4: Crack flank displacements. Open circle: point on the crack faces before loading. Filled circles: Position of point after loading.

Linear-elastic fracture mechanics for debonding of layered materials has been considered by several authors, see the extensive review provided by Hutchinson and Suo [10]. A "TSD like" specimen was considered, see Fig. 3. The loading and geometry shown in Fig. 3 are representative for a long TSD specimen with a long crack length with the face sheet subject to an axial edge load and edge moment[2]. The solution for the stress intensity factors for this specific geometry and loading may be extracted from the general analysis of beam-like specimens presented by Hutchinson and Suo [10],

$$K_1 + iK_2 = h^{-i\varepsilon}\left(\frac{1-\alpha}{1-\beta^2}\right)^{1/2}\frac{1}{\sqrt{2}}\left(Fh^{-1/2} - i2\sqrt{3}Mh^{-3/2}\right)e^{i\omega} \quad (1)$$

where K_1 and K_2 are "components" of the complex stress intensity factor, and h is the thickness of the face sheet, F is the axial load and M the pure moment acting at the edge of the debonded face sheet. ε is the oscillatory index given for isotropic materials by

$$\varepsilon = \frac{1}{2\pi}\ln\left(\frac{1-\beta}{1+\beta}\right) \quad (2)$$

where α and β are a bimaterial interface constants (Dundurs parameters [11]) and defined together with the geometry specific parameter ω in [10].

[2] The transverse load at the cut subsection is here neglected.

It is widely recognized that in most cases the stress oscillation occur in an extremely narrow region ahead of the crack tip. Further, it is common practice to suppress the oscillating singularity by letting $\alpha = \beta = 0$ in the expression (1) for the stress intensity factors. With $\alpha = \beta = 0$, K_1 and K_2 mathematically retain their conventional meaning as measures of the intensities of the tensile and shear stress fields ahead of the crack tip, i.e., $K = K_I + i\ K_{II}$. However, in this paper we will examine the TSD specimen using both complex and conventional stress intensity factors, and from here on designated as the full and reduced formulation respectively.

Consequently, both a reduced ($\varepsilon = 0$) and full ($\varepsilon \neq 0$) mode-mixity definition can be stated in terms of phase angles,

$$\psi_F = \arctan\left(\frac{\mathrm{Im}\left[Kl^{i\varepsilon}\right]}{\mathrm{Re}\left[Kl^{i\varepsilon}\right]}\right) \qquad \psi_R = \arctan\left(\frac{K_{II}}{K_I}\right) \tag{9a,b}$$

where l is defined as the characteristic length of the crack problem. For sandwich debond problems the characteristic length is often chosen as the face thickness, however, the characteristic length can be chosen arbitrary and will just phase-shift the phase angle. For more details see [10].

TSD Analysis

The TSD specimen can be approximately modeled applying (1) over a range of tilt angles, θ, with:

$$F = -P\sin\theta \qquad M = Pa\cos\theta \tag{10a,b}$$

where P is the vertical force and θ is the tilt angle, see Fig. 1. Assuming the reduced formulation ($\varepsilon = \beta = 0$), equations (1) and (10) yield,

$$K_I = \sqrt{\frac{(1-\alpha)}{2h}}\left(-\sin\theta\cos\omega + 2\sqrt{3}\left(\frac{a}{h}\right)\cos\theta\sin\omega\right) \tag{11a}$$

$$K_{II} = \sqrt{\frac{(1-\alpha)}{2h}}\left(-\sin\theta\sin\omega - 2\sqrt{3}\left(\frac{a}{h}\right)\cos\theta\cos\omega\right) \tag{11b}$$

For a TSD specimen with a thin face sheet and a long crack it is noted from Eqs. (11) that the 2nd terms will dominate the expressions for K_I and K_{II}. Hence, the phase angle, ψ_R, becomes

$$\psi_R = \arctan\left(\frac{K_{II}}{K_I}\right) = -\arctan(\cot\omega) \tag{12}$$

For a homogeneous TSD specimen, Hutchinson and Suo [10] found $\omega = 52.1^o$. Hence, the phase angle becomes: $\psi_R = -37.9^o$. For bimaterial specimens, Hutchinson and Suo [10] provides results for the angle ω in graphical form over the range ($-0.8 \leq \alpha \leq 0.8$). From the analysis in [10] it can be noted that ω is increasing, when α is increasing (larger bimaterial mismatch), which will result in a smaller magnitude of the negative phase angle, hence a more mode I dominated crack loading. It is further noted that the mode-mixity is independent of the tilt angle and the thickness of the face sheet according to this limit analysis ($a >> h$).

For shorter crack lengths, however, it is not appropriate to replace the moment, M, in Eq. (1) with the normal force component ($Pcos\theta$) times the crack length (a) as in Eq. (10b). When the crack length to face thickness ratio (a/h) becomes smaller it becomes necessary to consider the influence of the transverse shear component of force on the crack tip loading. Such analysis has been presented by Ferrie et al. [12] and Li et al. [13] for delaminations in composites and layered materials. Ferrie et al. [12] examined buckling-driven propagation of delaminations in compression loaded columns while Li et al. [13] examined more general loading configurations. By the Ferrie et al. and Li et al. analyses the framework developed by Hutchinson and Suo [10] for axial load and bending moment has been extended to incorporate shear loading. When a shear force is acting there will be an additional contribution to the energy release rate and shear will also alter the mode-mixity. The shear force will cause rotation near the crack tip of sections of the loaded face. Such rotations are due to shear strain and "root rotation", which is rotation of the crack tip in excess of the transverse shear strain.

For the geometry and loading examined by Li et al. [13] they found that reduced crack length-to-face thickness ratio (a/h) for a transversely loaded face sheet ($\theta = 0$ in the TSD configuration), led to quite substantial increases in the phase angle. Hence, for the TSD geometry, it seems plausible that a thicker face or a steel plate reinforced face may be a mean to substantially increase the shear loading. From a practical point of view it is difficult to increase the face thickness just for testing purposes. The most viable option to reinforce the loaded face is using a steel plate that is adhesively bonded to the upper face. Steel is readily available and is much stiffer than most composite face sheets. In this paper we will focus attention to sandwich specimens with composite face sheets, but the analysis is valid also for face sheets reinforced with the same material.

3 NUMERICAL FRACTURE MECHANICS PARAMETRIC ANALYSIS

The effect of the proposed stiffening of the loaded face sheet on the phase angle is investigated through a limited numerical parametric study. A schematic representation of the modified TSD-specimen can be seen in Figure 5.

The parameters that will be varied are the reinforcement thickness, h_r, and the tilt angle, θ. The chosen configuration consists of *2 mm* face sheets made of E-glass woven rovings with epoxy resin and a *25 mm* Divinycell H100 foam core. The reinforcement material, glued to the upper face sheet, is steel. Furthermore, in order to maximize the effect of the transverse shear effect a short crack length relative to the specimen length is chosen. Geometrical and mechanical properties applied in the parametric analysis can be found in Table 1 and 2 respectively.

In order to determine fracture mechanical properties, i.e. energy release rate and mode-mixity, for the various configurations of the modified TSD specimen, a J-integral calculation and the Crack Surface Extrapolation (CSDE) method was applied through relative crack flank displacements by means of a finite element analysis.

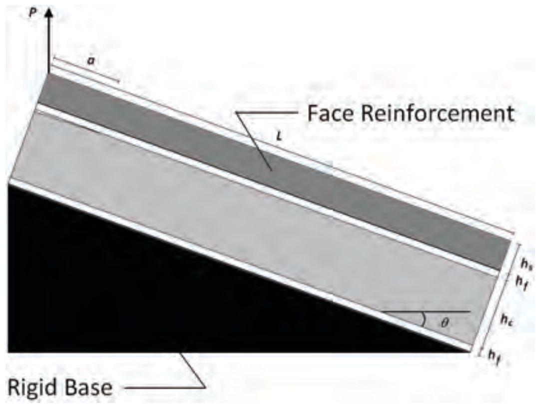

Figure 5: Schematic representation of the modified *plain* TSD specimen.

Geometrical Properties		
Specimen length (mm)	L	200
Face thickness (mm)	h_f	2
Core thickness (mm)	h_c	25
Crack length(mm)	a	25
Reinforcement thicknesses (mm)	h_r	1, 2, 4, 8, 12
Tilt angles (˚)	θ	-85, -75, -60, -30, 0, 30, 60, 75, 85

Table 1 : Geometrical properties in the parametric analysis.

Mechanical Properties					
Face			**Core**		
In-plane Young's modulus (GPa)	E_1, E_2	20.6	Young's modulus (MPa)	E_c	130
Out-of-plane Young's modulus (GPa)	E_3	9.9	Shear modulus (MPa)	G_c	35
In-plane shear modulus (GPa)	G_{12}	3.1	Poisson's ratio (-)	ν_c	0.32
Out-of-plane shear modulus (GPa)	G_{13}, G_{23}	2.9	**Steel**		
In-plane Poisson's ratio (-)	ν_{12}	0.12	Young's modulus (GPa)	E_s	210
Out-of-plane Poisson's ratio (-)	ν_{13}, ν_{23}	0.37	Poisson's ratio (-)	ν_s	0.3

Table 2 : Mechanical properties applied in the parametric analysis.

The CSDE-method was presented earlier by Berggreen [5] in combination with a 2D finite element model similar to the one applied in the present parametric analysis. Energy release rate and mode-mixity expressions as function of relative crack flank opening and shearing displacements (see Figure 4) can be found together with further details in [5].

The finite element model applied in the parametric analysis consists of 4 and 8 noded iso-parametric plane elements. In order to capture relative crack flank displacements a highly densified mesh is applied in a region close to the crack tip. Furthermore, the dense mesh region is divided into element rings which are used for individual J-integral calculations which are then averaged into a final value to be compared with the energy release rate achieved through relative crack flank displacements and the CSDE-method. The mesh densities applied in the finite element model can be seen in Figure 6.

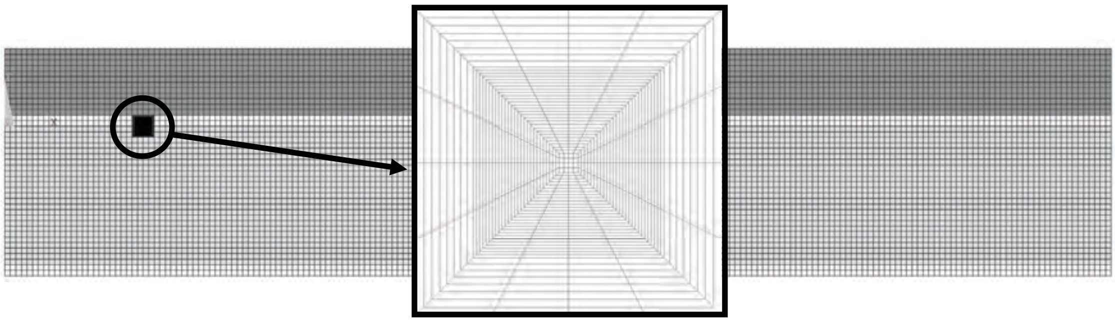

Figure 6: Finite element mesh applied in parametric analysis of the modified *plain* TSD specimen (h_r = *12 mm*). (a) global mesh and (b) near tip mesh region. Min. element size is *3.33 μm*.

The TSD loading configuration is applied by restricting all DOF's at the bottom surface of the lower face sheet. Axial, P_A, and normal, P_N, loads are applied at the upper left corner of the reinforcement layer according to the tilt angle, θ.

$$P_A = P\sin\theta \qquad\qquad P_N = P\cos\theta \qquad\qquad (13a,b)$$

The finite element analysis is geometrically linear, and the load is increased for all specimen configurations until an energy release rate level of *400 J/m²* has been reached, which is comparable to the fracture toughness, G_{Ic}, of the H100 foam core [14].

Figure 7 shows the phase angle calculated according to the reduced formulation ($\varepsilon = 0$) as a function of the tilt angle for various reinforcement thicknesses. First it can be seen that for the traditional TSD specimen with no reinforcement of the upper face sheet ($h_r = 0$) the mode-mixity is almost constant over a span of tilt angles between $\theta = -75^\circ$ to $\theta = 75^\circ$, confirming the earlier analyses and testing by Li and Carlsson [2]. However, as it also can be seen in Figure 7, the effect of reinforcing the upper face sheet with a stiff steel layer results as expected in an increased range of phase angles. With a reinforcement thickness of *12 mm* the variability of the phase angle range is increased to about $\psi_R = -70^\circ$ for $\theta = 85^\circ$ to $\psi_R = 70^\circ$ for $\theta = -85^\circ$.

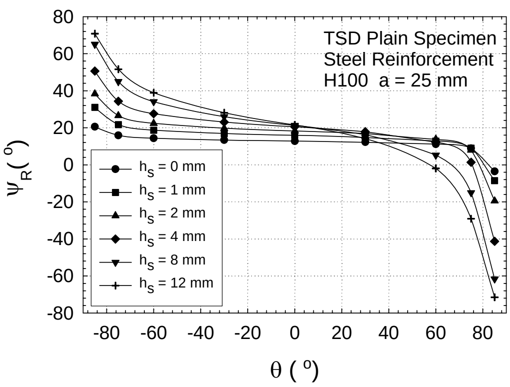

Figure 7: Phase angle (reduced formulation) as function of tilt angle for a *plain* reinforced TSD-specimen.

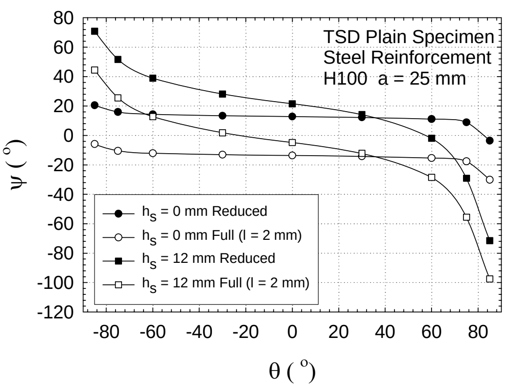

Figure 8: Full versus reduced phase angle formulation for the conventional (h_r = *0 mm)* and reinforced (h_r = *12 mm)* TSD-specimens. *l = 2 mm*.

As it was indicated earlier, the increase in the phase angle range can be associated with the increasing amount of shear loading and subsequent crack tip root rotation when the reinforcement layer thickness, h_r, is increased. The amount of root rotation at a tilt angle of $\theta = 75^\circ$ is compared in Figure 9 for the traditional ($h_r = 0$) and the modified TSD-specimen with a reinforcement thickness of $h_r = 12\ mm$. It is evident from the deformation plot that an increased root rotation is present for the reinforced TSD-specimen in accordance with the theoretical prediction by Li et al. [13].

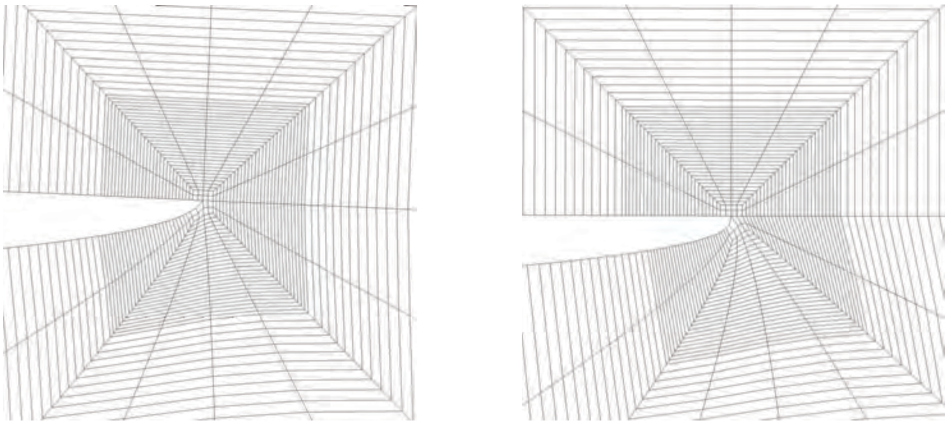

(a) (b)

Figure 9: Crack tip root deformations at $\theta = 75$. (a) traditional TSD-specimen, and (b) reinforced TSD-specimen, $h_r = 12\ mm$.

In Figure 7 it is furthermore observed that the phase angle for tilt angles up to between $\theta = 60^\circ$ to $\theta = 80^\circ$ is positive and mode I dominated for all investigated reinforcement thicknesses, indicating that kinking out of the interface is likely. It was mentioned earlier that the homogeneous TSD specimen has a negative phase angle, but that the mode-mixity was moving towards a mode I dominated condition when the bimaterial mismatch parameter α went towards the theoretical limit of 1. For the sandwich configuration chosen in the parametric study the mismatch is extreme (close to 1.0) and the calculated phase angles are shifted towards mode I dominance, which confirms the tendencies shown through the analytical modeling of the TSD specimen even though the effect of the transverse shear is not included. Furthermore, the kinking observations in the experimental investigation by Li and Carlsson [1] are furthermore confirmed by the calculated positive phase angles in present parametric analysis.

Originally prevention of kinking out of the interface was one of the main objectives for the development of the traditional TSD-specimen. As shown above, kinking is still a potential problem for the reinforced TSD-specimen for low tilt angles. However, as it can be observed in Figure 8, the magnitude of the characteristic length using the full mode-mixity formulation will phase shift the mode-mixity towards negative mode-mixities compared to the mode-mixities based on the reduced formulation. So in order to take account of kinking when measuring fracture toughnesses for specific mode-mixities, it is proposed that the mode-mixity is determined using the full formulation and the characteristic length is calibrated so that kinking sets in at a phase angle of $\psi_F = 0^\circ$.

4 DESIGN RECOMMENDATIONS

In the parametric analysis described above, the possibility for local failure of the TSD-specimen reinforced with a stiff steel layer of a given thickness was not considered. Especially at the right end of the face and reinforcement, see Figure 5, compression stresses in the core can potentially rise above the crushing strength of the core which would affect the mode-mixity at the crack tip. Exact modeling of the crushing behavior in the core is complicated due to the cellular micro-structure of the foam material, thus local crushing in the core should be avoided.

Furthermore it was observed in the parametric analysis that the free left end of the core, see Figure 5, undergoes extensive deformations due to the local crack tip root rotations, and in effect limiting the transverse shear effect on the mode-mixity. Thus, in order to localize the crack tip root rotations to the crack tip region and thereby maximizing the effect on the mode-mixity, it is desirable to reinforce the left core end, so that the edge is held straight for all load levels and tilt angles.

In Figure 10 the additional modifications to the TSD-specimen are illustrated. The crushing of the core is prevented by adding a vertical stiff link at both sides of the specimen pinned to the face reinforcement and base respectively. In order to further prevent localized loading of the core, the link is located as close to the reinforcement right end as possible, and the end of the face reinforcement have been rounded. The connection between the pins, links, reinforcement and base should furthermore be lubricated prior to testing or bearings should be added in order to limit friction. In Figure 10 the left end reinforcement of the core has been added, by bolting a stiff metal block to the base and gluing the left end of the core and lower face sheet onto the metal block.

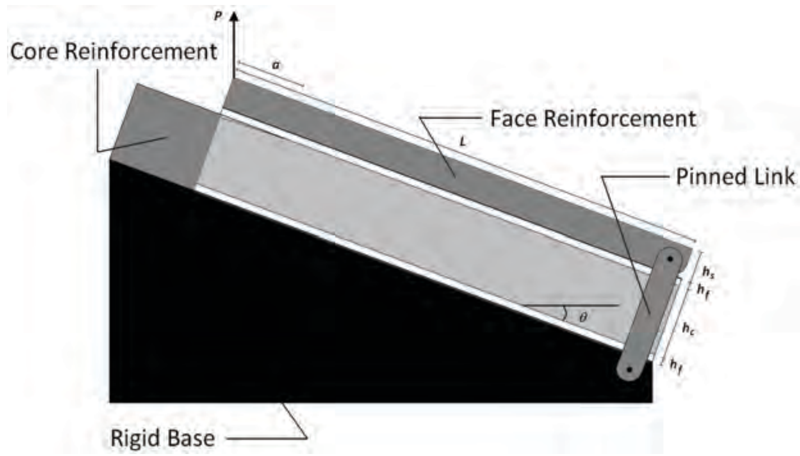

Figure 10: Further design modifications with pinned links at both sides of the specimen and an additional block, reinforcing the left end of the core and lower face.

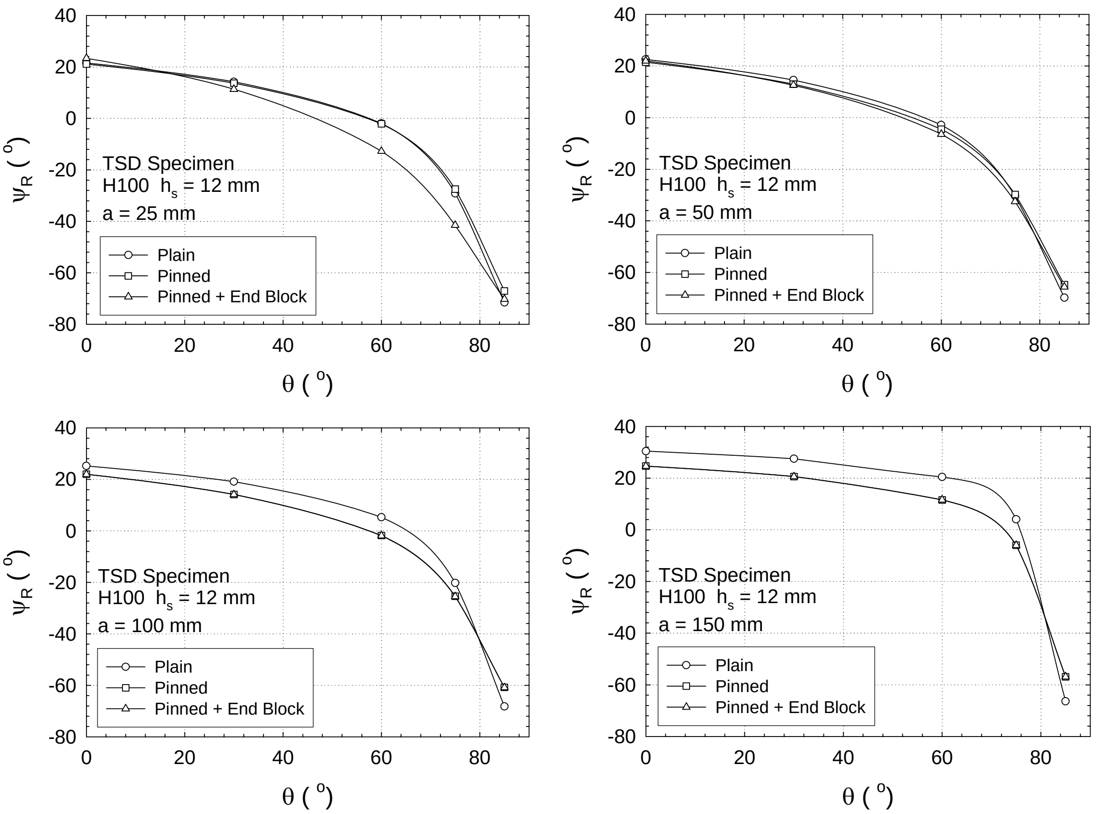

Figure 11: Phase angle vs. tilt angle for the *plain*, *pinned* and *pinned+block* modification versions. (top left) *a = 25 mm*, (top right) *a = 50 mm,* (bottom left) *a = 100 mm and* (bottom right) *a = 150 mm*. (Reduced formulation)

The effect on the phase angle (reduced formulation) by the additional design modifications depicted in Figure 10, have been investigated applying the same numerical model and for similar specimen configurations as in the previous section. Furthermore, the effect of the crack length, *a*, has been investigated. However, in the analyses only positive tilt angles have been included, as negative tilt angles most likely will result in kinking out of the interface. Three versions of the modified TSD specimen have been investigated, all with a reinforcement thickness of $h_r = 12$ *mm*:

- A plain version, similar to what was investigated in the parametric analysis in the previous section, (*plain*)
- A purely pinned version, similar to Figure 10 but without core reinforcement. (*pinned*)
- A pinned and end block reinforced version, similar to Figure 10. (*pinned+block*)

Figure 11 shows the phase angle for all three TSD specimen versions as a function of the tilt angle and for four different crack lengths, *a = 25, 50, 100, 150 mm*. It can be seen in Figure 11 (top left) that the reinforcement of the left core end of the specimen has a significant additional effect on the variability of the phase angle. For the *plain* version, the zero phase angle condition is reached at a tilt angle of approximately $\theta = 57^{\circ}$, but for the *pinned+block* version the zero crossing level is already reached at approximately $\theta = 46^{\circ}$. However, for high tilt angles the phase angle is approximately similar. As the crack length increases the effect of the block reinforcement of the left core end decreases, and at a crack length, $a = 50\ mm$, the effect on the mode-mixity is negligible, see Figure 11 (top right). Conversely, the pinned link modification (*pinned* version) is apart from limiting local crushing of the core as discussed above, seen to only have an effect on the variability of the phase angle for long crack lengths. In Figure 11 (bottom left and right) it can be seen that the zero phase angle condition is reached earlier compared to the *plain* version, however, the effect is less significant compared to the *pinned+block* version for small crack lengths. Furthermore, for very long crack lengths the phase angle variation is seen to be limited for all modification versions, and large tilt angles are necessary in order to provoke significant phase angle variation, and for these high tilt angles it is finally observed that the phase angle is approximately the same for all modification versions.

In Figure 12 the phase angle has been plotted against crack length for the *pinned* and *pinned+block* modification versions. It is evident that the phase angle is approximately constant for the *pinned* version until a crack length of about *100 mm*, where the angle decreases significantly. For the *pinned+block* version the phase angle variation for a propagating crack is more pronounced over the entire crack length regime.

Even though the *pinned* version has a nearly constant phase angle up to crack lengths of about *100 mm*, a significant variability of the mode-mixity is only achieved for high tilt angles, where the phase angle gradient is high, increasing the level of uncertainty in practical measurements. Thus, the modified TSD-specimen cannot easily be applied for fatigue crack growth characterization, where a constant phase angle is desired.

However, the present analyses illustrates that the modified TSD specimen and testing procedure is highly applicable for simple quasi-static face/core interface fracture toughness measurements, and especially the *pinned+block* modification version offers a significant variability of the phase angle, desirable from a practical point of view.

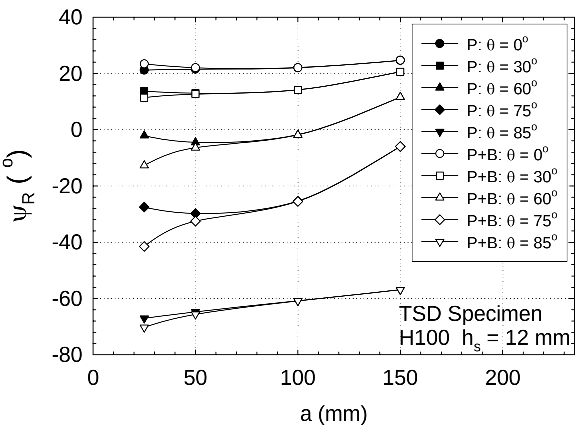

Figure 12: Phase angle vs. crack length for the *pinned* and *pinned+block* modification versions. "P" indicates the *pinned* version, and "P+B" the *pinned+block* version. (Reduced formulation)

5 CONCLUSION

The analysis of the conventional TSD specimen confirms a negligible variability of the phase angle for practical applicable tilt angles. However, it was proven through a limited parametric analysis that by reinforcing the loaded face sheet by a stiff metal plate, an increase in transverse shear lead to increased root rotation of the crack tip resulting in considerable expansion of the range of phase angles. Design considerations furthermore outlined that mode-mixity variability can be further improved by reinforcing the core at the cracked end of the specimen, and core crushing can be avoided by using stiff pinned links at the specimen end. The modified TSD specimen and test was identified as a viable and promising candidate for mixed mode fracture toughness measurements. Further parametric analyses should be carried out together with experimental benchmarking of the specimen against fixed phase angle specimens, such as for example the DCB and CSB.

AWKNOWLEDGEMENTS

This work has been performed within the context of the Network of Excellence on Marine Structures (MARSTRUCT) partially funded by the European Union through the Growth Programme under contract TNE3-CT-2003-506141.

REFERENCES

[1] X. Li and L. A. Carlsson, "The tilted sandwich debond (TSD) specimen for face/core interface fracture characterization", *Journal of Sandwich Structures and Materials*, 1, 60-75 (1999).
[2] X. Li and L. A. Carlsson, "Fracture mechanics analysis of the tilted sandwich debond (TSD) specimen", *Journal of Composite Materials*, 35:23, 2145-2168 (2001).
[3] S. Prasad and L. A. Carlsson, "Debonding and Crack Kinking in Foam Core Sandwich Beams – I. Analysis of Fracture Specimens", *Engineering Fracture Mechanics*, 47(6):813-824 (1994).
[4] S. Prasad and L. A. Carlsson, "Debonding and Crack Kinking in Foam Core Sandwich Beams – I. Analysis of Fracture Specimens", *Engineering Fracture Mechanics*, 47(6): 825-841 (1994).
[5] C. Berggreen, B. C. Simonsen and K. K. Borum, "Experimental and Numerical Study of Interface Crack Propagation in Foam Cored Sandwich Beams", *Journal of Composite Materials*, 41(4):493-520 (2007).
[6] C. Lundsgaard-Larsen, C. Berggreen and L. A. Carlsson, "On The Use of a Woven Mat to Control The Crack Path in Composite Sandwich Specimens with Foam Core", *ASME Int'l Mech. Eng. Congress and Exposition, Nov. 11-15, 2007, Seattle, WA.*
[7] B. F. Sørensen, K. Jørgensen, T. K. Jacobsen and R. C. Østergaard, "DBC Specimen Loaded with Uneven Bending Moments", *Int. J. Fract.*, 14(1): 163-176 (2006).
[8] R. C. Østergaard, B. F. Sørensen and P. Brøndsted, "Measurement of Interface Fracture

Toughness of Sandwich Structures under Mixed Mode Loadings", *Journal of Sandwich Structures and Materials*, 9, 445-466 (2007).
[9] C. Lundsgaard-Larsen, B. F. Sørensen, C. Berggreen and R. C. Østergaard, "A modified DCB sandwich specimen for measuring mixed mode cohesive laws", *Engineering Fracture Mechanics*, in press (2008).
[10] J. W. Hutchinson and Z. Suo, "Mixed Mode Cracking in Layered Materials", *Adv. Appl. Mech.*, 29: 63-191 (1992).
[11] J. Dundurs, "Edge-Bonded Dissimilar Orthogonal Elastic Wedges", *J. Appl. Mech.*, 36: 630-652, (1969).
[12] C. H. Ferrie, I. Sheinman and G. A. Kardomateas, "The effect of transverse shear on the postbuckling and growth characteristics of delaminations in composites", *Journal of Engineering Materials and Technology*, 121(4) (1999).
[13] S. Li, J. Wang and M. D. Thouless, "The Effects of Shear on Delamination in Layered Materials", *J. Mech. Phys. Solids*, 52:193-214 (2004).
[14] G. M. Viana and L. A. Carlsson, "Mechanical properties and fracture characterization of Cross-linked PVC foams", *Journal of Sandwich Structures and Materials*, 4, 99-113 (2002).

8th International Conference on Sandwich Structures
ICSS 8
A. J. M. Ferreira (Editor)

A DEBONDED SANDWICH SPECIMEN UNDER MIXED MODE BENDING (MMB)

Amilcar Quispitupa*, Christian Berggreen* and Leif A. Carlsson†

* Department of Mechanical Engineering
Technical University of Denmark
Nils Koppels Allé, Building 403, DK-2800 Kgs. Lyngby, Denmark
e-mail: amq@mek.dtu.dk and cbe@mek.dtu.dk, web page: http://www.mek.dtu.dk

† Department of Mechanical Engineering
Florida Atlantic University
777 Glades Road, Boca Raton, FL 33431, USA
e-mail: carlsson@fau.edu, web page: http://www.me.fau.edu

Key words: Sandwich structures, Mixed mode bending, Finite element modeling, Experimental mechanics.

Summary. *Face/core interface crack propagation in sandwich specimens is analyzed. A thorough analysis of the typical failure modes in sandwich composites was performed in order to design the MMB specimen to promote face/core debond fracture. Displacement, compliance and energy release rate expressions for the MMB specimen were derived from a superposition analysis. An experimental verification of the methodology proposed was performed using MMB sandwich specimens with H100 PVC foam core and E-glass/polyester non-crimp quadro-axial* $[0/45/90/-45]_s$ *DBLT-850 faces. Different mixed mode loadings were applied using the MMB test rig and debond propagation as failure mode was successfully achieved.*

1 INTRODUCTION

Debonds and other interfacial damages can occur during manufacturing processes, accidental overloads, material manipulation and they might grow under both static and cyclic loading scenarios during the service lifetime of the structure [1-4]. Debonds are of great concern, since the bending stiffness of a sandwich structure is dominated by the contribution of the faces with respect to the neutral axis of the entire sandwich, and in the absence of the bond between faces and core, almost the entire bending stiffness and thus the strength of the structure are lost.

To investigate and measure interface fracture properties, geometries such the cracked sandwich beam (CSB) [5], double cantilever sandwich beam (DCB) [6], tilted sandwich debond (TSD) [7], three point bending sandwich (TPBS) [8], center notched flexure sandwich CNFS [8], single cantilever sandwich (SCS), end-loaded sandwich structure (ELSS) and the DCB subjected to uneven bending moment named DCB-UBM [9] were proposed. However, most of the above mentioned sandwich specimens have their advantages and disadvantages. The disadvantages are typically under mixed mode loading conditions, for instance, the DCB and CSB specimens can only be loaded in global mode I or mode II, respectively. The TSD specimen which seems to be very promising needs a stiffer metal plate as reinforcement on the loaded face sheet in order to reach a wide range of mode-mixities at the debond tip [10]. The DCB-UBM specimen is a DCB sandwich specimen which is loaded by uneven bending moments [9]. The combination of the moments applied to the specimen determines the mode-mixity on the specimen. Despite its advantages, the DCB-UBM uses a complex test fixture to apply the moment to the specimen which might be a limitation if fatigue tests are envisioned. Therefore, a simpler test would be desired to study mixed mode debond fracture of sandwich specimens and the mixed mode bending (MMB) test is a promising candidate. The MMB test fixture originally developed for mixed mode delamination fracture characterization of unidirectional composites [11,12] has been applied in the present study to sandwich specimens, as presented in Figure 1. The MMB test rig subjects the debonded region of the sandwich composite to various combinations of mode I and mode II by varying the lever arm distance *c* of the loading application point.

The main objective of the paper is to provide the necessary tools and methodology for the design of the MMB sandwich specimen for debonds fracture characterization under mixed mode loading.

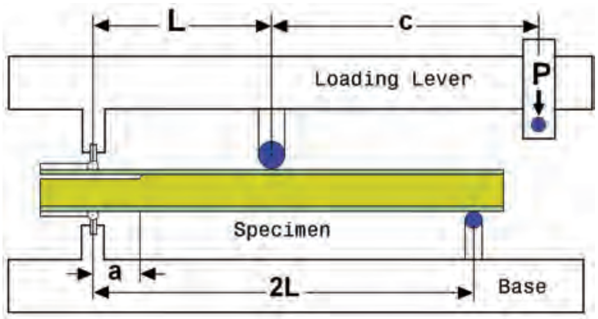

Figure 1 : Mixed mode bending fixture and the debonded sandwich specimen

2 COMPLIANCE AND ENERGY RELEASE RATE FOR THE MMB DEBONDED SANDWICH SPECIMEN

The MMB sandwich specimen is essentially a three-point flexure specimen with a through-width artificial crack at the upper face/core interface with a pulling load at the upper debonded face sheet of the specimen, as shown in Figure 2. The debond is placed at the specimen end to accommodate the sliding mode due to flexural loading (mode II) and the opening due to a pulling load acting at this end (mode I). To derive the analytic expressions for the displacement, compliance and energy release rate for the MMB sandwich specimen, the solutions for the double cantilever beam (DCB [6]) and cracked sandwich beam (CSB [5]) specimens were superimposed by applying a proper kinematic relationship for the loading configuration [13]. The analytical expressions for the MMB displacement, compliance and energy release rate are given in equations (1)-(3) [13].

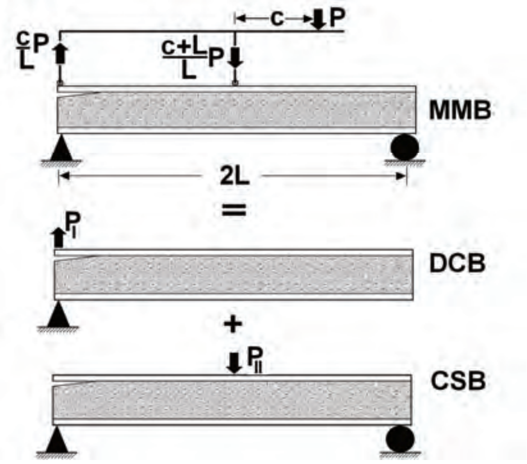

Figure 2 : MMB specimen decomposed into the DCB and CSB components

$$\delta_{MMB} = \frac{c}{L}\delta_{DCB\_upper} + \frac{c-L}{2L}\delta_{DCB\_lower} + \left(\frac{c+L}{L}\right)\delta_{CSB} \tag{1}$$

$$C_{MMB} = \left[\frac{c}{L}C_{DCB\_upper} + \frac{c-L}{2L}C_{DCB\_lower}\right]\left(\frac{c}{L} - \alpha\frac{c+L}{2L}\right) + \left(\frac{c+L}{L}\right)^2 C_{CSB} \tag{2}$$

$$G_{MMB} = \frac{P^2}{2b}\frac{d}{da}\left(\left[\frac{c}{L}C_{DCB\_upper} + \frac{c-L}{2L}C_{DCB\_lower}\right]\left(\frac{c}{L} - \alpha\frac{c+L}{2L}\right) + \left(\frac{c+L}{L}\right)^2 C_{CSB}\right) \tag{3a}$$

$$G_{MMB} = \frac{P^2}{2b^2}\left(\begin{array}{l} \frac{c}{L}\left(\frac{c}{L} - \alpha\frac{c+L}{2L}\right)\frac{4\cdot a^2}{E_f h_f^3}\left[3 + \frac{4.559}{a}\left(\frac{1}{\sqrt[4]{C_f}}\right)\left(\frac{h_f^3 h_c E_f}{E_c}\right)^{1/4} + \frac{1.732}{a^2}\left(\frac{1}{\sqrt[2]{C_f}}\right)\left(\frac{h_f^3 h_c E_f}{E_c}\right)^{1/2}\right] + \\ \frac{c-L}{2L}\left(\frac{c}{L} - \alpha\frac{c+L}{2L}\right)\left[\frac{1}{h_c G_{xz}} + \frac{a^2}{\left(D - \frac{B^2}{A}\right)}\right] + \left(\frac{c+L}{L}\right)^2\left(\frac{a^2\left[(d_{11})_{debonded} - (d_{11})_{\mathrm{int}act}\right]}{8}\right) \end{array}\right) \tag{3b}$$

Expressions for the compliances $C_{DCB\text{-}upper}$, $C_{DCB\text{-}lower}$ and C_{CSB} for upper DCB sub-beam, lower DCB sub-beam and CSB specimens respectively are provided in [5,6,13]. The load P applied to the specimen can be decomposed into two loads, one for mode I and other for the mode II component, as shown in equations (4).

$$P_I = \frac{c}{L}P - \alpha\frac{c+L}{2L}\ ,\ P_{II} = \left(1+\frac{c}{L}\right)P \tag{4a, 4b}$$

Notice that the “pure mode I” and “pure mode II” represents the global loading. As will be shown later, the local mode-mixity may be substantially different. The parameter α measures the asymmetry of the upper and lower sub-beams at the debonded region, further information regarding α can be found in [5,13].

3 DESIGN OF FRACTURE SPECIMEN

The MMB sandwich specimen may fail in several ways including tension or compression failure of the facings, shear failure of the core, core crushing, wrinkling failure of the face in compression, local indentation under concentrated loads besides the anticipated debonding failure of the face/core interface. Special attention is given to the following failure modes, core shear failure, indentation failure, and debond failure. Thus, for debond fracture characterization, the design of the MMB sandwich specimen must promote debond propagation of the face/core interface crack before other undesired failure modes are activated. The failure loads for each mode of failure were calculated in order to determine the controlling failure mechanism for some specific MMB sandwich and mixed mode loadings.

2.1 Core shear failure

The shear stress distribution in the MMB sandwich specimen is similar to the three-point bending loading in regions away from the crack tip. Therefore, for simplicity it is assumed that the shear force is solely carried by the core with a negligible additional contribution from the face sheets [14,15]. Furthermore, from equations (4), the load corresponding to the mode II, P_{II}, is larger than the mode I, P_I. The load P_{II} is also larger than the load P applied to the specimen by a factor of c/L, as shown in equation (4b). Consequently, the shear force at the right support of the MMB specimen is half of P_{II}. Thus, the shear stresses τ_c can be calculated using equation (5).

$$\tau_c = \frac{\frac{1}{2}\left(1+\frac{c}{L}\right)P}{h_c b} \tag{5}$$

Shear failure will occur if the ultimate shear strength of the core τ_{max} is reached or exceeded. The shear failure load can be calculated using equation (6),

$$P_{CS} = \frac{2h_c b\,\tau_{\max} L}{c+L} \tag{6}$$

where P_{CS} is the load that causes core shear failure, h_c is the core thickness, b is the width of the beam and L the half span length of the beam.

2.2 Indentation failure

Indentation failure is a predominant mode of failure in the case of highly localized loads, such as point or line loads. Indentation failure in sandwich structures is generally governed by local yielding of the core followed by plastic deformation of the foam material beneath the contact area. An indentation model for elastic faces and idealized plastic core presented in [14,15] for beams loaded in three-point bending is used to analyze indentation failure in the MMB sandwich specimens. The load P_{indent} that causes indentation, the displacement u_{max} underneath the loading point, and λ_{max} the wave length of the zone affected by the localized load are given by equations (7).

$$P_{indent.} = b \cdot h_f \cdot \left(\frac{\pi^2 \cdot d \cdot E_f \cdot \sigma_c{}^2}{6 \cdot L} \right)^{1/3} \tag{7a}$$

$$u_{\max} = 8t_f \cdot \left(\frac{d}{\pi \cdot L} \right)^{4/3} \left(\frac{E_f}{3 \cdot \sigma_c} \right)^{1/3} \tag{7b}$$

$$\lambda_{\max} = t_f \cdot \left(\frac{\pi^2 \cdot d \cdot E_f}{6 \cdot L \cdot \sigma_c} \right)^{1/3} \tag{7c}$$

where $d = h_c + h_f$, h_c is the core thickness, h_f is the face sheet thickness, σ_c is the compressive strength of the core, L is the half span length and E_f is the elastic modulus of the face sheets.

2.3 Debond failure

In order to predict the debond fracture load, the critical energy release rate (i.e. the fracture toughness, Γ) of the face/core interface at mode I, mode II and/or a combination of those are needed. Fracture toughness values for a few material combinations are available in the literature, however most of them are limited to pure mode I or II [1,3,4,16] with only few examples of measured mixed mode fracture toughness [1,3,4]. Thus, to provide an approximate estimate of the debond fracture load for the MMB sandwich specimen, fracture toughness (Γ) values were selected from the reference [16] for a similar combination of core and face sheet materials, see Tables 1 and 2. The fracture load is obtained from equation (8).

$$P_{DF} = \sqrt{\frac{2b^2 \cdot \Gamma}{\left(\begin{array}{l} \dfrac{c}{L}\left(\dfrac{c}{L} - \alpha\dfrac{c+L}{2L}\right)\dfrac{4 \cdot a^2}{E_f h_f^3}\left[3 + \dfrac{4.559}{a}\left(\dfrac{1}{\sqrt[4]{C_f}}\right)\left(\dfrac{h_f^3 h_c E_f}{E_c}\right)^{1/4} + \dfrac{1.732}{a^2}\left(\dfrac{1}{\sqrt[2]{C_f}}\right)\left(\dfrac{h_f^3 h_c E_f}{E_c}\right)^{1/2}\right] + \\ \dfrac{c-L}{2L}\left(\dfrac{c}{L} - \alpha\dfrac{c+L}{2L}\right)\left[\dfrac{1}{h_c G_{xz}} + \dfrac{a^2}{\left(D - \dfrac{B^2}{A}\right)}\right] + \left(\dfrac{c+L}{L}\right)^2\left(\dfrac{a^2\left[(d_{11})_{debonded} - (d_{11})_{intact}\right]}{8}\right) \end{array} \right)}} \tag{8}$$

It is important to point out that the value taken from the literature is used only for a preliminary design analysis. The assumed interfacial fracture toughnesses for H45, H100 and H200 foam cores are *150*, *310* and *625* J/m^2 respectively [16]. In general, the fracture toughness under mode I is less than mode II. Under mixed mode loading (combination of mode I and mode II) the fracture toughness will be bounded by those in mode I and II [8-10,13]. In addition, for a crack located in an interface between two dissimilar materials, the fracture toughness can depend on the mode-mixity [9,10,13]. Thus, in order to predict the debond fracture loads, the initially assumed fracture toughness values under mode I were increased by a factor of three. This factor was selected based on the results presented in [9] where the fracture toughness for GFRP/H80 as a function of the mode-mixity varies from approximately *300* J/m^2 (dominant mode I, with mode-mixity from ~ *-10°* to ~ *-35°*) to *800* J/m^2 (dominant mode II, with mode-mixity from ~ *-40°* to ~ *-60°*). Thus, a variation in the fracture toughness of around 3 times with respect to dominant mode I is present.

The analysis outlined will be illustrated on various sandwich materials. To enable calculations of the critical failure loads for each failure mode, the mechanical properties for the core and face sheets as well as fracture toughness values for debond fracture load estimation are provided in Tables 1 and 2.

Properties	**H45**	**H100**	**H200**
Compressive Strength (MPa)	0.6	2	4.8
Compressive Modulus (MPa)	50	135	240
Tensile Strength (MPa)	1.4	3.5	7.1
Tensile Modulus (MPa)	55	130	250
Shear Strength (MPa)	0.56	1.6	3.5
Shear Modulus (MPa)	15	35	85
Shear Strain (%)	12	40	40
Fracture Toughness G_{IC}(J/m^2)	150	310	625

Table 1 : Mechanical properties of PVC foams [16,17]

Face DBLT-850 (0/45/90/-45)	
Young's modulus (E), GPa	16.4
Shear modulus (G), GPa	2.7
Poisson's modulus (ν)	0.306

Table 2 : Mechanical properties in plane of the face sheets [1]

The properties listed in Tables 1 and 2 were used to estimate the failure loads for each failure mode, as presented in Table 3. The results presented in Table 3 were calculated using a face sheet thickness of *2 mm*, width of *35 mm* and length of *150 mm* (*2L*). Furthermore, three initial crack lengths (*2.5*, *5* and *25 mm*) and various core thicknesses were analyzed in order to evaluate their effect on the debond failure load. It is observed that for the combination of material properties and geometries considered, mainly debonding failure is achieved, however, for some MMB geometries core shear failure might occur, especially at small crack lengths. Therefore, it is recommended to avoid very short initial crack lengths in the MMB specimen to avoid the occurrence of other failure modes that would hinder debond failure characterization. In addition, using a relatively thick face sheet (*2 mm*), indentation failure can be avoided.

Foam Type	h_c (mm)	c (mm)	G_I/G_{II}	Initial crack a_o=25mm	Shear Failure KN) Eq.6	Indentation failure (KN) Eq.7a	Debond failure (KN) Eq.8	Dominant Failure mode
H45	29	40	31.8	25	0.74	1.11	0.202	Debonding
	29	40	35	5	0.74	1.11	0.605	Debonding
	29	40	22.8	2.5	0.74	1.11	0.910	Shear
H100	29	30	47.3	25	2.32	2.48	0.405	Debonding
	29	30	22.5	5	2.32	2.48	1.35	Debonding
	29	30	9.4	2.5	2.32	2.48	2.20	Debonding
	29	35	59	25	2.22	2.48	0.35	Debonding
	29	35	29	5	2. 22	2.48	1.10	Debonding
	29	35	14.4	2.5	2.22	2.48	1.75	Debonding
	29	40	70	25	2.12	2.48	0.32	Debonding
	29	40	37.5	5	2.12	2.48	0.96	Debonding
	29	40	19.8	2.5	2.12	2.48	1.48	Debonding
	29	45	82.7	25	2.03	2.48	0.275	Debonding
	29	45	45	5	2.03	2.48	0.855	Debonding
	29	45	25.6	2.5	2.03	2.48	1.28	Debonding
	29	50	94.3	25	1.95	2.48	0.245	Debonding
	29	50	53.3	5	1.95	2.48	0.76	Debonding
	29	50	31.6	2.5	1.95	2.48	1.12	Debonding
	20	40	26.5	25	1.46	2.21	0.308	Debonding
	20	40	26.6	5	1.46	2.21	0.995	Debonding
	20	40	16.9	2.5	1.46	2.21	1.530	Shear
	20	50	35.5	25	1.34	2.21	0.245	Debonding
	20	50	38	5	1.34	2.21	0.770	Debonding
	20	50	27.4	2.5	1.34	2.21	1.150	Debonding
	10	40	4	25	0.73	1.81	0.320	Debonding
	10	40	8.5	5	0.73	1.81	1.070	Shear
	10	40	10	2.5	0.73	1.81	1.690	Shear
H200	29	40	114.5	25	4.63	4.45	0.445	Debonding
	29	40	48	5	4.63	4.45	1.450	Debonding
	29	40	24.8	2.5	4.63	4.45	2.190	Debonding

Table 3 : Predicted failure loads for the MMB sandwich specimen (L=75mm, b=35mm, h_f=2mm)

4 EXPERIMENTAL SETUP

The experimental setup used for the mixed mode bending testing is shown in Figure 3. The MMB sandwich beams consisted of Divinycell H100 PVC foam core and E-glass/polyester non-crimp quadro-axial *[0/45/90/-45]$_s$* Devold AMT DBLT-850 face sheet with the mechanical properties listed in Tables 1 and 2. The face/core debonds in these sandwich specimens were created by use of a very thin razor blade of *0.35 mm* thickness. The load was introduced through steel hinges specially manufactured to avoid nonlinear rotations and/or friction forces during testing.

From Table 3, it can be determined that the optimum initial crack length in order to promote debond propagation is *25 mm* for the chosen specimen configuration. The steel hinges were glued (using epoxy) onto the debonded region of the MMB specimen such that the initial debond length, measured from the load line to the crack tip was *25 mm*. Two sandwich geometries with the same material constituents were evaluated. The specimen dimensions are a width of *35 mm*, face sheet thickness of *2 mm*, length *150 mm* (*2L*), and core thicknesses of *10* and *29 mm*. The cross-head rate applied to all specimens was 1mm/min. The mixed mode loading was varied by changing the lever arm distance *c* from *30* to *50 mm*.

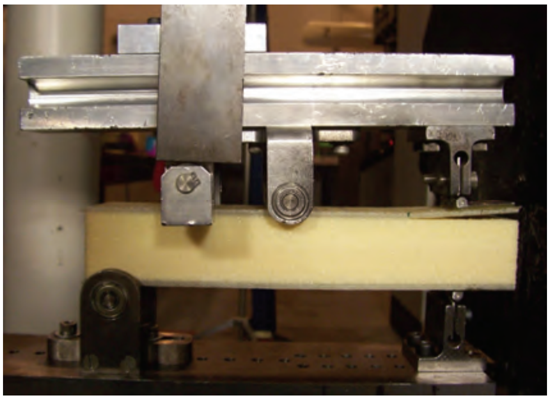

Figure 3 : MMB sandwich specimen and test rig

In addition, during the MMB experiments, some specimens were monitored visually by a commercial digital image correlation (DIC) system (ARAMIS 2M). The purpose of the DIC-measurements was to measure the actual deformations in the specimen during testing, especially in the core. A speckle pattern was applied to the lateral surface of the specimen, allowing a full field 3D displacement and 2D strain field measurement of the specimen surface.

5 EXPERIMENTAL RESULTS AND DISCUSSIONS

In the present paper, the design methodology to promote debond fracture as failure mode in the MMB sandwich specimens is validated against experiments. Examples of experimental load versus displacement results are presented in Figure 4. The load required to propagate the face/core debond is higher for small *c* values. This behavior can be attributed to the fact that at small *c* values the mixed mode applied to the specimen becomes a dominant mode II and at higher *c* values mode I is dominant. For instance, for $c=30$ *mm* the critical failure load was approximately *350 N* and for $c=50$ *mm* was *175 N*.

The comparison between the experimental and analytic load versus displacement results are in good agreement, as presented in Figure 4. The results presented in Figure 4 correspond to specimens with *29 mm* core thickness evaluated at different lever arm distances, *c*.

However, for specimens with *10 mm* core thickness the displacements were in the range of *10-18 mm* (see Figure 5) which caused large plastic and permanent deformation in the core, especially near the crack tip region. For this case, beam theory formulation for the MMB specimen is not valid since it was developed based on small deflections. Thus, the debond fracture characterization can therefore not be performed for this case.

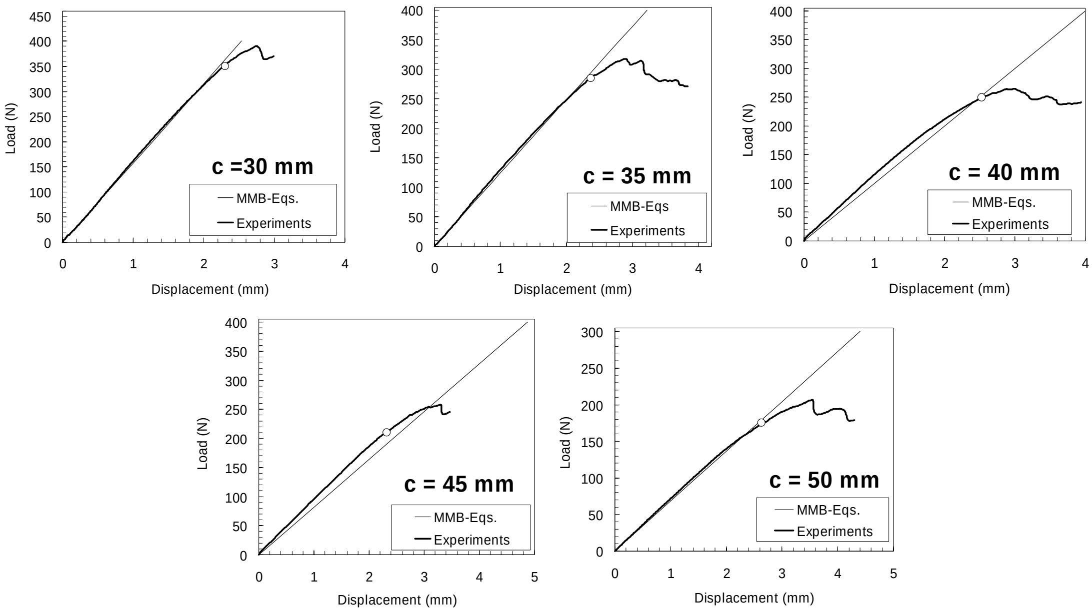

Figure 4 : MMB experimental results for load vs. displacement (“○” Onset of crack growth, hc=29mm, hf=2mm and b=35mm)

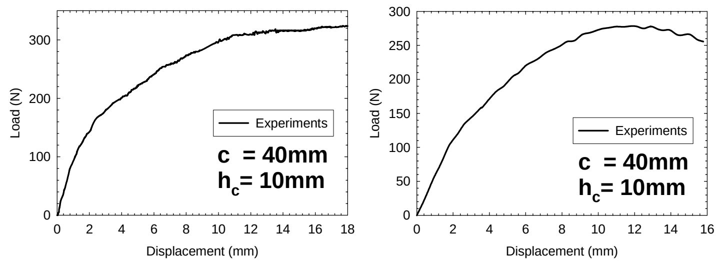

Figure 5 : MMB experimental for load vs. displacement (hc=10mm, hf=2mm and b=25mm)

The DIC images captured during testing of the MMB specimens are presented in Figure 6 showing major strain contours. As it can be observed in Figure 6a, the specimen with *10 mm* core thickness suffered large plastic (core crushing at crack tip) and permanent deformation in the core caused by the large displacements and a large crack tip process zone. Furthermore, this specimen failed by kinking into the face sheet, as shown in Figure 6b. Conversely, for the specimen with *29 mm* core thickness the deformations in the core (major strains, as shown in Figure 6c) at the crack tip is approximately *5%* which is within the linear elastic region [17]. In addition, the crack tip fracture process zone is small, and the specimen failed by debond propagation, as observed in Figure 6c.

In addition, the Crack Surface Displacement Extrapolation (CSDE) method developed by [1] was applied to extract the local mode-mixity at the crack tip in order to evaluate its effect on the debond fracture of the MMB specimens. The mode-mixity[1] was calculated for the specimens with *10* and *29mm* using a characteristic length equal to the specimen's face sheet thickness (*2 mm*). The specimens were loaded using a *c* value of *40 mm*. For the specimen with *10mm* core thickness, the mode-mixity was *-33°* and for *29mm* core thickness was *-19.5°*. The mode-mixity effect is evident since large mode-mixities will cause an elongation of the crack tip process zone (shear deformation) and can result in significant plastic deformation in the core material at the crack tip. Consequently the debond fracture characterization can be troublesome for these cases. For the specimen with *29 mm* core thickness, the mixed mode becomes dominant mode I. It is important to note that the pre-crack was introduced manually, which may result in the cracks being placed in an unrepresentative position within the sandwich specimen which can reduce or increase the resistance of the material to crack propagation. Therefore, a full experimental mixed mode fracture characterization of debonded sandwich specimens is underway and the face/core interface crack is created by inserting a thin Teflon film at the face/core interface ensuring that the crack is correctly located.

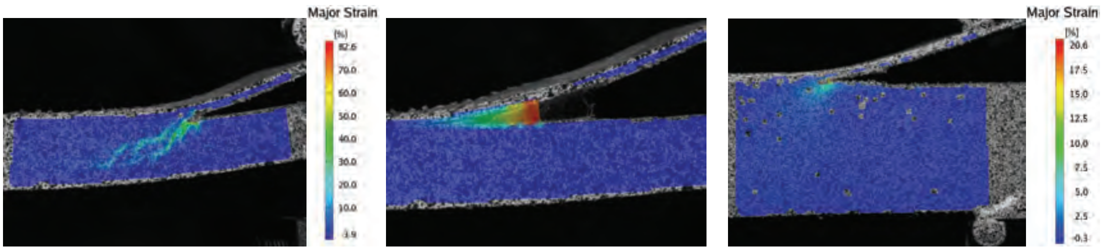

(a) (b) (c)

Figure 6 : DIC plots showing major strain during the MMB testing at c=40mm, a) h_c=10mm, b) h_c=10mm, kinking into the face sheet, and c) h_c=29mm, debond propagation.

The debond fracture loads and fracture toughnesses as function of the lever arm distance *c* and mode-mixity are shown in Figure 7. It is observed that the debond fracture load decreases as distance *c* increases (Figure 7a). The mode-mixity at the crack tip decreases as increasing the distance *c* (Figure 7b). And, the debond fracture toughness increases as function of increasing mode-mixity (Figure 7c). The mode-mixity values presented in Figure 7c are mainly dominant mode I and the fracture toughness reported (ranging from *481-687* J/m^2) agrees well with values reported in the literature [18]. In Ref. [18], a sandwich specimen with E-glass face sheets and H100 core evaluated using a pure DCB testing mode, the reported fracture toughness was ~*558* J/m^2.

[1] Assuming linear elastic fracture mechanics to be valid

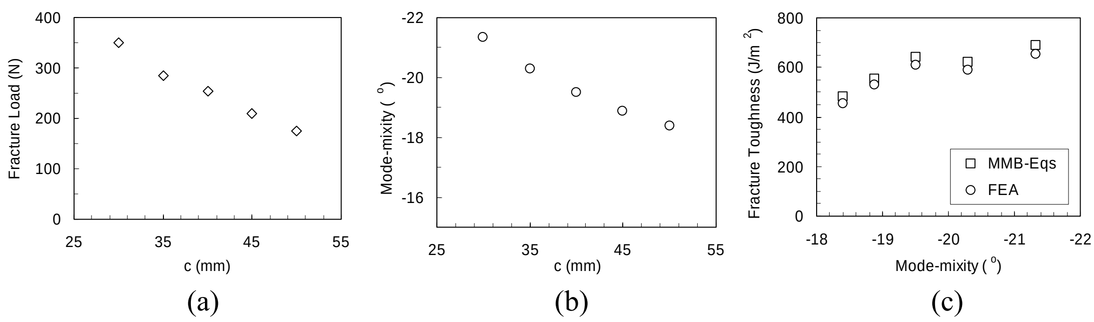

Figure 7 : a) Debond fracture loads, b) mode-mixity as function of various *c* values and c) fracture toughness as function of mode-mixity (h_c=29mm in all figures).

6 CONCLUSIONS

The methodology presented may be used to design MMB sandwich specimens with debond fracture as the controlling failure mode. Thus, the analysis presented can be applied for the design of an optimum sandwich geometry for debond fracture characterization under mixed mode loading. The formulation developed can be applied to any combination of materials and can assist in the determination whether debond propagation is the critical failure mode for a given beam geometry, initial crack length and mixed mode loading conditions. The present study showed that the load vs. displacement curves and fracture toughness vs. mode-mixity for the MMB specimens depends on the specimen geometry and loading conditions.

AWKNOWLEDGEMENTS

This work is carried out as an integrated part of the research project "Growth of Debonds in Foam Cored Sandwich Structures under Cyclic Loading" (SANTIGUE) funded by the Danish Research Agency (Grant nr. 274-05-0324). Furthermore, the sponsoring of test specimens by LM Glasfiber A/S is highly appreciated.

REFERENCES

[1] C. Berggreen, *Damage Tolerance in Debonded Sandwich Structures*, PhD. Thesis, Department of Mechanical Engineering, Technical University of Denmark, (2004).

[2] A. Nøkkentved, C. Lundsgaard-Larsen and C. Berggreen, "Non-Uniform Compressive Strength of Debonded Sandwich Panels - I. Experimental Investigation", *Journal of Sandwich Structures and Materials*, 7(6), 461-482 (2005).

[3] C. Berggreen and B.C. Simonsen, "Non-Uniform Compressive Strength of Debonded Sandwich Panels - II. Fracture Mechanics Investigation", *Journal of Sandwich Structures and Materials*, 7(6), 483-517 (2005).

[4] C. Berggreen, B.C. Simonsen and K.K. Borum, "Experimental and Numerical Study of Interface Crack Propagation in Foam Cored Sandwich Beams", *Journal of Composite Materials*, 41(4), 493-520 (2007).

[5] L.A. Carlsson, L.S. Sendlein and S.L. Merry, "Characterization of Face/Core Shear Fracture of Composite Sandwich Beams", *Journal of Composite Materials*, 25(1), 101-116 (1991).

[6] F. Avilés and L.A. Carlsson, "Analysis of the Sandwich DCB Specimens for Debond Characterization", *Engineering Fracture Mechanics*, 75, 153-168 (2008).

[7] X. Li and L.A. Carlsson, "Fracture mechanics analysis of the tilted sandwich debond (TSD) specimen", *Journal of Composite Materials*, 35 (23), 2145-2168 (2001).

[8] J. Ratcliffe and X. Cantwell, "A new test methods for characterizing skin-core debonding in composite sandwich structures", *Journal of Material Science and Letters*, 19, 1365-1367 (2000).

[9] R.C. Østergaard, B.F. Sørensen and P. Brøndsted, "Measurements of interface fracture toughness of sandwich structures under mixed mode loading", *Journal of Sandwich Structures and Materials*, 9, 445-466 (2007).

[10] C. Berggreen and L.A. Carlsson, "Fracture Mechanics Analysis of a Modified TSD Specimen", *8th International Conference on Sandwich Structures*, *Porto, May 3-6, (2008).*

[11] J. Reeder and J.H. Crews, "Mixed-Mode Bending Method for Delamination Testing", *AIAA Journal*, 28(7), 1270-1276 (1990).

[12] ASTM D6671/D 6671M-06, "Standard Test Method for Mixed Mode I-Mode II Interlaminar Fracture Toughness of Unidirectional Fiber Reinforced Polymer Matrix Composites", *ASTM International*, (2006).

[13] A. Quispitupa, C. Berggreen and L.A. Carlsson, "On the Analysis of the mixed mode bending (MMB) sandwich specimen for debond fracture characterization", *Engineering Fracture Mechanics, submitted, (*2008).

[14] C.A. Steeves and N. Fleck, "Collapse Mechanism of Sandwich Beams with Composite Faces and Foam Core, Loaded in Three-Point Bending. Part I: Analytical Models and Minimum Weight Design", *International Journal of Mechanical Sciences*, 46, 561-583 (2004).

[15] C.A. Steeves and N. Fleck, "Collapse Mechanism of Sandwich Beams with Composite Faces and Foam Core, Loaded in Three-Point Bending. Part II: Experimental Investigation and Numerical Modeling", *International Journal of Mechanical Sciences*, 46, 585-608 (2004).
[16] G.M. Viana and L.A. Carlsson, "Mechanical properties and fracture characterization of Cross-linked PVC foams", *Journal of Sandwich Structures and Materials*, 4, 99-113 (2002).
[17] DIAB. *Technical Manual*, Divinycell H, Denmark, (2006).
[18] K. Shivakumar and H. Chen, "An evaluation of data reduction methods for opening mode fracture toughness of sandwich panels", *Journal of Sandwich Structures and Materials*, 7, 77-90 (2005).

8th International Conference on Sandwich Structures
ICSS 8
A. J. M. Ferreira (Editor)

ENERGY ABSORPTION DURING PROJECTILE PERFORATION OF LIGHTWEIGHT SANDWICH PANELS WITH METALLIC FIBRE CORES

James Dean[*], Arash S. Fallah[†], Peter M. Brown[ξ], Luke A. Louca[†] & Trevor W. Clyne[*]

[*]Department of Materials Science and Metallurgy, University of Cambridge,
Pembroke Street, Cambridge, CB2 3QZ, UK

[†] Department of Civil and Environmental Engineering, Imperial College,
South Kensington, London, SW7 2AZ, UK

[ξ] Defence Science and Technology Laboratory, Porton Down,
Salisbury, Wiltshire, SP4 0JQ, UK

Key words: Sandwich structures, ABAQUS, Perforation, Cellular.

Summary. *This paper documents an experimental and numerical study of energy absorption in lightweight sandwich panels with metallic fibre cores, when perforated by hardened, spherical steel projectiles. The sandwich panels are manufactured entirely from austenitic stainless steel (type-304). The faceplates are 0.4 mm thick and the core material, composed of a bonded network of slender metallic fibres, is approximately 1-1.5 mm thick. The sandwich panels have been impacted over a range of impact velocities and the absorbed energy has been measured. Simulations were conducted using the explicit finite element code in ABAQUS/CAE. The faceplates were modelled using the phenomenological plasticity model of Johnson & Cook, coupled with a strain rate-dependent, critical plastic strain fracture model. The core was modelled as an anisotropic crushable foam material using a VUMAT subroutine. Failure of the core material was captured using a quadratic shear stress failure criterion. The agreement between the simulations and the experiments is found to be good in terms of failure mode. The absorbed energies are also in good agreement.*

1 INTRODUCTION

In a sandwich panel, two thin, stiff faces are bonded to, and separated by, a thick and lightweight core material. The faces may be composed of any material that satisfies the basic requirements of stiffness, strength and flexural rigidity. The core material has several functions. It must be sufficiently stiff in the direction perpendicular to the faceplates to maintain a constant separation distance, it must be stiff in shear to prevent relative movement between the faceplates during bending, and it must be stiff enough to keep the faceplates flat, in order to prevent local instabilities during in-plane compressive loading.

Provided the appropriate core and face materials are chosen, therefore, sandwich panels can satisfy a great range of demands and have long been utilised in applications requiring lightweight, high stiffness structures (notably in the aerospace, automotive, marine and construction industries). Their continued widespread use has been promoted by the availability and development of novel, porous core topologies [1]. These include micro-architectured trusses, honeycombs, metallic and polymeric foams and corrugations. A porous architecture also lends itself well to thermal insulation [2], noise attenuation [3] and heat exchange [4], providing a degree of multifunctionality which further widens the possible application range. In fact, the benefits of cellular materials are often best realised when configured as the cores of sandwich panels. This owes much to their plastic behaviour during compression, which also renders them candidate materials for energy absorbing applications.

Indeed, the impact response of sandwich panels containing lattice, foam-like and honeycomb cores has already been treated extensively [5, 6] [7]. However, a more novel type of cellular core topology is one comprised of an open network of bonded metallic fibres [8]. The mechanical properties of a lightweight sandwich panel with a fibrous metallic core were recently investigated by Zhou and Stronge [9], who went on to investigate the sandwich panel response under local impact denting [10]. The sandwich panel (termed HSSA) contained metal fibres in the core, sandwiched between 200 μm thick faceplates (type-316 stainless steel) and bonded with a polymeric adhesive. The fibres (type-316 stainless steel) were approximately 1 mm in length, 25 μm in diameter, and were oriented perpendicular to the plane of the faceplates.

Zhou and Stronge [10] developed analytical models based on quasi-static and dynamic deformation to predict the impact force generated by a low speed impact on HSSA sandwich panels. A finite element model was also developed which could accurately capture the residual indentation depth, although the authors noted the difficulty in trying to choose a suitable constitutive model for the core material. From a simple energy partition, Zhou and Stronge [10] also found that at low impact energies, bending and shearing were the dominant energy-absorbing mechanisms. Membrane stretching (faceplates) and indentation offered little in the way of energy absorption. As the impact energy increased, the contribution from membrane stretching increased significantly, to a value consistent with that of bending and greater than that of shearing. The energy absorbed through indentation remained comparatively low.

In a further paper [11], Zhou and Stronge implemented a VUMAT subroutine into the ABAQUS finite element code to model the compressible plastic behaviour of the fibrous core.

This VUMAT included a critical strain fracture criterion. The FE results were found to correlate well with their experimental data.

More recently, networks of slender metallic fibres have been fabricated in a mat-like form, consolidated by solid state sintering. Such networks have since been used as the core material in a series of lightweight sandwich panels, whose elastic properties [12] and resistance to delamination [13] have previously been evaluated. Their resistance welding characteristics have also been studied [14]. Their response to localised ballistic impact (including perforation) is the subject of the present investigation. The experimental tests have been simulated using the explicit finite element code in ABAQUS/CAE.

2 Materials, Manufacture and Experimental Procedures

2.1 Materials & Manufacture

The sandwich panel manufacturing process is depicted schematically in Figure 1. The panels are manufactured entirely from stainless steel (type 304) and the faceplates are 0.4 mm thick.

The fibres have a diameter which ranges from ~60 μm to 100 μm and are predominantly crescent shaped through their section. They are ~5 mm in length. Once the sandwich panel is assembled, the constituents are bonded together by solid state sintering at 1195°C for 1.5 hours. The sandwich panels are then gas quenched to room temperature. SEM micrographs of the sandwich panel, and of sintered fibre-to-fibre bonds are presented in Figure 2 (a-c)

The final sandwich panel assembly is depicted in Figure 3. Included are photographs of (b) some isolated and representative core material and (c) single and multilayer sandwich panels.

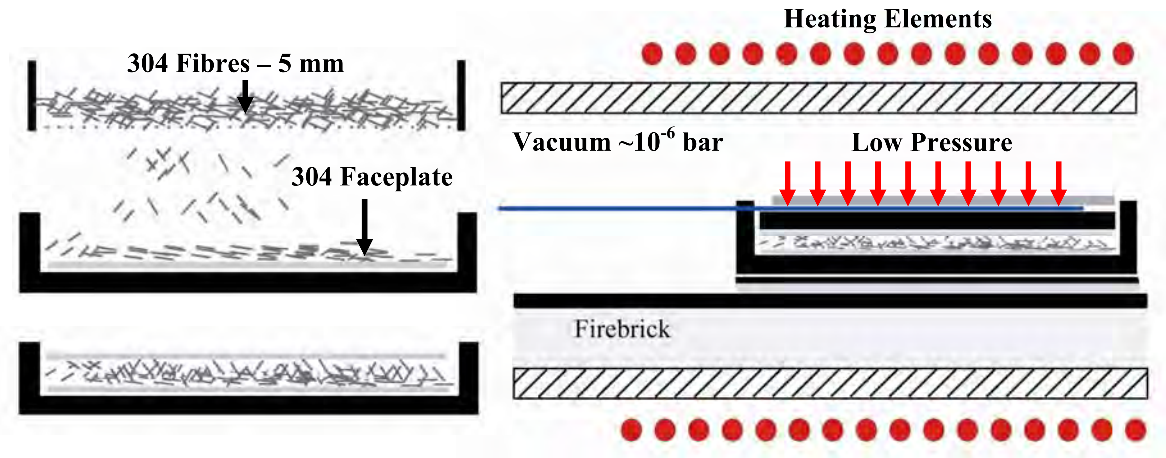

Figure 1: Sandwich panel manufacturing process, involving deposition of fibres, the addition of a second faceplate and bonding via solid state sintering under temperature, pressure and vacuum conditions

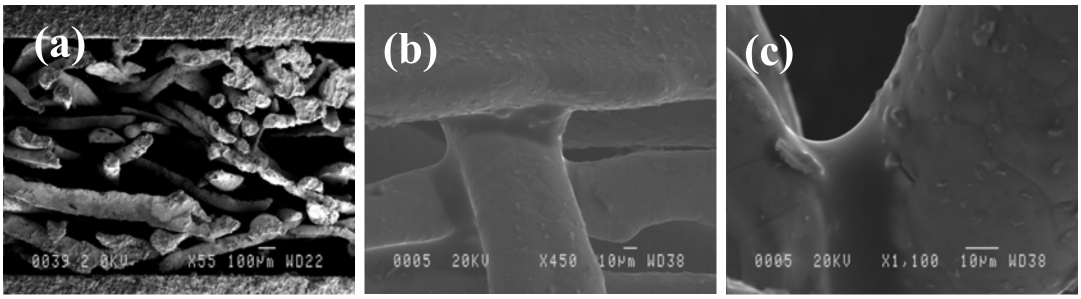

Figure 2: Scanning electron microgrpahs of (a) sandwich panel cross section and (b-c) sintered fibre-to-fibre joints

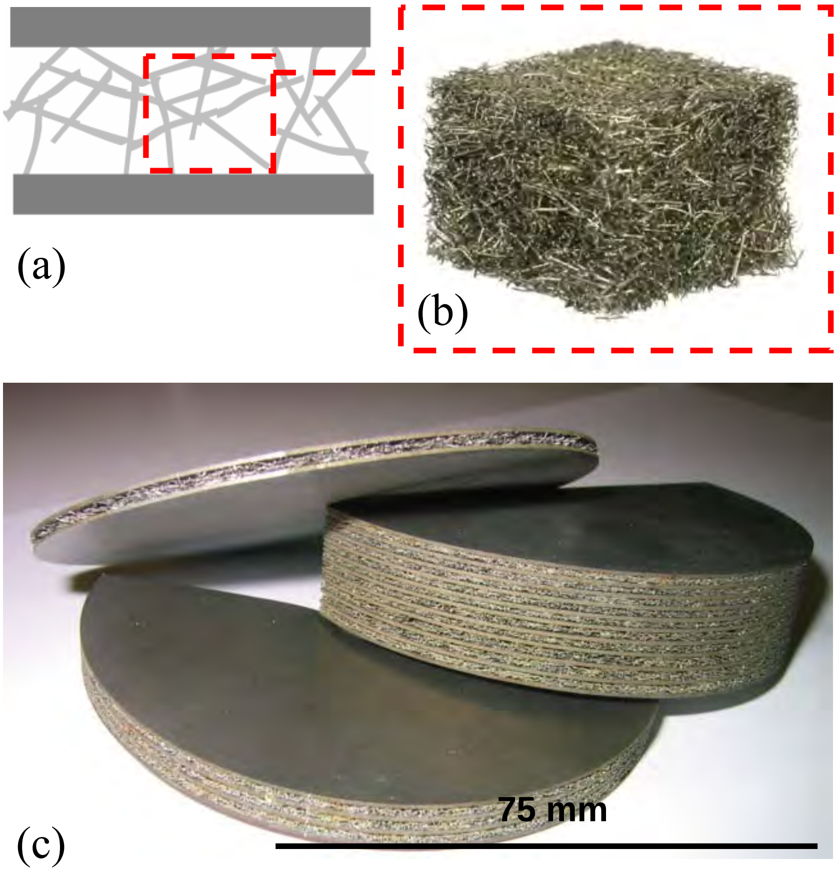

Figure 3**:** (a) Schematic depiction of a lightweight sandwich panel with a metallic fibre core. (b) Photograph of sintered fibre network material (representative of that in the core) and (c) final sandwich panel assemblies (single and multilayer)

2.2 Impact Tests

Specimens for impact testing were cut from sandwich panel plates (supplied by Fibretech Ltd.) using an Electric Discharge Machine (EDM). The specimens, 76.5 mm diameter, were rigidly clamped, such that 60 mm of the 76.5 mm diameter was exposed. The specimens were impacted at normal incidence over a range of velocities by hardened, spherical steel projectiles of 2 g mass and 8 mm diameter, fired from a single stage gas gun. The incident velocity was measured using a series of light gates comprising three light emitting diodes and three light receiving photodiodes. The residual velocity was measured using an electromagnetic induction technique, whereby the moving (magnetic) projectile induces a current in two spaced copper coils. The time between electrical pulses is recorded and the projectile velocity calculated. After penetration, the perforated specimens were sectioned using the EDM.

3 Model Development

All simulations were conducted with the ABAQUS/Explicit finite element code. The faceplates and core were modelled as elastic-plastic solids and meshed with 8-noded, linear brick, reduced integration solid elements – type C3D8R. The density of the mesh was refined in the region directly beneath the projectile, preventing the mesh from being coarse relative to gradients of strain. An encastre boundary condition was specified to simulate the experimental clamping conditions. The projectile was modelled as an analytical rigid body and simply assigned mass. This assertion assumes that projectile plastic deformation is negligible during structural impact problems of this type. (It was confirmed by visual inspection after impact that the projectile experienced no detectable plastic deformation). Penalty contact was defined between the projectile and the sandwich panel components. Friction between the projectile and the panel was ignored since Krafft [15] showed experimentally that, during the perforation process, sliding friction accounts for less than 3% of the total striking energy.

3.1 Constitutive Material Models - Faceplate Material

3.1.1 Plasticity

The plasticity model employed for the faceplates was the phenomenological model of Johnson & Cook, in which the flow stress is given as a function of equivalent plastic strain, strain rate and temperature. The isotropic strain hardening component is assumed to be of the following form [16]:

$$\sigma_0 = \left[A + B(\bar{\varepsilon}_{pl})^n \right](1 - \hat{\theta}^m) \tag{1}$$

where σ_0 is the static flow stress, $\bar{\varepsilon}_{pl}$ is the equivalent plastic strain and A, B, n and m are material parameters. $\hat{\theta}^m$ is the non-dimensional temperature, given by:

$$\hat{\theta} \equiv \begin{cases} 0 & \theta < \theta_{transition} \\ (\theta - \theta_{transition})/(\theta_{melt} - \theta_{transition}) & \theta_{transition} \le \theta_{melt} \\ 1 & \theta > \theta_{melt} \end{cases} \tag{2}$$

The strain rate component assumes that:

$$\sigma_d = \sigma_0(\bar{\varepsilon}_{pl}, \theta) R(\dot{\bar{\varepsilon}}_{pl}) \tag{3}$$

$$\dot{\bar{\varepsilon}}_{pl} = \dot{\varepsilon}_0 \exp\left[\frac{1}{C}(R-1)\right] \tag{4}$$

where σ_d is the dynamic flow stress, $\dot{\bar{\varepsilon}}_{pl}$ is the equivalent plastic strain rate, $\dot{\varepsilon}_0$ is a reference strain rate, C is a material parameter and $R(\dot{\bar{\varepsilon}}_{pl})$ is the ratio of the dynamic yield stress to the quasi-static yield stress.

The Johnson and Cook dynamic flow stress as a function of strain, strain rate and temperature is therefore given by the following expression:

$$\bar{\sigma}_d = \left[A + B(\bar{\varepsilon}_{pl})^n\right]\left[1 + C\ln\left(\frac{\dot{\bar{\varepsilon}}_{pl}}{\dot{\varepsilon}_0}\right)\right](1 - \hat{\theta}^m) \tag{5}$$

3.1.2 Damage and Fracture

A strain-based fracture model was employed to capture failure during faceplate perforation. The damage in an element accumulates incrementally with plastic deformation. It is represented by the state variable w_d computed as:

$$\Delta w_d = \frac{\Delta\bar{\varepsilon}_{pl}}{\bar{\varepsilon}_{D,pl}} \tag{6}$$

where $\Delta\bar{\varepsilon}_{pl}$ is the increment of accumulated equivalent plastic strain and $\bar{\varepsilon}_{D,pl}$ is the equivalent plastic strain at the onset of damage. The criterion for damage initiation is therefore met when:

$$w_d = \frac{d\bar{\varepsilon}_{pl}}{\bar{\varepsilon}_{D,pl}} \ge 1 \tag{7}$$

Once damage has initiated, the element stiffness degrades. When the element loses its load-carrying capacity, it is removed from the simulation. Implementation of this constitutive fracture model requires fracture strain data as a function of the strain rate. High strain rate fracture data were unavailable. However, in this study, the fracture strain was assumed to decrease linearly by 20% over the strain rate range $10^{-2} \leq \dot{\varepsilon}_{pl} \leq 10^{4}$, after Lichtenfeld et al [17] for 304 steel.

3.1.3 Temperature Effects

At high impact loading rates, adiabatic shear bands can form. This is characterised by a band of intense plastic shear strain and large local temperature rise. If thermal softening within the band exceeds strain hardening, then continued loading results in failure at stress levels well below the static strength of the material. The phenomenon has received considerable attention, and is summarised concisely in the books of Wright [18] and Bai and Dodd [19]. Adiabatic shear band formation has also been studied numerically [20] [21]. Chou et al [22], for example, have demonstrated, using Johnson & Cook constitutive relations, that shear bands can form in numerical simulations if thermal softening is accounted for in the material model. They noted that a fine mesh size was required in order to capture the formation of shear bands which, in steel, are typically 10-100 μm in width.

In order, therefore, to assess the need for high temperature material data in this study, simulations were conducted to predict the local adiabatic temperature rise during plate perforation. The inelastic heat fraction (α), which represents the proportion of plastic work converted to heat energy, was assumed to be 0.95. The maximum adiabatic temperature rise over the velocity range studied was found to be 272°C at 350 m s^{-1}. In the absence of thermo-mechanical data, the temperature effects were, therefore, neglected since the temperature rise was deemed insufficient to cause *significant* thermal softening.

3.2 Constitutive Material Models - Core Material

3.2.1 Plasticity

A VUMAT sub-routine was employed to model the plastic compression of the core material. The implemented sub-routine, for an anisotropic material, employs the constitutive material relationship developed by Xue and Hutchinson [23]. This compressible, anisotropic constitutive model is an extension of the isotropic crushable foam material model proposed by Deshpande and Fleck [24]. The VUMAT sub-routine has previously been used to model failure in sandwich panels with cores made from stainless steel fibres [11] and balsa wood [25], with good results.

3.2.2 Failure

Fracture of the material is simulated by deleting elements once the following fracture criterion is satisfied:

$$\left(\frac{\tau_{13}}{\overline{\tau}_c}\right)^2 + \left(\frac{\tau_{23}}{\overline{\tau}_c}\right)^2 \geq 1 \tag{8}$$

The fracture criterion is quadratic stress based and simulates shear failure of the core. τ_{13} and τ_{23} are the through-thickness shear stresses and $\overline{\tau}_c$ is the critical shear stress for core failure.

4 Projectile Perforation

4.1 Low Speed Impact

Figure 4 plots the predicted, post-elastic recovery, back-face deflection, as a function of impact velocity, for $80 \leq V_i \leq 200$ m s^{-1}. At these low striking velocities, the sandwich panels were not perforated. Experimental data are included for comparison and are found to correlate closely with the predictions. The actual (experimental) core thickness values are appended to the experimental data points for clarity. The agreement in terms of plastic strain field is shown to be excellent in Figure 5, which compares the sandwich panel profiles, post-elastic recovery.

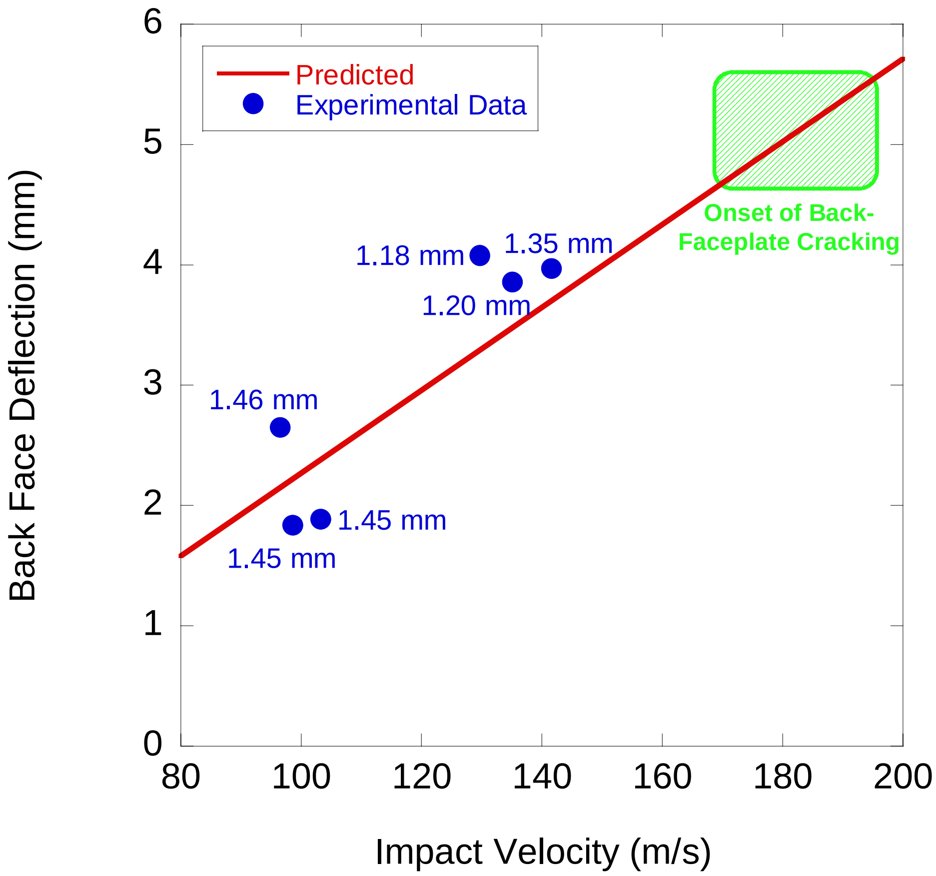

Figure 4: A comparison between predictions and measured data for impacted sandwich panels as a function of impact velocity

The predicted trend indicates a linear increase in back-face deflection with impact velocity. At impact speeds approaching ~200 m s^{-1}, however, cracking begins to occur in the rear faceplate (when the maximum deflection is ~7 mm). Beyond impact speeds of ~200 m/s, the panel performance is therefore best indicated by the total absorbed energy during complete perforation – see 4.2.

Figure 5: A comparison between the predicted and experimental sandwich panel profiles, post-projectile impact and post-elastic recovery

4.2 High Speed Impact

Figure 6 plots the energy absorbed by the sandwich panels, as a function of velocity, for impact speeds giving complete perforation. These data are compared to numerical predictions for single faceplates and for two faceplates separated by 1 mm (modelled as elastic-plastic shells (and not solids as in the sandwich panel case)).

The data and predictions for single faceplates agree closely over the velocity range indicated, thereby validating the faceplate material model. It was also necessary to model two faceplates separated by a distance equivalent to that of the core thickness (i.e. ~1 mm), to ascertain the merits of combining the constituents into sandwich panel form. Once more, the data and predictions for two separated faceplates closely agree. For the sandwich panels, the experimental data correlate reasonably well with the predictions, suggesting that the model is suitable for broadly capturing the quantitative features of the perforation process. There is, however, a clear over-prediction of the absorbed energies that may be explained from the assumption in the model that the core and the faceplates are rigidly bonded. In actual fact, the core and the faceplates can only be bonded at local regions of fibre-to-faceplate contact.

The contribution to energy absorption afforded by the addition of the core material, arising from core deformation (and perhaps through its synergy with the faceplates), is represented by the difference between the two curves. This additional energy absorption (predicted) corresponds to ~20 J above impact speeds of ~240 m/s. This constitutes ~40% of the total absorbed energy.

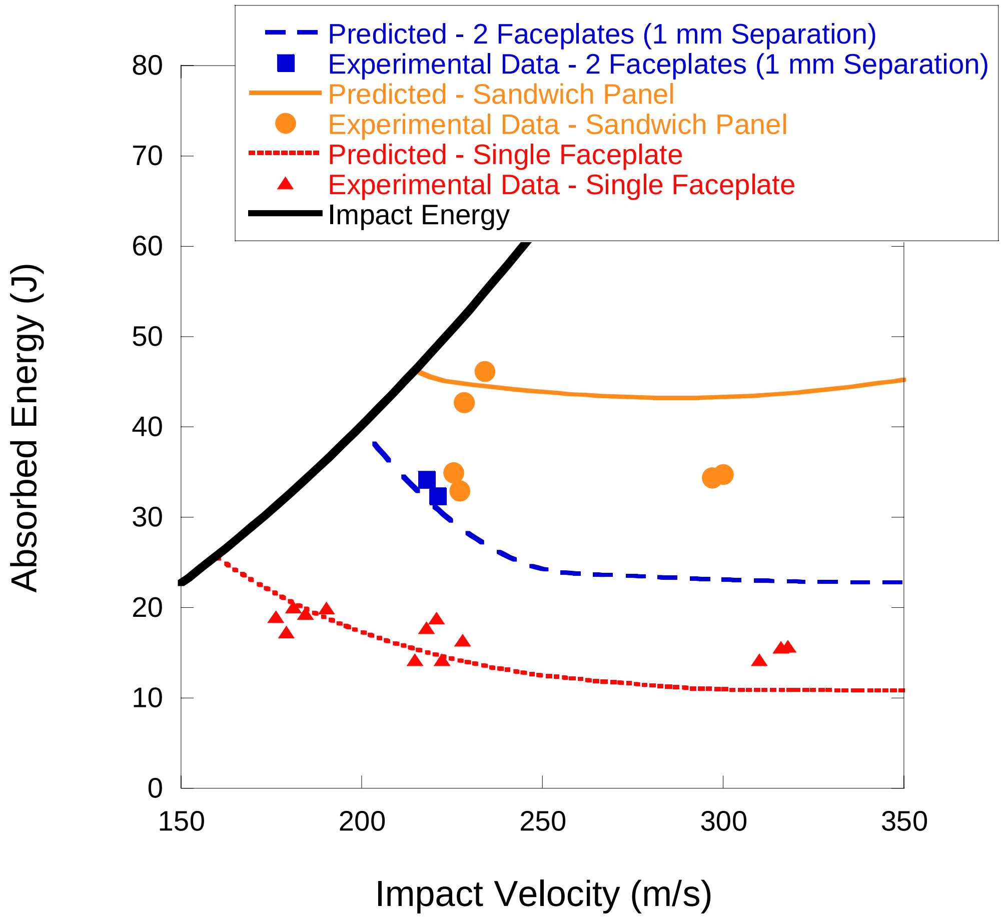

Figure 6: Measured and predicted sandwich panel absorbed energy as a function of impact velocity. Included are data and predictions for single faceplates and for two faceplates separated by 1 mm (approximate core thickness)

The model also captures the major qualitative features of the perforation process, as highlighted by Figure 7. These qualitative features include core crushing, core failure, faceplate stretching and faceplate fracture. The core-faceplate delamination is not captured numerically, since, as stated previously, the core is assumed to be rigidly bonded to the faces. Future modelling attempts should resolve this issue by integrating cohesive element zones at the interfaces.

Figure 7: Comparison between the predicted and experimental post-perforated sandwich panels when impacted at ~250 m/s

5 Conclusions

Sandwich panels containing a novel, porous core material (composed of a bonded network of slender metallic fibres) have been impacted by spherical projectiles over a range of impact velocities. The performance of the sandwich panels has been assessed in terms of their capacity to absorb the impact energy, either by deflection or by perforation. A finite element model has been developed. The faceplates were modelled as strain and strain-rate dependent solids, using the phenomenological plasticity model of Johnson and Cook, coupled with a critical strain failure model. The core material was modelled as an anisotropic, strain-rate independent, crushable continuum, coupled with a quadratic shear-stress failure criterion.

At striking velocities below the ballistic limit, the back-face deflection (post-elastic recovery) is found to increase linearly with velocity, until the initiation of back-face cracking. The predicted results are in close agreement and the qualitative sandwich panel profiles are similar in appearance. Above the ballistic limit, the sandwich panel plates are perforated and the absorbed energy has been measured. These data have been compared to data obtained from impact tests on single faceplates and on two faceplates separated by an air gap equivalent in distance to the thickness of the core material. The results show that the sandwich panels absorb ~40% more energy than two separated faceplates, although account should be taken of the increased areal density when assessing the value of this. The sandwich panel numerical model is in relatively good agreement with the data, although it over-predicts the total absorbed energy. Clearly, a more rigorous approach to modelling the core material and the interfaces is required, in order to improve the predictive capability of the model.

6 References

1. Wadley, H., *Cellular Metals Manufacturing.* Adv. Eng. Mater., 2002. **10**(4): p. 726-733.
2. Ashby, M.F., A.G. Evans, N.A. Fleck, L.J. Gibson, J.W. Hutchinson, and H.N.G. Wadley, *Metal Foams: A Design Guide*. 2000, Boston: Butterworth-Heinemann.
3. Barnhart, J. and J. Baumeister, *Damping Properties of Aluminium Foams.* Mat Sci & Eng, 1996. **205**(A): p. 221 - 228.
4. Lu, T.J., H.A. Stone, and M.F. Ashby, *Heat Transfer in Open-Cell Metal Foams.* Acta Mater., 1998. **46**(10): p. 3619-3635.
5. Foo, C.C., L.K. Seah, and G.B. Chai, *Low-Velocity Impact Failure of Aluminium Honeycomb Sandwich Panels.* Composite Structures (In Press), 2007.
6. Goldsmith, W., G.T. Wang, K. Li, and D. Crane, *Perforation of Cellular Sandwich Plates.* Int J Impact Eng, 1997. **19**(5-6): p. 361 - 379.
7. Caprino, G. and R. Teti, *Impact and Post-Impact Behaviour of Foam Core Sandwich Structures.* COMPOS STRUCT, 1994. **29**: p. 47-55.
8. Gustafsson, R.N.-G., *Formable Sandwich Construction Material and Use of the Material as Construction Material in Vehicles, Refrigerators, Boats etc*. 1998, AB Volvo: International.
9. Zhou, D. and W.J. Stronge, *Mechanical Properties of Fibrous Core Sandwich Panels.* Int J Mechanical Sciences, 2005. **47**(4-5): p. 775-798.
10. Zhou, D.W. and W.J. Stronge, *Low Velocity Impact Denting of HSSA Lightweight Sandwich Panel.* International Journal of Mechanical Sciences, 2006. **48**: p. 1031-1045.
11. Zhou, D.W. and W.J. Stronge, *Ballistic Limit for Oblique Impact of Thin Sandwich Panles and Spaced Plates.* International Journal of Impact Engineering (In Press), 2007.
12. Markaki, A.E. and T.W. Clyne, *Mechanics of Thin Ultra-Light Stainless Steel Sandwich Sheet Material: Part I - Stiffness.* Acta Mater., 2003. **51**(5): p. 1341-1350.
13. Markaki, A.E. and T.W. Clyne, *Mechanics of Thin Ultra-Light Stainless Steel Sandwich Sheet Material: Part II - Resistance to Delamination.* Acta Materialia, 2003. **51**(5): p. 1351-1357.
14. Tan, J.C., A.E. Markaki, and T.W. Clyne, *Resistance Welding of Thin Stainless Steel Sandwich Sheets with Fibrous Metallic Cores: Part I - Thermal and Electrical Properties.* submitted to Science and Technology of Welding and Joining, 2006.
15. Krafft, J.M., *Surface Friction in Ballistic Penetration.* Journal of Applied Physics, 1955. **26**(10): p. 1248-1253.
16. ABAQUS, *ABAQUS/Explicit User's Manuals, Version 6.6*. 2006.
17. Lichtenfeld, J.A., M.C. Mataya, and C.J. van-Tyne, *Effect of Strain Rate on Stress-Strain Behaviour of Alloy 309 and 304L Austenitic Stainless Steel.* Metallurgical and Materials Transactions A, 2006. **37A**: p. 147.
18. Wright, T.W., *The Physics and Mathematics of Adiabatic Shear Bands*. 2002: Cambridge University Press.

19. Bai, Y. and B. Dodd, *Adiabatic Shear Localization*. First ed. 1992, Oxford: Pergamon Press. 378.
20. Borvik, T., O.S. Hopperstad, T. Berstad, and M. Langseth, *Numerical Simulation of Plugging Failure in Ballistic Penetration.* International Journal of Solids and Structures, 1999. **38**: p. 6241-6264.
21. Roessig, K.M. and J.J. Mason, *Adiabatic Shear Localisation in the Dynamic Punch Test, Part 2: Numerical Simulations.* International Journal of Plasticity, 1999. **15**(2): p. 263-283.
22. Chou, P.C., J. Hashemi, A. Chou, and H.C. Rogers, *Experimentation and Finite Element Simulation of Adiabatic Shear Bands in Controlled Penetration Impact.* International Journal of Impact Engineering, 1991. **11**: p. 305-321.
23. Xue, Z. and J.W. Hutchinson, *Constitutive Model for Quasi-Static Deformation of Metallic Sandwich Cores.* International Journal for Numerical Methods in Engineering, 2004. **61**: p. 2205-2238.
24. Deshpande, V.S. and N.A. Fleck, *Isotropic Constitutive Models for Metallic Foams.* Journal of the Mechanics and Physics of Solids, 2000. **48**(6-7): p. 1253-1283.
25. Zhou, D., L.A. Louca, and M. Saunders, *Numerical Simulation of Sandwich T-joints under dynamic Loading.* Composites: Part B(2008), doi:10.1016/j.compositesb.2007.12.002, 2008`.
26. Lee, S., F. Barthelat, J.W. Hutchinson, and H.D. Espinosa, *Dynamic Failure of Metallic Pyramidal Truss Core Materials - Experiments and Modelling.* International Journal of Plasticity, 2006. **22**: p. 2118 - 2145.

8th International Conference on Sandwich Structures
ICSS 8
A. J. M. Ferreira (Editor)

DIGITAL IMAGE CORRELATION BASED FAILURE EXAMINATION OF SANDWICH STRUCTURES FOR WIND TURBINE BLADES

John P. Dear[a], Amit Puri[a], Alexander D. Fergusson[a], Andrew Morris[b], Ian D. Dear[c], Kim Branner[d] and Find M. Jensen[d]

[a] Department of Mechanical Engineering
Imperial College London
South Kensington, London, SW7 2AZ, UK
e-mail: j.dear@imperial.ac.uk, amit.puri01@imperial.ac.uk, alexander.fergusson01@imperial.ac.uk

[b] Power Technology
E.ON UK
Ratcliffe-on-Soar, Nottingham, NG11 0EE, UK
e-mail: Andy.P.Morris@eon-uk.com

[c] School of Engineering and Design
Brunel University
Uxbridge, Middlesex, UB8 3PH, UK
e-mail: Ian.Dear@brunel.ac.uk

[d] Wind Energy Department, Risø National Laboratory
Technical University of Denmark
Frederiksborgvej 399, Building 118, DK-4000 Roskilde, Denmark
e-mail: kim.branner@risoe.dk, peter.berring@risoe.dk, find.moelholt.jensen@risoe.dk

Key words: Sandwich structures, Digital image correlation, Wind turbine blade.

Summary. *This paper presents experimental data obtained from flexurally loaded wind turbine blade sandwich material. The need was to identify failure characteristics of the material and provide for in depth analysis. Digital Image Correlation (DIC) was used to obtain full field strain maps of the deforming specimens. Results highlight the capability of the DIC technique to identify the onset of failure related to causes. These results were compared with strain gauge data and those from a simple FE model. Overall, the results present a foundation for experiments on larger substructure, and eventually integration into manufacturing and maintenance aspects of the industry.*

1 INTRODUCTION

Wind turbines are a major need for the growth of renewable energy [1] and it is likely that the growth will continue at a even faster pace in the years to come, partly driven by the Kyoto protocol and partly by the industry as it finds ways to utilise the wind resources offshore. With this projected growth it is not surprising that the industry is looking at ways to develop larger and more reliable components to offset the high installation and maintenance costs. A trend is the increasing use of advanced lightweight materials such as glass and carbon fibre composites [2]. These materials are being used for the blades because of their high strength to weight ratio.

Modern wind turbine blades are designed without the use of stiffeners, except for usually two longitudinal webs. The blades therefore have large unstiffened panels and sandwich panels with a foam-core are widely used to obtain sufficient local out-of-plane stiffness of the panels. A recent study [3] shows that it also can be beneficial to use the sandwich panels in the load-carrying elements of very large blades to increase local bending stiffness to resist buckling. Webs of foam-core sandwich material also provide a structural spacer inside the aerofoil to maintain shape under the large crushing forces caused by longitudinal curvature of the blade, an effect termed the Brazier effect [4]. Therefore, a key concern with these sandwich webs is their flexural rigidity, a topic covered in a partner paper [5].

A focus of the research presented here is the failures that can occur in these sandwich structures and possible means of detection of damage inside components. To examine this, flexure experiments were conducted on sandwich specimens extracted from wind turbine blades. To aid the assessment of material behaviour, Digital Image Correlation (DIC) was used on all specimen cross sections. This non-destructive technique provided for full field strain evaluation of the specimens for this study of failure processes. This technique could be employed to verify manufacturers FE models and be integrated into the inspection and maintenance aspects of blade quality control and lifetime assessment.

This paper first presents an introduction to DIC and then moves onto a description of the testing methods employed. Data are presented, covering the DIC output, the failure methods, a comparison of DIC output to standard metrology and a comparison of DIC to FE output. Following on from this research, brief conclusions are given, which include future goals.

2 TEST METHODS

2.1 Digital Image Correlation (DIC)

DIC can be used to produce a full-field surface displacement and strain maps by comparing a series of images captured at various levels of deformations. For this research, a contrasting monochromatic paint pattern is applied to the component surface namely a black background with randomly orientated white dots, or vice-versa. The method can be applied without use of a paint pattern if there are distinguishing features on the surface with suitable contrast. An initial image is captured using digital cameras and is treated as the reference to which all subsequent images are compared. These subsequent images will show the surface paint pattern with some variations as a result of deformation [6]. To achieve a higher degree of accuracy, correlations are based on squares of pixels, known as facets, rather than using individual pixel tracing. These facets have an array of greyscale values corresponding to the pattern, thus allowing tracking through the subsequent image stages [7]. This process is demonstrated in Figure 1.

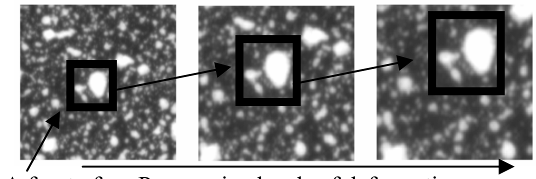

Figure 1: Example of DIC method.

It is usual to overlap the facets to increase the correlation accuracy, and reduce the risk that no data is missed in the evaluation. The size of the facets and the level of overlap play an important role in determining the correlation, for example strains can be measured in the range from 0.1 % to several 100 % with accuracy of ca. 0.05 % (500 micro-strain) under best conditions [6]. However, the resolution is related to the useable facet size, which in turn will determine the level of strain variation that can be obtained. For example, if there is a feature in the specimen, then selecting a facet size which eclipses it will result in a low strain resolution and the strain pattern associated with the feature may not be visible. However, using larger facets allows more data to be contained within the facet and the accuracy of measured displacement vector associated with the facet is increased.

To understand better the failure of this composite sandwich material, and to gauge whether the technique could provide a valuable tool for the wind turbine industry, DIC was conducted on all wind turbine blade specimen cross-sections. This was done using a DSLR camera, with images imported into the DIC package ARAMIS [8]. The higher sensor resolution (10 mega-pixel) of DSLRs allows for facets to represent a smaller physical size. There is little difference between the strain values produced by the different camera systems. This proved that DIC could be made easily transportable by using a DSLR, which would make for easier integration into the wind turbine industry, potentially at this juncture for use during certification tests or studies associated with assessing design integrity.

2.2 Flexural Testing

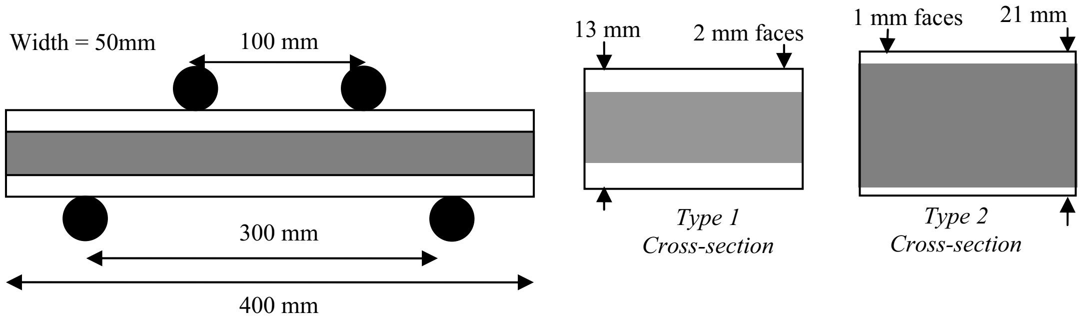

Figure 2: Sandwich panel loading configuration and cross-section dimensions (Type 1 and Type 2).

The specimen geometries and loading configurations are given in Figure 2 and are compliant with ASTM C393-00 loading configurations [9]. All specimens had widths of 50 mm. This material was extracted from two different regions of the blade, resulting in two different cross-sections, highlighted again in Figure 2. For clarity these have been termed Type 1, which has thick skins and a thin core, and Type 2, which has thin skins and a thick core. Both of these types have multiple biaxial $\pm$ 45^{o} glass fibre layers. The foam used for both specimen types was PVC. All specimens had been machined from larger components extracted from a full-scale blade that had passed all certification requirements. All tests were conducted at a constant crosshead displacement rate in the range of 0.16– 8.33 mm/s.

3 RESULTS

3.1 Bending Strain Results

Figures 3 and 4 show bending strain plots for Type 1 (Thick Skin) and Type 2 (Thin Skin) sandwich panels for crosshead displacements of 5, 10 and 16 mm (crosshead displacement rate 0.33 mm s^{-1}). These strain contour plots with a % strain scale have been overlaid onto the deformed image stages. In Figure 3 (Thick Skin), the strain is high underneath both inner and outer rollers as a result of foam core crushing. This is undesirable, yet between the inner rollers the distribution exhibits the usual compressive strain on the top surface and tensile strain on the lower surface. In contrast, the strain pattern for the Type 2 (Thin Skin) panel (Figure 4) shows stronger indentation related strains underneath the inner rollers. This effect is so severe that it strongly influences the strain pattern between the inner rollers especially at the higher load levels.

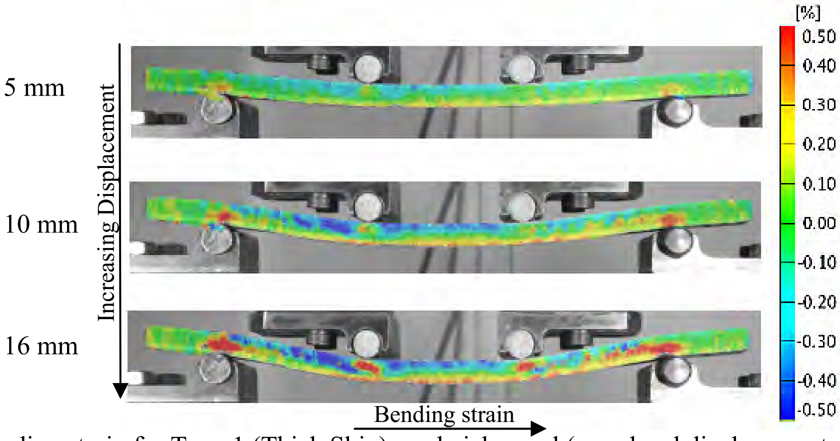

Figure 3: Bending strain for Type 1 (Thick Skin) sandwich panel (crosshead displacements of 5, 10 and 16 mm).

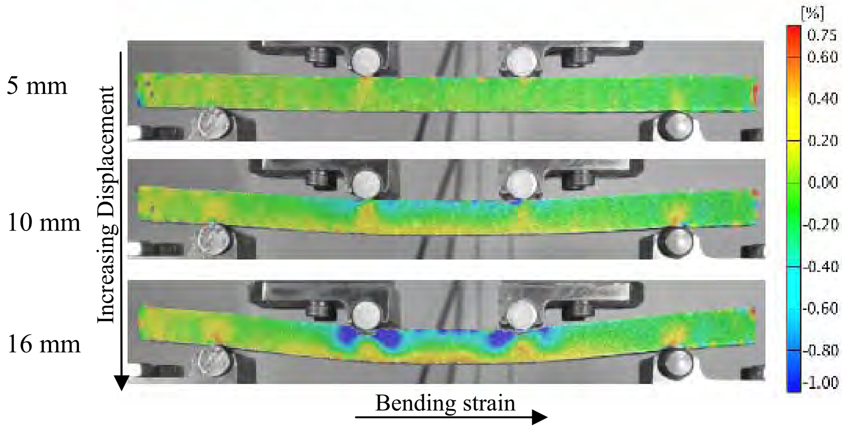

Figure 4: Bending strain for Type 2 (Thin Skin) sandwich panel (crosshead displacements of 5, 10 and 16 mm).

To quantify this analysis, Figure 5 shows the difference between the bending strain distributions for the two panel types along the specimen centreline for different levels of crosshead displacement (5, 10 and 16 mm at displacement rate of 0.33 mm s^{-1}). These crosshead displacements can be correlated to the load displacement graph shown in Figure 6. At 5 mm crosshead displacement, the Type 1 (Thick Skin) panel is showing a more conventional bending strain distribution, with the neutral axis close to halfway through the specimen. However, the Type 2 (Thin Skin) panel shows a significant amount of distortion along the profile. A clearer result is that of the intermediate displacement rate (10 mm), which shows bending strain at peak load for Type 2 (Thin Skin). At this stage both specimens are just leaving pure flexure, and the result is symbolic of the higher flexural rigidity of the Type 2 (Thin Skin) panel, i.e. the Type 2 panel has a higher load at this displacement compared to Type 1, and hence greater strain. It can be seen that the bending strain is more closely matched at 16 mm crosshead displacement, even though the two specimens are in states of failure via different mechanisms. A possible reason for this behaviour is because the Type 2 (Thin Skin) panel is entering the secondary loading stage where densification means that the foam is providing increasing resistance to further indentation.

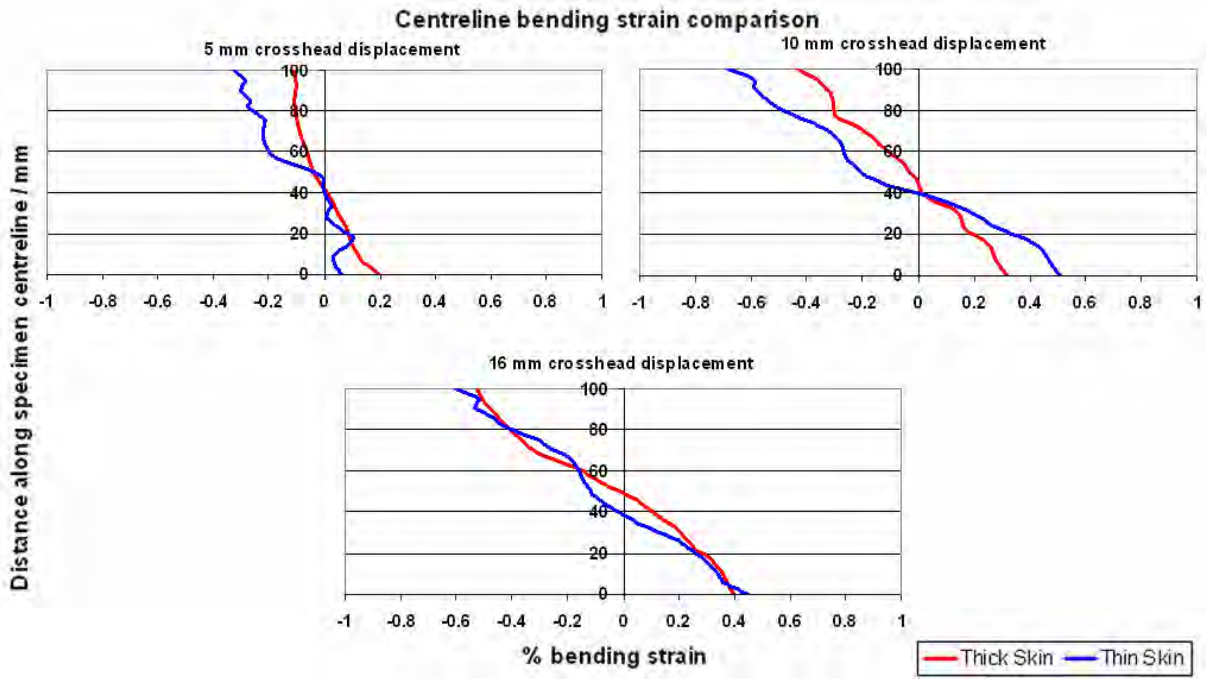

Figure 5: Comparison of specimen centreline bending strain for different crosshead displacements for the two sandwich panel (Type 1: Thick Skin and Type 2: Thin Skin).

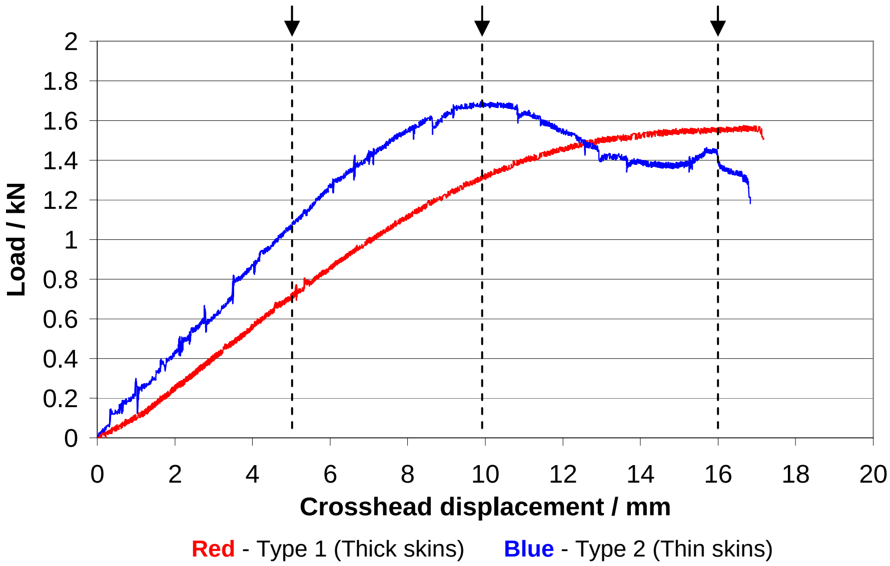

Figure 6: Comparison of load displacement data for two specimen geometries.

3.2 Failure Processes

Although indentation failure is undesirable, it does allow for an examination of the applicability of the DIC technique to this type of material. Indentation occurs as a result of insufficient resistance of the foam material, which collapses underneath the high level of compression of the inner roller. This is a result of the stress concentration of the roller. These results are shown in Figure 7, which is the principal strain ε_2 for increasing load levels, expressed as a percentage of the load causing initial indentation. The initial stage reveals no particular strain distributions or features. By 64% (of load causing initial indentation) the effects become detectable as a clear differentiation between the two sides where on the left of the roller the majority of strain is representative of bending, and on the right hand side where the strain is due to shear. At the higher loads, the strain contours are more representative of indentation, with high levels of compression occurring. From the loading graph it was deemed that crushing occurred in-between the stages 95% and 110% (of load causing initial indentation). Thus DIC could be used to estimate the strain level that would result in initial crushing of the core. It can be seen that the strain levels associated with crushing of the foam core are ca. 2% for this PVC foam core.

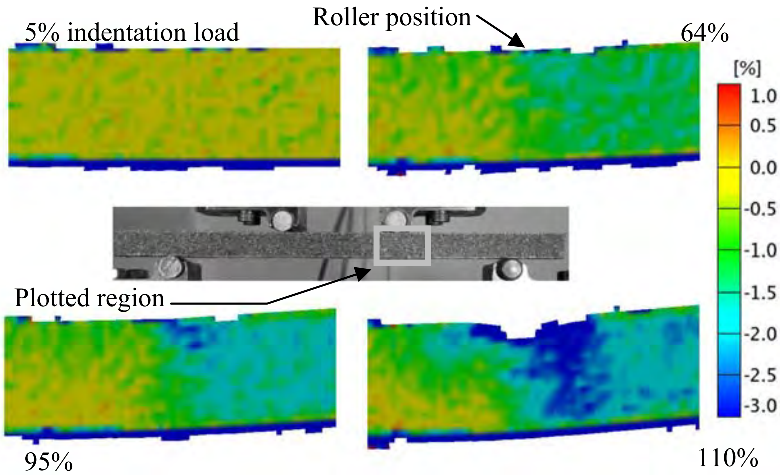

Figure 7: Close up of DIC ε_2 strain as indentation onsets.

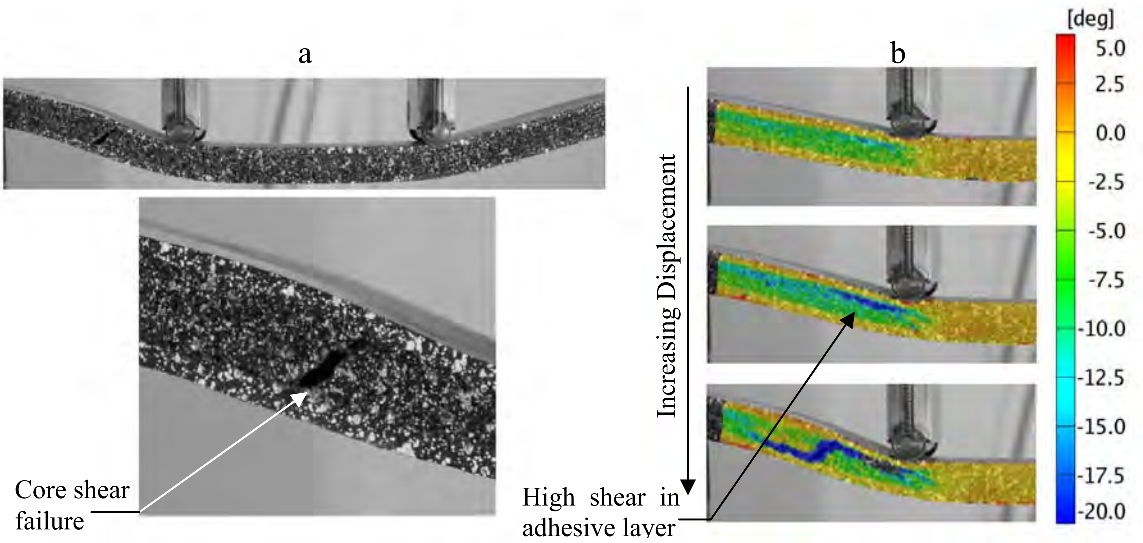

Figure 8: a) Core fracture of Type 1 sandwich specimen; b) Core shear failure DIC plot (shear angle).

Another failure was obtained on the Type 1 (Thick Skin) specimen. Here the shear in the core is at a high level, causing collapse of some cell walls along a 45^{o} line close to the inner roller, in-between the inner and outer rollers. This region is like a kink in the core that results in the departure from pure bending of the specimen, resulting in a plateau of the load levels. Further loading induced shear failure and eventually a crack did develop, as shown in the enlarged view in Figure 8a. Figure 8a also displays how the compressive skin hinges at the inner rollers, which is required to compensate for the core shear failure (otherwise the compressive skin in between the rollers would have greater curvature) [10].

The DIC strain plots for this failure are shown in Figure 8b, where shear angle has been plotted. To be noted is that the low level of indentation in Type 1 (Thick Skin) sandwich panels, results in shear in the adhesive layer between foam core and compressive skin. This is highlighted clearly in this the second stage of the image series. After further deformation, the shear of the adhesive is excessive, and it is believed that a disbond between the compressive skin and core triggers a fracture of the core, as shown in the third image stage. It is thought that the foam core is weaker than the adhesive and the foam fails in shear because of the shear-compression ratio. This result is particularly relevant to wind turbine blade loading geometry.

3.3 Comparison to Standard Metrology

In order to substantiate the DIC results, experiments were performed with DIC in addition to electrical resistance foil strain gauges on the tensile and compressive skins. A displacement transducer was also used, but for conciseness these results are not presented in this paper. Experiments were performed on both types of sandwich specimen under the same four-point configuration. In order to perform a fair comparison, experiments were kept to the low strain range, so that the gauges would continue to function throughout the entire range. Strain was extracted along the specimen centreline from the calibrated DIC results and used for the comparison. This information is shown below in Figure 9.

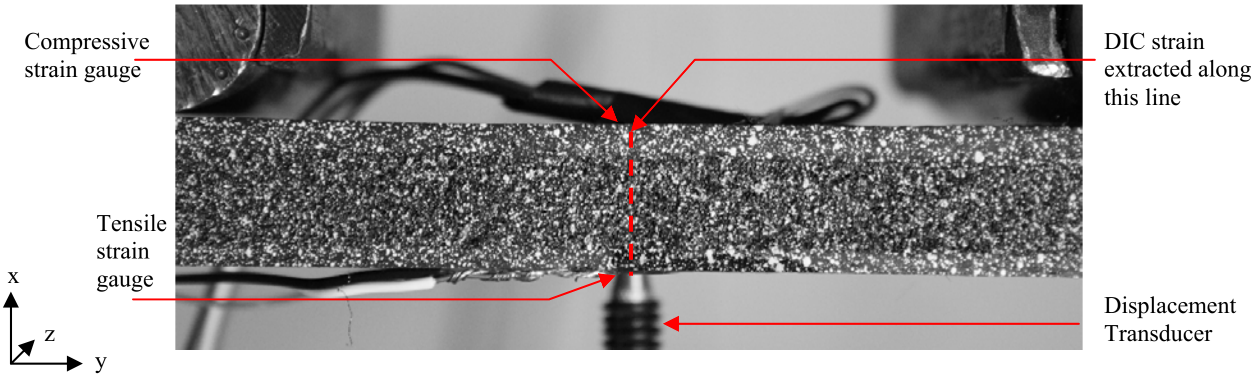

Figure 9: Position of strain gauges and displacement transducer.

The results for the strain comparison are given below in Figure 10, and as can be seen there is some general agreement. Specifically there is a good match of tensile behaviour for the

Type 2 (Thin Skin) sandwich panel, although there is some noise in the tensile results for the Type 1 (Thick Skin) sandwich panel at the higher load levels. Yet it is apparent that the compressive behaviour was more difficult to match. The two graphs show some matching between results early in the loading path, but then there are differences between the results at higher load levels.

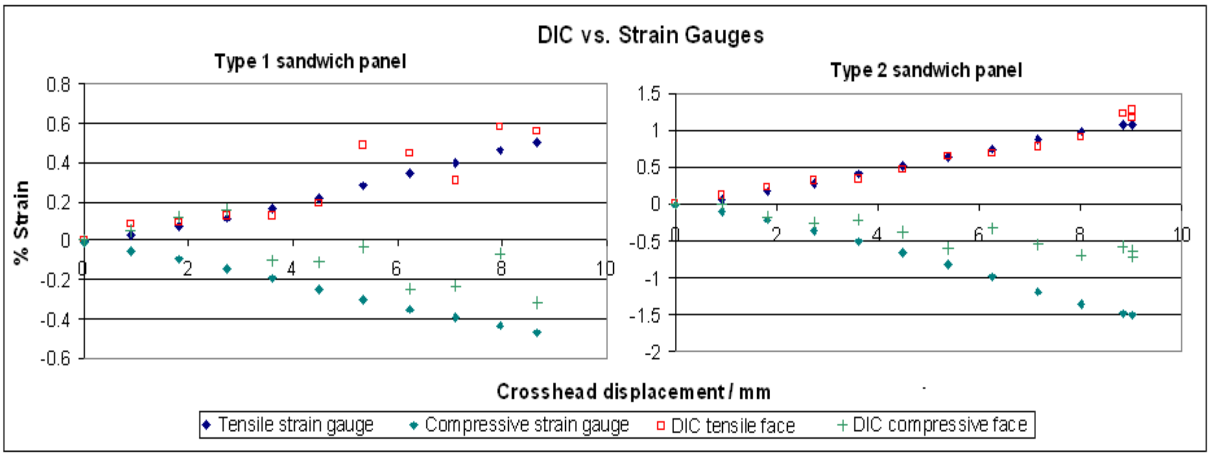

Figure 10: Comparison of DIC and strain gauge strain for Type 1 (Thick Skin) and Type 2 (Thin Skin) sandwich panels for both compressive and tensile faces.

To quantify the correlation, gradients along the linear sections of the strain results have been taken, setting the intercept to zero. The percentage differences between the strain gauges and DIC have been calculated and are presented in Table 1 below. Although tensile behaviour is matched to a difference of less than 10%, compressive behaviour is not so good.

Table 1: Percentage differences between DIC and strain gauge bending strain gradients.

		Bending strain gradient		% Diff	Width to thickness ratio
		SG	**DIC**		
Type 1	**Compressive**	-0.0549	-0.0225	59%	3.85
	Tensile	0.0626	0.0678	-8%	
Type 2	**Compressive**	-0.1796	-0.0906	50%	2.38
	Tensile	0.1330	0.1267	5%	

A logical explanation for this comes from the variation of thicknesses determining the degree of anticlastic behaviour. Research has shown that a reduced thickness to width ratio causes an increase in the anticlastic behaviour of a panel, causing high variations of out of plane strain in the z direction at the free surfaces of the specimen, [11, 12]. This is important because the strain gauges cannot be placed on the very edge of the specimen, and they have a finite width themselves, and thus resolve the strain at a point away from the free surface of the specimen, whereas DIC resolves at the free surface. From this it can be seen that the level of anticlastic behaviour should be worse for the Type 1 (Thick Skin) specimen, and as can be seen in Table 1 the matching of the gradients is worse for the Type 1, for both compressive and tensile direction.

A problem with this explanation is that literature shows that anticlastic curvature should be exhibited on both tensile and compressive skins [11, 13, 14]. However, for both specimens it can be seen that the effects are more pronounced on the compressive side, which could be due to the indentation effects being more prominent on the compressive side. Bending requires the compressive face to contract in the x direction. If indentation occurs then the face cannot slip past the roller effectively in the x direction, and is thus restricted. From Poisson's effect, expansion in the z direction must be increased to balance the contraction in the x direction (y direction expansion would be negligible considering the thin skin layers). Thus the indentation seems to magnify the anticlastic effect, and plays a part in the poor matching of the results. This explains why matching is better at lower strain levels, and why the tensile face strains do match well, as this face is still able to slide past the rollers.

3.4 FE to DIC comparison

To act as a direct comparison, a model of the Type 1 sandwich panels under 4-point bending was created using the finite element program ABAQUS. The panel was modelled as a 3D solid to allow out of plane strain of the foam. 20-node quadratic brick elements (C3D20R) were used for the foam core and 8-node doubly curved thin shell elements using 5 degrees of freedom per node (S8R5) were used for the composite skins. A refined, converging model consisted of 4056 elements. The loading was modelled as a pressure load over a contact area representative of the experimental roller diameters [15].

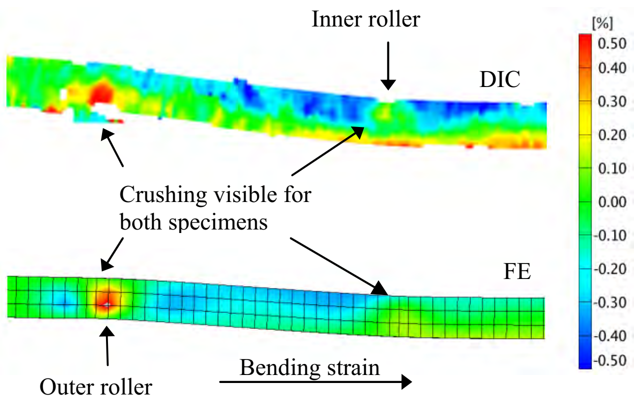

Figure 11: Comparison of DIC and FE results for Type 1 sandwich panel at same load level.

There was a degree of correlation between the FE results and the DIC, especially when looking at the bending strain results, as shown in Figure 11. The main similarities visible here are the crushing occurring at the inner and outer rollers. There is also some degree of compressive behaviour shown for both results in between the inner and outer rollers, although the DIC shows higher levels of this. Interestingly there is a clear difference when looking at the section in between the inner rollers. Here DIC and FE show strain synonymous to the flexure process. However, DIC shows higher strain levels and there is a significant difference between the results. An explanation for this is that the out-of-plane strain is picked up as inaccurate in-plane strain by the 2D DIC system, whereas it can be modelled exactly with FEA. Generally, there was some agreement between the results at this early stage, but improvements in both model and DIC technique would produce a closer match.

4 CONCLUSIONS

An aim of this research was to gain a better understanding into the failure processes that occur in lightweight sandwich material as a result of flexural loading that occurs inside a wind turbine blade. A feature was that the failure processes observed were affected by the indentation at the inner rollers. In particular, the Type 2 (Thin Skin) sandwich panel had indentation as its final failure mode which is of less relevance in a wind turbine blade. It did allow DIC to be proved a useful tool in the understanding of failure for this material. With a calibrated setup, preferably using 3D capture, the technique could benefit manufacturers design assessments, especially when coupled with the more conventional strain gauge data. It could also help to verify FE models, as was demonstrated with the Type 1 (Thick Skin) sandwich panel results. This could be a major benefit when a new blade geometry could be tested for structural integrity prior to major rollout of the design.

In addition to this, the experimental results for the Type 1 (Thick Skin) sandwich panel showed a representative failure mode with the high levels of shear in the adhesive and core. The capability of DIC to reveal relevant failures at load levels prior to non-reversible failure was demonstrated. This result has implications for inspection and maintenance of blades, where the technique could be used to flag up regions requiring attention on an aged or defected blade. To further this suggestion, DIC needs to be proved to be able to detect sub-surface defects, such as delaminations.

In summary, the test results presented show the versatility of the DIC system, and present a stepping stone for tests on larger substructure. At this early stage, it is believed that the technique could benefit blade development and manufacturing, as well as inspection and maintenance. Future experiments will develop upon the testing procedures shown, as well as introducing other aspects such as acoustic emissions monitoring. The final aim of this research is provide a toolbox of proven techniques and strategies that provide give wind turbine owners confidence about the structural integrity of their ageing blades.